Przemysław Lutkiewicz, M.Sc.
Graduate of doctoral program
Faculty of Civil Engineering
Cracow University of Technology
Graduate of CERN doctoral program

02.12.2009

PhD Thesis

The tightness conditions of UHV all-metal seals subjected to the radiation and inelastic deformation

mgr inż. Przemysław Lutkiewicz

Promotor: prof. dr hab. inż. Błażej Skoczeń

Completing the present Thesis has been possible thanks to the support of many people who during last couple of years have helped me in different ways.
Especially, I would like to thank my University supervisor (promoter), Professor B. Skoczeń as well as my CERN superiors: Ch. Rathjen, C. Garion and other colleagues from the AT/VAC group at CERN.
I also appreciate support from VECTOR AS Company (my current employer).
Neither would I have ever managed to finish it without the patience and understanding of my wife Halina Podsiadło. I also appreciate her advice, comments and big help when preparing most of the figures.

Streszczenie

Temat rozprawy doktorskiej jest związany z instrumentami naukowymi rozwijanymi przez Europejską Organizację Badań Jądrowych CERN, a ściślej z powstającym właśnie akceleratorem cząstek elementarnych LHC (tzw. Wielkim Zderzaczem Hadronów) oraz ogólnie pojętą technologią budowy akceleratorów.

Strona akademicka rozprawy, powiązana z rozwinięciem Kontynualnej Mechaniki Uszkodzeń w kierunku uszkodzeń radiacyjnych, przeplata się i ściśle łączy z praktycznym zastosowaniem nabytej wiedzy w procesie projektowania i definiowania nowych elementów konstrukcji akceleratora.

Początki tematyki pracy należy wiązać ze sformułowaną w CERNie potrzebą przeprowadzenia studiów nad połączeniami tzw. systemów wysokiej próżni typu ConFlat. Powyższe połączenia są stosowane od lat w urządzeniach UHV (ultra wysokiej próżni) na terenie CERN-u oraz są uznawane za rozwiązanie o raczej niskiej kosztochłonności i zadowalającej niezawodności. Idea połączenia polega na wciskaniu twardych metalowych (np. Stal 316LN) ostrzy kołnierzy w miękką, metalową (np. miedź) uszczelkę w postaci spłaszczonego pierścienia o przekroju prostokątnym.

Dokładny opis pracy połączenia został przedstawiony w Rozdziale 2.4 oraz 4. Po zaciśnięciu uszczelki powstaje na skutek odkształceń plastycznych charakterystyczna stożkowa powierzchnia odciśnięta w materiale uszczelki. Nazwa połączenia (ConFlat) jest wypadkową słów określających charakterystyczne jego cechy, a więc stożkową powierzchnię odciśniętą przez ostrza kołnierzy (*Conical*) i płaski kształt uszczelki (*Flat*). Miękki materiał uszczelki, ulega uplastycznieniu wskutek wbijania ostrzy i dopasowuje się do nierówności powierzchni kontaktowych uszczelniając połączenie. Rozwiązanie to stosowane jest powszechnie w akceleratorach istniejących na terenie CERNu (np.: w ISR około 6000 sztuk, w byłym LEP około 17000 sztuk). Dokładne zrozumienie mechanizmów uszczelniania zachodzących w powyższych połączeniach ma pomóc przy projektowaniu nowych typów połączeń.

Przykładem zastosowania zdobytej wiedzy jest zaprojektowanie alternatywnego połączenia dla przyszłego liniowego akceleratora CLIC (Rozdział 5). Akcelerator ten jest już obecnie w fazie projektowania i cząstkowych testów poszczególnych komponentów. Urządzenie stanowi zespół dwóch liniowych akceleratorów rozpędzających cząstki do energii 3TeV a następnie zderzanych w komorze detektora usytuowanego w środku między nimi. Dla powyższego kompleksu planuje się około 500000 połączeń typu UHV. Dlatego tak ważne stało się zaprojektowanie niezawodnego połączenia, spełniającego specyfikację wysokiej próżni UHV i wykazującego dobre właściwości RF (radio frequency) dla wysokich energii, lecz równocześnie zoptymalizowanego pod kątem zarówno kosztów produkcji jak i łatwości instalacji. Obecne rozwiązanie, bazujące na połączeniach typu X-band zaprojektowanych dla eksperymentu SLAC, jest połączeniem relatywnie drogim i problematycznym w montażu. <u>Zaproponowanie nowego typu połączenia spełniającego wszystkie wymagania jest znaczącym wkładem autora wniesionym w dziedzinę technologii wysokiej próżni (UHV)</u>.

W trakcie eksploatacji istniejących dotychczas połączeń wystąpiło jednak wiele przypadków nieszczelności. Jedna z hipotez zakłada, że uszkodzenia prowadzące do nieszczelności powstają w wyniku penetracji strumienia cząstek elementarnych w materiale połączenia. W akceleratorach cząstek (np.: LHC czy CLIC) tego rodzaju połączenia są często poddawane napromieniowaniu strumieniem cząstek elementarnych (jonów, protonów, neutronów, elektronów). Wskutek napromieniowania powstają w materiale defekty punktowe (pustki i atomy międzywęzłowe) oraz zgrupowania defektów nazywane klasterami. Powyższe defekty mają wpływ na zmianę mechanicznych własności materiału (wzmocnienie, kruchość, niestateczność plastycznego płynięcia

i inne). W niniejszej rozprawie przywołuję prace innych autorów, opisujących fizykalny aspekt procesu napromieniowania materiału. Dzięki symulacjom komputerowym na poziomie sieci krystalicznej (typu MD – dynamiki molekularnej czy przy użyciu metody Monte-Carlo) istnieje obszerne źródło wiedzy na ten temat. Do chwili obecnej nie istniał jednakże kompletny opis ewolucji uszkodzeń wywołanych napromieniowaniem w sensie równań konstytutywnych. Moim oryginalnym wkładem w do tej dziedziny jest stworzenie matematycznego opisu zachowania materiału z uwzględnieniem uszkodzenia wywołanego zarówno czynnikami mechanicznymi, jak i czynnikami wynikającymi z napromieniowania strumieniem cząstek elementarnych. Od strony akademickiej w mojej pracy poruszam się w dziedzinie równań konstytutywnych związanych z Kontynualną Mechaniką Uszkodzeń (KMU). Dziedzina ta opisuje – między innymi - materiał pracujący pod wpływem obciążeń mechanicznych, generujących pola odkształceń niesprężystych i stowarzyszone z nimi pola uszkodzeń. Samo uszkodzenie może mieć charakter kruchy lub ciągliwy, zaś parametr opisujący pole uszkodzeń może być skalarem (Kachanov [56], Rabotnov [102]), wektorem (Davison oraz Stevens [31], Kachanov [57]), tensorem drugiego rzędu (Rabotnov [103], Vaculenko i Kachanov [130], Murakami i Ohno [85], Litewka [74], Garion i Skoczeń [44]), tensorem czwartego rzędu (Chaboche [24], Simo i Ju [114], Krajcinovic [65], Chen i Chow [25], Voyiadjis i Park [133]) lub nawet tensorem wyższego rzędu. Wszystkie te podejścia opisują „mechaniczny" aspekt uszkodzenia. Nowatorstwo obecnej pracy jest związane z rozszerzeniem KMU o aspekt uszkodzeń powstałych pod wpływem napromieniowania wiązką cząstek elementarnych (Rozdział 3).

Ostatecznie cel pracy jest powiązany z trzema przedstawionymi poniżej aspektami. Każdy z nich jest logiczną kontynuacją i rozszerzeniem poprzedniego.Całość jest poprzedzona wstępem na temat istniejących obecnie rozwiązań konstrukcyjnych połączeń dla systemów ultra-wysokiej próżni UHV (Rozdzial 1 oraz 2) oraz bogatym zakresem badań doświadczalnych (Rozdział 7).

1. (Rozdział 4, publikacja [76]); Zbadanie i zrozumienie za pomocą symulacji komputerowej oraz stosownych eksperymentów mechanizmu szczelności oraz właściwości mechanicznych dla popularnego w CERN połączenia systemów wysokiej próżni typu ConFlat. Szczegółowy schemat pracy powyższego połączenia nie był podany wcześniej przez żadnego innego autora. Zbadano również wpływ właściwości materiałowych uszczelki oraz geometrii ostrza kołnierza typu ConFlat na zachowanie połączenia pod wpływem obciążeń mechanicznych (zamknięcie połączenia). Analiza wrażliwości połączenia na zmianę właściwości materiału uszczelki jest krokiem w kierunku badań nad wpływem napromieniowania strumieniem cząstek elementarnych. Poza czysto poznawczymi badaniami równocześnie przestudiowano przyczyny nieszczelności połączeń w warunkach pracy akceleratora LHC (hipoteza penetracji wiązki cząstek elementarnych w materiale połączenia). Stworzono również matematyczny opis mechanizmu uszczelnienia (na podstawie obliczeń numerycznych) przydatny przy inżynierskich pracach projektowych.

2. (Rozdział 5, publikacja [77]); Rozwinięcie alternatywnego typu połączenia dla nowego akceleratora CLIC (obecnie istnieje tylko jedna wersja połączenia). Połączenie takie ma spełniać warunki szczelności, przewodności fal elektromagnetycznych wysokich energii (high power RF), oraz ma być tanie i łatwe w montażu. Zaprojektowanie nowego połączenia jest znaczącym wkładem autora do projektu akceleratora CLIC.

3. (Rozdział 3 oraz 6, publikacja [78] oraz [79]); Stworzenie spójnego zestawu równań konstytutywnych opisujących zachowanie materiału pod wpływem obciążeń mechanicznych oraz radiacyjnych. Opis materiału obejmuje zachowanie sprężysto-plastyczne, ewolucję uszkodzeń mechanicznych, radiacyjnych, post-radiacyjnych oraz zmianę właściwości materiału pod wpływem napromieniowania. Jest to nowatorski aspekt pracy, zwłaszcza w części nawiązującej do mechaniki uszkodzeń radiacyjnych i post-radiacyjnych. Opis

uszkodzeń radiacyjnych w aspekcie Kontynualnej Mechaniki Uszkodzeń (KMU) nie był dotychchczas szeroko podejmowany przez autorów w kraju czy na świecie . Aspekt ten jest równocześnie ściśle związany z obliczeniami połączenia typu ConFlat (w kontekście projektu LHC) oraz połączenia projektowanego dla nowego akceleratora CLIC. Równania konstytutywne zostały zaimplementowane w środowisku obliczeniowym CASTEM, bazującym na Metodzie Elementów Skończonych.

Chapter I:

Introduction

1 INTRODUCTION

The scope of the present Thesis is dual, connecting theoretical and practical objectives. First of all, an extension of the Continuum Damage Mechanics (CDM) to the cases where radiation driven lattice damage is present remains the main goal. The irradiation and post-irradiation laws of damage evolution under mechanical loads will be formulated. Such extension of CDM may become a powerful and useful tool for the engineers working on the nuclear structures. Also, during the designing process of the biggest accelerators or space projects the extended CDM can help to predict behaviour and failure probability of components. For accelerators like the Large Hadron Collider (LHC) or the Compact Linear Collider (CLIC) the origin of damage is related to the high energy beam, whereas for the space structures it is rather related to the flux of particles coming from space.

The practical objective is connected with all-metal joints working under the radiation conditions. Because of high intensity of plastic strains the Continuum Damage Mechanics is a necessary step forward in the joint analysis. The micro-damage accumulated in the seal material can become an important factor for the joint sealing capacity. It will also be more appropriate to describe damage generated by the irradiation process and its post-irradiation evolution, especially for parts (components) subjected to high radiation dose.

The theory presented in the thesis covers the following important problems:

- How to unify the irradiation patterns (the dpa definition),
- The micro-voids creation during the irradiation process (irradiation damage),
- The post-irradiation damage evolution under mechanical loads,
- The evolution of material properties driven by the irradiation (yield point increase, decrease of ductility, irradiation hardening),

From the practical point of view, the so-called ConFlat joint will be examined in the framework of the elastic-plastic approach. The ConFlat joint has been chosen as a good example of all-metal joints. The joints subject is wide, complicated and contains number of different problems. In that thesis research will be focused on the innovative material behaviour description (gasket properties: mechanical and postirradiation damage) rather than on the complex description of joint behaviour (bolt pretension, load and thermal cycles). ConFlat type of joint remains the most common solution for the LHC project and deep insight into the degradation mechanisms may contribute to the increase of its reliability. In what follows, the sensitivity of material parameters with respect to joint behaviour will be presented for this type of seal. This is an important issue because of diversity of materials originally used for gasket manufacturing. Another important aspect is related to the fact that the mechanical properties of the material evolve during the irradiation process.

In the next sections the parametric optimisation of the joint, inscribed in the design process of the CLIC ultra-high vacuum (UHV) systems wave guide flanges is presented. During the shape optimisation process the knowledge gained within the previous ConFlat joint analysis will help in the work. Finally, the Continuum Damage Mechanics will be applied to the analysis of all-metal joints in order to predict and explain the joint failure mechanisms (in the sense of loss of tightness).

All the above mentioned studies are important in the light of design of components and safe operation of new accelerator structures, like in the case of LHC or CLIC. It should be mentioned, that some 17000 ConFlat joints will be installed in the LHC and nearly 500000 all-metal joins (new design presented in the thesis) will be used in the CLIC accelerator. Their reliable performance becomes vital for correct operation of both colliders.

The structural analysis has been carried out by means of self-implemented FE code (based on the extended Continuum Damage Mechanics). The code can be used for any future problem of similar nature related either to the classical ductile damage evolution or to irradiation induced micro-damage (irradiation and post-irradiation damage) or both.

1.1 Modern instruments of high energy physics

CERN – the European Laboratory for Particle Physics was funded in 1954 and belongs to the largest and most modern research centres in the world. The laboratory contains a number of sophisticated instruments of particle physics aimed at confirming and extrapolating the Standard Model of the matter, which assumes tree families of quarks and leptons as basic constituents. The CERN equipment for physics experiments includes accelerators, storage rings and colliders designed to produce, accelerate, store and collide the beams of high energy particles in the vacuum conditions.

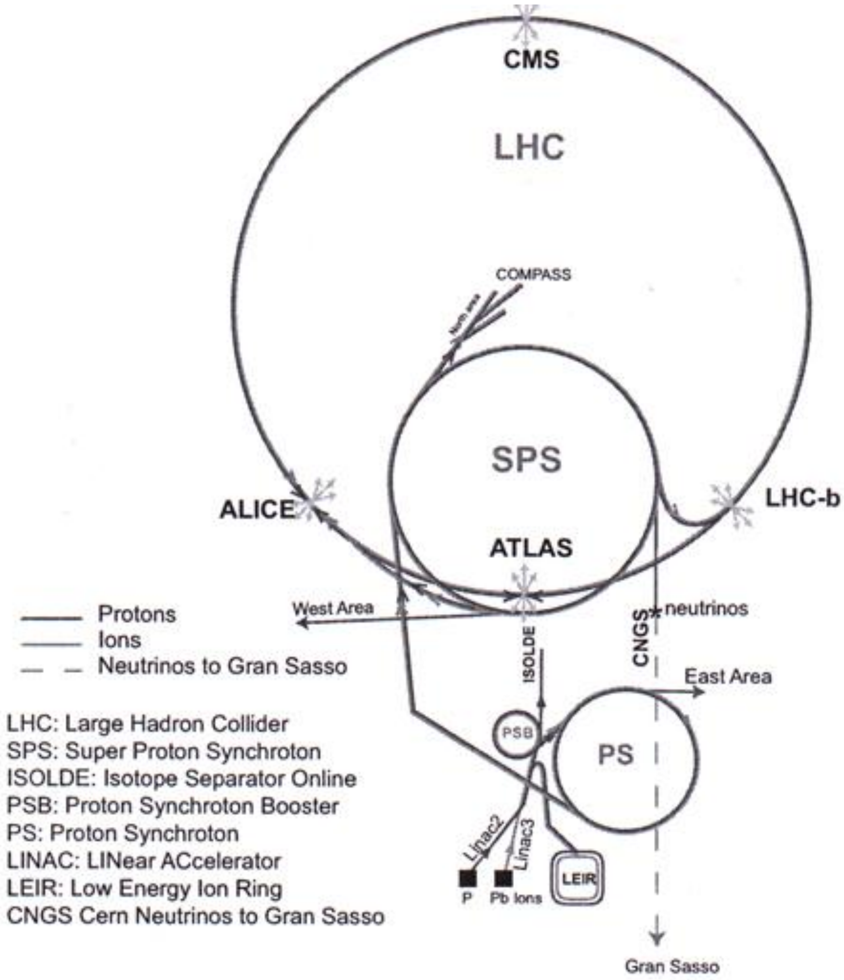

Figure 1 : CERN accelerator complex

Using these instruments it is possible to search and report on the new elementary events or deliver data for describing, understanding and confirming already known reactions. CERN deals with different types of particles such as electrons, positrons, protons, antiprotons and heavy ions. For each case there is a different technique to produce the beam, but all of them are based on acceleration first by a linear accelerator and - in the second stage - by a circular one. The circular machines are the heart of the laboratory. They constitute the last stage of acceleration and they are limited by the energy defined for the beam. The CERN accelerators complex is shown in Figure 1 [144].

On August 1, 1957, the Synchro-Cyclotron of 600MeV (SC) had reached its full design energy. SC was the first circular accelerator working at CERN. Afterwards, in 1959, the 28GeV Proton Synchrotron (PS) came to operation (after Knaster [60]). The design and construction work has taken eight years. These first accelerators were working with one beam of particles which was collided with a fixed target. The collision energy E_{CM} in this case was increased only with the square root of the accelerator energy (Eq. 1), where m is the particle mass and E is the beam energy.

$$E_{CM} = \sqrt{2mc^2E}$$ Eq. 1

Big disproportion between the beam energy and energy available during collision with fixed target pressed scientists to develop the accelerators where two particle beams with energies E_1 and E_2 were accelerated in opposite directions and collided head-on. The collision energy in such a design is described by Eq. 2 and it is more economical in terms of the beam energy. Also, it is worth pointing out that the number of interactions between beams is much lower than in the case of fixed target.

$$E_{CM} = \sqrt{E_1E_2},$$ Eq. 2

So, after the first two installations, the 2 km in circumference Intersecting Storage Ring of 31.4 GeV (ISR) was designed and constructed at CERN. This machine was designed for a nominal luminosity of $4x10^{30}$ $cm^{-2}s^{-1}$ but even in 1974 after three years of running reached only the 10^{28} $cm^{-2}s^{-1}$ level, which led to redesign of the vacuum system. The luminosity is proportional to the probability of an event to happen, which is fundamental for physics research and depends on the reliability of the vacuum system (the vacuum quality). The vacuum system for this machine contained more than 6000 seals, conical-flat in shape (further called CF seal or joint), reliability of which had a big influence on the operating vacuum range.

Next accelerator 400 GeV Super Proton Synchrotron (SPS) was aimed at confirming the so-called unified gauge theory known as the Standard Model of Particle Physics. The machine was operational in 1976. The Large Electron Positron (LEP) collider was a 27km circumference machine that stored the electrons and positrons up to an energy level between 50 and 60 GeV at the beginning and 104 GeV in its last runs in 2000. The construction took six years and LEP was completed in 1989. It consisted of 3368 dipols, 816 quadrupoles, 504 sextupoles and 700 other magnets installed in the 27 km round tunnel located at the depth between 40 and 140 m in order to reduce the background influence for experiments (cf.[144]). The vacuum system with operating pressure of 10^{-10} Torr was required to obtain designed luminosity. Also there, the CF seals have big contribution to the reliability of all UHV systems because of their particularly high number (17000 joints).

Finally, the Large Hadron Collider (LHC) has been designed and built, the concept of which has been worked out as a consequence of the analysis of data obtained from LEP. LHC is equipped with four experiments integrated in the main ring; the ALICE for ion physics study, the LHCb for CP violation research, the ATLAS and the CMS for general physics experiments, but mainly connected to the Higg’s model study. The goal of the collider is to reach 7 TeV energy per beam and the luminosity of $10^{32}cm^{-2}s^{-1}$. The LHC accelerator will be housed in the same tunnel where LEP was placed (Figure 2).

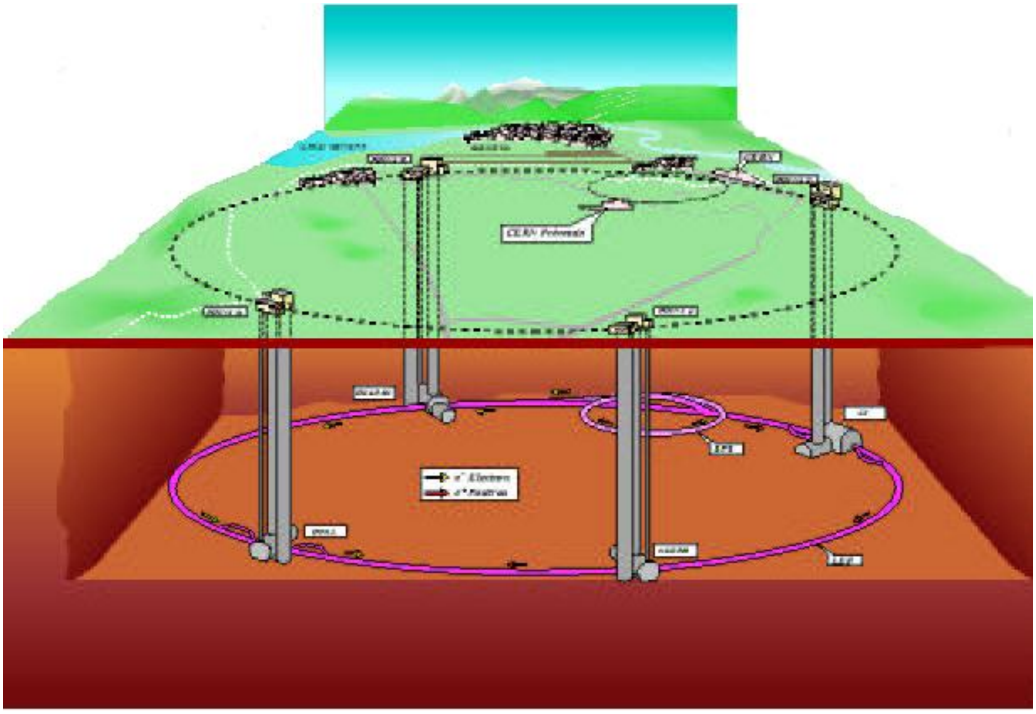

Figure 2 : 3D schematic view of LEP/LHC layout

It is planned to feed the LHC accelerator by the existing smaller accelerators (like PS and SPS), that will work as boosters. To keep the energy of beams in the designed limits sufficiently strong magnetic bending field is required. Thus, apart from the accelerating cavities and focusing/defocusing main quadrupole magnets, some 1232 bending dipoles (MB) were installed. The magnets operate at cryogenic temperature of 1.9 K in order to use the superconductivity and produce 8.36 T magnetic bending field. The LHC structure is unique and the superconducting magnets are cooled by means of the super-fluid helium (He-II) down to 1.9 K. Two magnetic channels housed in the same yoke and cryostat guide two parallel beams, which will save the space in the tunnel and reduce by about 25% the cost w.r.t. two separate lines (Figure 3).

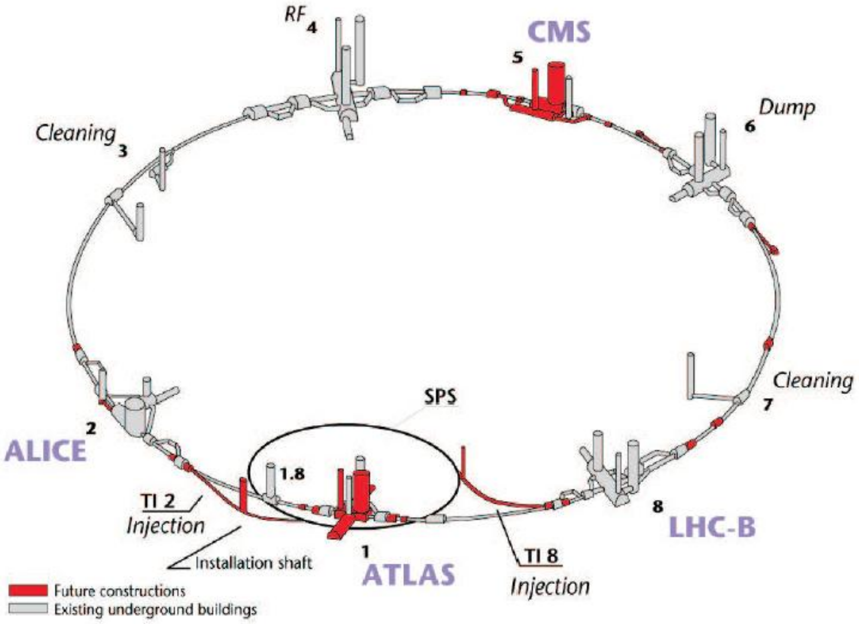

Figure 3 : LEP to LHC adaptation layout

Generally, the LHC is composed of about 1700 main magnets (dipoles and quadrupoles) and magnet to magnet interconnection zones, which have to be mounted in the common continuous cryostat (vacuum vessel).

The future CLIC accelerator will be of linear type in the TeV energy range. It is planned as the LHC successor. This new generation accelerator is planned for multi TeV lepton physics. This new electron-positron collider will provide significant fundamental physics information, even beyond this available from the LHC and from existing lower-energy linear e+/e- colliders. It will be based on normal conducting magnets because of high current frequency 12 GHz and high acceleration gradient of 100 MV/m (cf. Battaglia [11]). The machine will comprise two particle beams accelerated in two 21km long ultra-high vacuum (UHV) chambers. The particles within each beam will be accelerated towards each other and collided in the detector placed in-between. The layout of this machine is presented in Figure 4.

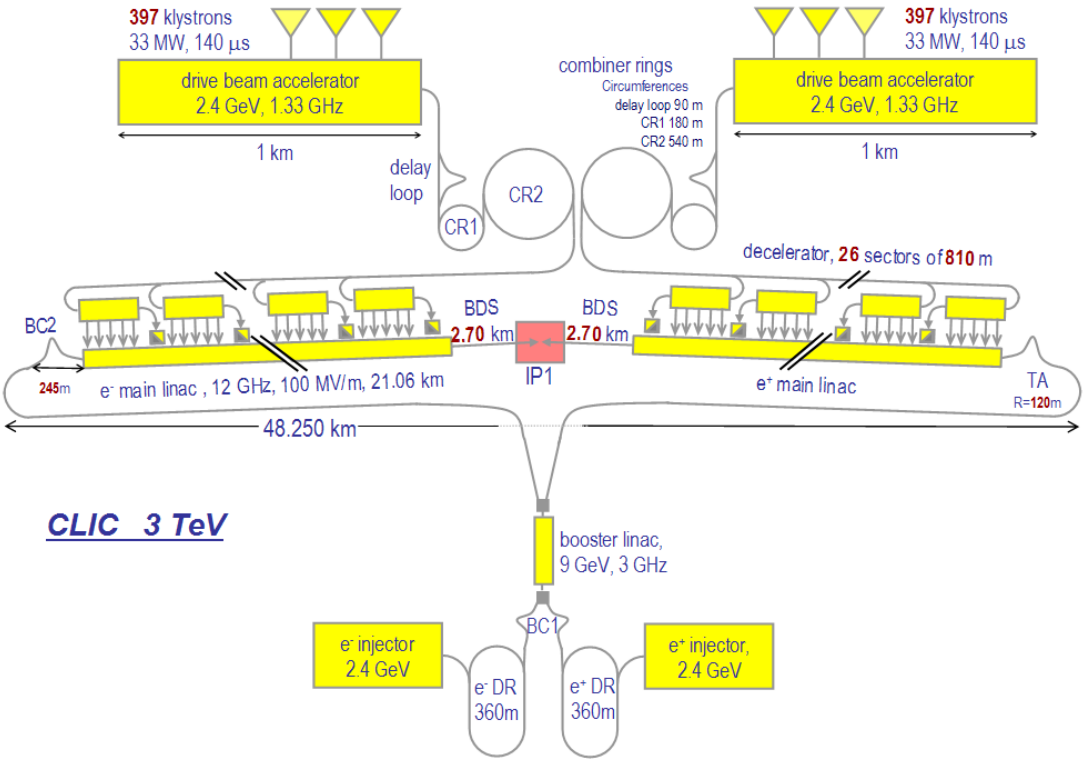

Figure 4 : Schematic layout of the future CLIC accelerator complex

1.2 Technical background of UHV systems

The UHV systems used in accelerators and other high energy physics machines are based on metal gasket seals. For example Schuman [110] mentions the radiation damage in the elastomer O-ring seals in the Alternating Gradient Synchrotron (AGS) at Brookhaven National Laboratory, which decided in 1965 to choose other metal joints. In the same paper other reliable candidates were compared and discussed: indium or aluminium wire, CF seals, Marma Conoseal, Parker Vee seal, Tetraflour Vee seal, Harison K seal, coined gasket, Adar seal, Ultec Curvac and aluminium foil seals. In 1989 Welch et al. [122] reported on some tests carried out on different seals used at AGS (C-rings, Al diamond seals, and others). Specific problems with C-rings were reported, which were spontaneously cracking. Because of this fact the Delta® seals replace about 300 old C-rings. As a result of special requirements for each machine, it is common to make tests and comparisons of existing makes in order to choose the suitable one.

The other work in the framework of sealing technology for high energy physics machines was carried out in 1977 by Wheeler [123], who presented a comparison of the seal candidates for the Tokomak Fusion Test Reactor constructed at the Princeton Plasma Physics Laboratory. Two years later the same problem was considered by Fleming et al. [39], who presented a comparison of the seal candidates for large non-circular ports in the TFTR. On the occasion of his works the multilayer-core seal consisting of the helical wire flex core bound with the jackets (usually two: the first made from normal metal, the second made from a soft one) was reported as the most suitable solution.

Finally, the comparison studies about the CF and multilayer-core seals for Advanced Photon Source (APS), Storage Ring Vacuum Chambers (SRVC) for Argonne National Laboratory were presented in 1991 by Gonczy at al. [48].

The vacuum systems at CERN are confronted with tight specifications. The number of existing joints pushed the scientists to search for the high reliability design. The radiation background is generated by the collision of the primary particles with other "artificial" particles resting in the beam vacuum chambers. In order to minimize this effect, the Ultra High Vacuum (UHV) standard is required. The UHV condition means the vacuum range of not less then 10^{-12} Torr. Such a low pressure is also convenient for adequate lifetime of the circulating particles. UHV systems require high temperature bake-out treatment to accelerate desorption of gas and vapour. The minimum required baking temperature is 300°C, as was mentioned by Elsword et al. [36]. The maximum temperature taken in to account in the LHC design is 350°C. On the other hand, some of the seals will work at the temperature of 1.4 K (close to absolute zero). Such a range of temperatures is not convenient for any elastomer gasket seal. High temperatures promote thermal degradation or cause rapid gas evolution in the organic materials. On the other hand, low temperatures make the organic materials really brittle. So the best solution is a soft metal gasket for the sealing joints.

Also the radiation means a real danger for any other material then metals. Peacock [98] for example showed the influence of the radiation damage on most common polymers. Very high radiation level is usually detected in the high energy physics equipment, such as LHC accelerator. High intensity radiation can modify the metal properties as well. However metals are certainly among the most resisting materials.

The other reasons why this type of joint is in common use at CERN are the advantages like: wide operation temperature range from -196°C to above 500°C, no male and female halves, quite easy gasket handling, not expensive gaskets (in case of the copper make), high resistance of the flange seals against damage and scratches (after Varian description [143]). The drawbacks are the high sealing forces required and the cost, especially for larger diameters. Summarizing, it is the question of high reliability compared with a reasonable cost that makes CF seals attractive. It is worth pointing out, that they were used at CERN over the past 35 years.

In 1968 Wikberg [125-126] reported some leaking problems with the CF flanges ordered for ISR accelerator and mounted on prototype tanks. After primary investigation it was clear that there were long micro-channels located near the knife edge. After having made the micrographs of the grain structure it was believed that the flanges were made from rolled plates rather than forged ones, which was probably the reason of leaking.

Two years later, in 1977 Unterlechner [120] presented wide report about the CF failure investigation for ISR ultra-high vacuum system. The leaking joints were detected as a result of three main mechanisms. The first is connected with the gasket material. It was stated by the author that the half-hard copper after bake-out at 300°C changed the yield point from about 200 MPa to 50 MPa in the annealed state. To overtake this weakness the OFS copper with high recrystalization threshold was proposed. Next reason was connected with the working and the mounting conditions. Sometimes two flanges with different knife-edge diameters were sealed, which led to the umbrella like deformation of the gasket. The overwhelming number of leaking gaskets was found with imprint of fibres (mostly organic). Another reason of fault was the non-uniform heating during bake-out treatment and using the low-strength material for bolts.

In addition, the problem of oxidation of the gasket surface was mentioned by Wikberg [126] during the same year. After comparison of different coatings, the most fitting solution for this problem - the Ag-coating was proposed.

The CF type joint has been presented by Varian in 1962. The solution consists of flat copper gasket compressed by two flanges with knife edges. The original geometry of the sealing surface was conical, normal to the gasket surface on one side and ridge inclined at an angle of 70° on the second side of the knife edge. Now, there exist a lot of variants of CF geometry. They are different from the point of view of both angles of the knife and the tip radius (Korokouchi at al. [61]), the gasket thickness (1.6 - 2.0mm) and the knife imprint depth (0.3 - 0.4mm).

Some work has been done by Kurokouchi et al. [61] to explain the influence of the knife geometry on the sealing process. The authors used experimental data and the FEM analysis to compare some different CF flange designs and explain the knife geometry influence on sealing mechanism. This interesting work injecting some ideas into the matter is composed of the experimental and the FEM analysis, but the authors were not precise enough in the description of the FEM analysis. For example, there is no information if the gasket material was considered elastic or elastic-plastic. Also, there is no information why the rigid body condition was assumed for the knife especially that the authors mentioned that the knife was deformed during operation. In addition, the authors haven't presented direct confrontation of the FE analysis with the experiments. In the other work, the same authors [63] compare two seal designs: CF flanges with normal and taper gasket, also using the FEM analysis.

Another work aimed at characterizing and describing the sealing mechanism of CF design was presented by Kitamura et al. [59]. The authors were using the FEM and the results were compared with the experimental data. Reasonable accuracy has been obtained, however the authors were modelling rather the whole, completed sealing system instead of going into details related to the gasket behaviour and the flange to gasket interaction. The shell elements were used to model the flanges, the beam elements for bolts and the truss elements for gasket instead of the axi-symmetric 2D plane elements like in the gasket analysis presented by Kurokouchi et al. [61-64]. Quite similar work describing the sealing mechanism was carried out by Diepens [33]. All of them took into account the temperature influence of the bake-out treatment.

What is the best configuration for the knife geometrical parameters and how do they affect the sealing process? This is one of the most important questions to be answered in the present work. The FEM analysis will be used in order to explain the sealing mechanism. The elastic-plastic model of the gasket and the flange material as well as the Continuum Damage Mechanics will be applied. Also, a comparison with the experimental data will be made, aimed at confirming the precision of FE modelling.

1.3 Radiation influence

There are two groups of the particles. The first one consists of electrons, beta particles, protons, alpha particles, ions, and they are called the charged radiation. The second one comprising photons (gamma or X-ray) and neutrons forms the group of neutral of particles.

The photons do not have mass, but they are pure energy and their velocity is equal to the speed of light. They belong to the particles easily penetrating the target. The range in air for 1MeV energy is equal to 82.0 cm, based on 99.9% reduction. The electrons have the lowest molecular weight (0.00054858 u), so they are easy to accelerate (for 1MeV energy the speed is equal to 94.1% of the speed of light) and have the range in the air equal to about 319.00 cm (cf. Holbert [51]). The electrons have the charge of -1. The next are the protons and the neutrons. Both have nearly the same molecular weight (1.007276 u and 1.008665 u, respectively) which leads to nearly the same velocity (for 1 MeV about 4.6% of the speed of light). The range in the air for protons is equal to 1.81cm and for neutrons 39.25 cm for 1 MeV energy. Protons have the charge of +1. The heaviest ones are the alpha particles with the molecular weight of 4.001506 u and the charge of +2. They need high energy to get accelerated (for 1MeV their speed is equal to 2.3% of the speed of light) and their range in air is the shortest one and equal to 0.56 cm for 1MeV energy.

All this information leads to the conclusion that the charged particles are passing through matter less easy then the neutral ones. This is connected to the fact that alpha, beta, and protons strongly interact with the orbital electrons of the target material, and lose their energy faster than the neutral ones. The second condition, which has the influence on the penetration distance, is the molecular mass. It is strong acting in case of the charged particles. This is the main reason to define the heavy charged particles (alpha particles, protons) and the light charged particles (beta particles, electrons) in the form of two groups. To calculate the range of penetration of particles, first the range in the air is needed. The range of protons in the air can be - for example - described by Eq. 3 (Holbert [51]), where E_p is the beam energy expressed in MeV.

$$R_{air} = \left(\frac{E_p}{9.3}\right)^{1.8} \qquad \text{Eq. 3}$$

When the range in the air is defined, the Gragg-Kleemen rule (Eq. 4 and Eq. 5) can be used to define the range R_{mat} in the other materials (mat), for example copper:

$$R_{mat} = 2.3\times10^{-4}\frac{\sqrt{M}}{\rho}R_{air} \qquad \text{Eq. 4}$$

$$R_{mat} = C_R R_{air} \qquad \text{Eq. 5}$$

This rule refers to the molecular weight M [u], density ρ [g/cm^3] and the range in air R_{air} [cm]. The transition multiplier values C_R for different gasket materials are presented in Table 1.

Table 1 Transition multiplier values C_R for different materials

Materials	Molecular weight M [u]	Density ρ [g/cm^3]	Multiplier value C_R []
Gold Au	196,967	19.3	0.0001673
Silver Ag	107.868	10.49	0.0002277
Copper Cu	63.549	8.96	0.0002046
Aluminum Al	26.981	2.375	0.000503
Lead Pb	207.2	11.34	0.000292

The heavy charged particles (such as protons or alphas) lose their energy in small steps, passing through solid material. Until the energy is sufficient, there interacts with the electrons and nucleus and energy loss is done due to nuclear collision. After that, there become atoms in form due to electron(s) capturing; hydrogen from protons, or helium from alpha particles. Because of the size and the weight it is easy to define their motion. Heavy charged particles travel deep into the solid by following the straight paths.

The light charged particles (electrons or X-rays) can lose their energy by passing through the solid in different ways. The first one is the ionization process, the second one is the Bremsstrahlung mechanism, which means creation of X-rays from electron deceleration, and the last one is the elastic scattering from nuclear and electronic interaction. Instead of the straight paths like for heavy ones, the light charged particles have greater range of penetration and variable trajectory (discontinuous in terms of the momentum vector).

The particles of the last group (the neutral ones), interact mainly with the atomic electrons. The main mechanism of energy loss is scattering and absorption. Photons can interact with solid in different ways depending on their energy. For the energy level lower than ionization energy (usually less than 200 KeV) all photon energy is transmitted into orbital electrons. For the photon energies of 200 KeV up to 1.5MeV the Compton scattering is the energy loss mechanism until the energy level will be less than 200 KeV. Finally, for photons with the energy higher than 1.5 MeV, there is the pair production process. Photon disappears and the electron (or negatron) – positron pairs are formed instead.

The radiation influence on solid materials is usually referred to as radiation damage. A proper formulation of the constitutive equations in the framework of continuum mechanics, including the properties of irradiated materials, will be developed. Changes in the material properties as well as evolution of radiation damage in the lattice shall be described by means of the continuum damage mechanics theory. The effect of radiation it caused by the particles accelerated and having the kinetic energy high enough to penetrate the solid. The radiation effect expressed in terms of intensity of damage fields depends strictly on the particle type.

Chapter II:

The Sealing Mechanisms

2 THE SEALING MECHANISMS

The gasket seals are defined as resilient parts placed between two rigid surfaces to obtain a leak-free seal. The seals form leak-tight joints loaded by compressing a gasket between the sealing parts.

It was shown that even flanges with good finished surfaces joined together are not sufficient to make proper connection in sense of the leak tightness (cf. Roth [107-108]). The very narrow channels have always appearing between them (Figure 5). Even the smallest ones are not permitted in Ultra High Vacuum (UHV) systems because they constitute considerable leaks. If there is no gasket in between, a very high force must be applied to both flanges in order to leak-tight joint. This is the reason why a soft gasket between the sealing parts is needed, which fills up small irregularities.

Some authors indicate that given the plastic flow of gasket material, practically any rough surface can be sealed. The soft metal gasket crushed between two flanges will fill the micro channels even for rough surfaces, up to at least 250-rms finish (cf. Moore [84]).

Because the gasket seals require constant conditions, perfect align the parts of the seal and usually high sealing force, the seal should be designed only for sealing purposes, that means not bear any other mechanical load.

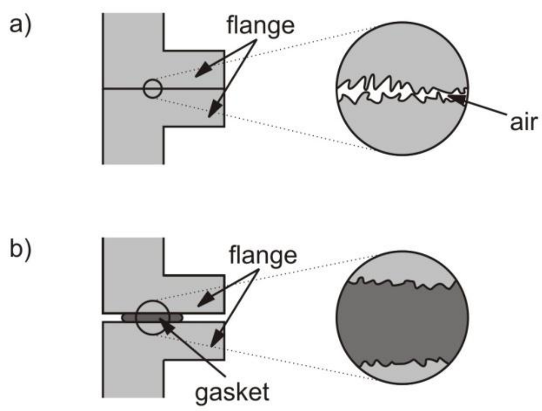

Figure 5 : Seal cross-section: (a) without gasket – not tight; (b) with inserted gasket – leak-tight joint

The ideal gasket behaviour should be elastic-plastic. Plastic behaviour is especially desired near the surfaces where the contact with flanges appears in order to easily filling the gaps between gasket and flanges. Elastic properties of the gasket material are needed in order to maintain the pressure exerted on the seal.

Unfortunately it is hard to find a material with the perfect plastic character near the contact surface and elastic behaviour in the core for the same material.

The most commonly used rubber is hyper elastic. Other quite often used materials for gaskets are soft metals (for example copper, gold, silver, indium, aluminium); all of them have good plastic properties. The advantage of the metal gaskets is that they can be used in the UHV systems because there resist bakeout treatment, which means that they can resist high temperature (150°C -350°C and even up to 800°C for copper gaskets). They can also work in radiation environment.

Plastic flow of the gasket material is connected with high pressure on the contact surfaces. In order to reduce the required force acting on the flanges the contact area in some designs is reduced to the minimum possible (for example knife-edge seals, ridge seals). If the elastic limit of gasket material is exceeded, the hardening of gasket material appears. The hardness of the gasket must be lower than of the flanges. Because of the plastic deformations, the hardening effect and residual stresses, hardened gaskets cannot be re-used after opening of the connection. There is a hypothesis that the ideal gasket consist of two layers: soft plastic material for the region near the contact surface and the elastic material with high strength for gasket core.

There are two possibilities to obtain the suitable deformations of the gasket in order to have leak tight joint. The seal can be obtained by compression (most common designs) or shear, where the compression also exists, but it does secondary influence on sealing mechanism (Figure 6).

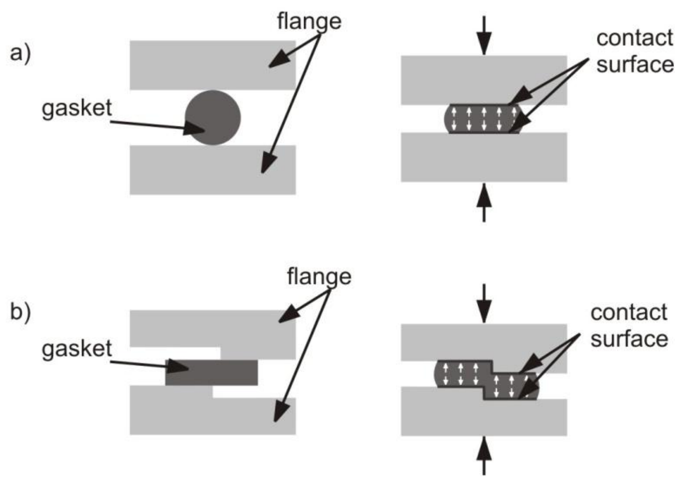

Figure 6 : Gasket under (a) compression; (b) shear

When compressing the joint the force is perpendicular to the supporting area. For metal gaskets it is common to use wedge shaped flanges or the coined type of gasket to minimize the required sealing force.

In shear mode the force is locally parallel to the supporting area. This type of joints requires theoretically less effort then the compressive ones for equal vacuum tightness. The possible deformation for shear seals is smaller than under crushing. However after a certain deformation any shearing systems become a compression seal type. The advantage of shear seals over compression ones at that conditions is insignificant.

Choosing a sealing system is difficult when vacuum requirements are combined with heat (bakeout treatment), chemical atmosphere or nuclear radiation. In case of the UHV systems the needs for reliable seals are obvious. Also for fusion research, particle accelerators, space applications the seals have to resist the radiation induced damage.

2.1 The surface roughness influence in leaking

There are two possible leaking mechanisms. The first is connected with the porosity, where leaking appears due to gas flow through the gasket material (permeation). This type of leaking is crucial for elastomer seals and it is significant in the range of 10^{-9}Torr. The permeation is mainly function of the temperature. Detailed data for permeation and out gassing for wide spectrum of vacuum materials (both polymers and metals, even for the laminated metals and ceramics material) can be found in the paper presented by Perkins [100].

The second possibility is connected with the surface roughness of sealing parts and takes place in the space between the surfaces of the gasket and the flange. This leaking process is sensitive to the sealing pressure acting between contact surfaces of gasket and flanges. If the pressure is not high enough to force the gasket material into the scratches of the surface (and fill them), the leak produced may be significant.

For quantitative evaluation of this leak path is necessary to determine the expression for the leak rate as a function of the geometry of the leak paths (roughness), and the deformation in that region.

The leak paths are determined by the profiles of the gasket surfaces in contact. These surfaces are covered by randomly distributed peaks and valleys and the leak path can be characterised by a triangular cross-section. It was verified by Roth [107] that on the machined surfaces more than 90% of the peaks has slopes of 1°-4°. This observation leads to the assumption of triangular cross-section with α~4° for leak paths (Figure 7). The typical length of the leak path is equal to the width *w*.

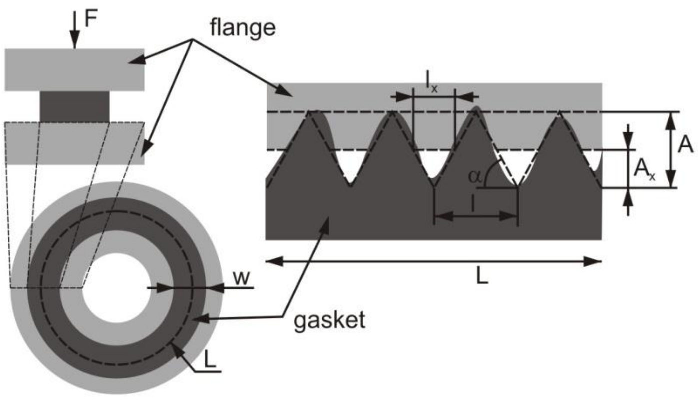

Figure 7 : Geometry of the gasket surface

2.1.1 Conductance of the Leak Path

The conductance (molecular flow) for simplified triangular cross-section leaking path was presented by Roth [107] in following form:

$$C = 19.3\left(\frac{T}{M}\right)^{\frac{1}{2}} \frac{A^3}{2(1+1/\cos\alpha)tg\alpha} \frac{K}{w} 10^4 \qquad \text{Eq. 6}$$

where C_1 denotes the molecular flow in l/s, T is the temperature [K] of the gas, M is the molecular weight of the gas [u], A is the height [m] of the triangular leak path cross-section (roughness), α is the slope (mainly α=4°), w is the length [m] of the leak path (usually equal to the gasket width), and K is a correction factor depending on the value of the ratio A/l. Because most of the leak tests are made by using helium leak detectors at room temperature (T=25°C) it can be transformed to the simplified form. For practical reasons, it is good to evaluate the equation for air environment. In this case there is a change of the C_{01} multiplier from about 1000 (for He, cf. Roth [108]) to 530 (for air composition: 78% N, 21%0_2 and 1% H, He, Ar, Ne, Kr).

$$C = C_{01}(\frac{A^3}{w}) \qquad \text{Eq. 7}$$

$$C_{01} = 19.3(\frac{T}{M})^{\frac{1}{2}} \frac{K}{2(1+1/\cos\alpha)tg\alpha} 10^4 \qquad \text{Eq. 8}$$

Considering the normal roughness of machined surface, the depth from valley to peak of the sealing surface is in range of 10^{-5} to 10^{-7} [m]. The molecular flow for that case corresponds to the range from $1\text{x}10^{-11}$ up to $5.4\text{x}10^{-5}$ [l/s], for helium leak test. The lowest sensitivity for standard helium leak detector is about $1\text{x}10^{-13}$ [atm l^3/s] or $1\text{x}10^{-13}$ [l/s] if the pressure drop is equal to 1 atm. The conductance of individual leak path on normal finished surface can be detected. Although for super-finishing techniques ($A \approx 6\text{x}10^{-8}$ m) the individual path conductance [$1\text{x}10^{-14}$l/s] is lower than the sensitivity of detector.

2.1.2 Conductance of the Interface Contact

The linear density of the leak paths n [1/m] on the surface $\sum l/L$ is described as follow, where l is the top line length of triangular cross-section [m] and L is the gasket circumference length [m].

$$n = (\frac{tg\alpha}{2A})(\frac{\sum l}{L}) \qquad \text{Eq. 9}$$

Using the previous equations the total conductance per unit length for a seal can be written as:

$$\frac{C}{L} = C_{01} tg(\alpha)\frac{A^2}{2w}(\frac{\sum l}{L})10^2 \qquad \text{Eq. 10}$$

$$\frac{C}{L} = C_{02}\frac{A^2}{w}(\frac{\sum l}{L}) \qquad \text{Eq. 11}$$

When helium is considered as a flow medium (standard leak test), and the temperature is set to 25°C, C_{02} is equal to 34. If the flow medium is air, C_{02} decreases to 18.7. The C_{02}

coefficient depends on the working condition (temperature T), the flow medium properties (M) and geometry parameters ($\sum l/L$, K, α) as shown below.

$$C_{02} = 19.3(\frac{T}{M})^{\frac{1}{2}} \frac{K}{4(1+1/\cos\alpha)} 10^6 \qquad \text{Eq. 12}$$

When the conductance is calculated for unit length of the sealing outline it is clear that even for roller burnishing technique, the total conductance density value [8.5x10^{-15}l/s m] is higher than the lowest sensitivity for standard helium leak detectors, which is about 1x10^{-15} [l/s m].

Those equations are valid for the cases, when no load is applied to the flanges. To reduce the cross-section of leaking path the compression of the gasket is required. This way, the height A (roughness) is decreased to A_x (Figure 7). The $\sum l/L = A_x/A$ relation leads to the following formula.

$$\frac{C}{L} = C_{02} \frac{A_x^{\ 2}}{w} (\frac{\sum l}{L}) = C_{02} \frac{A^2}{w} (\frac{A_x}{A})^3 \qquad \text{Eq. 13}$$

2.1.3 Equation of the Sealing Process

Roth [107] stated that the deformation factor A_x/A can be expressed as a function of the sealing pressure P and parameter R. This pressure acts due to the tightening force F and appears on the contact area. The sealing factor R expresses the sealing ability of the gasket material.

$$A_x / A = e^{-0.102P/R} \qquad \text{Eq. 14}$$

$$P = F / Lw \qquad \text{Eq. 15}$$

$$\frac{C}{L} = C_{02} \frac{A^2}{w} 10^2 \exp(-0.306 \frac{F/L}{wR}) \qquad \text{Eq. 16}$$

The sealing process can be expressed as dependent on the force applied to the flanges, geometry and gasket material properties R. The R factor can be expressed as P value needed to decrease the conductance by about 0.05 [l/s]. The sealing factor values for different gasket materials are presented in Table 2.

Table 2 The sealing factor for different gasket materials, cf. [107]

Materials	Hardness	Sealing factor *R* [MPa]
Copper (Cu)	Very Hard	323,6
	Hard	88.3
	Soft	49.0
Nickel (Ni)	-	117.7
Aluminium (Al)	Hard	58.8
	Soft	29.4
Stainless Steel (SS)	Hard	88.3
	Soft	58.8
Lead (Pb)	Soft	6.7

It can be deduced, that the conductance logarithmic value depends linearly on the gasket sealing factor, and effective width w. The other law is that the lower R, the lower force is required to get a satisfactory leak-tightness. Also decrease the effective width w decrease the sealing pressure P required for seal joint. The initial roughness A of the surface determines the initial leak-rate of the joint.

2.1.4 Typical Shapes of Sealing Curves

The tightening curve may contain three different sealing stages: accommodation, normal and local sealing. Accommodation appears at the beginning of the process and usually goes up to $P/R=5\text{-}6$ value [MPa/m]. In this stage the surfaces overcome the waviness, crush foreign peaks, or push them into the softer sealing surface. The interface contact is gradually established along the entire outline of the seal.

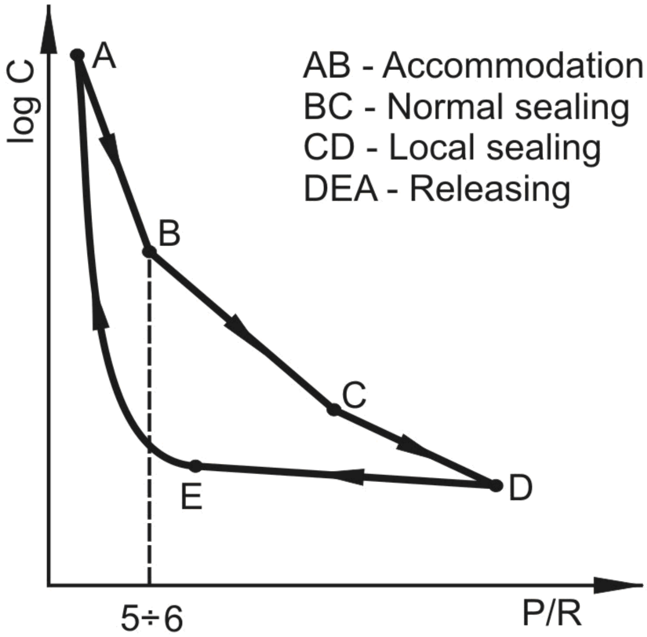

Figure 8 : Stages of the sealing process

After increase of the force acting on the flanges (*P/R* is rising), *normal sealing* (Figure 8) stage is reached. In this stage the leak paths existing at the interface contact are gradually throttled by interpenetration (the smooth sealing part is the harder one) or flattened (he smooth sealing surface is softer).

Upon further increase of the force applied to the flanges, the effect of *local sealing* (Figure 8) may appear. This stage is due to the conductance of local, deeper than other leak paths, grooves. Normally local groves are made by scratches, machining marks or other damage acting through the sealing surfaces. The sealing process for those groves proceeds less effective than for normal leaking path. The leaks exist with bigger applied force than by normal. This is why the slope for this stage (line CD) is lower than for *normal sealing* (line AB).

The realised curve reflects the deformation that took place before. If this deformation is entirely elastic, the releasing curve coincides exactly with the tightening curve. If the deformation during tightening was entirely plastic, then during the release the conductance remains constant, i.e., the releasing curve is a horizontal line. For elastic-plastic deformation the releasing curve is located between the two curves. It was shown that even when the releasing curve is horizontal, it stretches approximately to force corresponding to the limit between the accommodation and the normal sealing stage, where the conductance begins to rise (point E). This phenomenon was explained by the fact that in this region the elastic deformation of the waviness begins to separate the parts in contact (cf. Roth [107]).

2.2 Characterization of the sealing systems

To specify the gasket shape two subjects may be defined. First is the outline shape, second is the cross-section. The most common outline of gaskets is circular, but sometimes the rectangular or another gasket outline is needed in vacuum systems. The cross-sections of the gaskets are more diversified than their outline, although the circular cross-section is desired in many seals. The plastic and metal gaskets are of great variety of shapes (summary presented in Table 3) and their dimensions are not yet standardized. Typical cross-sections are shown in connection with each particular kind of seal.

Table 3 Typical gasket cross-sections and materials

No.	Cross-section	Gasket material	No.	Cross-section	Material
1		Elastomer, metal	10		Copper
2		Metal, Teflon (with core)	11		Copper (indium coated)
3		Elastomer	12		Elastomer
4		Elastomer with elastomer or metal web	13		Elastomer with metal protection
5		Elastomer	14		Elastomer
6		Copper	15		Copper
7		Copper	16		Copper
8		Copper	17		Copper
9		Copper	18		Copper

The cross-section of the gasket is normally connected with the cross-section of the flanges (sometimes flat or with groove, knife-edge) and the way all seal system works (additional spacers sometimes are used).

2.2.1 O-ring seals

The most common type of gasket is O-ring seal, which has a circular outline and circular cross-section. Usually, the gasket is made of a metal or an elastomer. A summary of different O-ring elastomer materials has been published by Gillette [47].

However, there is another gasket with circular cross-section, much more complicated and commonly in use. The multilayer-core gasket consisted of an Inconel helical wire surrounded by a stainless steel jacket. The hard stainless steel jacket is covered by a second layer of soft metal jacket made from copper, aluminium or silver (Figure 9). The jackets are usually constructed with a gap that can face any direction. For good practice the gaps usually face away from the vacuum [143]. The Inconel helical wire gives the elastic force and the soft jacket material fills the micro-channels in the contact area.

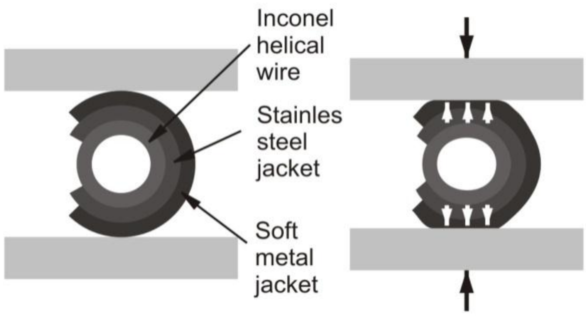

Figure 9 : Multilayer-core seal

The gasket is compressed (sometimes sheared) between the sealing parts. When the joint closes, the sealing parts (for example flanges) touch the cross-section of the gasket in at least two points, depending on the shape of the sealing parts. It is useful to distinguish additionally between the “flange seals” (when the main compression force is exerted axially on the gasket) and “shaft seals” (when force works radial to the O-ring).

The seal are designed either for “constant deflection” (seals with limited compression) or “constant load” (seals with unlimited compression). The “constant deflection” seals are designed to limit the compression of the gasket (limited to the specified compression ratio) when the sealing parts meet together in a metal-to-metal contact and enclosing the O-ring gasket in the groove. At “constant load” type there is no geometry limitation for compression of the gasket (Figure 10).

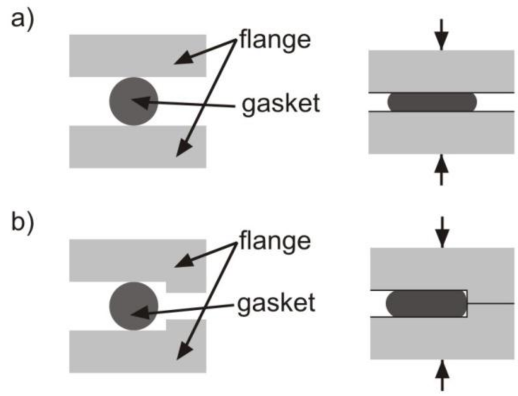

Figure 10 : a) unlimited; b) limited seals compression

However the most common practice is to divide all O-ring joints into two main groups: “flat flange” and “groove” joints. However the other groups exist and will be also presented.

2.2.1.1 Flat flange O-ring seals

The simplest system for O-ring seals can be designed as two flat flanges compressing the gasket between them. The drawback is that such system of seals does not provide alignment possibility, retention. Because of lack of a limit for compression it can be used only with metal gaskets. For alignment seals and to limit the compression the retaining rings are used or spacers.

An example a seal with spacer under axial compression was shown by Parraras at al [96]. Wheler [124] described the design containing the O-ring gold wire gasket and flat flanges. It is common to use other materials of O-ring seals together with flat flanges, for example: indium O-ring was used by Moore [84], Viton one was used by Yoshimura [141] and aluminium gasket by Langley [67].

2.2.1.2 Groove O-ring seals

In groove seals, one of the sealing parts has been machined in the way to receive the O-ring. The profile of the groove can be the rectangular one, V-shaped, rounded V-shaped, trapezium or semi-circular and elliptical (Figure 11).

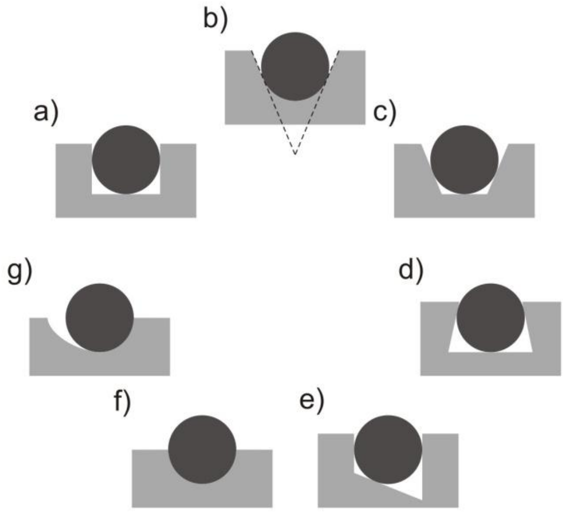

Figure 11 : Grove profiles

For rectangular groove (Figure 11;a), the width should be equal to the diameter of the gasket cross-section and having the area no less then equal to cross-section of the gasket. The O-ring seal is placed in the groove and compressed by the lip of the opposite flange. The drawback is that the removal of the deformed O-ring is difficult. In order to overcome this, it is advisable to construct such seals on some demountable parts.

The V-shaped grove is not commonly in used (Figure 11; b). The reason is that this type of groove should have an angle of about 112° for correct work, which does not allow retaining the O-ring. After rounding apex of the groove the rounded V-groove is obtained. There exist two types of such geometries: the limited compression and unlimited compression.

The groove cross-section can also have the trapezium shape. Three types of trapezium groves are used for O-ring seals: the open, the closed (dovetail) and the trapezium grove with parallel side walls (Figure 11:c,d,e).

The first is the easiest to machine, but is characterized by poor retention of the seal. The closed one is difficult to machine, has some trapped volumes in the seal but has a very good retention of the gasket especially for large diameters. The last trapezium grove type is based on the principle of minimum machining and reduction of trapped volumes. In case of trapezium grove with parallel side walls, the O-ring seal fills the vacuum side but a small volume is trapped on the other, atmospheric side.

Finally there is a grove with semi-circular or elliptical cross-section reported by Schuman [110]. These groves do not form trapped volumes but they cannot receive the entire volume of the O-ring. These shapes of grove are mainly used with the metal O-ring seals (for example made of aluminium, nickel, indium or lead).

2.2.1.3 Conical O-ring seals

The third type of sealing systems using the O-ring gaskets is based on the conical configuration. The conical O-ring is used in three basic arrangements. The first one is shown in Figure 12a. The conical surface is placed on the atmospheric side of the seal, and the vacuum seal located plane flange and cylindrical surface of the pipe. This arrangement for seal is the easiest to construct, because only the surface of the flange should be well finished. For second type (Figure 12b), the two sealing surfaces are the conical and the cylindrical ones. There is generally more difficult to obtain well finished surface on a conical part (which is required). The last case is used for better alignment of the parts. It is made of two parts instead of three and O-ring. This type does not permit sealing directly on the surface (Figure 12c).

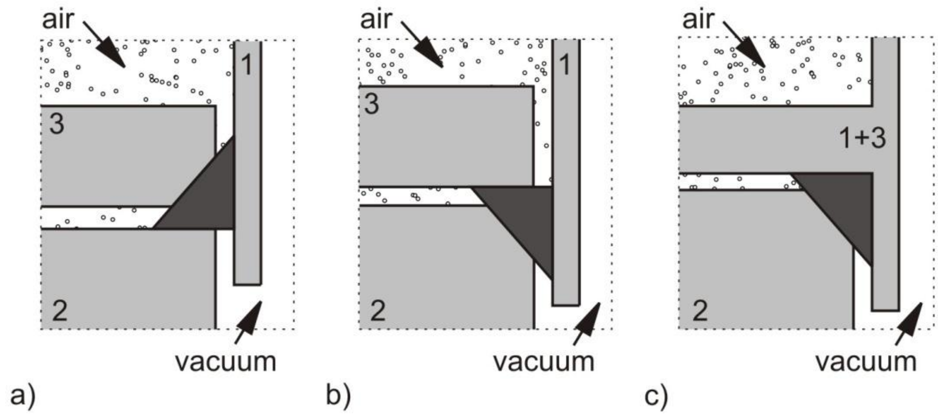

Figure 12 : Basic arrangements for conical O-ring seals

The metal square or circular in cross-section gaskets was presented by Wheeler [123-124] and by Varian Company [143]. The idea is to press the gasket, between two tapered parts (the CF flanges can be used), to obtain the symmetry-conical shape. It is common practice in order to ensure that the gasket is precisely located against the vertical face in flange profile, made somewhat undersized and is slightly stretched as it is snapped into place.

2.2.1.4 Corner O-ring seals

The other way to use the O-ring gasket consists in applying the corner seals. These seals are based on the principle of a metal O-ring located in the corner of a step machined on the sealing flanges. The O-ring seal is placed in the step machined in one of the sealing parts and compressed against the other flat flange surface or against a second step machined on the other sealing part. The diameter of the machined steps should be made equal to the inside and outside diameter of the O-ring. In Figure 13b the seal with limited compression is shown. The reduced version is presented in Figure 13a.

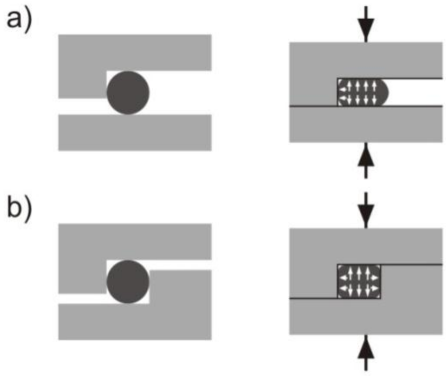

Figure 13 : Step seals with O-ring: (a) single step; (b) double step

A good example is the golden O-ring located in a counter bore of one flange and squeezed by a close fitting annular step described by Wheeler [123].

2.2.2 Cemented seals

The cemented seals are based on the special temperature treatment connected with sealing pressure to obtain a tight seal. In these seals, the aluminium wire is compressed between flat flanges and heated up enough to form a good adherence between the gasket and flanges. Even if the aluminium wire is compressed between two stainless steel flanges with linear load of 1400 kN/m at room temperature, it is not cold weld. On the other hand if gasket is baked at 250°C or higher, the gasket material adheres to the mating flanges even at pressure 90 kN/m.

Elsworth at al. [36] mentioned that a bond is formed between flange and gasket due to frictional adhesion when the seal is baked up more than 300°C and from the temperature of 400°C metal diffusion occurs with the formation of a brittle intermetallic surface layer. The cemented seals remain leak tight during and after repeated baking to the temperature of 450°C. It is claimed by Holden at al. [52] that it could be used also up to 550°C and these gaskets which have not been baked above 370°C can be peeled off from flanges.

The sealing mechanism can be described as follows. By baking the seals, aluminium flows and frictionally rubs against the flanges, thereby fracturing its surface oxide and adhering to the steel. Adhesion only occurs where the air has been previously expelled from between the junction of gasket and flange. And the leading edges of the flowing aluminium contact the degassing metal of the flange (cf. Roth [108]).

Because of the sealing mechanism the reliability of this joint depends on the baking temperature, which was shown by Roth [108]. The higher bakeout temperature, the higher strength of the cemented joint is, up to the forming temperature. The breaking strength of the seal depends upon the surface finish of the flanges and is greater when the finish is smoother. It is obvious that the breaking strength is connected also with compression force. Breaking strength up to 70 kN/m of wire gasket was measured by Elsworth at al. [36].

For better performance the indium coated surface can be used for flanges or for gasket. The indium coating helps to fill up surface imperfections on the flanges. Also, to decrease the sealing force, the aluminium-silicon (5%) is used for gasket material.

2.2.3 Thick gasket seals

The third group of the seal types are the thick gasket seals. They are somewhat similar to O-rings, but they use the gaskets with other cross-section shapes. According to the relative position and shape of the gasket and flanges, the seals could be classified in ten categories.

2.2.3.1 Plane seals

The simplest one is the plane tape. It consists of the flat gasket tightened between two plane flanges. The common cross-section of the gasket varies from square, through rectangular, to trapezium shape. In some applications specially shaped gaskets are sealed between two flat flanges. The motion possibility of the gasket compressed between flat flanges does not produce the leak. To better alignment it required subsequent tightening, which can lead to the gasket tearing. In the same way like before for O-ring gaskets, for centring and to control the compression ratio the groves are used for flanges. The other solution for easy centring is gasket with centring ears or even fixed in proper position by using screws. To control the compression ratio the metal spacers are used.

The example for spacer thick seals is the solution described by Bernard et al. [12] (also by SEVA company [142]). The design consists of the soft metal rectangular gasket with rounded top and bottom surfaces attached by two hard metal spacers (Figure 14).

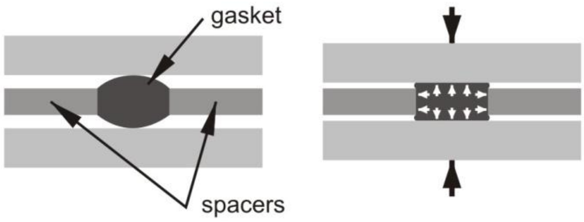

Figure 14 : The soft seals attached to hard metal spacers

In the concept of plane flange seals the rectangular or square shaped gaskets are pressed between plane flanges. For elastomer gaskets it is common to slightly grease the sealing contact surfaces. This practice enables to decrease the required sealing force to obtain the tight joint. Other materials used for gaskets are the Teflon, aluminium, gold or copper. This kind of seals is also used successfully with bell jars. Also it is used for sealing windows, end plates, joints between two pipes of the same diameter (using lock ring) or different diameters using two gaskets and the metal ring between them.

2.2.3.2 Grove thick seals

By using a groove machined in one of the flanges the so called groove seals are obtained. The groove prevents sliding of the gasket during the tightening of the seal. The grooves can be designed either to obtain the permanent loading or limited loading of the gasket. For first case the cross-section of the groove should be smaller than gasket cross-section. In the second case the grove should be bigger than gasket cross-section area. The groove should limit the compression ratio of the gasket to designed value. For rubber gaskets the grooves should also allow space for deformation in directions perpendicular to the sealing force (Figure 15b,c). Joint presented in Figure 15a is not accepted.

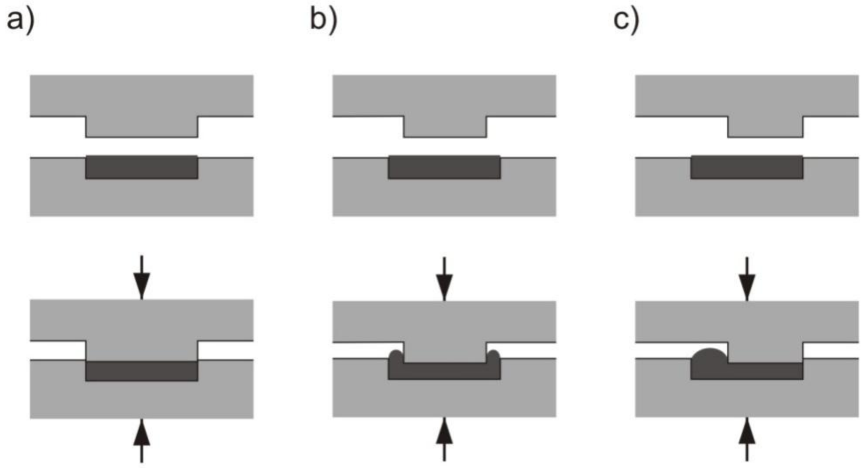

Figure 15 : Principles in designing flat gasket seals

When the seals (permanent loading type) with rectangular or square cross-section are used, the rectangular groove with tapered corners is preferred instead of a normal rectangular shape. This grove shape provides an expansion space for the gasket and because of this allows the re-use of the gasket after joint opening (for rectangular shape the gasket should be used only ones). This type of groove shape is used to make a seal between two flanges, but it can be adapted to seal more complicated joints too.

In order to obtain limited loading type of the gasket, the groove cross-section area should be 2 to 5% greater than the cross-section of the gasket. This leads to keep the gasket material fully in the groove after tightening. To hold the gasket in the groove the seals with trapezium cross-section shape instead of rectangular one may be used compared with the trapezium groove with tapered corners. Other design of the thick gasket consists in applying the square cross-section gasket in the rectangular cross-section step groove to minimize the surface of the gasket exposed to the atmospheric conditions.

2.2.3.3 Special gasket shaped thick seals

There exist joints, where special shapes of gaskets are used. One of the commonly used is the L-gasket. Those gaskets are made mainly from elastomers (Neoprene, Viton, etc.) and are available in different dimensions, fitting the bell jars or ports. They are used only in dynamic vacuum systems equipped with strong pumps. The drawback of L-gaskets consists in the fact a large surface is exposed to the atmospheric conditions.

One of the bake able metal seals is the copper rectangular gasket with small beads raised in both sides (Figure 16). These small beads are forced into the broad bulk of the gasket to ensure that the seal will be maintained throughout the bakeout cycle. The contact surface finish is not so important for that seal, but the height of the beads and distance from the beads to the atmospheric seal side end are important. The bead should be far from atmospheric side in order to avoid the oxidation in the vicinity of the bead and should be near the bolts position to minimize influence of the warping of the flange during the tightening (cf. Roth [108]).

Figure 16 : Plane seals with gaskets of special shapes: gasket with beads

Another type is coined gasket (Figure 17), where the beads are trapezoidal in shape. These gaskets were reported for example in tests made by Schuman [110]. Seals with this type of gaskets, made from OFHC copper, may be opened and closed with the same gasket safety about four times (it is reported about 35 successive sealing cycles). The ability to reuse the same gaskets is explained by the fact that the copper ridge is forced into the body of the gasket without the development of high lateral force. Because of that fact probably large amount of gasket material does not reached the elastic limit, and the seal still have the ability of resealing. The drawback is that the coined seals are very sensitive to the degree of flatness of the sealing flanges. The conical seals may be baked up to 400°C.

Figure 17 : Coined gasket

Similar design presents the seal where the OFHC copper for rectangular gasket with a raised ridge on both sides is used (Figure 18). This gasket was used also in the rectangular outline seals and could be applied up to 600°C.

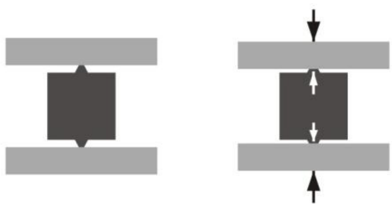

Figure 18 : Gasket with ridge

Another quite common special shape for the copper gasket cross-section is a diamond-shaped one (Figure 19 and Figure 20). For this type of gasket it is recommended to machine the rectangular groove in one of the flanges in order to put the gasket there. The seal may be baked up to 450°C.

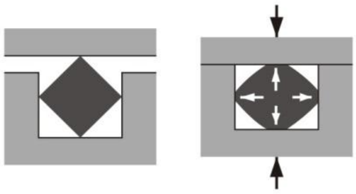

Figure 19 : Diamond-shaped seal

Figure 20 : Diamond cross section gasket between flat flanges

It was found that the oxidation of the copper during baking made such seals unsatisfactory for long term use. The oxidation problem can be solved by the use of two concentric diamond seals, but the sealing force becomes excessive, as stated by Elsworth et al. [36].

2.2.3.4 Conical thick seals

If the gasket is conical in cross-section or it gained this shape during compression between the sealing parts the conical seals are obtained. The simplest conical seal is the rubber plug or bung used to close the pipe with the vacuum inside.

The conical thick seals are commonly used to obtain the leak tight joints for Liquid Feedthrough and RF Feedthrough [143]. This kind of seals is also reported by Wheeler [124] to be used in the case of the tube coupling.

For example if the rectangular metal gasket (aluminium, copper, nickel) is places between two CF flanges, the reduced CF seal can be obtained (Figure 21). Such design can work at the temperature range from -273°C to 400°C, giving the leak tight joints, as reported by Frend [37]. This type of seal was evaluated from the CF (described in detail in section 2.4) seal system and aimed to decrees the sealing force. The seal requires about 50% lower sealing force than the CF one and is not sensitive to knife edge damage.

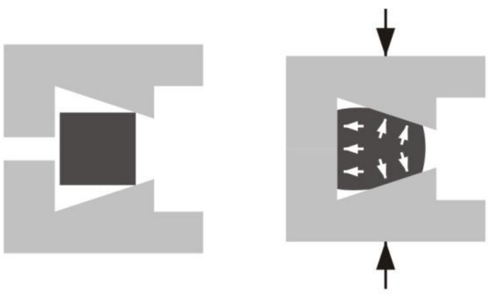

Figure 21 : Reduced CF seal type

Conical seals may be used also with the metal gaskets or even without gaskets. For example the sealing can be obtaining between two curved sealing surfaces or between a conical and a curved one (Fig. 2.18a). The sealing in the case of seals without gaskets is obtained due to a very high compressive stress that exists in the line contact between the sealing parts. This type of seal can be resealed and resists bakeout at 500°C. The other conical seals without gaskets are the flare seals and seals with conical spring washers (Figs. 2.18b, c).The flare seal is based on pushing the hard knife (corner of the flange part) against the soft material (copper tube). The second kind of the seal uses the conical washer made of spring steel compressed against the flat stainless steel surface. After removing the sealing force the conical washer comes back to the initial shape. The conical spring washer type was proposed for use as the closing component of valves or controlled seals (cf. Roth [108]).

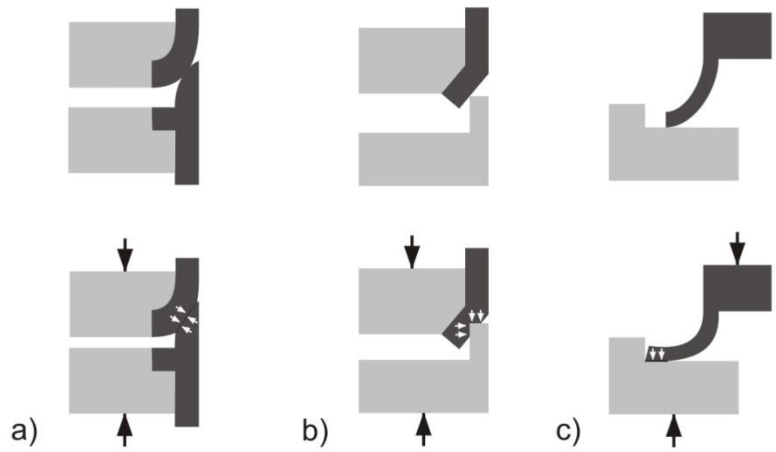

Figure 22 : Conical seals without gaskets

2.2.3.5 Cylindrical thick seals

The gasket in cylindrical seals is pressed radial on a cylindrical sealing surface. This kind of seals is represented by rubber tubing joints, compressed gasket seals and lip seals. The rubber tube should have sufficient wall thickness to prevent collapse. The inside diameter of rubber tube should be smaller compared to outside diameter of sealing tube (tubes) to obtain the radial pressure. The ends of sealing tubes are shaped to have ridges to enable easiest gripping of the tubing. To minimize the area of rubber tube exposed to atmospheric conditions the sealed tube ends should be as close as possible in the joint.

The sealing mechanism of the compressed gasket seal is based on the axial force. Due to this force, the gasket is deformed in radial direction, and by pressing on the pipe surface a tight joint is obtained (Figure 23). With this type of seal it is possible to obtain the tight joint between two pipes of the same or different diameter. The seals working in that way are used also to connect the diffusion pumps to vacuum system.

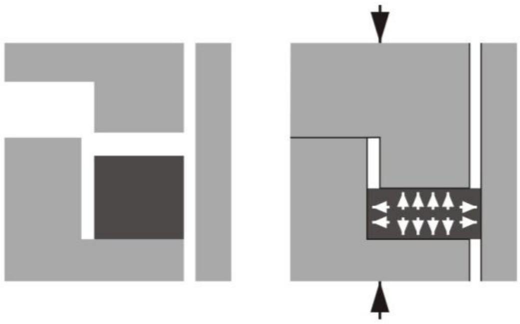

Figure 23 : Cylindrical seal

2.2.3.6 Lips thick seals

The lip seals are based on the gaskets with lips. The sealing is obtained between the lips and the flange surface, and the active seal forces are the axial and the radial ones. The best example of that kind of joint is the seal with U-shaped Teflon gasket with thin leaps, compressed between two gaskets surfaces inclined at 35° to the normal position (Figure 24).

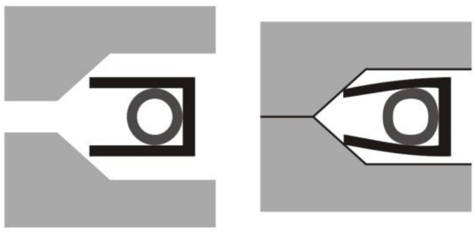

Figure 24 : Lip seals with Teflon gasket

The other interesting solution is a four lips metal gasket (rotated X shape) compressed between heavy flanges, mentioned by Verheyden and Klein [131-132] and Edwards et al. [34]. The seal has a cross section which is symmetric around its central point and inclined over small angle respect to the plane of the flange (Figure 25). It provides on each flange a leak tight contact on two lines with the spherical shaped outline. This solution assumes the sealing pressure due the cross-section shape rather than due to the material elasticity.

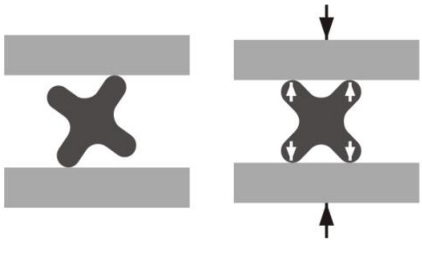

Figure 25 : X shape gasket

Some other designs aimed to obtain the lips seals refer to the gasket formed in V shape, where two lips are pointed outside the evacuated space or inside it. Also the K-shape gasket was reported in use. The K type contains two lips and connected with rectangular cross-section (taller than the distance between ends of lips) which forms the K shape. All these types were reported in tests made by Schuman [110].

2.2.3.7 Dumbbell seals

The next group of thick seals is the category of dumbbell seals. The joint consist the plane flanges and the seal made from two concentric gaskets connected by the web in one structure. The web is usually perforated and sometimes is screwed to one of the flanges for better alignment. For the elastomer material this kind of gasket had in addition the metal spacer ring on the inner side connected to the web to minimize the area exposed to the atmospheric side. There exist fully metal seal of this kind made from copper and with X-shaped cross-section that is leak-tight after baking to 450°C. The sealing mechanism is based on the axial compression and contact pressure between the gasket and the flanges.

2.2.3.8 Shear seals

The shear seals are quite different then the other so far presented seals. They are based on the shearing principle instead of the compression of the gasket. The other name for these joints is the step seal. The shear seals for rectangular gaskets can be obtained in two ways. First one involves the step flanges with a clearance between opposite steps and second one is based on overlapped steps (Figure 26). The main advantage of shear seals is that they require less force than based on the compression effect. They are easy to machine, easy of repair if damaged, and the bakeout temperature can reach 450°C, because of the OFHC copper used for the gasket.

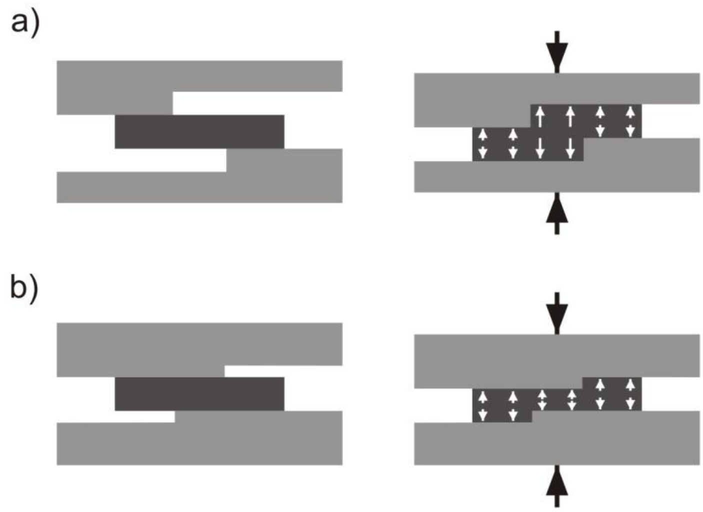

Figure 26 : Shear seals

There exists a special make of the shear corner seals, which involves a copper gasket with trapezium cross-section placed in the groove shown in Figure 27. This seal was successfully tested for temperatures up to 250°C and diameter up to 50 mm. The disadvantage is the trapped volume between the gasket and the grooved flange.

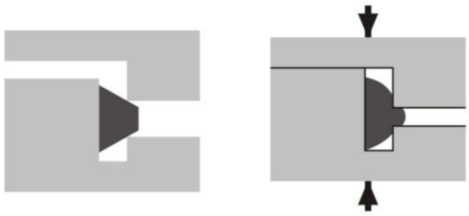

Figure 27 : Shear corner seal

2.2.3.9 Ridge thick seals

Ridge seals are the next category of thick gasket seals. In order to obtain lower required sealing force the ridges are designed on one or both flanges. The ridges are aimed at raising the local pressure on the contact surface between the flanges, ridges and gasket which leads to lower sealing force required for leak-tight joint than for the flat flanges. The ridges can be tongues-like in shape (rounded, V-shaped, trapezoid, rectangular) or rim-like (knife-edge, Figure 28).

Figure 28 : Knife-edge seal

The tongues form a seal without large deflection of the rubber gasket. For Teflon or a soft metal as gasket material the small grooves should be machined on the second flange to centre the gasket.

The example for ridge seals is design mentioned by Setsugu and Shirai [117]. The flat rectangular and quite wide ridges rise from the flanges and compress the copper gasket. This type of seal was found to be promising for connecting flanges of the beam duct with a complicated shape.

Knife edge seals are made by forcing the knife edge to beat into a soft metal gasket. Clumping the soft gasket between the hard, stiff knifes plastifies locally the gasket material, which fills all imperfections on the knife sealing surface and leads to a leak-tight joint. Microscopic imperfections of the gaskets used in such seals revealed that the sealing mechanism act mainly at the side of the knife edge, where strong shearing of the gasket material occurs.

The most common material for gasket is the OFHC copper, but other metals such as mild steel, nickel, silver, silver-plated copper, indium-plated copper are also used. Copper gaskets are usually annealed in hydrogen at 950°C, or air-fired to get annealed. It is also cleaned in order to remove the resulting oxides and reduce any scratches on the surfaces.

The most designers are using the fully annealed copper as gasket material but some of them have claimed that the copper should be quite hard for good (high elastic limit leads to higher sealing force value), reliable seal. The gasket thick is normally about 1-2 mm, but there exist very thin or very thick ones. It is a common law that the harder and tougher the knife edge the more reliable joint will be obtained with lower applied sealing force. The polishing of the knife edge is important, but it is relatively unimportant there where the gasket material will flow during the sealing process. It has been found that the copper of gasket will flow into scratches a few microns in depth and completely seal them, but 10 microns depth scratches will be only partially filled. There exist seals where knife-edge, gasket and flanges are made from the same material, but the knife surface is hardening by deposing on it a hard material. The knife is in principle V-shaped. The vertex is rounded or has flat edge to generate a planar surface of contact between the flange and gasket. The width of the flat land of vertex as well as rounded radius should be reduced to minimum, because by increasing its dimension the value of sealing force increases. The knife-edge seals are used mostly with circular outline but seals with other more complicated shapes are also applied. The knife for that type of seal can be sharp or rounded; can be located on one of the flanges or both flanges with the mirror symmetry between them.

Patte [97] described the knife-edge seal made between two stainless steel tubes and the copper gasket where the knife edges where machined in thick walled tubes, where the sealing force was coming from clamping screws and the seal was subjected to bakeout at temperature up to 500°C.

The knife edge seals, that described by Wheeler [123-124] are use also for bakeable valve sealing joints. For that seals the removable gasket is pressed into the piston and is captured between piston and seat to make the reliable seal. Also there exists the compression port knife-edge seal design (Wheeler [124], Yoshimura [141]). The sealing force applied in this solution acts radial. The end of the tube is captured by the split collet form outside and the flange knife on the inner side of the tube.

The solution for the knife seals is the design that uses the knife edge gasket on the one side and the flat one on the others, as described by Wheeler [123]. There is no metal foil between them but the knife is plated with gold which form the sealing material. This solution is called Gold Plated Ridge Seal. It consists of a 0.3mm high triangular ridge with a 0.1 mm radius at its apex on the face of one flange and plated with a thick layer of gold (Figure 29). When the ridge is compressed against the flat face of another flange, it produces highly reliable seals at low sealing force (275 to 680 kN/m). The seal configuration is equivalent to a gold foil bonded to one seal surface (and hence it will not rip upon flange opening) with the ridge shape strictly limiting the seal width (to approximately 0.3mm) in order to minimize the seal force requirement. This type of seal can be baked out to 450°C in open position and 200-250°C in the closed position. Also, the very good repeat seal reliability is mentioned. The disadvantage of this design is that the tolerance for flange or gasket damage is limited. The thinness of the gold layer ("gaskets") does not tolerate flange variations higher than 0.01mm. No seal gasket scratches are allowed too.

Figure 29 : Gold Plated Ridge Seal

The double ridge knife-edge seals are more difficult to machine. They need both much thicker flanges to avoid bending of the flanges and inner knife leaking. However they have some advantages too. These seals based on concentric knife edges acting on the soft gasket material may prevent the continuous knife penetration deep into the gasket by trapping a volume of copper in space between the ridges. Also with that kind of seal there is a possibility to use the guard vacuum.

The knife edges can be made on the gasket instead of the flanges. The gasket made from hard material is shaped on its cross-section to form knife edges on both sides (Figure 30). The hard gasket knife is bit into soft material of the flanges. The disadvantage for this solution is that the seal should not be opened and closed many times.

Figure 30 : Knife edges seal with hard gasket and soft flanges

CF seals are special variant of knife-edge seals. The name is coming from merging two words; *con*ical and *flat* (Yushimura [141]). The design consists of a conical sealing surface and the flat copper gasket. The sealing ridge is made at as vertical edge on one side and inclined at angle of 70° on other side (Figure 31). The edges are designed to bit 0.3-0.4 mm on each side of the 1.6-2.0 mm thick gasket. There exists recently lots of variation of knife geometry, changing both the knife side angles and the tip radius, as compared by Kurokouchi et al. [61]. The advantage of CF seals is that the gasket can be reused even up to 22 times, but it is recommended to use it only 3 times as was mentioned by Roh [108]. The CF seals are also bakeable at high temperature and its depends from the gasket material (OFC copper, OFHC copper, aluminium, silver-coated copper, Teflon-coated copper or polymer coated copper, mentioned by Danielson [30]).It was even reported by Edwards et al. [34] that a 2 3/4-in (64 mm) flange has been vacuum fired at 900°C for four hours and found to seal without leakage throughout each of 40 separate closures.

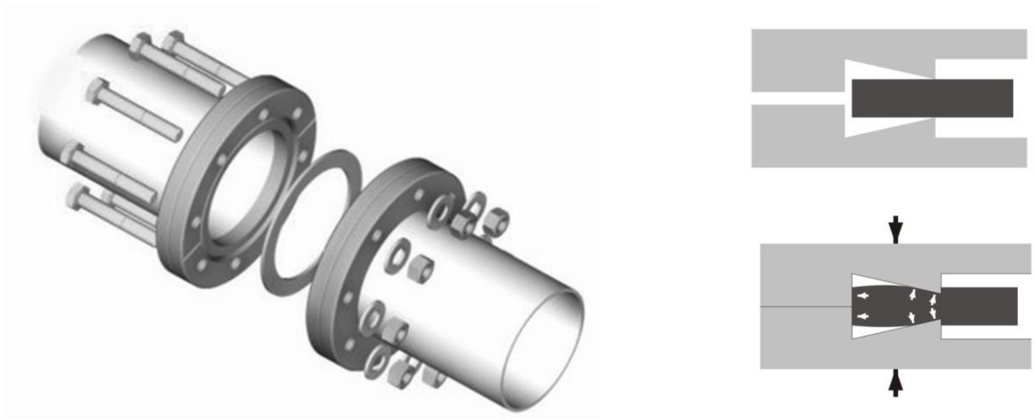

Figure 31 : ConFlat seal

The disadvantage of the knife edge seals is that they need special care during the assembly. In order to obtain good seal the diameter of the mating knife edges must be absolutely the same to avoid the umbrella like deformation of the gasket, as was reported by Unterlerchner [121]. It appears that the diameters of knife edges should be within ±0.05 mm precision and that the eccentricity should be held to within ±0.12 mm. Also the two mating knife edges must be assembled in line, which requires a positive alignment of the flanges. The sealing line in design should be as close as possible to the bolt position and the flanges should be strong enough to prevent excessive distortion. It is required that the sealing force should be applied normally to the gasket surfaces.

2.2.3.10 Inflatable gasket seals

The last type of the thick gasket seals is the inflatable gasket seal. It can be used for sealing the lock doors of vacuum vessels with pressures of 10^{-1}-10^{-2} Torr (13-1.3 Pa). These seals have a nominal displacement which can seal clearance gap up to 12 mm between the frame where the seal is placed and the movable door. There exist seals with square, round and T-shape ridge.

2.2.4 Thin gasket seals

The thin gasket seals consist of a foil (usually made of metal) tightened between a plane surface and a surface provided with a ridge, between two surfaces: one provided with groove and second with knife-edge or between two tapered surfaces (Figure 32).

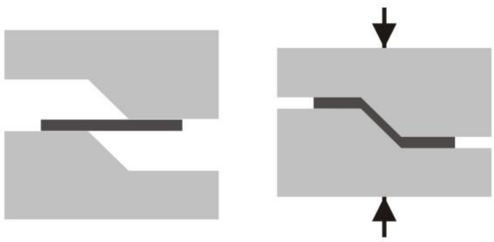

Figure 32 : Conical surface friction seal

The common foil thickness is about 0.01 mm for first case (gold, aluminium, silver and copper), 0.1-0.5 mm for groove and knife-edge seals with silver or copper foil, 0.2-0.5 mm thick for aluminium or Teflon gaskets reported (cf. Roth [108]). These two kinds of seals can be used up to 400°C.

There exist the foil seal type made from the aluminium foil thickness about 0.05 to 0.07 mm compressed between two 3mm wide raised seal surfaces on stainless steel flanges, described by Wheeler [123]. The seal surfaces are machined slightly conical so that as bolt force brings the flange peripheries together, the surfaces become nearly parallel. Capturing effect is very good as the width to thickness ratio exceeds 50. Outstanding features of this design are the ready availability and low cost of gaskets, sealing reliability and bake ability to 450°C (chemical treatment may be necessary to remove aluminium bonded to the flanges). The drawback for these seals is the high sealing force (2260-3390 kN/m). Also the tolerance for flange or gasket damage is limited. Thinness of gasket precludes the sealing of scratches deeper than 0.02mm during the first seal. The repeat seal reliability is poor because the thin gasket is subject to damage upon opening, especially after a bake.The polyimide is also used as a sealing foil material (cf. Edwards et al. [34]). Leak tightness in this solution is affected by small compressive force, allowing the use of lightweight flanges. The other advantage is that the polyimide is rather inexpensive. It can withstand the temperature up to 277°C. It was confirmed by Brymner and Steckelmacher [18], that the metal gasket shear seals may be used in temperature range from -188°C to 800°C. This type of seal does not require any special polishing of the sealing surfaces.

2.3 Materials for gaskets and flanges

All materials used for gaskets can be classified in the following categories: rubber, plastic and metal. To have a wide overview of all kind of materials, their main properties are collected and shortly described in Table 4 (after Roth [108]).

Table 4: Gasket materials

Feature	Rubber gaskets	Plastic gaskets	Metal gaskets
Compressibility	-	++	+
Pour Elasticity	++	-	-
Permanent set (in means of re-using)	++	+	-
Hardness	-	+	++
Bonding	++	-	+
Outgassing	-	+	++
Permeability	-	+	++
High temperature behaviour	+	-	++
Low temperature behaviour	-	+	++
Chemical behaviour	+	++	+

The main advantage of rubber (natural, Nitrite rubber, Neoprene and Silicone), which determines its extensive use, is the fully elastic behaviour. Other parameters decrease the range in which the rubber seal can be used. For the rubber the problems are laying in low mechanical resistance at extreme temperatures and its high permeability and chemical instability (especially for natural rubber). Only a rubber-like material, Viton (A and B) has a lower permeability than any other rubber. Its gas evolution is also the lowest and can be used to about 200°C (after Roth [108]) or 150°C (after Peacock [98]). The experimental results published by Yoshimura [141] for Viton, showed that the atmospheric water vapour permeates seals at high rates. Oxygen also permeates Viton seals, but on the other hand, other gases in the atmosphere such as N_2, CO, CO_2, and Ar do not permeate in a practical sense.

Vacuum plants used in the pressure range of 10^{-5} to 10^{-7} Torr (1.3 Pa^{-3} to 1.3 Pa^{-5}) are almost entirely sealed with elastomer gaskets, of which Viton is the most commonly used material. Sometimes the elastomer gaskets are cooled to reduce desorption. Also, using a double gasket seals with evacuated interspaces reduces the gas permeation which is the main reason not to use such seals in the vacuum conditions lower than 10^{-7} Torr (1.3 Pa^{-5}) as mentioned by Elsworth et al. [36].

If the pressures of 10^{-9} Torr (1.3 Pa^{-7}) or less are required it is necessary to bake the components of the system to accelerate desorption of gas and vapour. The minimum baking temperature required is 300°C. This temperature is sufficient to promote thermal degradation of elastomers resulting in rapid gas evolution. The polyimide polymers can withstand baking at this temperature without degradation. On the other hand, they have high rates of water adsorption, greater than Viton (cf. Edwards et al. [34-35]).

Fluocarbons as material for gaskets is mostly well known as Teflon, but the other trade names as: PTFE, Fluon, Kel-F, Hodtaflon are also used in vacuum technique. Teflon gaskets need higher sealing pressure then the rubber ones. The temperature range in which the fluocarbon gaskets may be used is quite wide. The maximum temperature for vacuum systems containing Teflon is specified to 425°C. At this temperature material changes from being relatively dense to porous and its volume grows by a large factor (after Roth [108]). When a seal is broken for cleaning or repair, no cleaning of the sealing area is required, and the gasket can be frequently reused. If the seal is made from Teflon rope material the joint is made by merely overlapping or crossing the material as mentioned by Magee [80]. Also the Teflon-to-Teflon seal seems to be as effective as the Teflon-to-metal seal. The Teflon is impervious to most chemicals except alkali metals, never hardens, never adheres and is completely inert. Teflon seals are easy to install by means of its self-adhering surface and it decrease the repair time.

The last group of gasket materials are metals. This group contains mainly gold, aluminium, copper, as well as indium, lead and rarely nickel, silver, iron or other gasket materials.

Certain advantages of gold are its low yield point and no oxidation while heating. Also it has similar coefficient of thermal expansion as stainless steel. On the other side, gold gaskets have to be highly compressed (gold becomes much harder when it is deformed) and the gaskets are quite expensive especially for sealing the large diameters, as mentioned by Holden et al. [52]. The cost of the gasket is high but not unreasonable due to the high salvage of the gold, 75% of the initial value. The other way to make the gold as more economical material for gasket is to reuse it. It was undefined by Frohn et al. [42], that the gold O-ring gasket, compressed between the flat flange and V-groove, can be reused after turning it by 180° and annealing to remove the strain hardening.

There exists special technique to obtain soft (not hardened) uniform gasket from a gold wire using the spot welding machine with graphite or carbon blocs and after flame clean at 700°C to 800°C. This technique, described by Shultz [111] avoids the introduction of impurities during fusion of the gold.

On opposite side there are gaskets made of aluminium, which is one of the cheapest materials for seals. Aluminium is mostly used as wire or a thin foil. The other advantage of aluminium is that it can be used up to about 400°C. The problems are with high sealing force required and the diffusion of the aluminium into the flange through cracks in the oxide surface layer.

Indium as a gasket material is used generally in wire form. The gasket is usually just an indium wire with overlapped end, instead of proper O-ring shape, which is sealed in the joint by indium cold welding during compression between flanges. The normal O-ring seals also exist but they are not very common. Indium can resist the temperatures up to 150°C and can be used for ultimate pressure not lower than 10^{-8} Torr (1.3 x 10^{-6} Pa). The reason is that the indium is melt at 155°C and is therefore not suitable for bakeable systems. It was suggested by Elsworth et al. [36], that theoretically, when the metals melted, the surface tension forces between flange and liquid metal were greater than the atmospheric pressure pushing the fillet of liquid metal into the vacuum. However this fact has never been used in real design. Indium is also used to plate the flanges and to coat the gaskets (after Shuchman [110]). Indium is certainly a good material for seals at low temperature. It retains high ductility at these temperatures and no high sealing pressure is required.

The other metals like lead, silver or stainless steel are rarely used for gaskets. Copper is one of the most common materials for gaskets. The advantage of this material is a possibility to use it up to temperature 800°C. A disadvantage of copper gasket is the fact that it oxidizes rapidly when heated in air. The copper oxide evaporates and condenses on the faces of the flanges (near the seal) which periodically have to be cleaned. During bakeout of UHV systems, hard oxide layers will form on the surface of the copper gaskets that are exposed to air, unless the gaskets are provided with some protection. This oxide layers can be quite heavy even after a “mild” bakeout and will then peel off when the gaskets are removed. At CERN, several surface protections have been tried on the copper gaskets (silver, gold, indium, nickel), reported by Wikberg [126]. Only silver and gold plated gaskets gave good UHV performance. The gold layer however interfaces fairly rapidly with the copper at bakeaout temperature, so in the end the best solution seems to be a silver layer. The oxidation of the copper has been overcome by silver plating the gaskets at minimum 5µm, but it is not in common use (perhaps due to the higher cost then pure copper gaskets).

2.4 Detailed description of the CF seals

Extensive investigations mentioned by Unterlerchner [120] have proved that zero leakage cannot be reached by simply bolting two, even carefully machined, flanges together. To reach the desired leak tightness plastically deformed gaskets are used to fill the unavoidable surface roughness and waviness of the flanges.

The CF seals seem to be one of the most reliable and common solution for UHV systems. Due to the metal gasket it can withstand high temperatures (needed for bakeout treatment) and radiation background (normal for the accelerator systems). A typical CF joint compresses a 1.6-2mm thick pure copper gasket between 20° angled sealing edges machined on the faces of opposing flanges.

The seal edges sink into the gasket to a normal depth of 0.36-0.40 mm per edge, produce interface pressure several times exceeding the gasket's yield strength. The seal is used in flanges to 300 mm diameter and as a valve main seal to 100 mm diameter. The cost of larger gaskets has discouraged applications for larger sizes.

Advantages described by Wheeler [123] include good resealing if the flanges are not closed, bakeout ability to 500°C, easy gasket handling with bakeout temperature 250°C, and very good tolerance for flange and gasket damage and particle inclusion. Other features are the identical flange seals (no male and female halves) and no special techniques required for sealing (Yoshimura [141]). Also important is immunity to leaks from gasket scratches and flange nicks which means no polishing or refinishing of flanges between seals and flat copper gasket which is inexpensive material. Disadvantages are high force (2260 kN/m) and severe requirements for repeating seal position when used as a valve main seal.

2.4.1 The sealing mechanism

Sealing of the CF demountable joints is affected by compressing against each other pairs of flanges, which are made of aluminium or stainless steel. Flanges are acting to squeeze a soft metal gasket between them in order to obtain a leak-tight joint. To describe the tightening mechanism a joint consisting of two blank flanges and a gasket will be considered after Diepens [33], as shown in Figure 33.

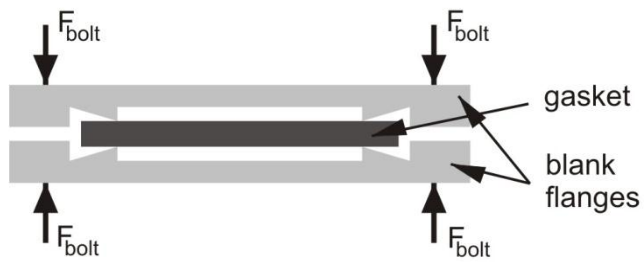

Figure 33 : Joint, before tightening

When the tightening of the joint was started, the flanges are hinge supported in the radial direction at the interface between the flange and the gasket (Figure 34a).

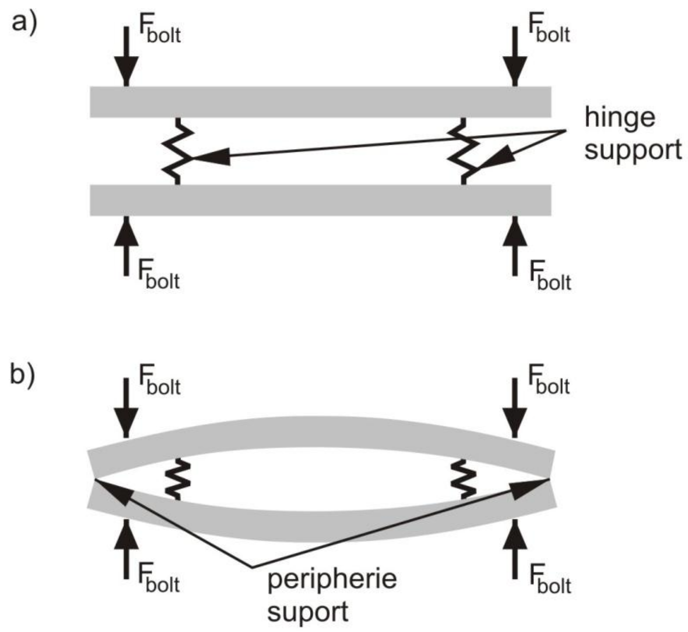

Figure 34 : Joint, tightening

This hinge support will, because of the elastic and plastic compression of the gasket, move in the axial direction. The forces working on the flanges are the bolt forces, which are in this stage and because of axial balance, equal to the total gasket (sealing) force. This is the first stage of the tightening, which will continue until the flanges get in contact at their peripheries (Figure 34 b). After this contact the boundary conditions for the flanges change. Beside the hinge support at the flange – gasket interface, the flanges are now also supported in the contact area at the peripheries. The forces working on the flanges are the bolt forces needed to tighten the joint, and in this stage they are equal to the sum of the gasket (sealing) force and the contact force between the flanges at their peripheries. This support is in the first approximation a hinge support. Continuing the tightening of the joint after contact (second stage), results in straightening of the flanges.

This straightening of the flanges occurs because of the possibility of axial movement of the hinge support at the flange – gasket interface (as in stage 1), and the impossibility of axial movement at the flange peripheries. The straightening of the flanges will result in lower maximum stresses in the flanges, which means that the highest stresses in the flanges occur during the first stage of the tightening, at the moment when the flanges start getting in contact at the peripheries.

The leak tightness is maintained as long as a given minimum sealing force is provided at the interfaces between the flanges and the gasket. This sealing force must be provided by stored energy in the joint elements, i.e. the gasket, the flanges or the fasteners, individually or in combination. This elastic interaction between the components is the so called "sealing mechanism".

To describe the situation in the gasket the "capture model" is useful (Figure 35). Applying the force to the flanges the knife-edges penetrate the gasket material and forcing towards the middle point of the thickness under the knife and outward radial up to retaining gasket counter. This model is based on the hypothesis that the due to the expansion of the outer diameter of the gasket it is touched and somehow sealing the counter of the flange. It is claimed that the sealing force coming from the compression of the gasket is compare with the stresses received from pushing the gasket material toward the counter of the flange. This second influence into the sealing force was denied by Kurokouchi [62]. The experimentally obtained results demonstrated that no relationship existed between expansion of the outer diameter of a tightened gasket and the sealing ability of the CF system. The sealing was accomplished by tightening, and succeeded without the capture of the gasket's entire outer rim.

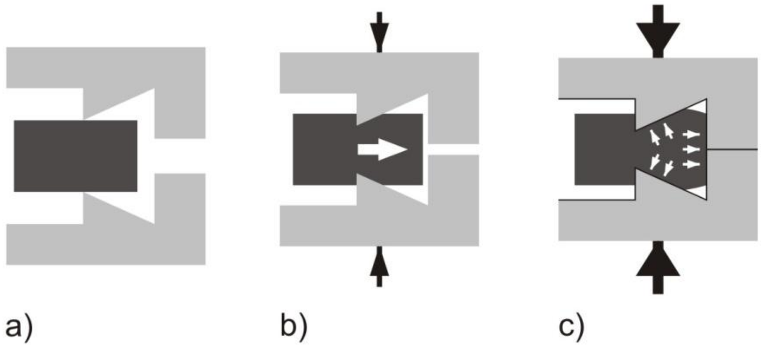

Figure 35 : CF system sealing process

Knife-edges during the tightening process produce deformations, elastic as well as plastic. Plastic deformation occurs in the gasket (especially at the interfaces) and will result in a "replica" of the surfaces of the flanges on the mating gasket surfaces. This allows the seal to be leak tight as long as a minimum sealing force is provided. Elastic deformations occur in the flanges as well as in the gasket. These elastic deformations can be seen as stored energy (potential energy in a compressed spring) in the joint elements, which provides the sealing force. The elastic interaction between them will allow the joint elements to follow each other's relative movements as long as there is stored energy (elastic deformation) left in the joint elements.

The quality of the joint depends on the sealing force, i.e. the more constant the sealing force, the better the sealing. It is therefore clear that one wants to have, within reasonable limits, as big and constant the gasket force as possible.

From experiments it was observed that the sealing process for CF seals is subdivided in four steps. Al stages are shown in Figure 36. The value of dislocation reflects the distance between flanges, which is decreasing.

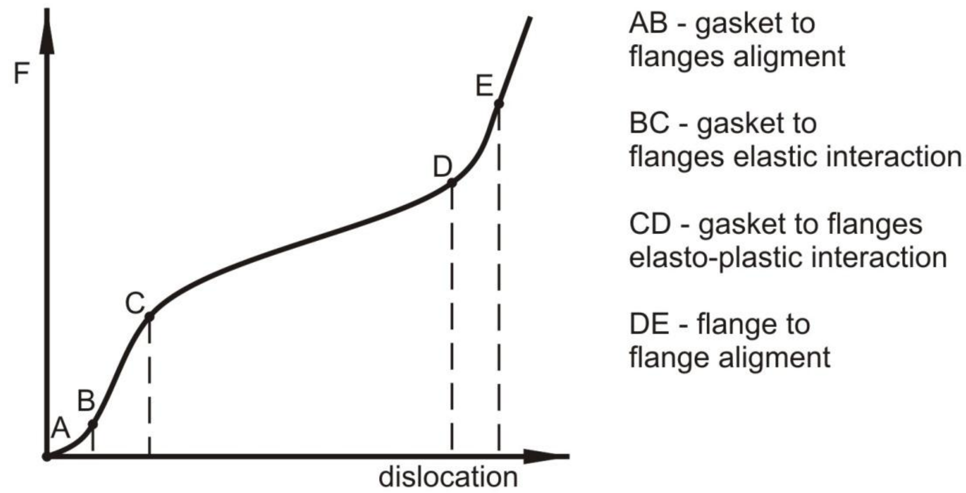

Figure 36 : Sealing stages

At first stage AB the gasket is aligned to the knife edges. In this stage an additional low force is needed to close the flanges. When the gasket and flanges are perfect in shape this stage is despaired (as usually assumed in calculation, theories). The first stage can be significant and influent mainly to second stage BC in case of large initial imperfection in gasket and flanges shapes. After alignment between the gasket and flanges the elastic interaction appears. The effort to compress the gasket is depends mainly on elastic properties as well as the knife shape. After, when knifes have gone deep enough the elastic-plastic stage CD takes place. This stage is terminated when the flanges touch each other; first only one line (point D) afterwards available flange surface (point E).

2.4.2 Materials aspects for gasket and flanges

The commonly used gasket material for CF flanges is OFHC-copper. One can demonstrate that homogeneously baked flanges are repeatedly bakeable without failure. But in the presence of sometimes unavoidable temperature differences in the flanges during bakeout, leaks appear.

It was showed by Unterlerchner [120] that gaskets lose their elastic properties due to the OFHC copper recrystalization at bakeout temperatures. It is common practice to increase the elastic limit and hardness of gasket by cold work. During the bakeout treatment (heating up to 200-300°C), even after a short time, the recrystalization of the OFHC copper (cold worked) appears. Cause the recrystalization, material backs to its previous soft and ductile state. This effected to the elastic limit and hardness drop and depends on temperature, time of baking and how much the material is cold worked.

The same author [121] claimed that for copper OFHC gaskets, baked at temperatures about 300°C and time of 50 hours the drop of the yield point from 200 MPa to about 50 MPa (characteristic value in the annealed state) occurs. This phenomenon is important in case of the sealing energy accumulated by gasket, which varies quadratically with the elastic limit of the gasket material.

This problem can be overtaken by using the material with high recrystalization thresholds. After some investigations made by Unterlerchner at CERN [120-121] on copper alloys, the

OFC copper was find as a stable material under bakeout conditions. The OFS copper is the alloy with low silver content (0.1% Ag), which leads to the higher threshold for recrystalization process (the gasket can withstand the 350°C for several hundred hours).

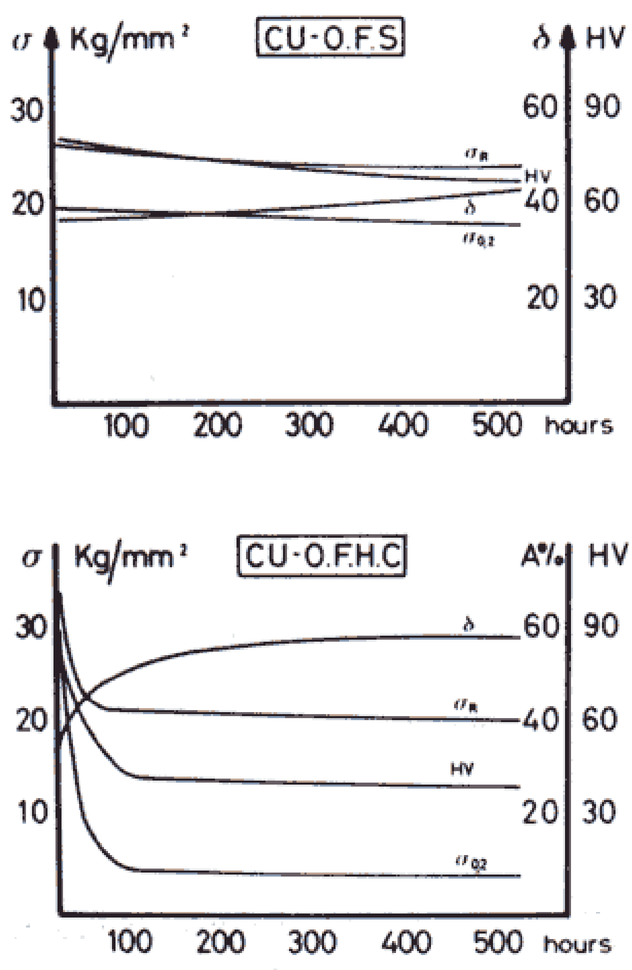

Figure 37 : Copper mechanical properties of copper in elevated temperature

For higher bakeout temperatures (~400°C) precipitation hard-enable alloys such as Cu-Cr, Cu-Zr or Cu-Be, installed and used in soft or half-hard condition, are much more stable. In such alloys, the recrystalization threshold is in the range of 500°C (cf. Unterlerchner [120]).

Second problem to overtake is the oxidation of the copper especially in high temperature. Experiments revealed that the CF seal with OHFC copper gasket leaked after 53 cycles. Analysis of the flange showed that the cause of leakage was due to oxidation of the copper gasket. During bakeout of UHV systems, hard oxide layers will form on the surface of the copper gaskets which is exposed to air, unless the gaskets are provided with some protection. This oxide layers can be quite heavy even after a "mild" bakeout and will then peel off when the gaskets are removed. At CERN, several surface protections have been tried and reported by Wikberg [126], for the copper gaskets (silver, gold, indium, nickel). Only silver and gold plated gaskets gave good UHV performance. The gold layer however interfuses fairly rapidly with the copper at bakeout temperature. So at the end the best solution seems to be a silver layer. The oxidation of the copper has been overcome by silver plating the gaskets at minimum 5μm. Numerous gaskets have shown excellent performance and appearance even after 800h at 350°C (200 cycles each of 4h) (cf. Wikberg [126]).

The other solution for cancelling the oxidation problem is to use other material for gasket, for example nickel (grade 200) suggested by Fuente [41]. This material is known as having excellent resistance to high temperature corrosion and to its commercial availability. No form of oxidation was present on the nickel gasket after 53 cycles. After a total of 130 thermal cycles, the nickel gasket CF seal remained leak free.

The other material properties aspects must also be considered. Metal sealed flanges stay leak tight as long as formed gasket is able to follow all relative of the flanges. Inhomogeneous temperature distribution during bakeouts, however, can cause considerable differences of diameter within a pair of flanges because of the bad heat conductance and high expansion coefficient of stainless steel. Leaks appear as soon as the difference is too great and sliding occurs between the mating sealing surfaces. The stainless steel has a very high coefficient of thermal expansion which is identical to that of copper (λ=17.5x10^{-6} m/m°C), but has a very bad thermal conductivity which is 26 times worse than that of copper (α=0.035 cal/cm s°C). Comparing this information with bakeout jackets mounted on the outer circumference of flanges can lead (in the first phase of the bakeout) up to 30°C average temperature difference in a pair of flanges of dissimilar mass distribution mentioned by Unterlerchner [120]. This expansion causes a parallel displacement of the flanges which results in a destruction of the formed seal.

The problem connected with the thermal expansion of the sealing parts is important at situation when one of the flanges is the blank flange (after Unterlerchner [121]). The temperature plotted against time during a bakeout, has shown differences of up to 60°C between the average temperature of an open flange and the centre of a blank flange of 215 mm outer diameter. The precaution adopted to cope with the differential expansion between flanges due to these differences was the replacement of the massive central part of a blank flange by a welded-in thin walled domed end. By this means, the two flanges had about the same mass and differences in temperature and subsequent differential thermal expansion was eliminated.

2.4.3 Other reliability aspects

Flanges with too small gasket grooves or flange pairs with different knife-edge diameters or profile shapes sometimes caused umbrella-like gasket deformations or in certain cases even prevented a correct assembly of the joint (Figure 38) as reported by Unterlerchner [121].

Figure 38 : Umbrella-like deformation of a gasket

Also at CERN in the Intersecting Storage Ring (IRS) during operation with circulating proton beam the imprints of fibres were reported at overwhelming number of leaking gaskets. With the exception of specific metal fibres, all of them were of organic material. The leak occurred only after some bakeouts or, perhaps, after a certain radiation exposure.

The standard solution for connecting the flanges is to use the bolts for tightening. The bolts are subjected to high stresses due to the forming of the gasket and, in addition, for the mechanical stability of the joint. This load may be change during the bakeout as a consequence of temperature differences and differential expansion between the flanges and the bolts which may reach differences of up to 50° in the heating-up phase of bakeouts. Subsequent plastic deformations are unavoidable if the bolts are already pre-stressed up to the yield point, as described by Unterlerchner [120].

The bolt sections withstand; the tensile stresses, shear stresses which depend on the tolerances and friction in the bolt-nut interface. The stresses can reach considerable values especially on reused material and the loss of axial bolt force can reach, at a given tightening torque, more than 50%. The sum of all these stresses requires high strength bolts of yield point of about 900 MPa. Low strength material may impair considerably the reliability of the joint.

An additional feature that sometimes is incorporated is silver plating both the bolts and plate nuts in order to prevent galling during thermal cycling. Both the bolts and plate nuts can be silver plated to 0.0001 in. (0.025 mm) thickness in accordance to ANSI/ASTM standard B254-79 and were considered by Fuente [41].

Kurokouchi [61] showed that friction around bolt heads and threads has a serious effect on the penetration of the flange knife edge into the gasket as well as on the formation of the contact seal area. Thus, the lubricating conditions of the bolts can affect the seal reliability of the CF system. Experimental results on the influence of bolt lubricating conditions on the penetration of the flange knife edge into the gasket were reported. The experimental results showed by the author lead to conclusion that penetration of the knife edge is insensitive to the lubricating conditions under torque of 100 kgf cm (9.8 Nm), while it is clearly dependent on lubrication at torque of 150 kgf cm (14.7 Nm). It was confirmed that using the washers increases penetration of flange knife edge as long as the washers are placed on the correct side. It should be noticed that the use of washers on the reverse side serves to decrease the penetration only.

In UHV systems it is often desirable to place two tanks as close as possible to one another with a dismountable and routable flange connection which can be baked. To minimize this required operating distance other not classical solutions (reported by Zanoli [137] or Mapes [81]) can be used. Normal technique of gaining axial space is cutting out the bolt holes and introducing the bolts laterally. For that solution a flange can be rotated with respect to the other one only by the fixed angle at which the holes are placed. This disadvantage can be removed by mounting on one side a fixed flange with slotted bolt holes, and on the other side a rotateable one. Another solution is based on the machined or forged clamps. The last solution uses the chain-type coupling which seems to be applicable for vacuum of 10^{-12}Torr ($1.3x10^{-10}$ Pa) and bakeout treatment at 350°C.

The advantage of using the chain coupling is reduction of radiation exposure of vacuum personnel in the accelerator environment, especially proton machines where high background radiation exists. A number of different solutions for quick chain-type coupling were used at Brookhaven National Laboratory (Mapes [81]).

Chapter III:

Constitutive Equations

3 CONSTITUTIVE EQUATIONS

3.1 Formulation in the light of Continuum Damage Mechanics

The gasket operates usually under the conditions of large deformations. This implies application of the elastic-plastic regime, including evolution of micro-damage. In addition, the gasket material is exposed to radiation (that induces damage originating from particle beam and synchrotron radiation) and heating process (bakeout treatment and heating induced by radiation).

At the level of atoms the elastic interactions are first of all observed. The atoms are held together by atomic bonds. Elasticity at the micro-scale level can be detected by a physical study of the atoms correlations and interactions in the lattice. For engineering purpose a mathematical description using the constitutive equations at the meso-scale is developed. This leads to the well known equations of the linear theory of elasticity.

The plastic deformation takes place at the level of lattice. This phenomenon is directly connected with slips. When the shear stresses are acting in the material, the dislocations move in the lattice. This leads to the irreversible plastic strains. The bonds between the lattice molecules are broken, displaced and slip occurs partially without rebounding in the lattice structure (Figure 39). The other plastic mechanisms are: climbing of dislocations and twinning. All these processes can be locally described at the level of crystals or molecules.

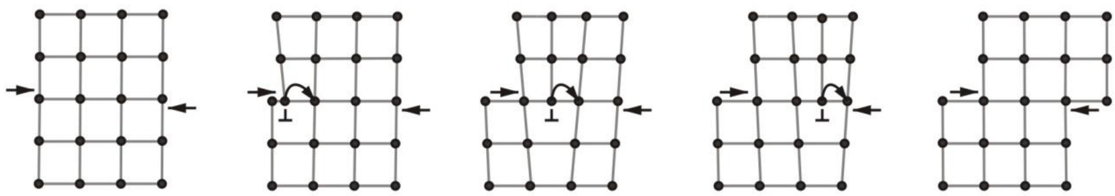

Figure 39 :Plastic slip in the lattice

Plastic yielding is correlated with the motion of dislocations. On the other hand, plastic softening or hardening is related to the mechanism of dislocations motion in the presence of obstacles. Plastic behaviour of nonirradiated materials is defined by formation of sessile junctions or dipoles and by dislocation – dislocation interactions processes. Generally, in the metals plastic flow and upper yield point can be changed by additional impurities. This influence is described by the Cottrell mechanism where the evolution in plastic behaviour is caused by mechanism of dislocation de-trapping from “clouds” of impurities. Irradiation process can be treated as a source of defects similar to the “clouds” of impurities (cf. Ghoniem at al. [46]) (contains dislocation loops, SIA/vacancy clusters, Frank loops, He bubbles). It is worth pointing out, that the irradiation defects (impurities) are much more complex and can move, interact with each other, shrink, grow and recombine.

The micro-damage can originate from two sources. The first one is of mechanical nature and is related to the response to tension, compression, shear or bending. The damage mechanism is present at both atomic and meso-scale levels. At the atomic level the material structure is discontinues and it is represented by the lattice atoms or the molecular chains. The damage consists mainly in the de-bounding (number of broken bonds) or the reduction of inter-atomic energy (cf Lemaitre [72]). The dislocations move due to applied force (plastic stage). Sometimes the movement is stopped by micro-defects or micro-stress concentrations or inclusions. It may lead to the micro-crack formation because of the dislocations accumulation as indicated in Figure 40 (cf Lemaitre [70]).

Figure 40 : Nucleation of a micro-crack due to accumulation of dislocations

Another mechanism consists in the inter-granular debonding and decohesion (especially for composite materials like concrete or materials with inclusions) and it appears at the level of grains in the metals.

The process of micro-damage evolution can be of brittle or ductile nature. In the case of brittle damage a crack is initiated without a large amount of plastic strain. Here the inter-granular damage mechanism plays a fundamental role. It is related mainly to micro-cracks and micro-voids nucleation and evolution at the grain boundaries. On the other hand, in the case of ductile materials, damage process is initiated after a certain accumulated plastic strain has been reached (plastic strain threshold p_D). Damage mechanism is related to material instability that occurs in the slip-bands created in the favourably oriented crystal grains (Basista and Nowacki [9]). The constitutive models describing ductile damage remain part of the continuum damage mechanics (CDM). The material behaviour at the micro scale is integrated in the mesoscopic representative volume element (RVE) and presented in the form of constitutive equations. The main concept consists in describing discontinuous and heterogeneous damaged material via a fictitious pseudo-damaged continuum, where damage influences the state variables like stress, strain or hardening parameters. Coupling between the real state variables and the effective ones (in the fictitious continuum) is obtained by means of different principles:

- the strain equivalence principle (Lemaitre [71]; Lemaitre and Chaboche [73]),
- the stress equivalence principle (Simo and Ju [114]),
- the energy equivalence principle (Cordebois and Sidoroff [26-27]; Sidoroff [112]; Chow and Lu [28]; Chow and Yang [29]; Abu Al.-Rub and Voyiadjis [1]),

From the mathematical point of view, the coupling is obtained by introducing the damage variable into the constitutive equations:

- scalar variable (Kachanov [56]; Rabotnov [102]),
- vector variable (Davison and Stevens [31]; Kachanov [57]),
- second-rank tensor (Rabotnov [104]; Vaculenko and Kachanov [130]; Murakami and Ohno [85]; Litewka [74]; Garion and Skoczen [43]),
- fourth-rank tensor (Chaboche [24]; Simo and Ju [114]; Krajcinovic [65]; Chen and Chow [25]; Voyiadjis and Park, [133]; Voyiadjis and Delictas [135-136]),

The evolution of damage variable (damage flow) as well as the plastic flow equations can be governed by associated or non-associated rules (Voyiadjis and Delictis [135-136]; Bonora and Milella [14]).

The CDM theory develops constantly and within new fields like composite materials (Voyiadjis and Delictis [135-136]), extremely low temperatures (Garion and Skoczen [43]) or by involving stochastic formulation (Battacharya and Ellingwood [10]). Also, a considerable research has been done in order to stretch the CDM to large strains (Voyiadjis and Park [134]; Lammer and Tsakmakis [68]; Bonora and Milella [14]; Brunig[15-16]; Brunig and Rici, 2005 [17]). Several authors decompose the constitutive equations into elastic, plastic and damage parts (Voyiadjis and Delictis [135-136]), or decompose the damage variable as a function of micro-damage mechanism (Abu Al.-Rub and Voyiadjis [1]; Lammer and Tsakmakis [68]). CDM theory has been also extrapolated to nonlocal or gradient formulation. Such approach is much more effective in the situations where high stain gradients appear. A review of these methods was presented by Peerling at al. [99] and by Pamin [94]. Further work on experimental characterization of damage evolution and coupling with the methods of statistical mechanics was postulated by Krajcinovic [66], as a future of CDM.

In the present work the second source of damage will be established and studied. A beam of high energy particles is supposed to eject the atoms from their right positions in the lattice and move them to other places. The interstitials and vacancies are created. They can group to form the clusters of vacancies (micro-voids) or interstitials (micro-inclusions). The micro-cracks and the micro-voids can evolve. Such defects can be treated in a similar way like the damage fields induced by a mechanical load. In the thesis the radiation damage will be defined and linked with the well known scalar theory of CDM.

3.1.1 Scalar damage parameter

The Representative Volume Element (RVE) containing the micro-voids and the micro-cracks of mechanical origin as well as the irradiation induced clusters of local defects of lattice is indicated in Fig. 41.

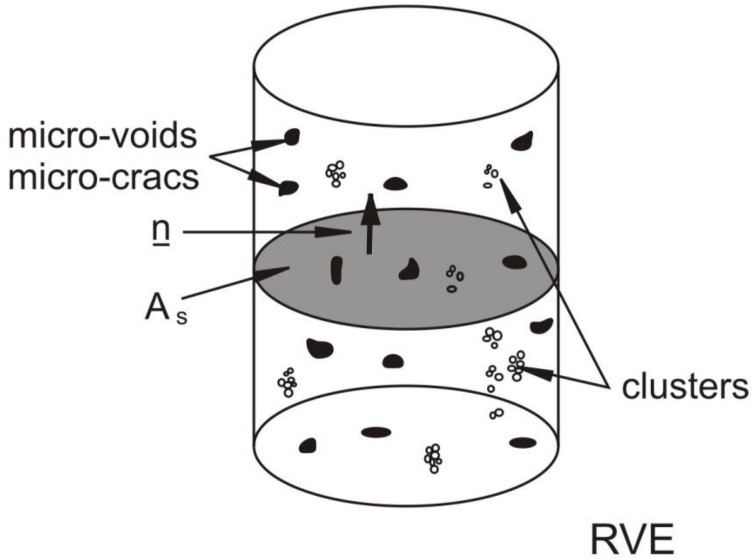

Figure 41 : The Representative Volume Element (RVE)

In the case of classical isotropic approach the damage parameter D does not depend on the orientation of the plane of cross-section and is defined as the ratio of the surface of micro-cracks and micro-voids to the area of intersection of the plane characterized by the normal vector n at point M and the Representative Volume Element (RVE).

$$D_{(M,\underline{n})} = \frac{\delta A_D}{\delta A_s} \qquad \text{Eq. 17}$$

If the RVE is homogenous and isotropic the same value of damage parameter D is obtained for each normal vector and at each point in the RVE. The damage parameter D does not depend on the orientation of the plane of intersection and is defined as:

$$D = \frac{A_D}{A_s} \qquad \text{Eq. 18}$$

where A_D denotes the integrated cross-section of damage entities, and A_S is the total cross-section. The damage parameter D stays in the range from 0 to 1. The damage parameter D equal to 0 stands for the material without any damage, while the damage parameter D equal to 1 represents total decohesion. However, the experiments confirm existence of a critical value D_{cr} for which the initiation of meso-crack takes place.In 1968 Rabotnov [103] presented the so called Effective Stress Concept. If the RVE is uniaxially loaded by the force F, the stress can be defined as:

$$\sigma = \frac{F}{A_s}$$ Eq. 19

If the material is damaged the area is smaller (minus the cross-section area of micro-cracks and micro-voids) and the effective stress is higher and can be written as:

$$\tilde{\sigma} = \frac{F}{A_s - A_D}$$ Eq. 20

If the definition of damage parameter is used the effective stress can be expressed as:

$$\tilde{\sigma} = \frac{F}{A_s(1-D)}$$ Eq. 21

It leads to a global definition of the effective stress expressed by the normal stress and the damage parameter:

$$\tilde{\sigma} = \frac{\sigma}{1-D}$$ Eq. 22

Also, the Effective Young Modulus can be defined as:

$$\tilde{E} = E(1-D)$$ Eq. 23

In 1971 the Strain Equivalence Principle was defined by Lemaitre [71]:

$$\underline{\underline{\tilde{\varepsilon}}}\left(\underline{\underline{\tilde{\sigma}}},0\right) = \underline{\underline{\varepsilon}}(\underline{\underline{\sigma}},D)$$ Eq. 24

Based on this principle the damage parameter can be interpreted in terms of the loss of the elastic stiffness. Another proposal is based on the Energy Equivalence Principle (EEP) which is more general and can be expressed by the following equation:

$$\phi^e\left(\underline{\underline{\tilde{\sigma}}},0\right) = \phi^e(\underline{\underline{\sigma}},D)$$ Eq. 25

The basic elastic-plastic formulation assumes the following constitutive law:

$$\underline{\underline{\sigma}} = (1-D)\underline{\underline{\underline{\underline{E}}}} : \underline{\underline{\varepsilon}}^e$$ Eq. 26

The yield function is expressed in terms of the yield stress σ_y, position of the centre of the yield surface represented by the back-stress tensor $\underline{\underline{X}}$ as well as the damage parameter D:

$$f = J_2\left(\frac{\underline{\underline{\sigma}}}{1-D} - \frac{\underline{\underline{X}}}{1-D}\right) - R - \sigma_y = 0$$ Eq. 27

Or:

$$f = J_2\left(\underline{\underline{\tilde{\sigma}}} - \underline{\underline{\tilde{X}}}\right) - R - \sigma_y = 0$$ Eq. 28

where:

$$J_2\left(\underline{\underline{\tilde{\sigma}}} - \underline{\underline{\tilde{X}}}\right) = \sqrt{\frac{2}{3}\left(\underline{\underline{\tilde{s}}} - \underline{\underline{\tilde{X}}}\right):\left(\underline{\underline{\tilde{s}}} - \underline{\underline{\tilde{X}}}\right)}$$ Eq. 29

3.1.2 Strain energy density release rate Y

The state laws are derived from the state potential function. The damage is interpreted as the irreversible thermodynamic process. The state potential function is understood as the Helmholtz free energy which takes into account also damage parameter D. The state potential function can be written as:

$$\Psi = \Psi\left(\underline{\underline{\varepsilon}}, \underline{\underline{\varepsilon}}^e, \underline{\underline{\varepsilon}}^p, T, \underline{\underline{\alpha}}, D\right)$$ Eq. 30

But in the case of the elastic-plastic material the strains obey the following equation:

$$\underline{\underline{\varepsilon}}^e = \underline{\underline{\varepsilon}} - \underline{\underline{\varepsilon}}^p$$ Eq. 31

The potential function can be expressed with the reduced number of parameters.

$$\Psi = \Psi\left(\underline{\underline{\varepsilon}} - \underline{\underline{\varepsilon}}^p, T, \underline{\underline{\alpha}}, D\right)$$ Eq. 32

Assume that the material density is constant at all points of the body. Using the thermodynamic principle the thermodynamic forces (variables) read:

$$\underline{\underline{\sigma}} = \rho \frac{\partial \Psi}{\partial \underline{\underline{\varepsilon}}^e}$$ stress coupled to the elastic strain

$$s = -\frac{\partial \Psi}{\partial T}$$ entropy density coupled to the temperature

$$R = \rho \frac{\partial \Psi}{\partial r}$$ isotropic hardening parameter coupled to the plastic strain

$$\underline{\underline{X}} = \rho \frac{\partial \Psi}{\partial \underline{\underline{\alpha}}}$$ back stress coupled to the back strain

$$Y = -\rho \frac{\partial \Psi}{\partial D}$$ strain energy density release rate coupled to damage

Also, the energy dissipated in the damage process is defined:

$$\dot{W}^D = Y\dot{D} \qquad \text{Eq. 33}$$

The Helmholz free energy potential can be written for the elastic-plastic material either in the undamaged or in the damaged form. The Ψ_γ part is associated with the isotropic hardening.

$$\Psi = \frac{1}{\rho}\left(\frac{1}{2}\underline{\underline{\varepsilon}}^e : \underline{\underline{\underline{E}}} : \underline{\underline{\varepsilon}}^e + \frac{1}{3}H\underline{\underline{\alpha}} : \underline{\underline{\alpha}}\right) + \Psi_r \qquad \text{Eq. 34}$$

$$\Psi = \frac{1}{\rho}\left(\frac{1}{2}(1-D)\underline{\underline{\varepsilon}}^e : \underline{\underline{\underline{E}}} : \underline{\underline{\varepsilon}}^e + \frac{1}{3}H\underline{\underline{\alpha}} : \underline{\underline{\alpha}}\right) + \Psi_r \qquad \text{Eq. 35}$$

Going through the definition of the strain energy density release rate made before, the Y and D parameters form a pair of dual variables related to each other by the following law:

$$Y = -\rho \frac{\partial \Psi}{\partial D} = \frac{1}{2}\underline{\underline{\varepsilon}}^e : \underline{\underline{\underline{E}}} : \underline{\underline{\varepsilon}}^e \qquad \text{Eq. 36}$$

The same variable can be defined by using the elastic strain energy density w_e. The elastic strain energy density is defined as:

$$w_e = \int (1-D)\underline{\underline{\varepsilon}}^e \cdot \underline{\underline{\underline{E}}} d\underline{\underline{\varepsilon}}^e = \frac{1}{2}(1-D)\underline{\underline{\varepsilon}}^e : \underline{\underline{\underline{E}}} : \underline{\underline{\varepsilon}}^e \qquad \text{Eq. 37}$$

It leads to the equation that explains exactly why variable Y is called the strain energy density release rate.

$$Y = \frac{w_e}{1-D} \qquad \text{Eq. 38}$$

It corresponds to the half of variation of the elastic energy generated by the evolution of damage at constant stress and temperature.

$$d\underline{\underline{\sigma}} = \underline{\underline{\underline{\underline{E}}}}[(1-D)d\underline{\underline{\varepsilon}}^e - \underline{\underline{\varepsilon}}^e dD] = 0$$ Eq. 39

$$d\underline{\underline{\varepsilon}}^e = \underline{\underline{\varepsilon}}^e \frac{dD}{1-D}$$ Eq. 40

$$dw_e\big|_{\sigma,T} = \underline{\underline{\sigma}} d\underline{\underline{\varepsilon}}^e = \underline{\underline{\sigma}}\,\underline{\underline{\varepsilon}}^e \frac{dD}{1-D}$$ Eq. 41

$$\frac{1}{2}\frac{dw_e}{dD}\bigg|_{\sigma,T} = \underline{\underline{\varepsilon}}^e : \underline{\underline{\underline{\underline{E}}}} : \underline{\underline{\varepsilon}}^e$$ Eq. 42

$$Y = \frac{1}{2}\underline{\underline{\varepsilon}}^e : \underline{\underline{\underline{\underline{E}}}} : \underline{\underline{\varepsilon}}^e = \frac{1}{2}\frac{dw_e}{dD}\bigg|_{\sigma,T}$$ Eq. 43

The stress and the strain tensors can be split into two parts: the deviatoric and the hydrostatic. The hydrostatic part can be defined as a spherical (axiator) tensor.

$$\underline{\underline{\sigma}} = \underline{\underline{s}} + \frac{1}{3}tr(\underline{\underline{\sigma}})\underline{\underline{I}} = \underline{\underline{s}} + \underline{\underline{\sigma}}_H$$ Eq. 44

$$\underline{\underline{\varepsilon}} = \underline{\underline{e}} + \frac{1}{3}tr(\underline{\underline{\varepsilon}})\underline{\underline{I}} = \underline{\underline{e}} + \underline{\underline{\varepsilon}}_H$$ Eq. 45

The Huber-Misses-Hencky equivalent stress is defined as:

$$\sigma_{eq} = \sqrt{\frac{3}{2}\left(\left(\underline{\underline{\tilde{s}}} - \underline{\underline{\tilde{X}}}\right)\cdot\left(\underline{\underline{\tilde{s}}} - \underline{\underline{\tilde{X}}}\right)\right)}$$ Eq. 46

where $\underline{\underline{\tilde{s}}}; \underline{\underline{\tilde{X}}}$ denote the effective deviatoric stress and the effective back stress tensors, respectively. Taking into account three last equations, together with the definition of the elastic strain energy density the Y variable can be derived in the following way (Lemaitre [70]):

$$w_e = \int \underline{\underline{\sigma}} d\underline{\underline{\varepsilon}}^e = \int \underline{\underline{s}} d\underline{\underline{e}}^e + \int \underline{\underline{\sigma}}_H d\underline{\underline{\varepsilon}}_H^e \quad \text{Eq. 47}$$

$$\underline{\underline{e}}^e = \frac{1+\nu}{E} \frac{\underline{\underline{s}}}{(1-D)} \quad \text{Eq. 48}$$

$$\underline{\underline{\varepsilon}}_H^e = \frac{1-2\nu}{E} \frac{\underline{\underline{\sigma}}_H}{(1-D)} \quad \text{Eq. 49}$$

$$Y = \frac{\sigma_{eq}^2}{2E(1-D)^2} \left(\frac{2}{3}(1+\nu) + 3(1-2\nu)\left(\frac{\sigma_H}{\sigma_{eq}} \right)^2 \right) \quad \text{Eq. 50}$$

The ratio (σ_H/σ_{eq})is called triaxiality function. When increasing this ratio the ductility is decreasing. For isotropic material, Y variable can be expressed by the Huber-Misses-Hencky equivalent stress and the triaxility function R_v:

$$Y = \frac{\sigma_{eq}^2}{2E(1-D)^2} R_v = \frac{\tilde{\sigma}_{eq}^2}{2E} R_v \quad \text{Eq. 51}$$

$$R_v = \frac{2}{3}(1+\nu) + 3(1-2\nu)\left(\frac{\sigma_H}{\sigma_{eq}} \right)^2 \quad \text{Eq. 52}$$

$$\sigma_H = \frac{1}{3} Tr\left[\underline{\underline{\sigma}}\right] \quad \text{Eq. 53}$$

3.1.3 Kinetic Law of Damage Evolution

To define the kinetic law of damage evolution the second principle of thermodynamics must be written:

$$\underline{\underline{\sigma}}\dot{\underline{\underline{\varepsilon}}} - \rho\left(\dot{\Psi} + s\dot{T}\right) - \underline{q}\frac{\underline{\nabla T}}{T} \geq 0 \quad \text{Eq. 54}$$

The differential of the free energy can be expressed as a function of state variables:

$$d\Psi = \frac{\partial \Psi}{\partial \underline{\underline{\varepsilon}}^e} d\underline{\underline{\varepsilon}}^e + \frac{\partial \Psi}{\partial T} dT + \frac{\partial \Psi}{\partial r} dr + \frac{\partial \Psi}{\partial \underline{\underline{\alpha}}} d\underline{\underline{\alpha}} + \frac{\partial \Psi}{\partial D} dD \quad \text{Eq. 55}$$

Considering that the strain rate is equal to the sum of the elastic and the plastic parts, one obtains:

$$\left(\underline{\underline{\sigma}} - \rho \frac{\partial \Psi}{\partial \underline{\underline{\varepsilon}}^{e}}\right)\dot{\underline{\underline{\varepsilon}}}^{e} - \rho\left(s + \frac{\partial \Psi}{\partial T}\right)\dot{T} + \underline{\underline{\sigma}}\,\dot{\underline{\underline{\varepsilon}}}^{p} - \rho \frac{\partial \Psi}{\partial \underline{\underline{\alpha}}}\dot{\underline{\underline{\alpha}}} - \rho \frac{\partial \Psi}{\partial D}\dot{D} - \underline{q}\frac{\underline{\nabla T}}{T} \geq 0 \qquad \text{Eq. 56}$$

After having used the associated variables the other form of this equation can be obtained:

$$\underline{\underline{\sigma}}\,\dot{\underline{\underline{\varepsilon}}}^{p} - R\dot{r} - \underline{\underline{X}}\,\dot{\underline{\underline{\alpha}}} + Y\dot{D} - \underline{q}\frac{\underline{\nabla T}}{T} \geq 0 \qquad \text{Eq. 57}$$

The above can be decoupled by using the thermo-mechanical criteria, which leads to two independent conditions (the mechanical and the thermal):

$$\underline{\underline{\sigma}}\,\dot{\underline{\underline{\varepsilon}}}^{p} - R\dot{r} - \underline{\underline{X}}\,\dot{\underline{\underline{\alpha}}} + Y\dot{D} \geq 0 \qquad \text{Eq. 58}$$

$$\underline{q}\frac{\underline{\nabla T}}{T} \geq 0 \qquad \text{Eq. 59}$$

To satisfy these conditions the dissipated power connected with the damage process must be positive, especially that the plastic dissipation for isothermal process is negligible [69], [69]:

$$Y\dot{D} = \dot{W}^{D} \geq 0 \qquad \text{Eq. 60}$$

After Lemaitre [70] all kinetic laws can be defined by using a dissipation potential. The potential is defined by using the following variables and parameters:

$$F\{variables \quad || \quad parameters\} = F\left\{\underline{\underline{\sigma}},\, R,\, \underline{\underline{X}},\, Y \,||\, \underline{\underline{\varepsilon}}^{e},\, r,\, \underline{\underline{\alpha}},\, D\right\} \qquad \text{Eq. 61}$$

Using the so-called normality rule the constitutive equations connected with the evolution of plastic strain fields can be derived. The evolution of the plastic strain, the isotropic strain hardening and the back stress can be expressed by using the plastic multiplier and proper definition of the dissipation potential.

$$\underline{\underline{\dot{\varepsilon}}}^{p} = \frac{\partial F}{\partial \underline{\underline{\sigma}}} \dot{\lambda}$$ Eq. 62

$$\dot{r} = \frac{\partial F}{\partial R} \dot{\lambda}$$ Eq. 63

$$\underline{\underline{\alpha}} = \frac{\partial F}{\partial \underline{\underline{X}}} \dot{\lambda}$$ Eq. 64

Similarity between the damage and the plastic strain evolution leads to the formulation of damage evolution low expressed by the potential of dissipation function F_d:

$$\dot{D} = \frac{\partial F_d}{\partial Y} \dot{\lambda}$$ Eq. 65

The dissipation potential F_d can be expressed as a function of two material parameters S and s:

$$F_d = \frac{S}{(s+1)(1-D)} \left(\frac{Y}{S}\right)^{s+1}$$ Eq. 66

The parameter S is understood as the strength energy of damage and it is defined as material parameter (obtained via the experiments). Also, the parameter s is identified in the same way (experimental data). Before this functional will be used the other helpful variable must be defined. It is the accumulated plastic strain and its rate:

$$\dot{p} = \sqrt{\frac{2}{3} \underline{\underline{\dot{\varepsilon}}}^{p} : \underline{\underline{\dot{\varepsilon}}}^{p}}$$ Eq. 67

$$p = \int_0^t \dot{p} d\tau = \int_0^t \sqrt{\frac{2}{3} \underline{\underline{\dot{\varepsilon}}}^{p} : \underline{\underline{\dot{\varepsilon}}}^{p}} d\tau$$ Eq. 68

Also, relation with the plastic multiplier can be deduced:

$$\dot{p} = \sqrt{\frac{2}{3} \underline{\underline{\dot{\varepsilon}}}^{p} : \underline{\underline{\dot{\varepsilon}}}^{p}} = \frac{\dot{\lambda}}{1-D}$$ Eq. 69

It leads to the following form of the kinetic law of damage evolution:

$$\dot{D} = \frac{\partial F_d}{\partial Y}\dot{\lambda} = \left(\frac{Y}{S}\right)^s \dot{p} = \left[\frac{\sigma_{eq}^2 R_v}{2ES(1-D)^2}\right]^s \dot{p}$$ Eq. 70

Including the initiation condition (damage threshold), the isotropic damage evolution law for ductile materials can be described by the equation:

$$\dot{D} = 0 \text{ if: } p < p_D$$ Eq. 71

$$\dot{D} = \left(\frac{Y}{S}\right)^s \dot{p} \text{ if: } p \geq p_D$$ Eq. 72

Finally, concerning the initiation damage condition (damage threshold), the isotropic damage evolution law for ductile materials can be described using the Heaviside function:

$$\dot{D} = \left(\frac{Y}{S}\right)^s \dot{p} H\left(p - p_D\right)$$ Eq. 73

3.1.4 Orthotropic ductile damage using second order damage tensor

Assume at a given point a local set of unit base vectors, tangent to the principal directions. The relevant damage tensor is introduced in the form:

$$\underline{\underline{D}} = \sum_{i=1,3} D_i \vec{n}_i \otimes \vec{n}_i$$ Eq. 74

where $\vec{n}_i$ stands for the base vector associated with the principal direction i and D_i denotes the component of the damage tensor related to the direction "i". It is defined by:

$$D_i = \frac{dS_{D_{\vec{n}_i}}}{dS_{\vec{n}_i}}$$ Eq. 75

where $S_{D_{\vec{n}_i}}$ is the area of damage in the section $S_{\vec{n}_i}$, represented by the normal $\vec{n}_i$. The effective stress $\underline{\underline{\tilde{\sigma}}}$ is supposed to obey the strain equivalence principle (Lemaitre [70]):

$$\underline{\underline{\tilde{\sigma}}} = \underline{\underline{\underline{\underline{E}}}} : \underline{\underline{\varepsilon}}^e$$ Eq. 76

The relation between the stress and the effective stress tensors is postulated in the following form:

$$\underline{\underline{\sigma}} = \frac{1}{2}\left(\left(\underline{\underline{I}} - \underline{\underline{D}}\right)\underline{\underline{\tilde{\sigma}}} + \underline{\underline{\tilde{\sigma}}}\left(\underline{\underline{I}} - \underline{\underline{D}}\right)\right) \quad \text{Eq. 77}$$

with $\underline{\underline{I}}$ being the identity tensor. The general relationship between the stress and the effective stress tensors reads:

$$\underline{\underline{\tilde{\sigma}}} = \underline{\underline{\underline{M}}}^{-1} : \underline{\underline{\sigma}} \quad \text{Eq. 78}$$

$$\underline{\underline{\sigma}} = \underline{\underline{\underline{M}}} : \underline{\underline{\tilde{\sigma}}} \quad \text{Eq. 79}$$

Where $\underline{\underline{\underline{M}}}$ stands for the symmetric damage effect tensor, that depends on the damage state and fulfils the conditions:

$$M_{ijkl} = M_{jikl} = M_{klij} \quad \text{Eq. 80}$$

In its general form, the damage effect tensor reads:

$$\begin{aligned}\underline{\underline{\underline{M}}} &= \frac{1}{4}\left[\left(\underline{\underline{I}} - \underline{\underline{D}}\right)\underline{\otimes}\underline{\underline{I}} + \left(\underline{\underline{I}} - \underline{\underline{D}}\right)\overline{\underline{\otimes}}\underline{\underline{I}} + \underline{\underline{I}}\underline{\otimes}\left(\underline{\underline{I}} - \underline{\underline{D}}\right) + \underline{\underline{I}}\overline{\underline{\otimes}}\left(\underline{\underline{I}} - \underline{\underline{D}}\right)\right] \\ &= \frac{1}{2}I - \frac{1}{4}\left(\underline{\underline{D}}\underline{\otimes}\underline{\underline{I}} + \underline{\underline{D}}\overline{\underline{\otimes}}\underline{\underline{I}} + \underline{\underline{I}}\underline{\otimes}\underline{\underline{D}} + \underline{\underline{I}}\overline{\underline{\otimes}}\underline{\underline{D}}\right)\end{aligned} \quad \text{Eq. 81}$$

or in direct notation:

$$M_{ijkl} = \frac{1}{2}\left(\delta_{ik}\delta_{jl} + \delta_{il}\delta_{jk}\right) - \frac{1}{4}\left(D_{ik}\delta_{jl} + D_{il}\delta_{jk} + \delta_{ik}D_{jl} + \delta_{il}D_{jk}\right) \quad \text{Eq. 82}$$

Hence, the Helmholtz free energy state potential for linear elasticity coupled with damage is written in the following form:

$$\Psi = \frac{1}{\rho}\left(\frac{1}{2}\underline{\varepsilon}^{e} : \underline{\underline{\underline{M}}} : \underline{\underline{\underline{E}}} : \underline{\varepsilon}^{e}\right) + \Psi_{p} \quad \text{Eq. 83}$$

where ψ_p is the plastic part which does not explicitly depend upon $\underline{\underline{D}}$. In the same way, the effective back stress tensor is introduced and reads:

$$\underline{\underline{\tilde{X}}} = \underline{\underline{\underline{M}}}^{-1} : \underline{\underline{X}} \quad \text{Eq. 84}$$

In the case of anisotropic ductile damage the damage parameter D is replaced by the damage tensor $\underline{\underline{D}}$ (Murakami and Ohno [85]) and the scalar function of the strain energy density release rate Y is replaced by the relevant tensor $\underline{\underline{Y}}$ (Leamaitr [70]). Again both $\underline{\underline{D}}$ and $\underline{\underline{Y}}$ form a pair of dual state variables. It is assumed that the driving force of evolution of orthotropic ductile damage remains the accumulated plastic strain. Thus, the kinetic law of damage evolution is postulated in the following form (Garion and Skoczen [43-44]):

$$\underline{\underline{\dot{D}}} = \underline{\underline{C}}\,\underline{\underline{Y}}\,\underline{\underline{C}}^T \dot{p} H\left(p - p_D\right) \qquad \text{Eq. 85}$$

which assures that the tensor of damage is symmetric. Tensor $\underline{\underline{C}}$ is defined as follows:

$$\underline{\underline{C}} = \sum_{i=1,3} C_i \vec{n}_i \otimes \vec{n}_i \qquad \text{Eq. 86}$$

and can be classified as the symmetric tensor containing the material moduli. The strain energy density release rate tensor is defined by:

$$\underline{\underline{Y}} = -\rho \frac{\partial \Psi}{\partial \underline{\underline{D}}} \qquad \text{Eq. 87}$$

$$\underline{\underline{Y}} = \frac{1}{4}\left[\underline{\underline{\varepsilon}}^e \left(\underline{\underline{\underline{\underline{E}}}} : \underline{\underline{\varepsilon}}^e\right) + \left(\underline{\underline{\underline{\underline{E}}}} : \underline{\underline{\varepsilon}}^e\right)\underline{\underline{\varepsilon}}^e\right] \qquad \text{Eq. 88}$$

The relevant potential of dissipation reads:

$$\Phi = \frac{1}{2}\left(\underline{\underline{C}}\,\underline{\underline{Y}}\,\underline{\underline{C}}^T\right) : \underline{\underline{Y}} \sqrt{\frac{\left(\underline{\underline{\tilde{s}}} - \underline{\underline{X}}\right) : \underline{\underline{\underline{\underline{M}}}}^{-1} : \underline{\underline{\underline{\underline{M}}}}^{-1} : \left(\underline{\underline{\tilde{s}}} - \underline{\underline{X}}\right)}{\left(\underline{\underline{\tilde{s}}} - \underline{\underline{X}}\right) : \left(\underline{\underline{\tilde{s}}} - \underline{\underline{X}}\right)}} \qquad \text{Eq. 89}$$

The isotropic conjugate damage variables, D and Y, can be obtained from the orthotropic state variables $\underline{\underline{D}}$ and $\underline{\underline{Y}}$ by the following operations:

$$Y = Tr\left\lfloor \underline{\underline{Y}} \right\rfloor \qquad \text{Eq. 90}$$

and, assuming that $\underline{\underline{C}}=C\underline{\underline{I}}$ for isotropic material, the first invariant of damage rate tensor reads:

$$\dot{D} = Tr\left\lfloor \underline{\underline{\dot{D}}} \right\rfloor = C^2 Y \dot{p} \qquad \text{Eq. 91}$$

which corresponds to the isotropic damage evolution law with $S = 1/C^2$.

3.1.5 Criterion of the macro-crack onset

In order to predict at which contact pressure (external load) the onset of macro-crack occurs a criterion of critical value of damage parameter (in the isotropic case) has been used. The criterion is based on the assumption that the local micro-damage field of sufficiently high intensity enhances the probability of macro-crack nucleation. The simplest form of such criterion reads:

$$D = D_{cr} \qquad \text{Eq. 92}$$

where D_{cr} corresponds to the critical value of damage parameter. Generally, the critical value of damage depends on the material properties and loading conditions. In the simplest case of one-dimensional monotonic tension the critical damage is estimated as (Lemaitre [70]):

$$D_{cr}^{0} = 1 - \frac{\sigma_r}{\sigma_u} \qquad \text{Eq. 93}$$

where σ_u denotes the ultimate strength and σ_r is the stress to rupture. Both values can be easily identified by means of the stress-strain experimental curve. In the three dimensional case the critical value of damage parameter can be computed by means of the following formula:

$$D_{cr} = D_{cr}^{0} \frac{\sigma_u^2}{\sigma_s^2 T_r} \qquad \text{Eq. 94}$$

where σ_s is a plastic threshold to be chosen in the range from yield to ultimate stress and T_r represents triaxiality and is given by:

$$T_r = \frac{2}{3}(1+\nu) + 3(1-2\nu)\frac{\sigma_H^2}{\sigma_i^2} \qquad \text{Eq. 95}$$

Here, σ_H denotes the hydrostatic stress and σ_i is the stress intensity. In the case of ductile materials (for instance copper), assuming that $\sigma_s = \sigma_u$, the critical damage parameter reduces to:

$$D_{cr} = \frac{D_{cr}^{0}}{T_r} \qquad \text{Eq. 96}$$

and can be easily computed at any point of loaded structure. The criterion of onset of macro-crack becomes more complex when anisotropic representation of damage is included. In such a case, the criterion has to be generalized in the following way:

$$\left\| \underline{\underline{D}} \right\| = D_{cr} \qquad \text{Eq. 97}$$

where a norm has been imposed on damage tensor. In the present Thesis the following formulation has been applied:

$$\left\| \underline{\underline{D}} \right\| = \sqrt{\underline{\underline{D}} : \underline{\underline{D}}} \qquad \text{Eq. 98}$$

Thus, the final formulation of macro-crack onset criterion reads:

$$\sqrt{\underline{\underline{D}} : \underline{\underline{D}}} = \frac{D_{cr}^{0}}{T_r} \qquad \text{Eq. 99}$$

or

$$\left[\frac{2}{3}(1+\nu) + 3(1-2\nu)\frac{\sigma_H^2}{\sigma_i^2} \right] \sqrt{\underline{\underline{D}} : \underline{\underline{D}}} = D_{cr}^{0} \qquad \text{Eq. 100}$$

3.2 Radiation Damage formulation

Irradiation can influence the material in four ways: heating, impurity production, ionization and displacement damage. The irradiation of metals results in a strong heat generation in the material lattice. Thus, interaction of particle flux with material lattice can be represented from the thermodynamic point of view via the heat generation rate. The other source is the nuclear energy gained when the particle hits the atom and produces new particles and pure energy.

On the other hand, the *impurity production effect* appears mainly due to neutron and ion irradiation. Neutrons and ions which loose energy and can become atomic impurities in the material. Also, in the case of high energy particles during the collision the target atom can be destroyed and produce secondary particles.

Next type of radiation influence is called the *ionization process*. Ionization consists in adding or removing electrons from atoms or ions existing previously in the solid. It can also raise their energy level by moving the electrons to higher orbit layers. Ionizing radiation tends to increase damage of chemical bounds. It has the biggest influence on covalent bonds (mostly existing in organic matter), medium influence on ionic bonds and small influence on the metallic ones (mostly affected by the heat, instead).

Exposure to irradiation (flux of particles) implies creation of clusters of defects in the material. This process is usually termed the *atomic displacement damage process*. It correlates strongly with the onset and evolution of classical micro-damage (by treating clusters as micro-voids). The energy brought by the particles into the solid is dissipated mainly by the elastic collisions with lattice atoms. Collision with a particle of enhanced energy can eject the atom from its initial position in the lattice and transfer the energy to the next collision with its neighbours or simply move the atom to the interstitial position. These nuclear interactions lead to creation of the cascade of atoms moving (travelling) inside lattice as shown in Figure 42, and production of defects in the lattice (interstitials and vacancies).

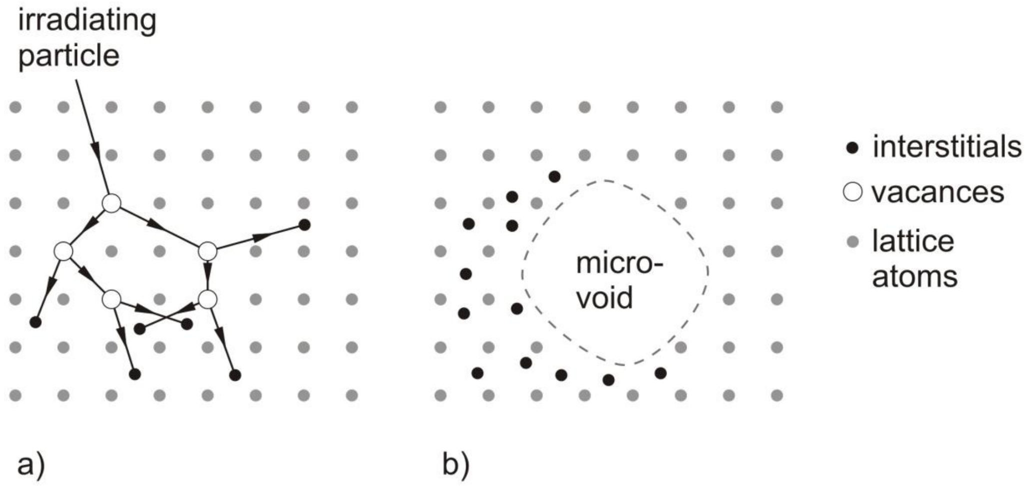

Figure 42 : Production of defects in the lattice of irradiated material

An interstitial atom together with the corresponding vacancy is referred to *Frenkel pair*. If the energy carried by particles is high enough it may lead to a cascade process in the material. During the cascade process atoms which were ejected from their lattice positions by incoming particles usually have enough energy to eject subsequent atoms from their lattice positions. When the ejected atoms reach sufficient energy, the cascades are again divided into sub-cascades. Interstitials and vacancies form clusters and grow into the cavities (Bacon at al. [5-8]). The clusters can be fixed or mobile (especially at higher temperatures) which can even lead to curing the radiation induced damage. Both the vacancies and the interstitials may also disappear by sinking into dislocations, grain boundaries and precipitates. The displacement damage process occurs when the energy dissipation mechanism takes place for ions, protons and electrons carrying energy larger than 150keV as well as for the neutron irradiation. The highly energetic Gamma-rays (1 to 10 MeV) interact with the metal lattice and produce several MeV recoil energetic electrons (Compton scattering). These electrons produce by ballistic collisions the PKA atoms and are source of displacement damage (Alexander et al. [4]).

In the recent years, the computer modelling of irradiation process has become one of the fastest growing areas of material research. At lower scale, to calculate the basic defect properties the ab-initio electronic structure calculation method is used (Wirth at al., [128]). Using pseudo-potential code with the generalized gradient and suitable local density approximation the formation, binding and energy migration can be calculated. The atomic scale modelling (ASM) is used to study the irradiation effects in metals. Recently available computer power is strong enough to simulate the atomic lattice in the range of ~10^{-15}s and 10^{-10} m (Bacon et al. [7]). Usually there is some 130.000 to 2.000.000 atoms in the model. In addition, the Molecular Dynamics (MD) and/or the kinetic Monte Carlo (kMC) methods are widely used (Diaz de la Rubia and Phythian [32]). The first one is rather applied to the primary stage of irradiation damage that means nucleation and clustering. The second one is dedicated to study the evolution of the defects produced by irradiation process (Caturla et al. [23]). In the MD simulations the dynamic and the static boundary conditions can be used. Also two different empirical inter-atomic potentials describe the atomic behaviour in the lattice: the equilibrium, short range, many-body potential (MBP) and the long range non-equilibrium pair potential. Electronic interactions are usually switched off but some authors suggest involving them in the future calculations (Matthews [83]).

Because of the stochastic nature of the simulation the population of about 40 calculations is suggested in order to obtain the reliable conclusions. At higher scale, the three-dimensional dislocation dynamics is used (Wirth et al. [128]). This method is especially useful to compute the forces acting on each dislocation, interaction process between them and between dislocations and other defects (for example irradiation defects). Also, the energy spectrum studies (irradiation source) are important for correct analysis of radiation damage (Matthews [83]). Some differences in the applied methods, potentials and computer codes used for calculations were summarized in the literature (Souidi et al. [116], Zinkle and Matsukawa [139]). Also, there is clearly a problem of comparison between the computer simulation results and the experimental data in the case of metal structure (Marian et al. [82]). This is because of short time range and the atomic size of irradiation defects (TEM observation resolution). Based on this information, some concepts of the displacement damage and associated mechanical behaviour will be proposed in frame of CDM theory.

3.2.1 Atomic displacement

In order to move an atom in the lattice, energy larger than the threshold value E_d (usually about 20-40 eV) must be received from the irradiated particle (Ivanow and Platov [54]). Minimum energy $E_{\min}$ transferred from the particle is equal to double energy required for atom displacement inside the lattice E_d.

$$E_{\min} = 2E_d \qquad \text{Eq. 101}$$

Also, the maximum amount of received energy $E_{\max}$ has been established for neutrons and heavy ions:

$$E_{\max} = \frac{4E_0 A A_1}{(A + A_1)^2} \qquad \text{Eq. 102}$$

and for electrons:

$$E_{\max} = \frac{2E_0 (E_0 + 1.022)}{A_1 M_0 c^2} \qquad \text{Eq. 103}$$

where E_0 is the energy carried by the particle; A and A_1 are the atomic masses of particle and lattice atoms; c is the speed of light and $M_0 c^2$=913.5 MeV is the equivalent energy for 1 amu (atomic mass unit – 1/12 of carbon atomic mass). For light particles such as electrons the amount of energy transferred into the solid is different than for ions and protons. The reason is the difference in their masses and some relativistic effects.

Depending on the energy carried by the Primary Knock-out Atoms (PKA), which is based on the irradiation nature and the angle of collision between the lattice atom and the particle, several types of defects in the structure may appear. In the case of low energy, the point defects like self interstitials atoms (SIA), vacancies formed in Frenkel pairs and micro-voids are created (Russell and Kim [105]). For higher energy (more than 2.5 E_d) PKA affect other lattice atoms. In such a case the displacement cascade may appear and the clusters of radiation defects may be created due to intensive atomic collisions in the core (vicinity of the trajectory of PKA). For much higher recoil energy the cascade caused by PKA can be divided into sub-cascades structure.

First clear theoretical estimation of the irradiation defects production was made by Kinchin and Peane (after Bacon et al. [5]). Their theory describes the relationship between the kinetic energy carried by primary knock-out atoms (PKAs) and the Frenkel defects production (number of SIA – pairs of vacancies *N*).

$$N_{KP} = \begin{cases} 1 \quad dla \quad E_v \in \left\langle E_D, 2.5E_D \right\rangle \\ \dfrac{E_v}{2.5E_D} \quad dla \quad E_v > 2.5E_D \end{cases} \qquad \text{Eq. 104}$$

where N_{KP} denotes the number of Frankel defects and E_v stands for energy threshold needed to move the particle. After some corrections made by Norgett (after Bacon et al., [5] and Osetsky et al. [91]), this theory was converted to the simple Norgett-Robinson-Torrens (NRT) equation (Norgett et al. [89]):

$$N_{NRT} = \frac{0.8E_{dam}}{2\bar{E}_d} \qquad \text{Eq. 105}$$

Here N_{NRT} is the number of Frankel defects, E_d is the average energy threshold over all crystallographic directions and E_{dam} denotes the energy available for elastic collision. Usually E_{dam} is equal to the energy carried by PKAs, when it is assumed that there are no electronic losses (standard assumption in the MD simulations). This equation is based on the binary collision model. It is not suitable to describe all processes (atomic interactions) during the displacement cascade process (especially for thermal spike stage).

In order to estimate E_{dam} or E_v the Non Ionizing Energy Loss (NIEL) can be used instead (after Akkerman et al. [2] and Huhtinen [53]). This parameter expressed the energy transfer from primary particle to the lattice atoms by inelastic scattering process. It is defined as portion of energy E_0 carried by a particle lost per unit travelling length (expressed in mass per area). It can be expressed as:

$$NIEL(E_0) = \frac{N_A}{A} \int_{E_{min}}^{E_{max}} dE \cdot Q(E) E \left(\frac{d\delta}{d\Omega} \right)_{E_0} \qquad \text{Eq. 106}$$

or in a different way as:

$$NIEL(E_0) = \frac{N_A}{A}\int_{\theta_{min}}^{180^o} d\Omega Q[E(E_0,\theta)]E(E_0,\theta)\left(\frac{d\delta}{d\Omega}\right)_{E_0} \qquad \text{Eq. 107}$$

where N_A is the Avogadro's number, $Q(E)$ is the partition factor and $d\delta/d\Omega$ is the so-called elastic cross-section. The minimum scattering angle θ_{min} is a function of the threshold energy E_d and the maximum transfer energy E_{max} .

$$\theta_{min} = 2\arcsin\left(\sqrt{\frac{E_{max}}{2E_d}}\right) \qquad \text{Eq. 108}$$

In order to define the partition factor (Lindhard) $Q(E)$, the dimensionless energy η ("universal potential"), Borh radius a_0, the atomic numbers Z and Z_1 (primary particle and lattice atom), and the universal function $g(\eta)$ are used.

$$Q = \frac{1}{[1 + k_L g(\eta)]} \qquad \text{Eq. 109}$$

$$k_L = 0.0794\frac{Z^{2/3}Z_1^{1/2}(A + A_1)^{3/2}}{(Z^{2/3} + Z_1^{2/3})^{3/4}A^{3/2}A_1^{1/2}} \qquad \text{Eq. 110}$$

$$g(\eta) = \eta + 0.40244\eta^{3/4} + 3.4008\eta^{1/6} \qquad \text{Eq. 111}$$

$$\eta = T\frac{aA_1}{ZZ_1e^2(A + A_1)} \qquad \text{Eq. 112}$$

$$a = a_0 0.8853(Z^{2/3} + Z_1^{2/3})^{-1/2} \qquad \text{Eq. 113}$$

The elastic cross-section is calculated in a different way for different types of irradiation (after Akkerman et al. [2]). For the electron irradiation (relativistic case) it can be expressed by using Moth differential cross-section $(d\delta/d\Omega)_M$ approximated by the Rutherford cross-section $(d\delta/d\Omega)_R$.

$$\left(\frac{d\delta}{d\Omega}\right)_M = \left(\frac{d\delta}{d\Omega}\right)_R \cdot \sum_{j=0}^{4} a_j(E_0, Z)(1-\cos\theta)^{j/2}$$ Eq. 114

$$\left(\frac{d\delta}{d\Omega}\right)_R = \frac{r_0^2 Z^2 (1-\beta^2)}{\beta^4 (1-\cos\theta)^2}$$ Eq. 115

Here r_0 is the classical electron radius, β is the electron velocity expressed in c unit and a_j are the fitting coefficients. For gamma-rays the main process of losing energy is the Compton scattering (for energy higher than about 0.511 MeV). The differential cross-section in this case can be described by the formula proposed by Heitler (after Akkerman et al [3]):

$$\left(\frac{d\delta}{dE}\right) = \left(\frac{\pi r_0^2 m_0 c^2 Z}{E_\gamma}\right)\left[2 - \frac{2E}{\alpha(E_\gamma - E)} + \frac{E^2\left(E_\gamma + \alpha^2(E_\gamma - E)\right)}{\alpha^2 (E_\gamma - E)^2 E_\gamma}\right]$$ Eq. 116

where E_γ is the energy carried by gamma-rays from a 60Co source and α is the proportionality factor between E_γ and electron rest energy:

$$E_\gamma = 1.25 MeV$$ Eq. 117

$$\alpha = \frac{E_\gamma}{m_0 c^2}$$ Eq. 118

$$m_0 c^2 = 0.511 MeV$$ Eq. 119

For proton irradiation the differential cross-section is connected with two different mechanisms: elastic and inelastic scattering. The elastic scattering (elastic collisions) is dominant for proton energy below 30MeV. In this range the inelastic scattering might be assumed negligible (after Akkerman et al. [3]). For higher energy, the latter is important and is responsible for variety of nuclear interactions (creation of light particles and energetic recoils). Differential cross-section for elastic scattering can be expressed in terms of differential non-relativistic Rutherford cross-section.

$$\left(\frac{d\delta}{d\Omega}\right)_{E_o\_inelastic\_sc.} = \left(\frac{d\delta}{d\Omega}\right)_R = \frac{e^4 Z_1^2}{4E_0(1-\cos\theta)^2}$$ Eq. 120

Differential cross-section for inelastic scattering can be calculated by using semi-empirical model presented by Akkerman, [2]. As it has been shown that the neutrons and the protons behave in a similar way, the same approach is used for neutron's NIEL calculation. The differences occur only at lower energies when the Coulomb barrier plays role (it has other value for neutrons and protons).

In order to compute the NIEL or the stopping power LET (essential to express radiation dose in Gy) the programs based on kMC (kinetic Monte Carlo) method could be used. In order to calculate NIEL and LET for ions and neutrons the SRIM program is applied (Ziegler [138]), for electrons the CASINO is used, for electrons and photons the PENELOPE is employed and for all irradiation types the FLUKA became very popular.

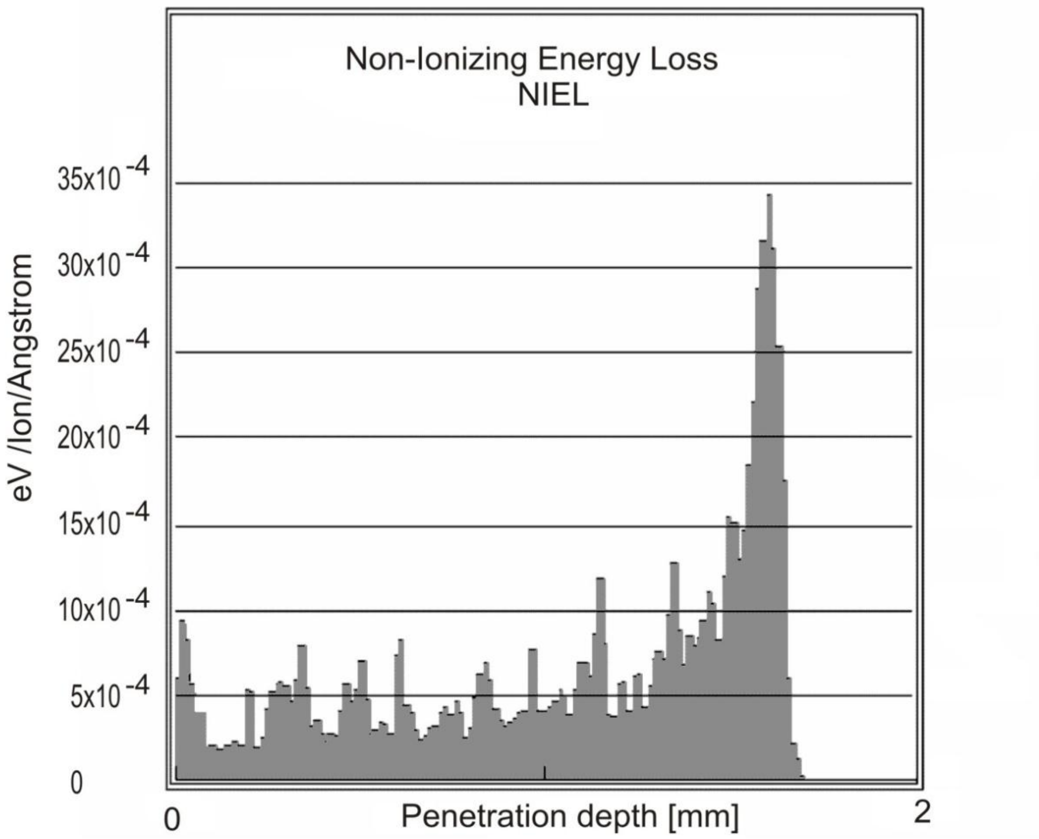

Figure 43 : NIEL profile for copper irradiated by hydrogen 30MeV ions

As indicated in Figure 43, the particle loses the energy over a long distance at a nearly constant rate. The distance is longer when the energy carried by the particle is larger. Also the maximum energy loss in the end of the particle range is higher for higher energy level. This is true for total energy loss, ionizing energy loss and NIEL. This phenomenon is used in radiotherapy to destroy the cancer cells. The beam energy in this case is chosen in such a way that the maximum energy loss is located in the proximity of the cancer cells. For the helium ions accelerated to the energy of 7 TeV, the range in the copper lattice is about 32cm and the maximum energy loss occurs over last 2-3 cm (according to the Monte Carlo simulation by using SRIM).

Usually the particle beam consists of particles with a different energy (energy spectrum). This information is fundamental in order to compute the displacement production (Mathews [83]). To get the number of displacements caused by particle flux (displacement production), the spectral density of the flux of particles φ_{pd} as well as the NIEL profiles must be integrated and compared with the NRT formula. For this reason the flux density is subdivided into narrow groups (in the sense of energy value E) linked with proper NIEL profiles (Figure 43) for the average energy E_i (Luneville [75]).

$$N = \sum_{i=1}^{n} N_i(E_i)$$ Eq. 121

Using the displacement production value N it is possible to compare and link the effects made by different irradiation types. This is why to measure the initial irradiation damage usually the displacement per atom dpa is used. The dpa value is defined as a total number of displacements caused by the particle flux, divided by the number of lattice atoms where the energy carried by the particles was accommodated. Using the displacement production N the irradiation damage can stay in relation to the dpa. Thus, the dpa can be expressed in the following way:

$$dpa = \frac{N_\phi}{\rho_{at}}$$ Eq. 122

where

$$N_\phi = \phi \cdot N$$ Eq. 123

and

$$\phi = \varphi \cdot t_r$$ Eq. 124

Here φ is the particle flux, t_r stands for the irradiation time, ϕ denotes the total particle flux and ρ_{at} represents atomic density of the material. It is also possible to define the equivalent flux of 1MeV neutrons (or other particles, for example He 1MeV ions), when the radiation character is unknown and the radiation dose is given by suitable measurements.

$$\varphi_{pd\_eq} = \frac{D_G}{t_r \cdot LET \cdot 1.6x10^{-10}}$$ Eq. 125

Where LET denotes the stopping power and D_G is the radiation stopping power expressed in terms of Gy (J/kg).

3.2.2 Clustering

The point irradiation defects (interstitials and vacancies) evolve rather than remain single. They usually group themselves into the SIAs or vacancies clusters. The clusters appear mainly near the cascade core during the thermal spike phase. This mechanism is related to the short range diffusion as a result of reorganization due to large elastic interaction between nearest interstitials. The fact that SIAs clusters are created during the cooling down phase is one of the most important discoveries (Osetsky et al. [92]). Some clusters seem to be formed by groups of atoms displaced outwards the cascade core, that it's trapped by the interstitials sites (Bacon et al. [5]). The SIAs displacement is created at such location by the initial shock wave. This mechanism appears quite early, during the transition from the collision to the thermal spike phase. The direct creation of SIAs clusters during displacement cascade was predicted by MD simulations, theoretical diffusion-based calculations and confirmed by TEM (after Osetsky and Bacon [93]). Also, the vacancies migrations may appear (stage III) (Gauster [45]), which leads to vacancies clustering. The probability of cluster production is higher with higher PKA energy. In the cluster population, the SIAs have always higher fraction then the clusters composed of the vacancies (Bacon et al. [5], Osetsky and Bacon [93]). This law is valid for all metals. The proportions can be slightly different for different materials (due to crystal structure), but usually with the same tendency. The reason of such behaviour consists in the fact that SIAs clusters are thermally stable whereas the vacancy clusters are not. The vacancy clusters can dissociate into individual point defects (interstitials) at the temperature high enough for thermal activation (Bacon et al. [5]). The well known theory which describes the irradiation defects creation is called "production bias model" (Woo et al. [129], Byun and Farrell [20]).

There are two types of SIAs clusters. Both have very high binding energy (2-3eV/SIA). During the thermal treatment they cannot easily dissociate, but they can transform from a metastable to a stable form (Osetsky and Bacon [93]). Some clusters are mobile and they can migrate over sizeable distance. High jump rate is possible due to low value of their migration energy (Bacon et al. [5]). These mobile clusters are called glissile. They arise just after the cascade process and are formed by transformation from metastable sessile clusters to glissile type. The glissile stable clusters are the main SIAs clustering product (Osetsky and Bacon [93]). In all metals, glissile clusters are densely packed with parallel crowdions structure. Their glissile character is connected with the form of Burgers vector (after Osetsky et al. [92]). The crowdions axes are oriented along the close packed direction (Table 5).

Table 5 Cluster mobility overview ([5], [7], [82], [92])

	Cluster Burgers vector (crowdions axis)	Form of vacancies clusters	Form of SIA clusters	Mobility
Bcc metals	$\frac{1}{2}\langle 1 \quad 1 \quad 1 \rangle$	Perfect loop evaluated from compact set of first neighbours vacancies	Crowdions cluster converted into edge or non-edge <1 0 0> dislocation loop	Glissile
	$\langle 1 \quad 0 \quad 0 \rangle$	Perfect dislocation loop evaluated from set of di-vacancies	Crowdions cluster converted into edge or non-edge dislocation loop	Glissile
	$\langle 1 \quad 1 \quad 0 \rangle$	Stable loop at faulted 1/2< 1 1 0 > for more than 40-60 vacancies transformed into 1/2< 1 1 1 > or < 1 0 0 > perfect loop	Dumbbell form transfer from <5 SIAs into < 1 1 1 > crowdions cluster	Sessile
Fcc metals	$\frac{1}{2}\langle 1 \quad 1 \quad 0 \rangle$	Perfect vacancies loop thermally active and dissociated into SFT	Crowdions cluster growth and transformation into perfect loop (edge or Shockley partial dislocations)	Glissile
	$\frac{1}{3}\langle 1 \quad 1 \quad 1 \rangle$		Frank faulted loop	Sessile
	$\langle 1 \quad 0 \quad 0 \rangle$		Dumbbell form growth and transformation into Frank faulted loop 1/3 < 1 1 1 >	Sessile
		SFT and faulted clusters growth and transformation into faulted Frank loop 1/3 < 1 1 1 >		Sessile
Hcp metals	$\frac{1}{3}\langle 1 \quad 1 \quad \bar{2} \quad 0 \rangle$	No data	No data	Glissile
	$\frac{1}{2}\langle 1 \quad 0 \quad \bar{1} \quad 0 \rangle$	No data	No data	Sessile
	Other	No data	No data	No data

The small glissile dislocation loop, mobile in crowdions direction is the most common form of SIAs clusters. It was postulated that <1 0 0> loops are created from direct interaction between small ½<1 1 1> clusters, which are nucleated during the displacement cascade process (Marian et al. [82]). It is worth pointing out that for bcc Fe SIAs cluster with less than 5 interstitials, the dumbbells < 1 1 0 > stable form is also possible (Osecky at al. [92]). For more than 4 interstitials the clusters change their form into glissile of <1 1 1> crowdions (Osecky at al. [91], [92]). In the fcc and bcc metals such clusters are prismatic in shape (Wirth et al. [128]). For the smallest clusters (bi- and tri-interstitials clusters) the glide occurs also along crowdions direction, but occasionally the crowdions direction may be rotated in the equivalent direction. In such a case a 3D motion is observed for smallest clusters (Osecky at al. [91], [92]). Clusters which have more than three SIAs are thermally activated and glide in one dimension only (the crowdions direction). In the case of bcc Fe gliding in crowdions direction, it appears for all loops (cluster) of size larger than 3 interstitials. In the case of fcc Cu gliding in crowdions direction, it takes place for cluster size smaller than 25 interstitials. For biggest ones the motion is also in one direction. The glissile clusters produce displacements of the atoms in the lattice during their glide. It was shown by MD simulations that this process cannot be explained by using the classical diffusion mechanism. The main reasons are: the extremely low activation energy and the non-random character of jumps (Osetsky et al., [92]). MD simulations were carried out for Cu (after Wirth el al. [128]) and clearly indicate that "diffusivity" is function of the cluster size (Osetsky and Bacon [93]). The same studies show that cluster mobility for the size larger than 100 is rapidly reduced. The motion is suppressed for ~300 SIAs for Fe and ~120 SIAs for Cu clusters. This fact was also reported by Osetsky (after Byun and Farrell [20]). This implies that rather small interstitial clusters are mobile, which is in agreement with the other research sources (Caturla et al. [23]). The activation energy does not depend on size and remains always close to the individual crowdion activation energy, but mobility decreases with the cluster size (Osetsky and Bacon [93]).

The second group, sessile stable clusters, are mainly based on faulted Frank loops or meta-stable SIAs arrangements. Sessile clusters were reported in titanium, zirconium and iron (after Bacon et al. [5]). These clusters are formed both by ballistic events and by the SIAs interaction during the thermal spike phase. The majority of the SIAs clusters are formed during the cascade process and are sessile. Sessile clusters fraction is the lowest for bcc metals, and the highest (up to 30-40%) for fcc metals with low stacking fault energy (LSFE). For hcp metals the sessile clusters fraction remains in-between. In the bcc lattice they take form of meta-stable 3D clusters, whereas for fcc lattice they occur in the faulted Frank dislocation loop form (after Osetsky and Bacon [7], [93]).

The vacancy clustering strongly depends on the lattice type. The clusters of vacancies usually have the initial form of dislocation loops. Glissile and sessile types are possible and depend on the Burgers vector (see the Table 5). Perfect vacancy dislocation loops show similar behaviour to SIAs loops with the same size (Osetsky et al. [92]). The clusters of vacancies for fcc metals with low stacking fault energies usually collapse to the SFT form (Osetsky and Bacon [92], [93], Bacon et al. [5], [7]). This vacancies formation is caused by dislocation mechanism at room temperature within a few picoseconds after displacement cascade. SFTs are usually not of perfect tetrahedron type but consist rather of truncated tetrahedron forms (sometimes overlapping) (Wirth et al. [128]). For Cu SFTs vacancies constitute about 90% of visible defects after irradiation. Their mean size is constant with increasing irradiation dose and is nearly temperature independent between 25˚C to 300˚C (Caturla et al. [23]).

Another formation that occurs in the fcc metals is the faulted Frank dislocation loop (Osetsky and Bacon [93], Caturla et al. [23]). Both formations in the fcc metals are stable (SFTs are stable up to 1000K for a few ns) Faulted dislocation loops have tendency to dissociate into SFT form. Also for other metals the vacancy-rich regions collapse into stable configurations. In the hcp metals, for example Zr, vacancy clusters form planar defects (like prisms) or basal dislocation loops. In the bcc metals no compact planar or 3D vacancy clusters were observed. The vacancies group into very loose complexes located near the second and the higher order neighbour shells. They form stable perfectly plane loops. In the case of bcc metals the other stable configurations are 3D voids (for large clusters) and perfect edge dislocation loops.

The temperature has less important effect on the irradiation defects production, but has considerable influence on the clustering process. Temperature increases the mobility of defects and as a result of recombination process the number of clusters decreases at higher temperatures (for example in Cu). It was also mentioned that the clustering process is rather complex and strongly non-linear (Zinkle and Matsukawa, [139]). The vacancy clusters creation is mutually affected by the vacancy and the interstitials production.

In summary, there is a big difference between fcc Cu and bcc Fe response to irradiation. According to Table 5, all stable forms of SIA clusters are glissile in the case of bcc metals. The opposite situation occurs for fcc metals where only part of the cluster population is glissile. In the case of fcc Cu all stable vacancy clusters / loops are sessile. On the other hand, in the case of bcc Fe vacancies clusters /loops they seem to be rather thermally activated and of one-dimensional glissile type. The hcp metals remain between these two extremes.

During the irradiation the clusters of defects grow rapidly in number and in size up to the threshold dose (Figure 44) (after Nita et al. [88]). The irradiation dose is expressed in dpa units. After the critical dpa value has been reached the cluster size evolution stops and corresponds to about 28 atoms size. Also, the number of clusters is saturated and changes slowly for higher doses. For copper the dpa threshold value stays in the range from 10^{-2} to 10^{-1}. For stainless steel it stays rather in the range from 1.0 to 6.0. The dependence between the cluster density q_c, the average cluster radius r_c and the dpa value is of power type:

$$q_c = \begin{cases} C_{qI}(dpa)^{n_{qI}} & for \quad dpa < D_S \\ C_{qII}(dpa)^{n_{qII}} & for \quad dpa \geq D_S \end{cases} \qquad \text{Eq. 126}$$

$$r_c = \begin{cases} C_r(dpa)^{n_r} & for \quad dpa < D_S \\ r_{cr} & for \quad dpa \geq D_S \end{cases} \qquad \text{Eq. 127}$$

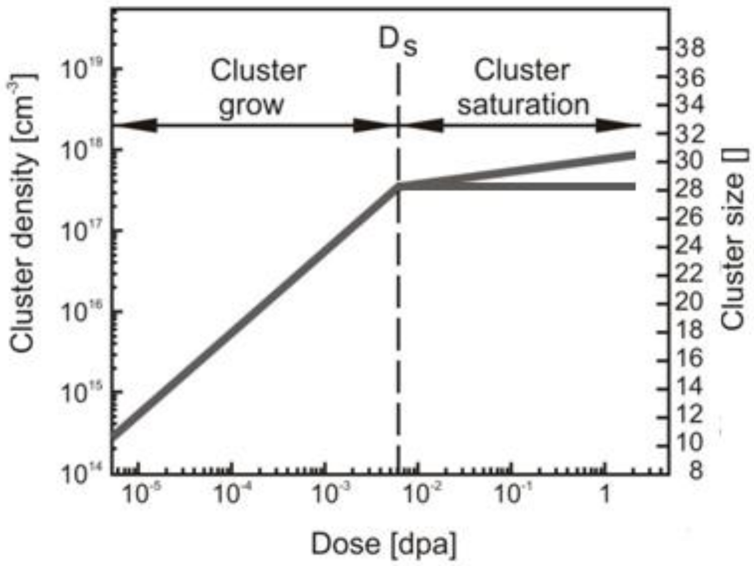

Figure 44 : Average cluster size and cluster density

where C_{qI}, C_{qII}, C_r, n_{qI}, n_{qII}, n_r denote material parameters, D_S is the saturation irradiation dose (in dpa units), r_{cr} is the mean cluster radius with respect to the irradiation dose equal to D_S. For copper, the mean cluster radius r_{cr} corresponds to 2.1 nm (28 atoms in the lattice). However, in the experimental measurements this value is equal rather to 2- 3nm.

3.2.3 Irradiation defects reorganization

During the MD simulations it turns out that the defects production (N_F) is usually much lower than the value predicted by NRF formula (Osetsky et al. [91], Bacon et al. [5]). Typically, the scale factor $C_{F\text{-}NRF}$ between the defect production N_{NRT} and the final defect production N_F gains the level of 0.2-0.4 (Zinkle and Singh [140]). That can lead to the following equation.

$$C_{F-NRF} = \frac{N_F}{N_{NRF}} \qquad \text{Eq. 128}$$

In the case of displacement cascade, most of the SIAs are formed at the boundary of the thermal spike core and not at the end of the collision chains. This can be the reason of such low defects production observed during MD simulations. High energy (temperature) during the thermal spike leads to SIA-vacancy recombination (annihilation) during the cool-down stage. Based on the MD simulations it is possible to carry out an empirical estimation of radiation defects production in the following form (after Bacon, Osetsky and Gao [5], [7], [93]):

$$N_F = A(E_p)^m \qquad \text{Eq. 129}$$

It suits well the PKA energy up to some 10eV. The bulk temperature corresponds to 100K (10K for Al and Ni). The parameters *A* and *m* are listed in Table 6.

Table 6 Parameters A and m for typical metals (after Bacon et al. [5]).

Metal	Ti	Fe	Ni_3Al	Cu	Zr	Ni	Al
A	6.01	5.57	5.47	5.13	4.55	4.37	8.07
m	0.80	0.83	0.71	0.75	0.74	0.74	0.83

This equation works well, even for energy level up to several tens of keV. It should be mentioned that when a simple cascade is broken into sub-cascades (at high energy level) this formula may no longer be valid (the total defects production is the sum of the defects production from each sub-cascade), because the production efficiency slightly increases in the case of cascade to sub-cascade broke-up (Ostetsky et al. [91]). The cascade to sub-cascade broke-up appears at lower PKA energy for lightest metals.

Bacon et al. [5] suggested that the defects number does not depend on the crystal structure. The differences in defects numbers appear to be solely due to the atomic mass. The atomic mass influences *A* and *m* values. The lighter atoms the better fitting exists with respect to the theoretical values. This is because the displacement cascades have tendency to break into sub-cascades with less energy.

The temperature during the irradiation affects the stable defects production via the recombination process. The higher irradiation temperature, the lower number of Frenkel pairs remains. This is due to the extension of the thermal spike phase lifetime. Intensive defects motion (interstitial-vacancy recombination) occurs before the temperature finally goes down due to the cooling effect (after Bacon et al. [5]). The temperature influence has nearly linear character for higher temperatures but it is strongly non-linear for lower temperatures as indicated in Figure 45 (after Zinkle and Singh [140]).

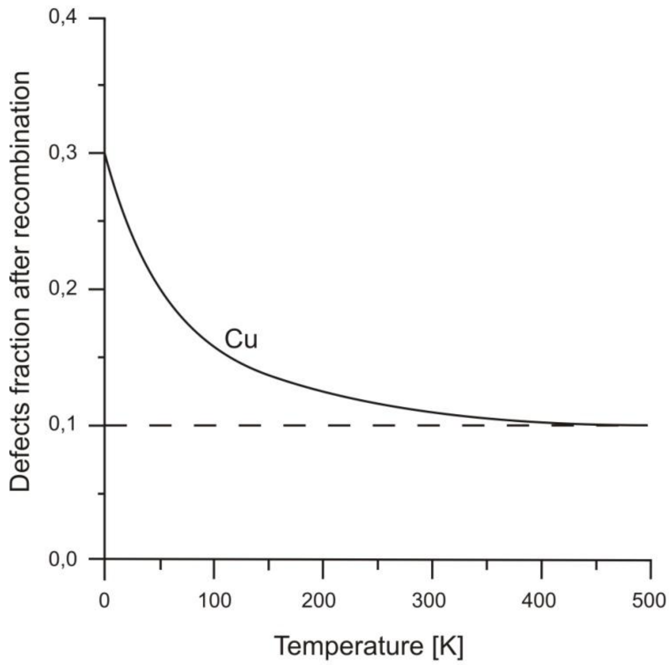

Figure 45 : Defects fraction remaining after recombination

The defects production in alloys is similar as in pure metals. After the corresponding MD simulation studies it was found that the defects number does not depend on the alloy composition, and no "impurity" cluster production was observed (Bacon et al. [5]).

3.2.4 Interaction between the clusters of irradiation defects and dislocations

The knowledge how the irradiation defects interact with the dislocations and between each other (cause glissile SIAs clusters movements) is fundamental to understand the material properties, and the micro-structural evolution.

The interactions between mobile clusters and point defects can lead to their growth or shrinkage. For example mobile glissile SIAs cluster can be slowed down or even stopped by interaction with vacancy or impurity atoms for example C atom for Fe (Bacon and Osetsky [7], [93], Puigvi et al.[101]). The most critical for cluster mobility is an impurity atom trapped at its edge. The mechanism of this interaction depends on the type of material. In the bcc materials the SIAs cluster-vacancy interactions lead to shrinkage (vacancy is absorbed by the cluster edge). For fcc Cu it depends on the SIAs cluster size. For small clusters the vacancy can recombine with the SIA at the cluster edge. It can also reduce the motion of SIAs cluster when laid on the glide prism. Large SIAs clusters do not absorb the vacancies. Vacancy simply reduces mobility of such clusters. For hcp metals the interaction mechanisms are somewhere between the fcc and the bcc behaviour.

Glissile clusters can interact when their glide prisms intersect. In such a case the result depends on the temperature, the clusters size and their orientation. Often, other atomic structures can be obtained. For example small clusters at higher temperatures can change their Burgers vectors and coalesce. If the clusters are big enough, their collision can produce a complex and immobile cluster (Bacon and Osetsky [7], [93]). This occurs in much simpler way in fcc Cu than in bcc Fe.

Also, the glissile clusters or loops with parallel Burgers vectors attract each other and form spatially extended complex structures (Ghoniem et al. [46]). These complex structures are stable and can be glissile or immobile. Immobility is obtained when the structure contains higher number of clusters (>5 for bcc Fe) and total number of SIAs is high enough (>300 SIAs for bcc Fe). This structure can grow during the gliding process by attracting more clusters and loops.

Interaction between small glissile SIAs clusters (in the form of Dislocation Loops) has also been studied (also Bacon and Osetsky [6]). The following mechanisms were reported: the cluster drag (decoration), the cluster absorption (at dislocation line and jogs), the dislocation pinning and unpinning. It has been mentioned that the cluster drag / decoration of dislocation does not pin the dislocation directly, but increases its interaction cross-section.

Another mechanism is related to the glisile with sessile cluster interaction. Especially in the bcc Fe there is a big number of sessile clusters that appear just after the irradiation process. Most of them transform to the stable glissile form, but before they can interact with mobile SIAs clusters produced by the same cascade (Bacon et al. [5]). Such interaction can change the glide direction of mobile SIAs clusters.

Vacancy clusters interact with dislocations as soft spots (at the simplest level), attract the dislocations and pine them by reducing their length. This situation is described by Russell-Brown theory and is equivalent to the Scattergood and Bacon proposal (if the surface energy of the voids is zero). That second method treats the dislocation line as flexible and constructed from piecewise segments. Dislocation line when moving through the voids creates the surface steps. It is assumed that the dislocation line is cutting through the voids row, characterized by the diameter D_v and the spacing L (both in correlation with the dislocation core radius r_0). In such a case, the dislocation is bending between two neighbouring voids into the arc (Figure 46).

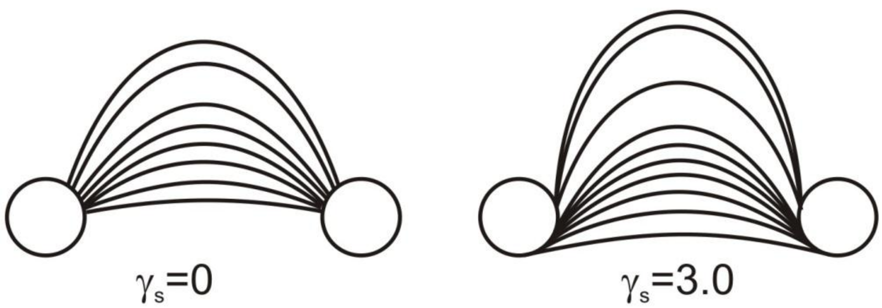

Figure 46 : Dislocation cutting through the voids – equilibrium shapes

When increasing the shear stress the line becomes tangential to the voids for high surface energy γ_s and finally the line overcomes the voids in the Orowan-like mode (Bacon and Osetsky [7], Figure 47).

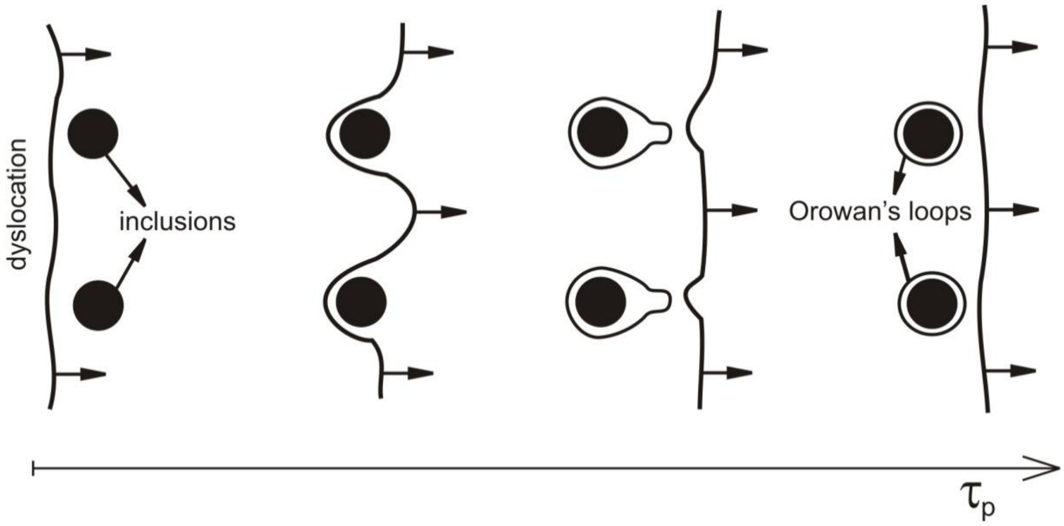

Figure 47 : The Orowan mechanism - dislocation line interacts with vacancies clusters

The critical shear stress due to this theory is expressed as:

$$\gamma_s = 3\frac{Gb}{4\pi L}\ln\left(\frac{R}{r_0}\right) \qquad \text{Eq. 130}$$

where G is the shear modulus and R is the outer cut-off radius in the shape of dislocation. This can be compared with the critical shear stress value in the Orowan theory for the dislocation passing through the strong obstacles (Bacon and Osetsky [7]).

$$\gamma_{Orowan} = \frac{Gb}{2\pi L}\left[\ln\left(\frac{1}{D_v}+\frac{1}{L}\right)^{-1} + 0.77\right] \qquad \text{Eq. 131}$$

In order to obtain similar results for both theories it is suggested to replace the value 0.77 (connected with Orowan obstacles) by 1.52 connected with realistic void surface energy, (Bacon and Osetsky [6]). Also, MD simulations were precious source of information about interaction between dislocation line and cluster of vacancies. During the simulations a dislocation line attracted and entered the cluster. Afterwards, it glided over the cluster surface, absorbed some vacancies and created a surface step. Finally, it broke away from the obstacle. The vacancy cluster (obstacle) shrunk and became weaker obstacle for next dislocation line.

It should be also mentioned that a dislocation line can pass over the cluster of obstacles under lower shear stress than critical if it reaches its steady-state velocity. This is a kinetic effect of dislocation motion. Also, high temperature decreases the critical shear stress value.

If the dislocation line is subdivided into two Shockley partials (trailing and leading) with the stacking fault between them (of ~13a_0 width, where a_0 is the lattice parameter), the mechanism is quite different (such situation for example is common for fcc Cu). If the distance between dislocation partials is larger than the size of obstacles, they interact separately. The critical shear stress is characterized by the trailing partial up to the void size of 2nm, and above by the leading partial up to the size of 4nm. For obstacles bigger than 4nm the dislocation line acts as described before for bcc metals.

Detailed MD simulation between dislocation line and SFT was described by Wirth et al. [128] and also Diaz de la Rubia and Phythian [32]. In the simulation ~ 1ml of Cu structure at 100K was analyzed. The overlapping, truncated SFT structure was situated together with some small clusters of defects (dislocation line “decoration”). SFT acted like strong obstacles for dislocation line motion. The dislocation line was split into two Shockley partial dislocations (leading and trailing). When the leading dislocation edge got in contact with SFT, the SFT structure was pinned and absorbed the dislocation line. The leading partial climbed, when the trailing part approached. Finally, the trailing part caught the leading partial in the SFT region. It constricted and climbed with simultaneous defect absorption. Afterwards, the dislocation line continued to move but due to the super-jog pining with lower mobility. Other authors (Osetsky and Bacon [93]) suggest that SFT absorption depends on the size, the dislocation velocity, the density and the stress level applied. After several dislocations have passed through the SFT, it was completely absorbed by them. The SFT absorption caused by dislocation line depends mainly on the size and the shape (high) (Osetsky and Bacon [6]). This double-step mechanism is also confirmed by other studies (Lee et al. [69]). The critical shear stress seems to be similar like for the vacancies clusters. The 2.5 nm SFTs have about the same critical shear stress value like the 2nm vacancies clusters with the same spacing (Osetsky and Bacon [6]).

Also the SIAs cluster drag, absorption and annihilation by dislocation line was observed (Osetsky and Bacon [7]). The SIAs cluster can be dragged by dislocation line when the glissile cluster is attracted by the tensile side of dislocation. SIAs clusters can also pin and unpin the dislocation line. Loops which have the same Burgers vector form a decoration w.r.t. dislocation line. Such loops of immobile type are raising the applied stress and move together with dislocation line.

3.2.5 Dislocation channelling

During the mechanical loading of irradiated materials the so-called dislocation channelling can be observed. Due to the applied load interaction between the lattice dislocations and irradiation defects occurs. Channelling is a process of localization and concentration of plastic deformation in narrow bands and it consists in removing the irradiation defects from the channels located in the slip system. This defects cleaning process is supposed to be done by gliding of hundreds of thousands of dislocations during the time period l less than a millisecond (Lee et al. [69]). The newly generated and fast gliding dislocations are cleaning the narrow bands. The irradiation defects (small clusters, vacancies and interstitial atoms are not strong enough to stop the gliding process and are annihilated. The initial slip dislocation cleans the irradiation defects and makes the passage easier for next dislocations (Cottrell mechanism mentioned by Singh et al. [113]).

It is believed that clear-channels creation made by Shockley partial dislocation is inherently linked with pile-up dislocations, stacking fault ribbons and twins bands (Lee et al. [69]). During interaction with the irradiation defects the leading partial produces jogs and stair-rods. Partials are separated by jog-pining and stair-rod locking. Dislocation cross-slip is suppressed and nano-twins and stacking fault ribbons appear between them. Afterwards, Frank loops are cleared by pile-up dislocation stress. It is believed that dominant defect-reduced channels creation is due to un-faulting process done by isolated (nucleated inside loop) Shockley partials (Lee et al. [69]). Dislocation channelling creates the localized “run-away” slip. The local shear strains inside the channels are high. In Cu the stain level in the channels reaches some 550% (4% bulk strain), and in Nb reaches some 220-370% (6.6% bulk strain) (Byun et al. [21]). Practically, all plastic strains are localized in the channels. The shear strains are distributed uniformly throughout the channel’s width. In the blocks between the channels there is only weak dislocations activity. The dislocation motion in poly-crystals can be stopped by grain boundaries. The back stress due to the pileup of dislocations can stop slip in the channel. To cross this barrier a large number of dislocations must accumulate at the head of pile-up channel against the grain boundary. When the critical stress is reached at the head of pile-up, it may cause an avalanche to the next grain in the form of two-dimensional pileup or an array.

The critical stress corresponds to the stress required for the first dislocation loop in the environment of the clusters of defects. It can be estimated as:

$$\tau_c = \tau_o + \frac{GN_c b}{H_c} \qquad \text{Eq. 132}$$

$$N_c = \frac{s_c}{b} \qquad \text{Eq. 133}$$

where N_c is the number of channeling dislocations for the Burgers vector b; s_c is the largest shift at the channel intersections; H_c is the characteristic height of channels; τ_o is the yield shear stress.

3.3 Mechanical aspects of irradiation

The previous sections were focused on the physical mechanisms of processes taking place in the irradiated body. In the present section the mechanical results of these processes will be shown. The main aspects taken into account are:

- The radiation as a source of heat,
- Irradiation damage in the light of CDM,
- Irradiation induced plastic hardening,
- Plastic instability at yield,

3.3.1 The radiation as a source of heat

All kinds of radiation lead to the energy transfer into the material by the ionization process. In liquid or organic bodies ionization energy breaks the chemical bonds. In the metals almost all energy transfer appears as heat production Q and can be described by a simple law (after Holbert [51]):

$$\dot{Q} = \dot{E}_{id}\ \rho \qquad \text{Eq. 134}$$

where E_{id} is the absorbed dose and ρ is the material density.

3.3.2 The yield point increase

Generally the irradiation can affect the material by changing the organized and well defined material lattice to a disordered and chaotic structure. This is due to a number of additional dislocations, vacancies (micro-voids), interstitials, and helium or hydrogen bubbles in the material, which affect its mechanical properties. The defects caused by radiation create the obstacles to dislocation motion - the basic mechanism of plastic deformation. Irradiation defects usually pin and "decorate" the dislocations [82]. This process depends on irradiation temperature and type of Bravais lattice (BCC or FCC) and can be eliminated (cured) by high temperature treatment. Increasing the yield point ($\Delta\sigma_y$) in the course of irradiation process is called the radiation hardening.

The increasing strength is the first effect of radiation hardening. From engineering point of view this is a desirable effect. However, the radiation hardening drastically reduces tensile elongation, which leads practically to more restricted design rules (2% maximum uniform elongation). The other effect of irradiation is increasing of the ductile to brittle transition temperature and decrease of toughness in the ductile regime. It has been shown by Boehmert et al. [13] that these effects depend on the square root of the the volume fraction of radiation defects.

The "Zone Theory of Radiation Hardening" is well known and often called dispersed barrier hardening (DBH) theory. This theory was developed by Seeger. The "Zone" in this theory is referred to the "vacancy reach zone" connected with the centre of the cascade spike. Vacancies concentrated there are supposed to collapse and transform to vacancy loops/clusters or SFTs. The critical shear stress is higher for irradiated materials. The idea of the DBH theory is that defects are assumed to act as barriers for gliding dislocations which leads to the hardening. The dislocations are "hung up" against the obstacles (Vacancy loops/clusters, SFTs). Using the modified Orowan theory the dislocation line is bowing around the obstacles and this is why the critical shear stresses for plastic slip increases (like described before in section 3.2.4). Another form is presented by equations, where the average distance between the obstacles is replaced by $L_{ev}=(Nd)^{-1/2}$ and α is the obstacle strength parameter (Marian et al.[82], Kim et al. [58]):

$$\tau_{cr} = \alpha G b \sqrt{Nd} \qquad \text{Eq. 135}$$

For random deposition of obstacles caused by irradiation the increment of the yield point can be written as:

$$\Delta\sigma_y = M_T \alpha G b \sqrt{Nd}$$ Eq. 136

Here, b is the magnitude of the Burgers vector of the glissile dislocation, M is the Taylor factor which relates the shear stress on the slip plane in a single crystal to the applied stress needed to move a dislocation in a polycrystal (~3.06), G is the shear modulus, N denotes defects density, and d is the defect diameter. The critical angle θ (for <1 0 0> loops in bcc Fe it is 70˚ (Russell and Kim [105]); for SFT in fcc Cu it is ~165˚ (Ghoniem et al. [46]) created by dislocation which is passing through the obstacle, is used to estimate the obstacle strength parameter. This data can be provided by MD simulations too (Marian et al. [82]). It is suggested that θ value should be rather calculated from the energy of dislocation cutting through the irradiation defects than simply from their geometry (Ghoniem et al. [46]).

$$\alpha = \cos\left(\frac{\theta}{2}\right)$$ Eq. 137

Robertson et al. [106] proposed to collect all contributions to the yield point following the superposition law, where the influence of the short range obstacles (like loops, voids, bubbles) $\Delta\sigma_{SR,i}$ is treated in a different way than the influence of long range obstacles (for example lattice dislocations) $\Delta\sigma_{LRi}$.

$$\Delta\sigma_y^{total} = \sqrt{\sum_i \left(\Delta\sigma_{SR,i}\right)^2} + \Delta\sigma_{LR}$$ Eq. 138

The second model is the weak barrier model addressing the weak obstacles. It works well when in the material mostly single interstitial atoms and vacancies exist – it means that no displacement cascade appeared (usually small radiation dose). This theory was formulated by Friedel in 1963 as well as Kruppa and Hirsch in 1964. The theory assumes that "defect clouds" are caused by irradiation process along the grown-in dislocations. Because of this they cannot act as dislocation sources (decoration process of dislocation source). It can be stated that the dislocation sources are locked by the irradiation defects and plastic deformations are impossible. To unlock these sources the dislocation lines must be pilled away from the defects region. High enough shear stresses can unlock dislocation source and allow the plastic deformation process to act (cf. Singh et al. [113]):

$$\tau = 0.1G\left(\frac{b}{l}\right)\left(\frac{d}{y}\right)^2$$ Eq. 139

Here, G is the shear modulus, b is the Burgers vector, N denotes the defects density, d is the defect diameter, l is the distance between the radiation defects and y is the distance from the dislocation to the "defects cloud". The increment of the yield point in the light of this theory is equal to (Robertson et al. [106]):

$$\Delta\sigma_y = \frac{1}{8} M_T G b \left(2 r_c q_c\right)^{\frac{2}{3}}$$ Eq. 140

Where q_c.is the number of clusters and r_c denotes the average cluster radius.Another approach was described by Byon and Farrell [18] and has a phenomenological character. In this theory the authors establish simple correlation between the irradiation dose Φ_{dpa} and the yield point increment $\Delta\sigma_y$ described by the Figure 48. This relation is in the form of power law but it is subdivided into two stages. The first one is the low-dose regime (range up to the critical value Φ_{cr}) with much higher slope of log-log dependence, and the second is called high-dose regime ($dpa > D_S$).

$$\Delta\sigma_y = h \cdot dpa^n$$ Eq. 141

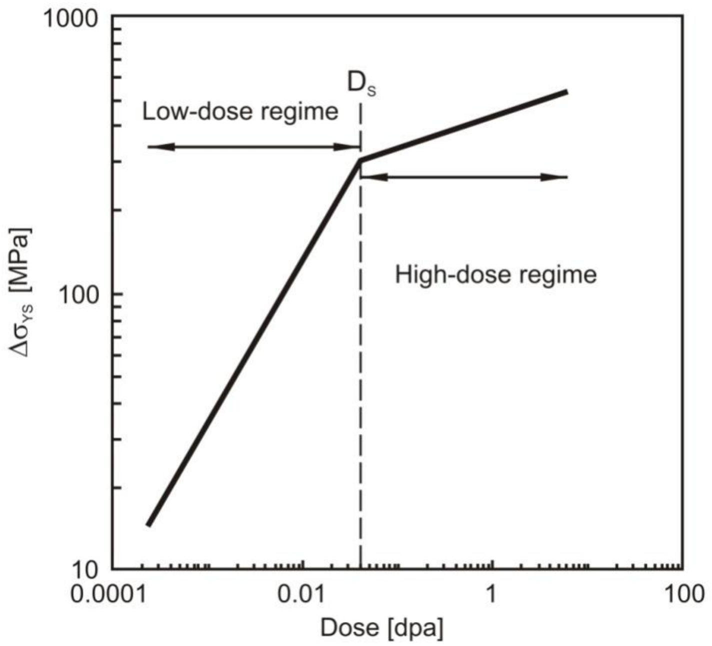

Figure 48 : Yield point increment as a function of the irradiation dose

Lower value of the second slope is explained by the fact that the material undergoes prompt plastic instability at yield and reaches the saturation level with respect to the density of defects clusters. The values of h, n and D_s as a function of different materials for both stages are presented in Table 7.

Table 7 Material parameters used for yield point increment calculation

Materials	D_S (dpa)	$\Phi_{dpa} < D_S$		$\Phi_{dpa} > D_S$	
		H	*n*	*h*	*n*
A533B-a	0.05	2300	0.62	530	0.08
3Cr-3WV	0.05	1590	0.62	290	0.07
9Cr-2WV	0.04	1230	0.54	320	0.11
Nb	0.003	1970	0.52	280	0.18
V	0.003	4510	0.62	280	0.13
bcc metals average:			0.55		0.12
316LN	0.04	1020	0.39	390	0.08
Cu	0.05	710	0.31	290	0.01
Ni	0.04	1660	0.44	700	0.19
fcc metals average:			0.40		0.14
Zr-4-a	0.01	2350	0.62	210	0.11
Zr	0.07	350	0.35	150	0.02
hcp metals average:			0.49		0.07
all metals average:			0.50		0.12

This theory is based on relation observed between the dose (dpa) and the growth of the yield point value. It is easy to prove that simple power low is in fact strictly linked to the formula of type presented before. It can be shown that Byon and Farrell formula is related to the law presented before by setting the scalar factor to 10 (instead of 1.0 or 1/8) and power to 0.24 (instead of 1/2 or 2/3).

The last two models converge in good agreement if the scalar coefficients are set in the following way:

$$\Delta\sigma_y = 1.31 M_T G b \left(2 r_c q_c\right)^{0.24} \qquad \text{Eq. 142}$$

3.3.3 Plastic instability at yield

The experimental observations show, that exposing metals to radiation leads to significant changes in their mechanical properties. To describe these changes (radiation hardening and loss of ductility) a number of theories and related equations were developed. One of the observed phenomena in the irradiated materials is connected with the ultimate tensile strength (UTS). If this value is transformed to the "real" state of stress the true stress at maximum load (σ_{ML}) will be defined. The other name existing for this true stress value is the plastic instability stress (σ_{IS}). This value does not depend on the irradiation dose up to some critical value (Boehmert et al. [13]). The yield point (σ_{YP}) is usually lower than the plastic instability stress defined before for nonirradiated metals. After significant irradiation the yield point may turn out to be equal or even higher than the plastic instability stress for nonirradiated materials. The critical level of irradiation dose needed to observe such phenomenon is called the dose corresponding to plastic instability at yield D_c. Such behaviour is illustrated in Figure 49.

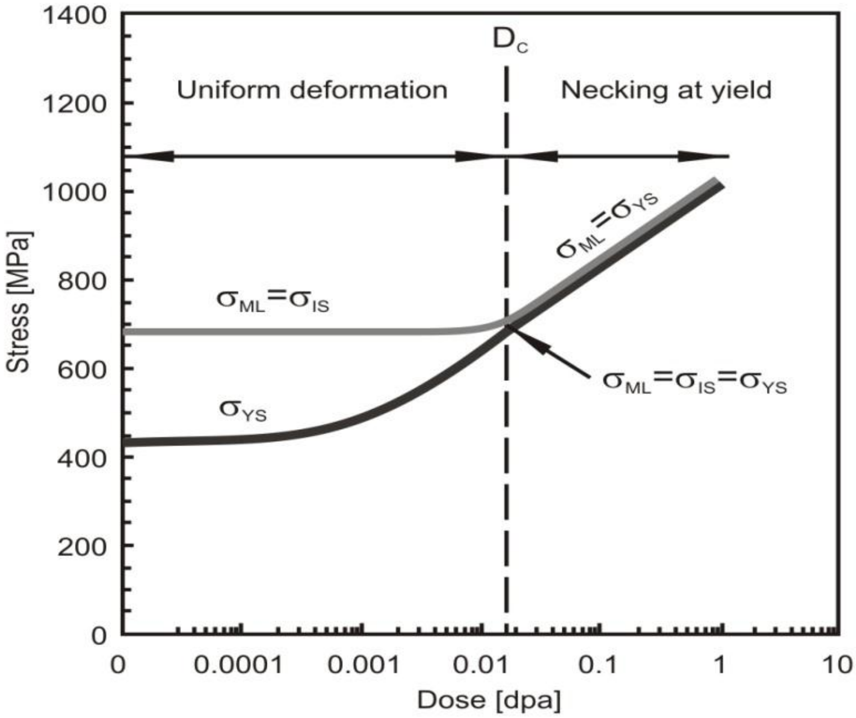

Figure 49 : Plastic instability versus applied dose

It seems that the most important for D_c value is the difference between the yield point and the plastic instability stress. The higher difference the more radiation is needed to increase the yield point σ_{yp} value up to the plastic instability stress σ_{IS}. Critical irradiation doses D_c for different metallic materials are presented in Table 8.

Table 8 Plastic instability versus critical irradiation dose

Materials	Crystal structure	Plastic instability stress [σ_{IS}]	Critical irradiation dose [D_c]
A533B-a	bcc	715	0.02
3Cr-3WV	bcc	707	0.025
9Cr-2WV	bcc	753	0.054
Nb (pure metal)	bcc	368	0.007
V (pure metal)	bcc	397	0.0017
316LN	fcc	948	40
Cu (pure metal)	fcc	300	0.12
Ni (pure metal)	fcc	542	0.15
Zr-4-b	hcp	500	0.004
Zr (pure metal)	hcp	159	0.09

There exists a relation between the critical values D_c and D_s illustrated in Figure 50 (after Byun and Farell [19]). For the D_c values less than about 0.05 dpa both parameters are equal. Above this threshold D_s saturates at the level of around 0.04-0.07 dpa.

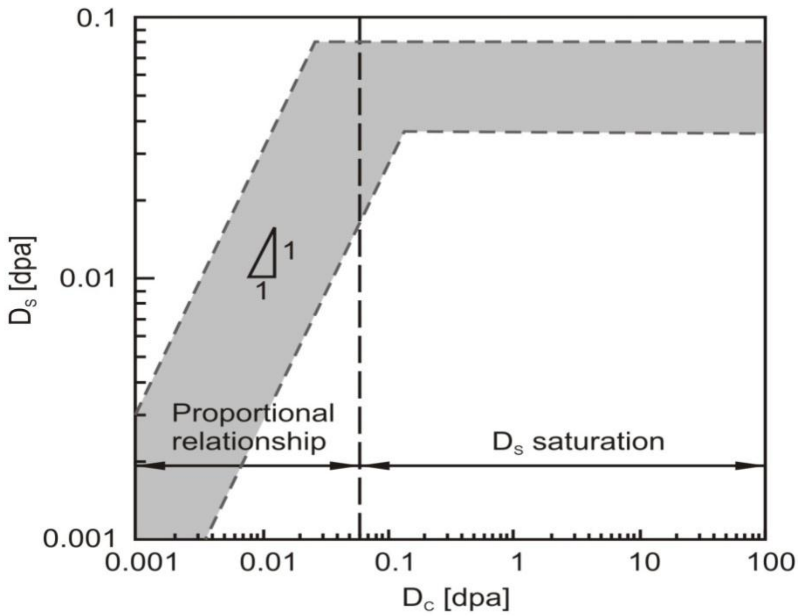

Figure 50 : Relationship between the critical values D_c and D_S

To better understand the hardening process induced by irradiation at the microscopic scale in metals, special deformation mode maps (DMM) were constructed. As an example the DMM for 316LN stainless steel is presented below (after Byun et al. [22]).

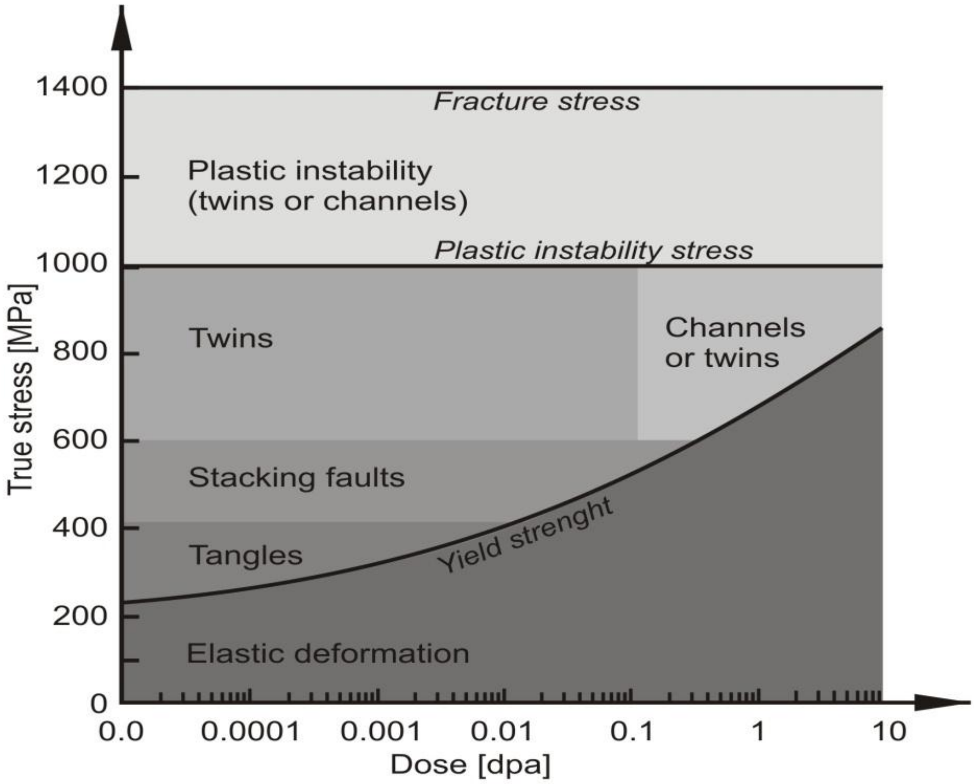

Figure 51 : Deformation mode map (DMM) in true stress versus dose space for 316LN stainless steel

3.3.4 Irradiation induced hardening mechanism

As already underlined in the previous section, the defects caused by radiation create obstacles to dislocation motion. Such a mechanism affects the hardening behaviour and has to be taken into account when building a constitutive model of irradiated materials. It is assumed in the present Thesis that the irradiation affects primarily the kinematic hardening. If the massive motion of dislocations occurs they are stopped by the clusters of defects and the corresponding local stress fields. Furthermore, it is assumed that the hardening parameter representing the response of pure, non-irradiated material is equal to C_0. Thus, the evolution of back stress reads:

$$d\underline{\underline{X}} = \frac{2}{3} C_0 d\underline{\underline{\varepsilon}}^p \qquad \text{Eq. 143}$$

As the irradiation creates additional defects in the lattice, the hardening modulus has to be updated. For the material containing the clusters, the hardening modulus C_0 is replaced by the modulus C, that is higher than C_0 because of the interactions between the dislocations and the clusters:

$$C = C_0\varphi(\xi) \quad ; \quad \varphi(0) = 1 \qquad \text{Eq. 144}$$

As already stated, it can be easily shown that the shear stress necessary for a dislocation to pass across two clusters of average size d, separated by the distance l, depends roughly linearly on the volume fraction of clusters ξ (Skoczeń [115]):

$$\tau_p = \frac{Gb}{d}\left(\frac{6\xi_0}{\pi}\right)^{\frac{1}{3}}\left(1 + \frac{\xi - \xi_0}{3\xi_0}\right) \qquad \text{Eq. 145}$$

where G denotes the shear modulus, b is the length of the Burgers vector and ξ_0 stands for the initial volume fraction of inclusions. Here, for the sake of simplicity, an assumption has been made that the average size of clusters (d) is constant and much smaller than the distance between two clusters ($d << l$). In the light of the above equation, the function $\varphi(\xi)$ takes the linear form:

$$\varphi(\xi) = h\xi + 1 \qquad \text{Eq. 146}$$

where h is a material dependent parameter. The function $\varphi(\xi)$ can be interpreted as this part of the hardening process that corresponds to the increase in volume fraction of clusters and enhanced probability that a dislocation will stack on a cluster of defects. The back stress increment corresponding to the behavior of material in the presence of highly localized clusters of irradiation induced defects can be decomposed in the following way:

$$d\underline{\underline{X}} = \frac{2}{3}C_0 d\underline{\underline{\varepsilon}}^p + \frac{2}{3}C_0 h\xi d\underline{\underline{\varepsilon}}^p = \frac{2}{3}C(\xi)d\underline{\underline{\varepsilon}}^p \qquad \text{Eq. 147}$$

where the second part corresponds to the interactions between the dislocations in the lattice and the irradiation induced inclusions.

It is worth pointing out that the irradiation contribution to the back stress depends on the irradiation level expressed in terms of *dpa*.

$$C_0 h\xi \sim dpa \qquad \text{Eq. 148}$$

3.3.5 Irradiation and post-irradiation damage in the light of CDM

The irradiation damage affects material behaviour via the scalar parameter D_r. The main concept consists in the fact that damage induced by irradiation does not depend on the damage of mechanical origin. In addition a fundamental assumption is made that the irradiation damage parameter D_r and the mechanical damage parameter D_m are additive and contribute to total damage value D.

It was mentioned by Zinkle [139-140] that the true stress - true strain curve for irradiated material coincides with non-irradiated one after strain shift (Figure 52). The strain shift corresponds to a suitable translation of the stress-strain curve along the strain axis. Zinkle suggested that the yield point actualization should correspond to the partially exhausted strain capacity in the plastic regime. This effect seems to confirm the analogy between neutron irradiation and plastic deformation (cold work effect). Moreover, it suggests that the dislocation-dislocation interactions (plasticity) and dislocation – irradiation products (defects) interactions produce similar net yield point actualization effect.

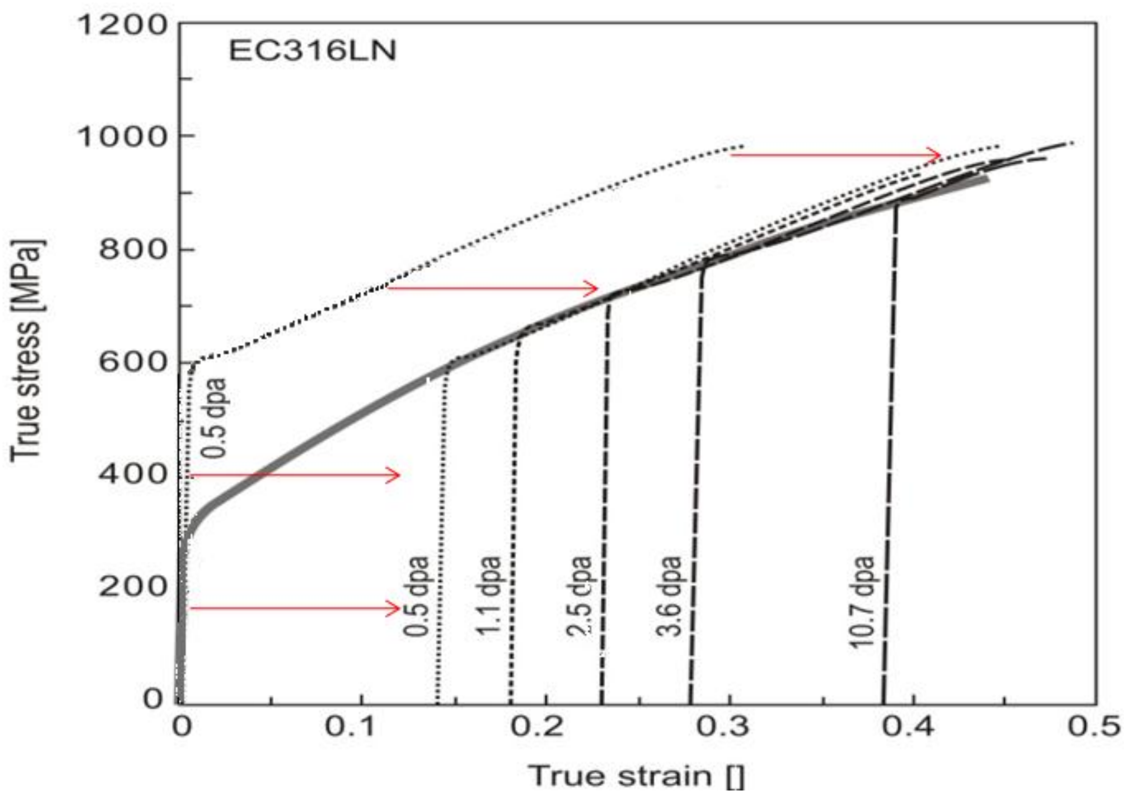

Figure 52 : True strain - true stress curves for irradiated material

The offset in the true stress – true strain evolution is important information about the material evolution. The value of the slip along the strain axis ("strain offset") can be easily calculated from the irradiation induced hardening. The evolution of irradiation damage consists of two parts. The first one consists in the cluster (micro-voids) formation. This phase depends purely on the irradiation process. The irradiated particles lose their energy, by travelling through the material. A portion of this energy is reflected by NIEL which is connected with pure elastic scattering process and nuclear collisions. This is the source of the irradiation defects creation and clustering. The irradiation process was widely described in the previous sections. The result of the irradiation process is observed as Frenkel pairs and clusters formation. Assuming that the clusters are homogenously distributed in the representative volume element (RVE), it is possible to define cluster density in a compatible manner with the definition of standard damage parameter D. Thus, the volumetric definition of the cluster density (q_V=q_c) must be reduced to the density expressed by the number of clusters per unit cross-section area. The reduced value q_A is therefore expressed by the following formula:

$$q_A = \left(\sqrt[3]{q_V}\right)^2 = q_c^{\ 2/3} \quad \text{Eq. 149}$$

Based on the definition of damage parameter (cf. Lemaitre [69]), the following equation defines the irradiation damage D_{r0}:

$$D_{r0} = q_A \pi r_c^{\ 2} \quad \text{Eq. 150}$$

It should be mentioned that as soon as the threshold irradiation dose (D_S) is reached, the cluster saturation process starts, the irradiation damage increases at smaller rate with the dose. Typically, the saturation level for copper amounts to around 0.06.

The evolution of post-irradiation damage is related to the growth of clusters under mechanical loads. The cluster shape in general was assumed as a spherical micro-void. To describe the evolution of micro-voids the equations similar to the Gurson model for porous material can be used (Lutkiewicz and Skoczen [79]). The original model has been split into two parts. The first describes formation of new cavities whereas the second describes the cavity growth. For the post-irradiation case no creation of new clusters of defects is assumed. However, the cavity growth mechanism is adopted. The equation of cavity growth is based on the formulation by Rice and Tracey [109]. The post-irradiation damage can be calculated in two different ways. At first the cluster average radius is used and multiplied by the cluster density in order to obtain the damage value. The post-irradiation damage evolution is related to the void/cluster radius growth caused by the mechanical loads. The radius increment dr_c is defined as a function of the equivalent plastic strain dp, the stress triaxiality factor ($3\sigma_m/2\sigma_{eq}$), the initial radius r_{c0} and a scalar multiplier α_r by means of the following equation:

$$dr_c = r_{c0}\alpha_r \exp\left(\frac{3\sigma_m}{2\sigma_{eq}}\right)dp \quad \text{Eq. 151}$$

The value of the scalar coefficient α_r is defined in a different way by the authors (Rousselier [109], Pardoen et all [95], Krajcinovic [65]). The spread of value of this parameter can be explained by assuming the influence of triaxiality factor on α_r. Originally, it has been set by Rice and Tracey to 0.283 (Rousselier [109]). On the other hand, Huang (Pardoen et all [95]) proposed to calculate α_r as a function of the mean stress σ_m to equivalent stress σ_{eq} ratio.

$$\alpha_r = 0.427\left(\frac{\sigma_m}{\sigma_{eq}}\right)^{0.25} \quad for \quad \frac{\sigma_m}{\sigma_{eq}} \le 1$$
$$\alpha_r = 0.427 \quad for \quad \frac{\sigma_m}{\sigma_{eq}} > 1 \qquad \text{Eq. 152}$$

Following Eq. 157 the post-irradiation damage increment dD_{rm} is defined as a function of the mean size of cluster cross-section. The increment dA_{rm} of the mean size of cluster cross-section can be expressed as a difference between the post-irradiated and the initial mean cluster size (A_r and A_{r0} respectively):

$$dA_{rm} = A_r - A_{r0} \qquad \text{Eq. 153}$$

$$dA_{rm} = \pi((r_{c0} + dr_c)^2 - r_{c0}{}^2) = \pi(2r_{c0}dr_c + dr_c{}^2) \qquad \text{Eq. 154}$$

As the radius increment dr_c is small when compared to r_{c0}, the value $dr_c{}^2$ can be neglected. Thus, the cluster size increment is computed with a reasonably good accuracy in the following way:

$$dA_{rm} = 2\pi r_{c0} dr_c \qquad \text{Eq. 155}$$

The number of clusters q_c related to irradiation treatment (after recombination) is assumed constant for post-irradiation loads. Moreover, it is assumed that the cluster size can grow under mechanical loads only. Finally, the post-irradiation damage increment dD_{rm} can be computed by using the cluster surface density q_A and the mean cluster cross-section increment dA_{rm}:

$$dD_{rm} = q_A dA_{rm} = q_A 2\pi r_{c0} dr_c \qquad \text{Eq. 156}$$

Referring to Eq. 158 one obtains the following formula:

$$dD_{rm} = 2q_A \pi r_{c0}{}^2 \alpha_r \exp\left(\frac{3\sigma_m}{2\sigma_{eq}}\right) dp \qquad \text{Eq. 157}$$

Finally, applying once again Eq. 157, the post-irradiation damage evolution law is derived as a function of initial damage D_{r0} and the accumulated plastic strain p:

$$dD_{rm} = 2D_{r0}\alpha_r \exp\left(\frac{3\sigma_m}{2\sigma_{eq}}\right)dp \qquad \text{Eq. 158}$$

According to the model presented by J. Lemaitre the scalar parameter is equal to 0.573 (Pardoen et all [95]). On the other hand, other authors define its value by connecting the evolution equation to the Lemaitre approach for uniaxial loading. In this way the parameter α_r is expressed as a function of the parameters of Lemaitre model:

$$\alpha_r = \frac{1}{1.65}\left(\frac{D_{cr}}{\varepsilon_R - \varepsilon_D}\right) \qquad \text{Eq. 159}$$

where $\varepsilon_R, \varepsilon_D$ denote the strain to rupture and the damage threshold, respectively. For what concerns both the mechanical and the irradiation induced damage fields, a scalar additive rule is applied in order to compute the total value of damage parameter:

$$D = D_m + D_r \qquad \text{Eq. 160}$$

where

$$D_r = D_{r0} + \int_0^{\hat{p}} dD_{rm} \qquad \text{Eq. 161}$$

3.3.6 Criterion of macro-crack nucleation for combined damage

In order to predict at which external load the onset of macro-crack occurs, a criterion of critical value of total damage parameter is used. The criterion is based on the assumption that the local micro-damage fields of both mechanical and radiation origins and of sufficiently high intensity enhances the probability of macro-crack nucleation. The simplest form of such criterion reads:

$$D_m + D_r = D_{cr} \qquad \text{Eq. 162}$$

where D_{cr} corresponds to the critical value of damage parameter. In a three dimensional case the critical value of damage parameter can be computed in the way presented before (section 3.1.5). In the case of ductile materials (for instance copper) one may assume that $\sigma_s = \sigma_u$ and the critical damage parameter reduces to:

$$D_{cr} = \frac{D_{cr}^0}{T_r} \qquad \text{Eq. 163}$$

which can be easily computed at any point of loaded structure. The criterion of onset of macro-crack becomes more complex when anisotropic representation of damage is involved. In such a case, the criterion can be generalized in the following way:

$$\left\| \underline{\underline{D}} \right\| = \left\| \underline{\underline{D}}_m + \underline{\underline{D}}_r \right\| = D_{cr} \qquad \text{Eq. 164}$$

where $\underline{\underline{D}}_m ; \underline{\underline{D}}_r$ denote the mechanically and the radiation induced damage tensors, respectively. Here, an assumption has been made that both tensors represent the same principal directions. The norm is understood in the following way:

$$\left\| \underline{\underline{D}} \right\| = \sqrt{\underline{\underline{D}} : \underline{\underline{D}}} \qquad \text{Eq. 165}$$

and has been imposed on the total damage tensor resulting from a "superposition" of both individual damage fields (additive rule). Thus, the final criterion for anisotropic damage representation reads:

$$\sqrt{\left(\underline{\underline{D}}_m + \underline{\underline{D}}_r \right) : \left(\underline{\underline{D}}_m + \underline{\underline{D}}_r \right)} = \frac{D_{cr}^0}{T_r} \qquad \text{Eq. 166}$$

and can be easily numerically verified for each subsequent load step.

Chapter IV:

Elastic-Plastic FE Analysis of CF joint

4 ELASTIC-PLASTIC FE ANALYSIS OF CF JOINT

CF joints are widely used for Ultra High Vacuum (UHV) systems. Because of their high reliability and rather low cost (about 1950 CHF) the joints are used in the long straight sections of CERNs new accelerator LHC. Since a single leak stops machine operation, CERN has a vivid interest to better understand the sealing mechanism than it is currently possible with the existing theories. The basic motivation to support this study is to have better tools in hand to develop counter measures against leaks.

The principle of CF joints consists in compressing a soft, flat metal gasket (usually copper) between two conical knives. The original knife design was characterized by external taper angle of 20°, perpendicular internal knife side and a sharp tip. The current standard at CERN corresponds to 20° inclination of flat knife side, 70° inclination of steep knife side and 0.2 mm tip radius (Figure 53). The gasket thickness is 2.0 mm and the gasket is made from OFS copper alternatively equipped with Ag-coating to prevent oxidation where this is crucial (Unterlerchner [120], Wikberg [126]). The knife penetrates the gasket up to 0.4 mm in depth.

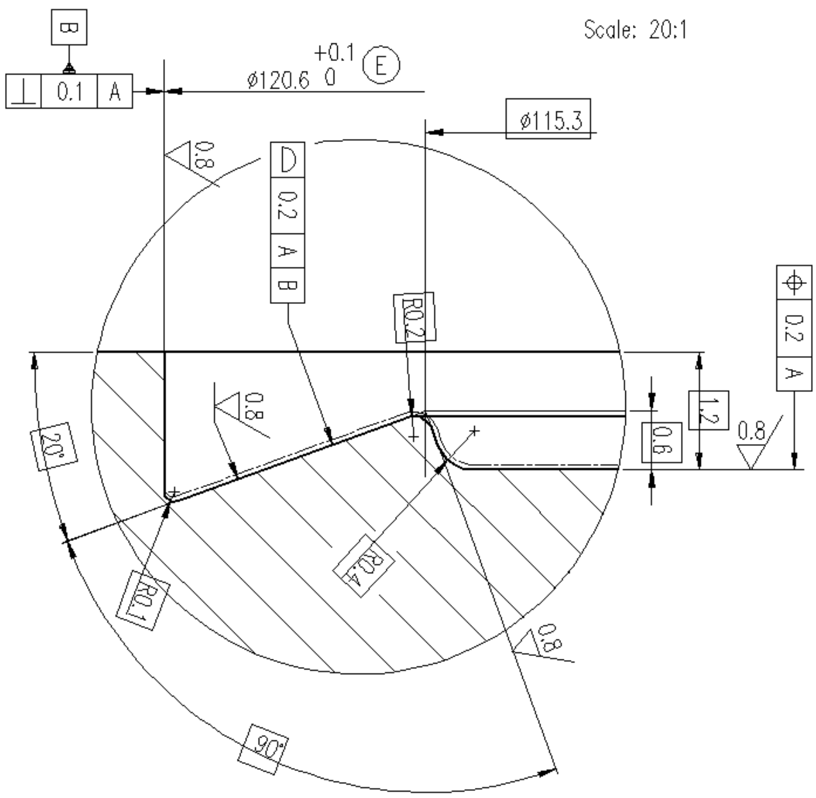

Figure 53 : CF knife geometry used at CERN

Other designs of the knife shape exist. They have different tip radii, modified knife surface inclination and gasket thickness or total possible knife penetration (Roth [108], Kurokouchi [61]). Also, various grades of copper (OF, OFS, OFHC) characterized by various hardening stages are used as gasket material.

The sealing process is generally described by means of a “capture model”(after Kurokouchi and Morita [62]). Initially the gasket is compressed between two opposite knives. As knives penetrate, the gasket compression in the radial direction is produced between the knife and the flange collars. Such model was discussed by Kurokouchi and Morita [62]. Some other research was done to explain the influence of the knife geometry on the sealing process (Kurokouchi et al. [61], [63]). Unfortunately the authors did not describe the FE implementation, which seems to be a 2D elastic (based on the linear theory) gasket with a rigid knife. Such an approach is not sufficient in this problem. It neither gives adequate information on the sealing process nor realistic stress and strain fields in the gasket. The sealing process of CF joints consists in large deformations and requires an elastic-plastic (non-linear) material model to describe the gasket behaviour. In particular, the gaskets elastic modulus *E*, yield point σ_o and the hardening modulus *H* are important for the compression force evolution.

4.1 ConFlat joint FE analysis

The sealing mechanism of flat copper gaskets and ConFlat (CF) flanges is studied. Finite Element (FE) modelling was used and the results were validated through experiments. Only a part of the CF flange knife surface contributes to the sealing. A bilinear character of compression force & displacement evolution was identified numerically. The influence of the flange collar and gasket material properties on the sealing mechanism was studied. The possibility of crack propagation was studied because of large plastic deformation (FE results) near the knife tip. The CDM was also sued to analyse the micro-damage aspects. Also, the irradiation influence was investigated using extended CDM theory.

4.2 Model description

The standard CERN CF joint was analyzed in the framework of elastic-plastic theory. A 2D rotationally symmetric model with in-plane symmetry was implemented by using ANSYS FE code [145]. The geometry is shown in Figure 54. The model contains 2929 elements.

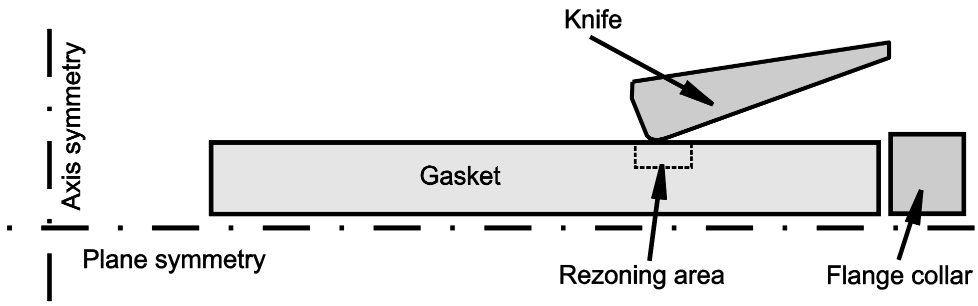

Figure 54 : Model of CF joint

The linear plane element PLAN183 (gasket, knife, flange collar) and contact elements CONTA172 (on the knife side), TARGE169 (on the gasket side) were used. The model was equipped with a rezoning procedure for the region located under the knife. The rezoning procedure was applied at different stages of the knife penetration (between 0.2 and 0.35 mm). It consists in redefining the mesh in the rezoning zone. The gasket material was assumed elastic-plastic with linear kinematic hardening BKIN. The material properties were defined by three parameters: elastic modulus *E*, yield point σ_o, and hardening modulus *H*. During the experiments no plastic deformation of the flange knife was observed. The selected material for the flange knife's was 316LN stainless steel.. Compared to the gasket material, the knife and the flange collars were considered as rigid bodies in the FE model. The full Newton-Raphson algorithm was used to solve this strongly non-linear problem (material and geometrical nonlinearity, as well as contact elements). The material model is presented in Figure 55: the elastic modulus E is equal to 125 GPa, the yield point σ_o is equal to 210 MPa, and the hardening modulus H is equal to 205 MPa.

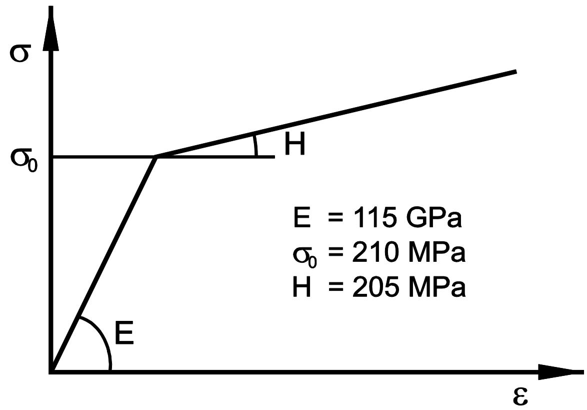

Figure 55 : Gasket material model

These values correspond to the data obtained from tensile tests carried out by using gasket material (taken as reference) at room temperature. The geometry corresponds to the CERN standard CF joint with 2 mm thickness, 101.7 mm inner and 120.4 mm outer diameter for gasket. The maximum imprint depth for knife is equal to 0.4 mm.

4.3 FE analysis results

A displacement field is shown in Figure 56 for 0.4 mm knife penetration. The gasket material flows mainly in the direction perpendicular to the knife contour. On the flat knife side the material flows outwards in the radial direction. On the other hand, on the steep knife side and under the knife tip, the material flows inwards in the radial direction.

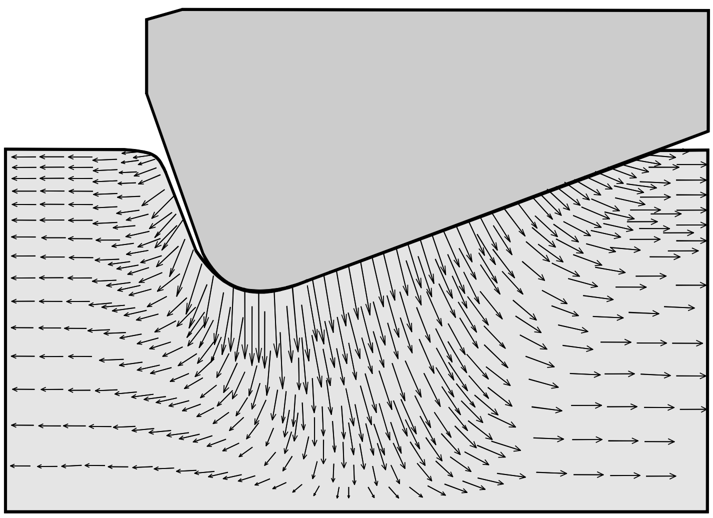

Figure 56 : Total displacement in the gasket cross-section

The plastic strain field corresponding to the displacement field shown in Figure 56 is illustrated in Figure 57, after 0.4 mm knife penetration and without constrained outer diameter. A high intensity plastic strain zone near the knife tip is observed. It can lead to evolution of micro-damage and further macro-crack propagation. The plastic strains have smaller values for the case when the seal is blocked by the collar.

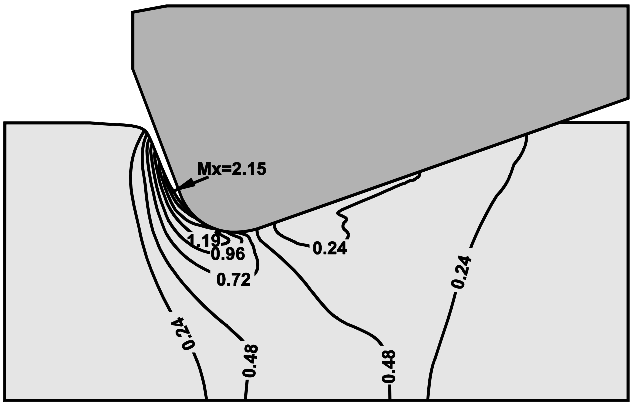

Figure 57 : Plastic strains intensity

The maximum Huber-Misses-Hencky (HMH) equivalent stress is located roughly in the middle of the steep knife side as shown in Figure 58. The flange collar increases the average HMH equivalent stresses in the gasket but decreases locally the maximum value (from 696 MPa to about 520 MPa) and moves the point of maximum value just under the knife tip (after Lutkiewicz and Rathjen [76]).

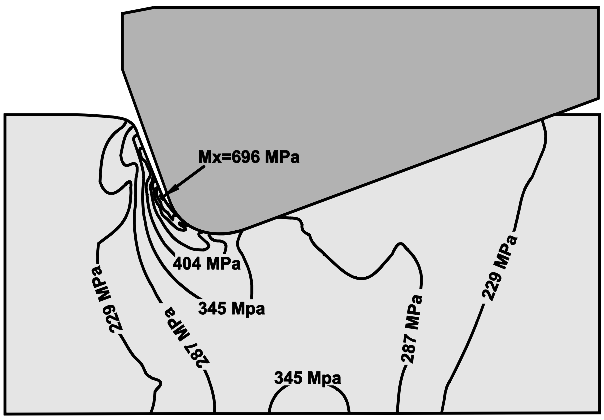

Figure 58 : The Huber-Misses-Hencky (HMH) equivalent stresses

The knife divides the gasket into two stress zones (shown in Figure 59). The inner zone is compressed in the circumferential direction. The outer zone is subjected to the circumferential traction. The clear division between the compressed and the tensile zones disappears when the collar stops the flow of the gasket material in the radial direction.

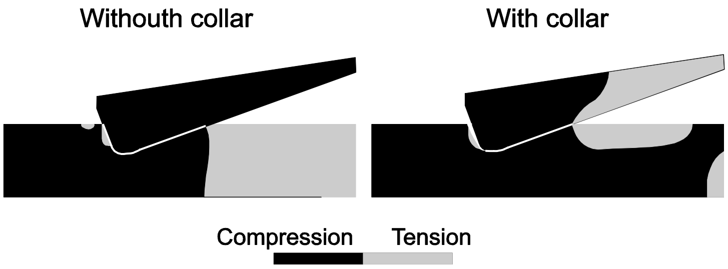

Figure 59 : Circumferential stresses distribution

High contact pressure, responsible for vacuum tight sealing (Roth [107]), appears mainly under the flat knife side (shown in the Figure 60). The contact pressure is quite homogeneous and its average value is 319 MPa. The maximum value under the knife tip is close to 968 MPa. The steep knife side seems not to contribute significantly. The maximum value under the knife tip stays the same for the case when the seal is blocked by the collar. However the average value for the flat knife side is higher (480MPa). Sealing is made under the flat knife side, where the contact pressure value is nearly homogenous. The sealing does not appear under the steep knife side. There is a gap between the steep knife side and the gasket surface. It leads to the conclusion that the surface finishing is important only at 20 deg declined side of the knife and is less important on the other side. Contact with the flange collar increases the contact pressure (after Lutkiewicz and Rathjen [76]).

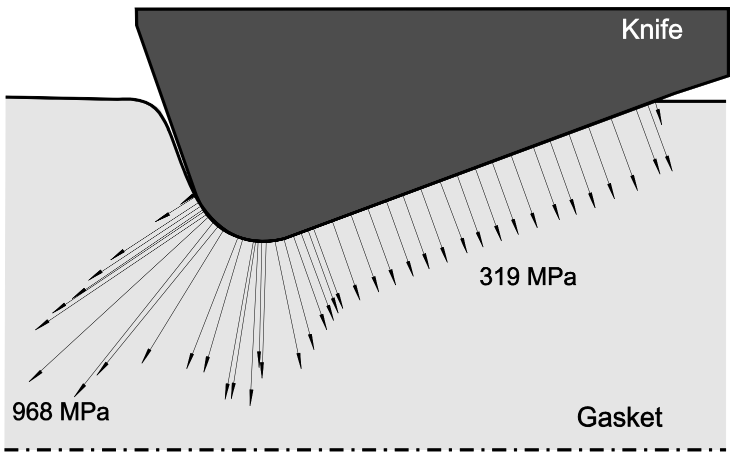

Figure 60 : Contact pressure distribution

As a description of the sealing process the compression force evolution during the knife penetration has been used and is shown in Figure 61. With FE calculations two stages of this process were identified. During the first “quasi-elastic” stage, a local plastic region appears just under the knife edge. With increasing knife penetration local plastic regions are continuously growing to finally fill the area from knife to knife. During the second “plastic” stage the plastic zone is growing in radial direction. The plastic region in the second stage remains only between the knife-to-gasket contact areas.

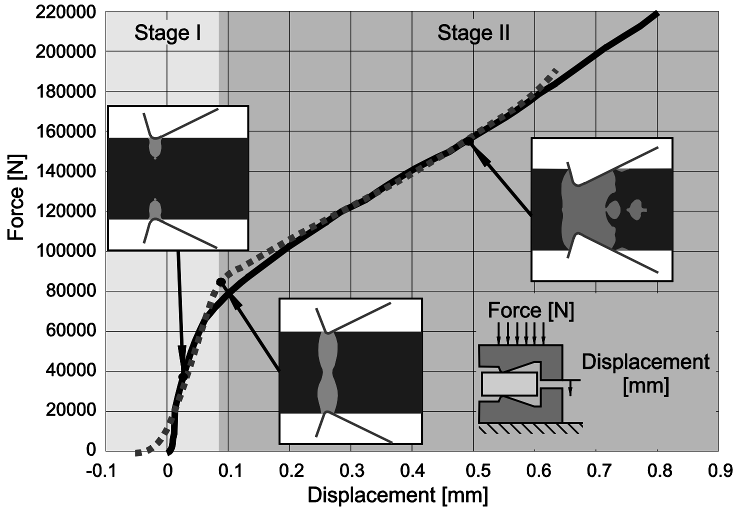

Figure 61 : Evolution of plastic zones

4.4 The sensitivity analysis

A sensitivity analysis has been carried out w.r.t. different elastic moduli, yield point values, and hardening moduli. All cases related to different material proprieties are presented in Table 9.

Table 9: Gasket material properties for different setups

No	E [GPa]	σ_o [MPa]	H [MPa]	No	E [GPa]	σ_o [MPa]	H [MPa]
1	*10*	270	200	9	121	*250*	200
2	*25*	270	200	10	121	*270*	200
3	*50*	270	200	11	121	270	*50*
4	*100*	270	200	12	121	270	*100*
5	*150*	270	200	13	121	270	*150*
6	121	*180*	200	14	121	270	*200*
7	121	*200*	200	15	121	270	*250*
8	121	*230*	200	16	121	270	*300*

The reference standard design parameters for ConFlat joint used at CERN are listed in Table 10.

Table 10 The reference parameters

	Name	Value
Material parameters	Elastic modulus E	121 GPa
	Yield point σ_o	270 MPa
	Hardening modulus H	200 MPa
Geometrical parameters	The inside diameter D_{CF}	102 mm
	Knife tip radius R_{tip}	0.2 mm
	Knife declination angle γ	20 deg

The results of analyses corresponding to different material parameters are presented in Figures 62 - 64.

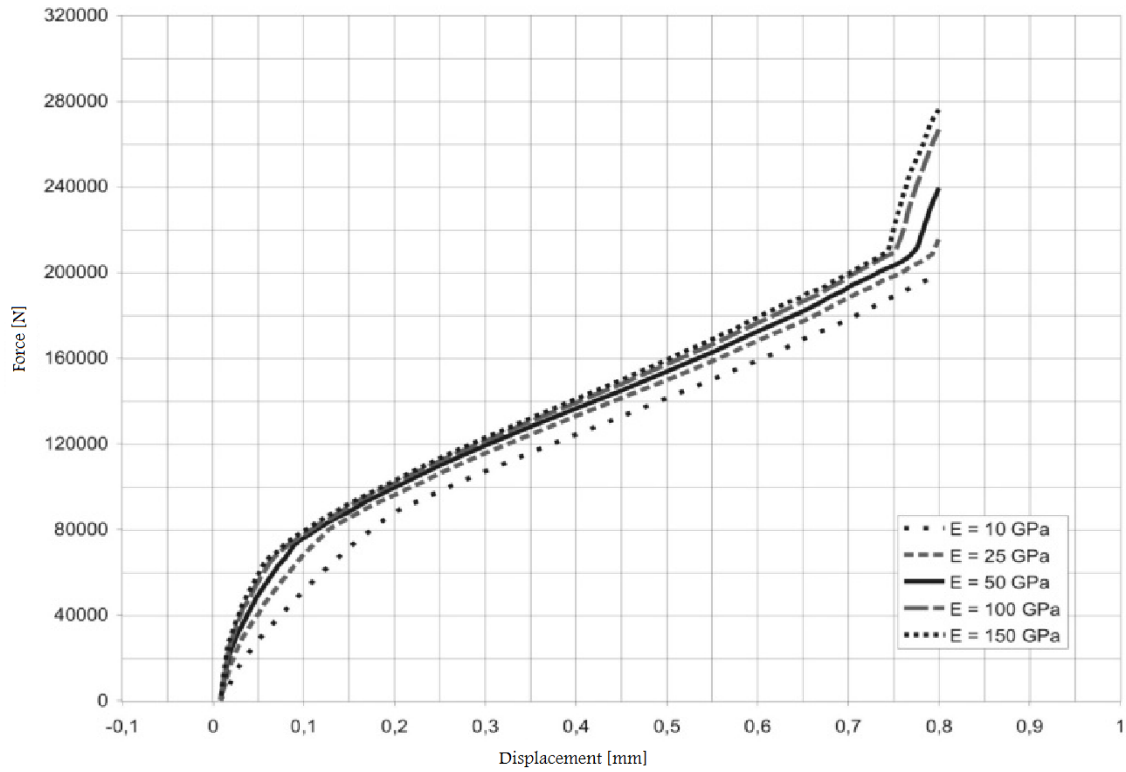

Figure 62 : Force verus displacement curves presented for different elastic moduli

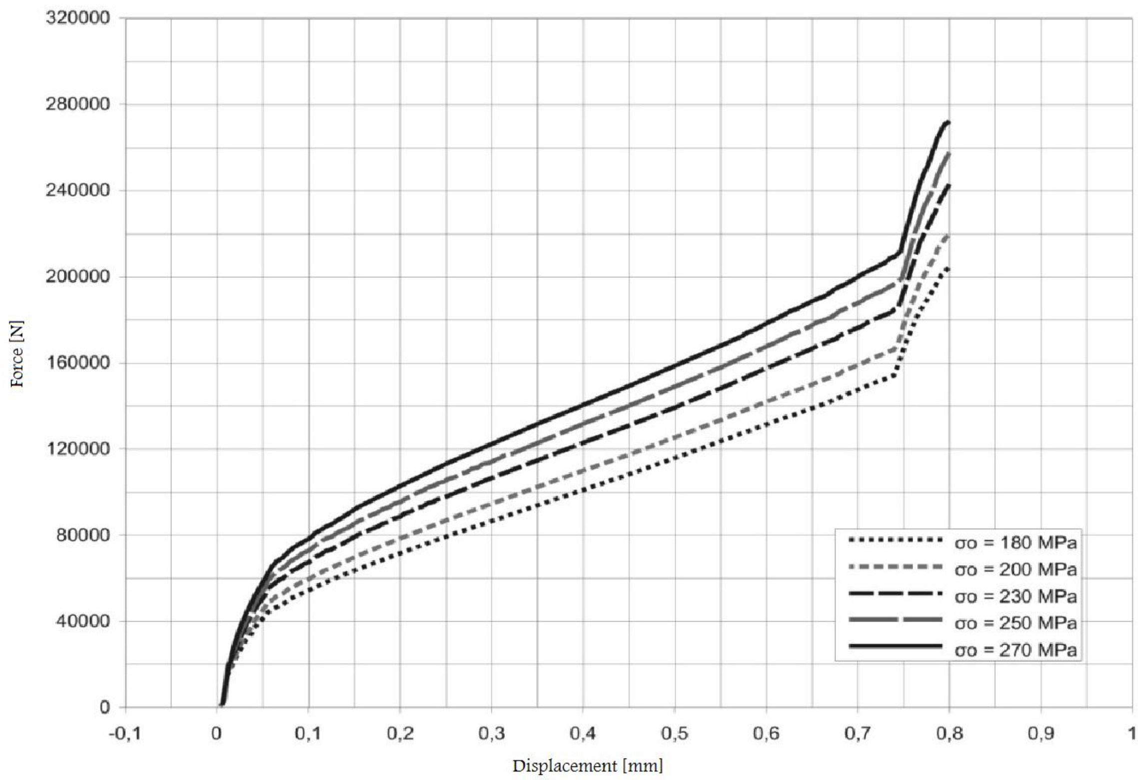

Figure 63 : Force versus displacement curves presented for different yield point values

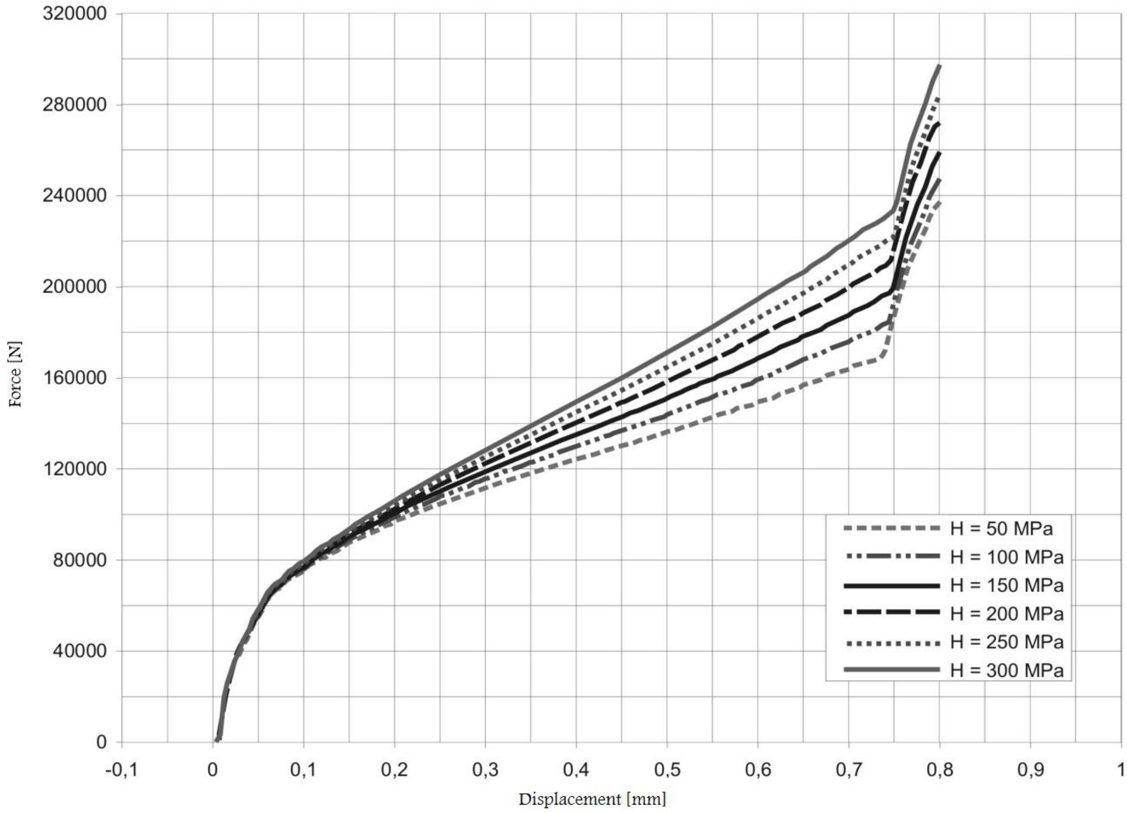

Figure 64 : Force versus displacement curves presented for different kinematic hardening values

There is a good correlation between the material properties bilinear model and the compression force evolution (shown in Figure 65). The local elastic plastic behaviour described by the bilinear law (parameters E, σ_0 and H) is translated to global bilinear behaviour of the gasket during the compression force evolution (shown in Figures 61-65). The elastic modulus E influences the slope during the first "quasi-elastic" stage (stage I in Figure 61). The material between knives works elastically and local plastic zones are created only (zones under the knife tips). The force value, corresponding to the onset of the plastic regime (beginning of the "plastic" stage), depends mainly on the yield point σ_0 and on the elastic modulus E. Nearly all material properties (σ_0 and H) affect the slope of the second "plastic" stage. The force value, when the collar boundaries start to act depends on two material parameters: σ_0 and H. The hardening modulus H and the yield point σ_0 influence considerably the slope of the second, "plastic" stage.

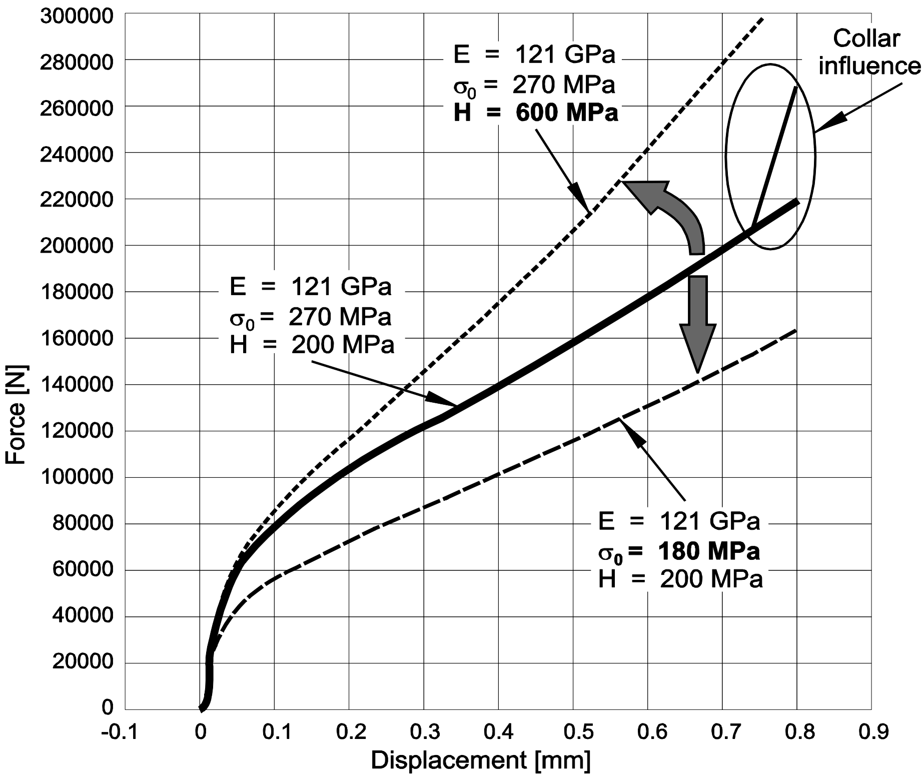

Figure 65 : Evolution of plastic zones

As the knife shape, gasket thickness, and gasket width in CERN used configurations are generally the same for all CF joints, the gasket outer diameter dependence was studied only. The material properties were used the same as the reference. A wide range of diameter dimensions was studied. All of them are listed in Table 11.

Table 11: Joint geometry parameters for different setups

No	γ [deg]	R_{tip} [mm]	D_{CF} [mm]
1	20	0.200	*50*
2	20	0.200	*82*
3	20	0.200	*92*
4	20	0.200	*112*
5	20	0.200	*122*
6	20	0.200	*132*
7	20	0.200	*142*
8	20	0.200	*152*

The results for different seal diameters are shown in Figure 66.

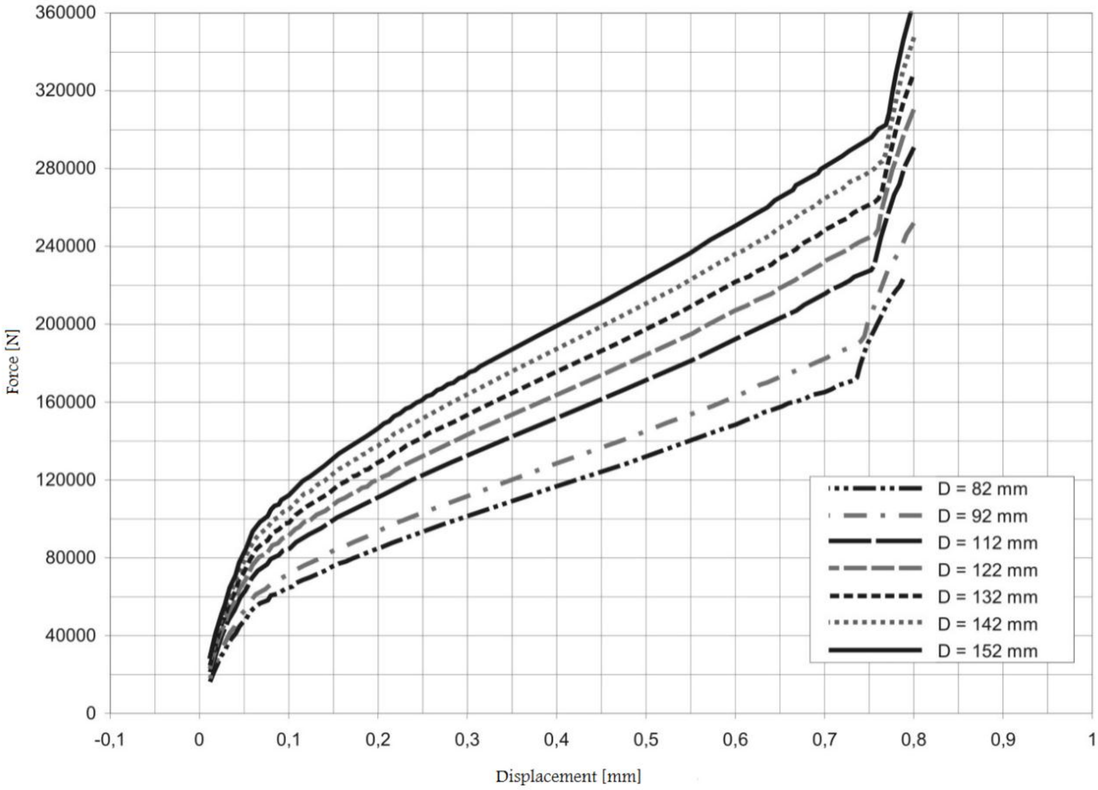

Figure 66 : Force versus displacement curves presented for different joint internal radii

Under these conditions the compression force evolution is proportional to the gasket diameter.

Analyzing the FE results, a phenomenological formula can be derived to describe the sealing force evolution. The formula depends on the elastic modulus E, the yield point σ_o, the hardening modulus H, the gasket outer diameter D_{CF} and the flange displacement (double knife penetration; explained in Figure 9) denoted u. For the first "quasi-elastic" stage the function depends on the elastic modulus E and the gasket diameter D_{CF} only. The slope corresponding to this stage is defined by the following equation:

$$A_I = 26200 \ln\left(\frac{E}{1000}\right)\left(0.008 D_{CF} + 0.18\right) \qquad \text{Eq. 167}$$

where E is expressed in MPa and D_{CF} is measured in mm. The displacement value, at which the compression force evolution enters the second "plastic" stage, is defined by:

$$u_{I-II} = \frac{\left(-\frac{1350000}{E} + 2.8\sigma_0 - 0.6H + 42\right)}{2620\ln\left(\frac{E}{1000}\right) - \frac{1.14E}{1000} - 4\sigma_0 - 4.25H + 165} \quad \text{Eq. 168}$$

where $\sigma_0 ; H$ are expressed in MPa and u is measured in mm. The slope in the second stage is expressed as:

$$A_{II} = \left(\frac{114E}{1000} + 400\sigma_0 + 425H - 16500\right)\left(0.008D_{CF} + 0.18\right) \quad \text{Eq. 169}$$

If the flange collar is taken into account a third line appears in the diagram of the compression force evolution. The third slope appears at the displacement level defined by:

$$u_{II-III} = \frac{\left(385.1\ln\left(\frac{E}{1000}\right) + \frac{1350000}{E} - 35.7\sigma_0 - 6.3H + 1473\right)}{-\frac{1.14E}{1000} - 46.68\sigma_0 - 7.82H + 3865}\left(0.0007D_{CF} + 0.9298\right) \quad \text{Eq. 170}$$

The slope in this additional stage is expressed as:

$$A_{III} = \left(5068\sigma_0 + 1207H - 403000\right)\left(0.0129D_{CF} - 0.3114\right) \quad \text{Eq. 171}$$

The above formula was obtained as the best fit to the FE results for different settings (gasket material properties and gasket outer diameter). General material parameters that affect these equations (sealing process parameters) are presented in Table 12. The diameter acts like a scalar factor for the forces in the connection.

Table 12: Material influence on the joint behaviour

	A_I	A_{II}	A_{III}	u_{I-II}	u_{II-III}
E	**Strong**	Weak	-	**Strong**	Weak
σ_0	**Strong**	**Strong**	**Strong**	**Strong**	Weak
H	-	**Strong**	**Strong**	Weak	Weak

4.5 Elastic-plastic analysis. Results Discussion

FE calculations with rigid and elastic flange parts as well as the application of the rezoning procedure are time consuming. Additionally, problems with convergence were noticed. They are more pronounced for the case with elastic knife. It leads to the conclusion that a simple model shall be used. Models with elastic and rigid flange parts gave the same sealing force evolution, but created different stress fields in the gasket cross-section. It is advisable to keep the elastic knife properties for general calculations. It is also possible to use rigid flange parts to decrease the CPU time for the case, when the compression force evolution is of main interest. The results with the rezoning procedure made after 0.2, 0.25, 0.3, 0.35 mm penetration, were similar and nearly the same as for the case without rezoning procedure. This means that the rezoning approach did not improve the results and can be omitted. The geometrical non-linearity is essential and must be included due to large deformations. Also, in view of significant inelastic strains a nonlinear material model must be used.

Even using the elastic-plastic model with linear kinematic hardening, very high values of plastic strains are obtained. The seal is expected to fracture due to such high plastic strains. In reality there is no dramatic failure and only small cracks were found just under the knife tip where the highest plastic stain values were identified. Possible explanation of this behaviour is the high tri-axial compression of the gasket material under the knife. Another explanation is related to high grid deformation during the FE calculations.

The gasket material flows outwards in the radial direction for the material located outside the knife edge, and inwards for the material located inside the knife edge. The contact pressure build-up between the gasket and the knife was observed on the flat knife side and under the knife tip where the sealing is obtained. The sealing does not occur on the steep knife side. The flange collar has a positive influence on the sealing. It increases the contact pressure and makes it more homogenous. In this case maximum HMH stress under the knife tip is lower (local effect) but average HMH stresses are higher for the rest of the gasket cross-section (global effect). The contact with the flange collar also decreases the plastic strains.

The most interesting observation is the fact that the compression force evolution is similar to the microscopic behaviour described by bilinear material model (micro behaviour). This aspect together with the knife geometry influence is studied in the detail in the other chapters.

A correlation between the FE modelling and the experimental results is not good for all experimental data. It is believed that the reason is the imperfection of real components. The axi-symmetric 2D model assumes an ideal co-axiality for all joint elements (ideal assembly process). In reality it is difficult to satisfy this condition. Usually there is a little offset between the canter of the gasket and the flange. Also, perfect contact between the knife tips and the gasket surfaces around the whole circumference is assumed for the FE model. In reality it depends on the flatness of gasket surfaces, and probably on the knife flatness. Non-uniform imprint depth measurements confirm this supposition. The difference between the total imprint depth and the displacement of the gasket measured during the experiment is similar to the lateral offset value between the FE results and the experimental data. This confirms also the hypothesis that in the first stage there is a fitting process between the flange knives and the gasket surfaces (not possible to take into account in the 2D FE modelling). There is a good correlation between the “plastic” stage slopes and the FE results. Because of these facts the local behaviour is similar to this based on the FE, but the global behaviour can be quite different until all gasket cross-sections enter into the “plastic” stage. The initial imperfect contact between the knives and the gasket surfaces should be considered to obtain better correlation between the experimental measurements and the FE or semi-empirical results. It can be obtained by using the lateral offset equal to about 0.3 mm for the majority of joints from the experiments.

Using a phenomenological formula of the compression force evolution (based on the FE results) it is possible to estimate the sealing loss for CF joint in the case of the material properties changes (for example during annealing at elevated temperatures or irradiation process) without employing time consuming calculations. It is also possible to estimate the spring rate or force evolution for CF gasket by using results of a simple tensile test: elastic modulus E, yield point σ_o, and hardening modulus H. This is very helpful in the design process of vacuum installations. For example, for the joint presented before and for the knife imprint depth equal to 0.3 mm the required force is 166 kN. When the yield point was reduced to 100 MPa during the thermal treatment the required force was equal to 107 kN.

Chapter V:

CLIC Joint Designing Process

5 CLIC JOINT DESIGNING PROCESS

All-metal joints are widely used in the vacuum systems of particle accelerators. The most common ConFlat® design consists of a flat soft copper gasket captured between two stainless steel flanges with sharp edges (knifes). The gasket is plastically deformed and a high contact pressure develops around knifes to obtain leak tightness. For large accelerators, a high reliability and a cost-optimized design are required. A smooth internal transition between flanges is needed for the RF waveguides of the Compact Linear Collider (CLIC), with limited deformation of the inner part of the gasket. A study of the flange meeting these requirements is carried out in the present chapter. First the Finite element (FE) analysis of the SLAC X-band all metal joint, which has a similar specification, is shown. Some drawbacks, such as non-homogeneous sealing properties, are highlighted. Then, a new joint design is described.

5.1 CLIC design based on SLAC joint

CLIC is planned as a linear type accelerator in the TeV energy range for lepton physics. It will consist of two particle beams accelerated in two 21 km long lines (see Figure 4). The beams will then be steered into collision in a detector placed between them. The accelerating energy of the main beam is given by extracting energy from a second beam called a ‘drive beam’. The RF power is transferred to the main beam via wave guides. The whole accelerator will require about 500000 vacuum-tight connections on the beam lines.

Reliable leak tightness is the basic requirement for any joint. Accelerators in particular require the highest reliability since one leaking joint will stop operation of the whole installation. Besides this, CLIC imposes additional performance-related requirements in terms of electrical continuity and the avoidance of spurious cavities. Further requirements for large scale installations are cost saving design and ease of assembly. Obtaining an optimum joint solution is therefore critical, especially for such large quantities. The work started with investigating the previously accepted design (a reference to SLAC X-band joint (Fowkes et al. [40]). The analysis revealed several points that can be improved without changing the basic approach of using flat copper structures as the gasket material and hard stainless steel flanges. After that, the work concentrated on a new joint design process. A new joint was evolved from the knife-based joint type by using sensitivity analysis. The aim was to get superior sealing properties coming together with low complexity and relaxed machining tolerances. This approach is more aimed at joint leak tightness capability rather than the general joint stress and force analysis presented by Korokouchi et al. [61-64] and Lutkiewicz and Rathjen [76]).

5.2 Model description

The existing design from the SLAC X-band is considered a reliable solution. However, the non-symmetrical flanges (two types: male and female) and complex gasket shape were the main motivations to look for an alternative solution. Besides that, after careful examination using FE some other drawbacks were uncovered. The joint scheme is presented in Figure 67.

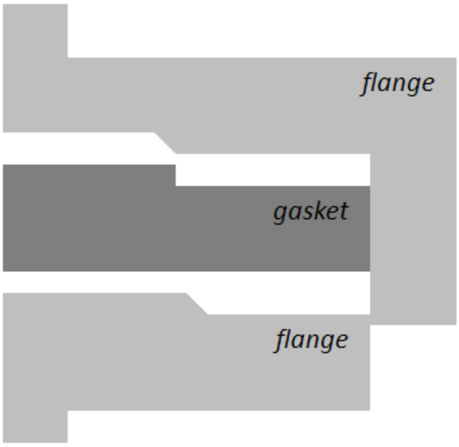

Figure 67 : Original CLIC joint design scheme

The gasket aperture is rectangular in shape and has internal dimensions 31.9 x 19.2 mm. Because the joint is not symmetrical it could not be modelled in 2D. The joint was modelled by using ANSYS FE code [145]. One quarter of the gasket was meshed (considering double symmetry of the joint, Figure 68). The flanges were modelled as rigid surfaces. Between all parts suitable contact elements were used. The FE model is shown in Figure 68.

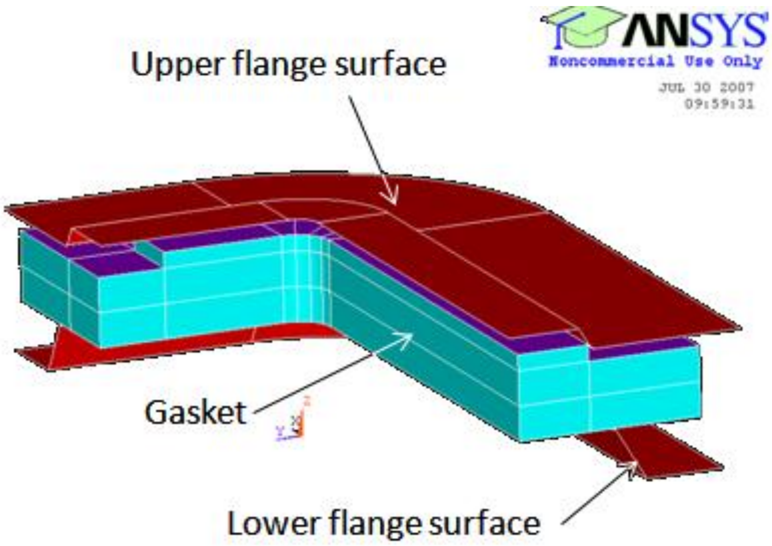

Figure 68 : FE model of the original CLIC joint

The model contains 2929 solid, 122 shell and 1223 contact elements. The linear solid element SOLID84 for gasket and shell183 elements for flanges were applied. The contact elements of type CONTA172 (between the knife and the flange collar side) and TARGE169 (on the gasket side) were used to solve the contact problem. The gasket material was assumed elastic-plastic with linear kinematic hardening (BKIN). The material properties were defined by three parameters: the elastic modulus E, the yield point σ_o, and the hardening modulus H. The knife and the flange collar were considered rigid in the FE model. The full Newton-Raphson algorithm was applied to solve this strongly non-linear problem (material and geometrical nonlinearity as well as contact elements). The same material model for gasket, as used in the ConFlat joint, has been selected.

5.3 Results of elastic-plastic analysis

During the calculations two important elements were checked: the flange-gasket-flange "smooth transition" RF (radio frequency) requirements and the tightening properties. At first the maximum displacement into the beam aperture was verified. It should be less than 0.1 mm because of the proper RF conditions. Using the FE calculations it was found that maximum displacement is about 0.25 mm, which is 2.5 times more than expected. This displacement is located near the corners on both sides and is illustrated in Figure 69.

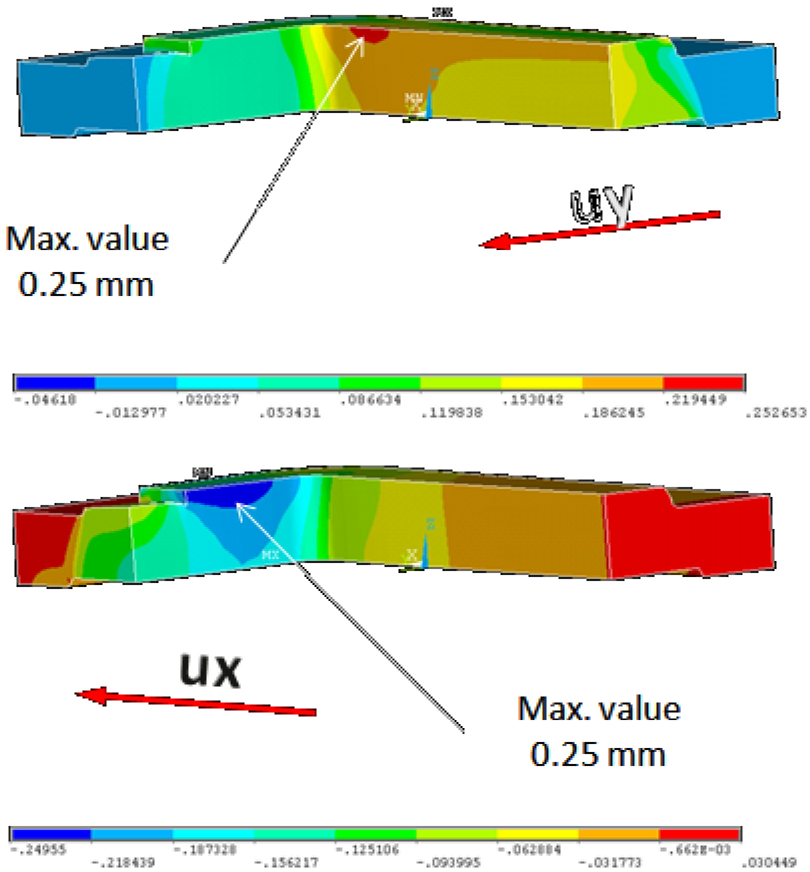

Figure 69 : Displacement into the beam aperture – FE results

The contact pressure is closely connected with the joint tightness. The higher contact pressure and the larger contact area the better sealing is obtained. The investigation revealed that the sealing properties on both gasket sides are different.

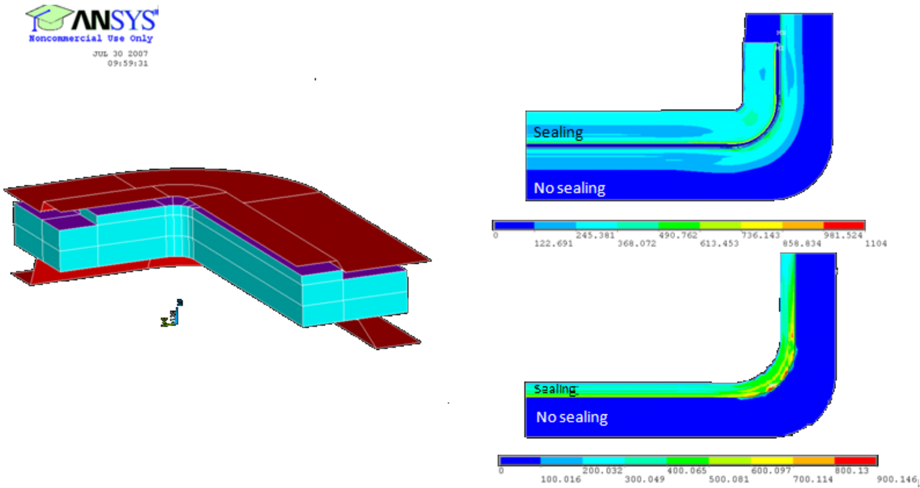

Figure 70 : Different sealing efficiency on both gasket sides

It means that one gasket side has better sealing than the other, but the worst side determines the joint tightness. To obtain perfect solution the sealing should be the same on both sides. It can be also seen that with the step in the top gasket side there is a possibility of creating the so-called trapped volume. Some air can be trapped between the gasket and the flange surfaces in contact. In consequence, it can produce a virtual leak during joint operation. There is also a grove on the step of the top gasket side. This is another weakness of the joint. Because of this the sealing obtained by the upper step is neglected.

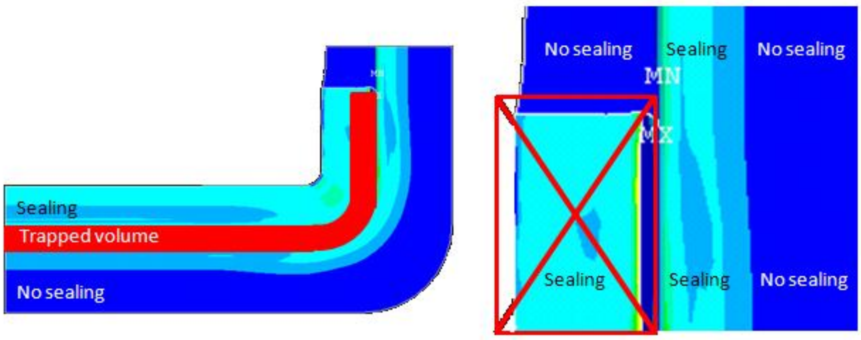

Figure 71 : The weakness points of the joint: trapped volume and grove influence

This joint is based mainly on the shear mechanism. However the compression mechanism also appears. This dual joint character is certainly the result of RF requirements. For RF reasons there is no gap between the flange and the gasket allowed. This is the source of the compression mechanism on the top inner side. Half of the gasket cross-section is then compressed and the second half is free of this load (see Figure 72).

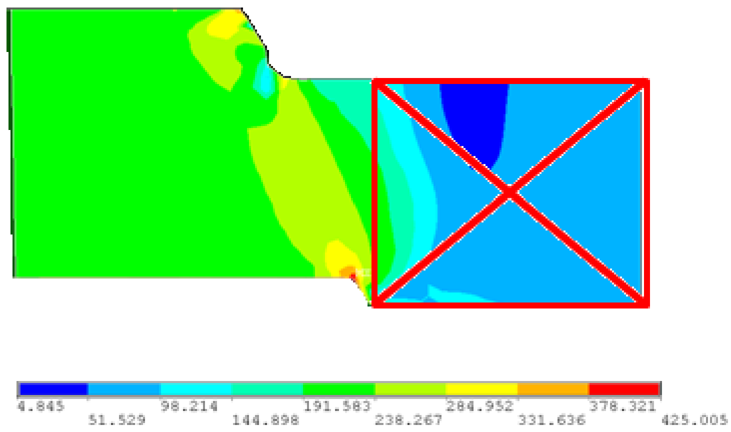

Figure 72 : Compression of the gasket

Another disadvantage of this design is torsion induced in the gasket cross-section. The source of this is dual shear-compression mode and asymmetric design.

5.4 New concept of joint for CLIC facility

Main motivation for developing a new joint is to find a cost-effective design. To this end, the new joint should have simple shape, should be fast and easy when assembling and still keep high reliability for vacuum and RF. The new concept is still based on the knife - flange idea (Lutkiewicz et al. [77]). The flanges are made from hard material and soft gasket is compressed between the knives. Both flanges have the same shape – the joint is symmetric. The gasket has simple rectangular cross-section providing the same tightness conditions on both contact/sealing sides (contrary to the old design). The joint is cheaper in production (there is only one type of flange). It is also less difficult to install, as it is impossible to mix up both flanges. To maintain the RF requirements, the gasket is also rectangular in plane layout. Joint parameters (knife slopes: α, β, gasket thickness, nominal imprint depth and initial offset) were defined to satisfy three important conditions: first of all, to minimize the displacement into the aperture (RF conditions), second, to provide high sealing properties and - third - to keep knife and flange either in the elastic range or to reduce plastic deformations as low as possible considering all other conditions. Also, the machining costs were taken into account. The new joint concept is presented in Figure 73b.

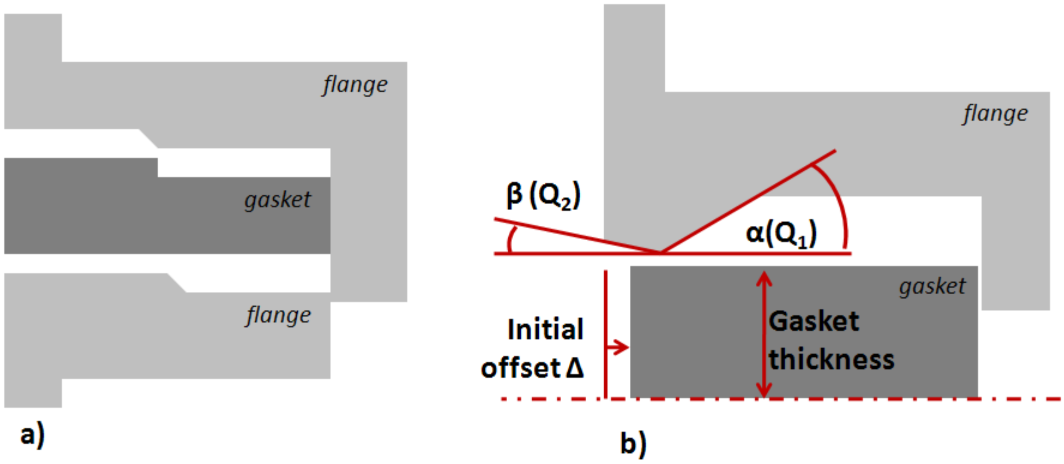

Figure 73 : a) old asymmetric joint concept, b) new symmetric joint concept

5.5 Parametric optimization process

All calculations were made using the commercial FE code ANSYS. A 2D axi-symmetric model was created. The radius of the joint was taken as the average of different aperture dimensions. Also, it should be mentioned that the theoretical leak rate is calculated for the joint using the equation in the form proposed by Roth [107-108] and the resistivity superposition rule.

$$Q = 3400\frac{A^2}{w}\exp\left(-0.306\frac{P}{R}\right) \quad \text{Eq. 172}$$

$$\frac{1}{Q_T} = \frac{1}{Q_1} + \frac{1}{Q_2} \quad \text{Eq. 173}$$

The leak rate Q can be expressed as a function of the contact pressure P (average values for each knife slope) and R, which is a material parameter. Q_T corresponds to the total leak rate, Q_1 is generated by the α slope and Q_2 by the β slope. R is called the sealing factor which expresses the sealing ability of the gasket material. A is the surface roughness and w denotes the width of the contact area. The scalar value 3400 corresponds to the situation, when the He is considered as a flow medium (standard leak test), and the temperature is set to 25°C. The design process starts from the following parameters: 2 mm gasket thickness, 0.3 mm imprint depth, 30 deg for α, 5 deg for β, 0.35 mm initial offset. Geometrical parameters of the joint are defined mainly by the leak rate and the gasket protrusion into the aperture.

Based on the calculations and the experiments the final joint parameters are optimized to fulfil all requirements. As a first step, the gasket thickness influence was studied over the range 1.5 to 3.5 mm. Calculated leak rate is strongly dependant on the gasket thickness for the case without collar interaction (four orders of magnitude), however for the case with collar interaction the dependence is low (one order of magnitude, see Figure 74). As expected, leak tightness is better with the collar interaction.

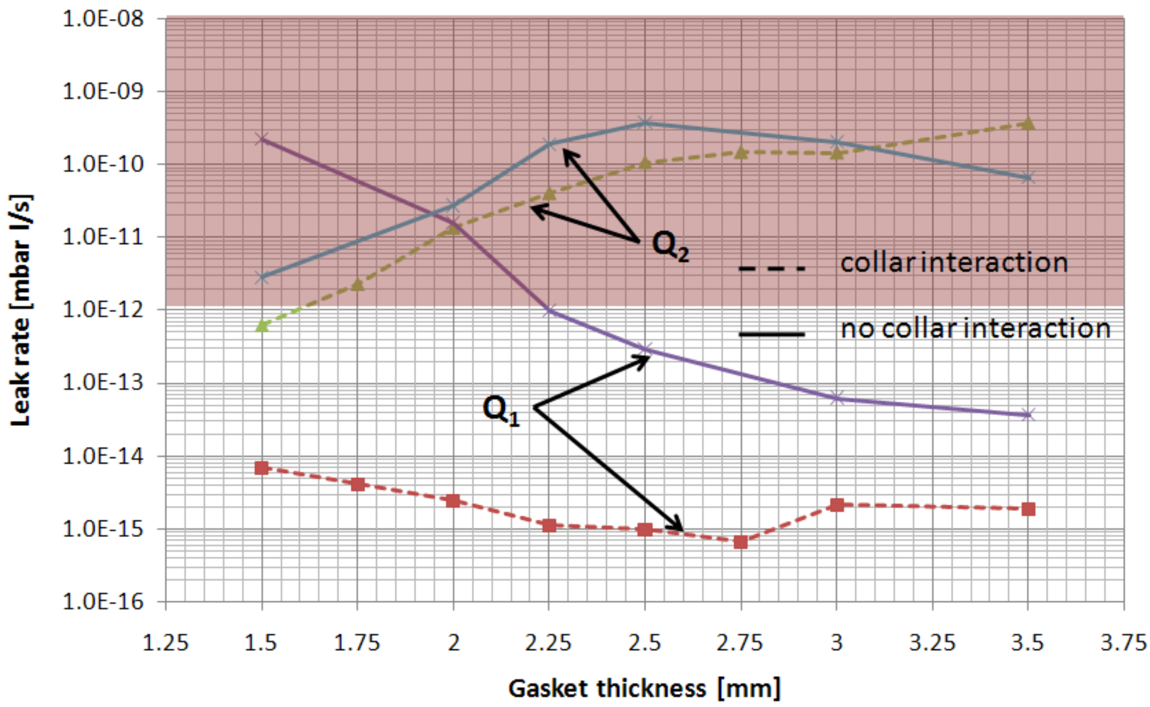

Figure 74 : Calculated leak rate vs. gasket thickness

Also, for the thickness range from 2.0 to 2.5 mm the minimum protrusion into the aperture is equal to 0.14 mm for the case without collar interaction. When the collar interaction is included the displacement is 0.58 mm for the 1.5mm gasket thickness and 0.27 mm for thicknesses higher than 3.0 mm. In order to minimize manufacturing cost, the case without interaction between collar and gasket was chosen. It leads on one hand to the reduction of the contact pressure between the gasket and α knife slope (i.e. reduction of leak tightness), but on the other hand, the joint gains two important advantages. Firstly, the plastic strains are much lower in the flange knife regions. The plastic strain level for the knife varies greatly between the cases with collar interaction (10^{-2} to 10^{-1}) and without (10^{-6} to 10^{-5}). Secondly, there is less constraint on the manufacturing precision of the flange. The nominal gasket thickness is defined as 2.5 mm to keep the leak rate level below 10^{-12} mbar l/s for the 'no collar interaction' case (no plastic deformation).

A new initial gasket offset of 0.1 mm was also defined based on the FE analysis. This minimizes the gasket penetration into the aperture to the level of about 0.05 mm.

The imprint depth also influences the leak rate (see Figure 75). A minimum value is obtained for 0.2 mm imprint according to FE calculations ($6.7\text{x}10^{-15}$ mbar l/s). The maximum value is for 0.4 mm imprint ($2\text{x}10^{-11}$ mbar l/s) and above that it again decreases. Plastic strain is nearly constant and equal to $5\text{x}10^{-5}$ for an imprint higher than 0.25 mm. The displacement into the aperture is in the range from 0.1 to 0.18 mm (maximum for 0.24 mm imprint depth). To allow for machining tolerances, the nominal imprint depth is then defined as equal to 0.3 mm.

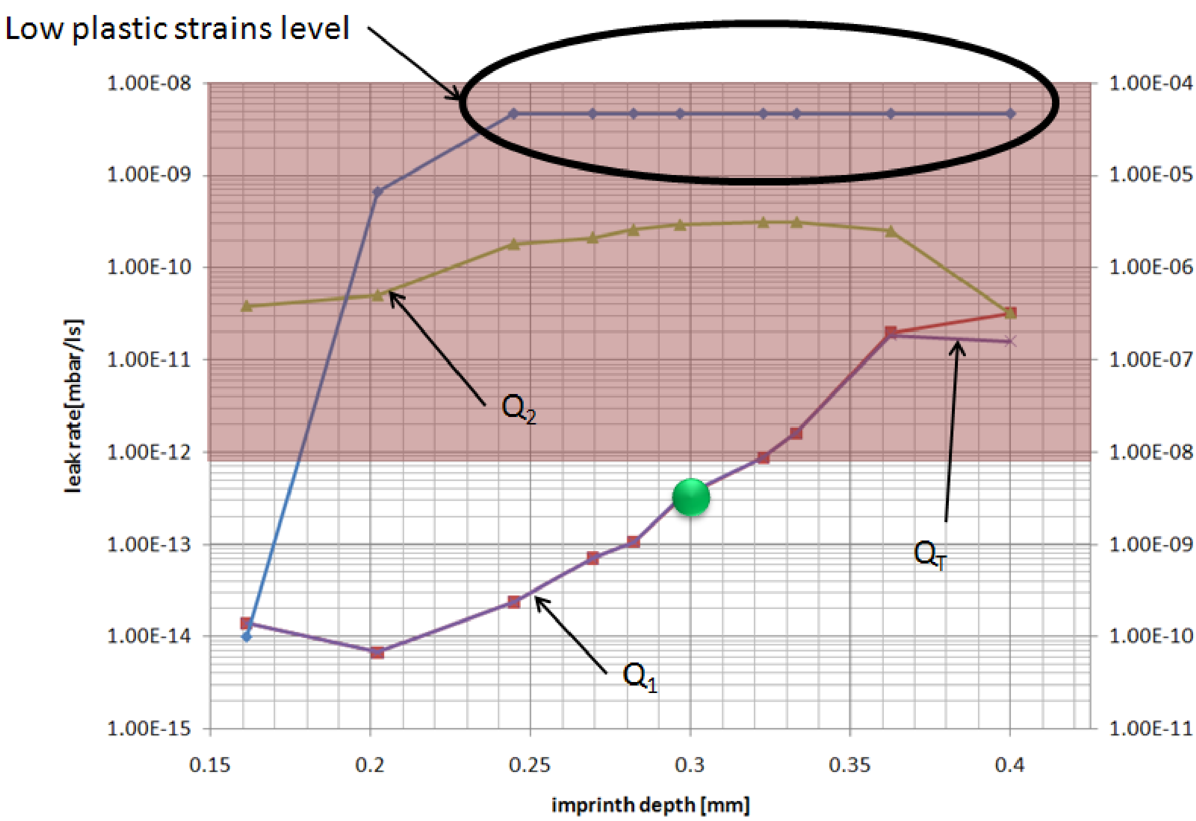

Figure 75 : Calculated leak rate vs. imprint depth

The α knife angle influence is studied in the range 25° to 55° (see Figure 76). The calculated leak rate range is from 1.5×10^{-12} to 6×10^{-15} mbar l/s and has a local minimum for α equal to 40° (1.5×10^{-14} mbar l/s). The leak rate is mainly determined by *α*. Plastic deformations are from 10^{-5} to 10^{-3} for an *α* range from 30° to 55°. The displacement into the aperture is from 0.14 to 0.15 mm for an *α* angle from 25° to 30°. For higher angle values displacement increases linearly up to 0.2 mm for 55°. Finally, the nominal α angle is set at 35° to minimize plastic deformations.

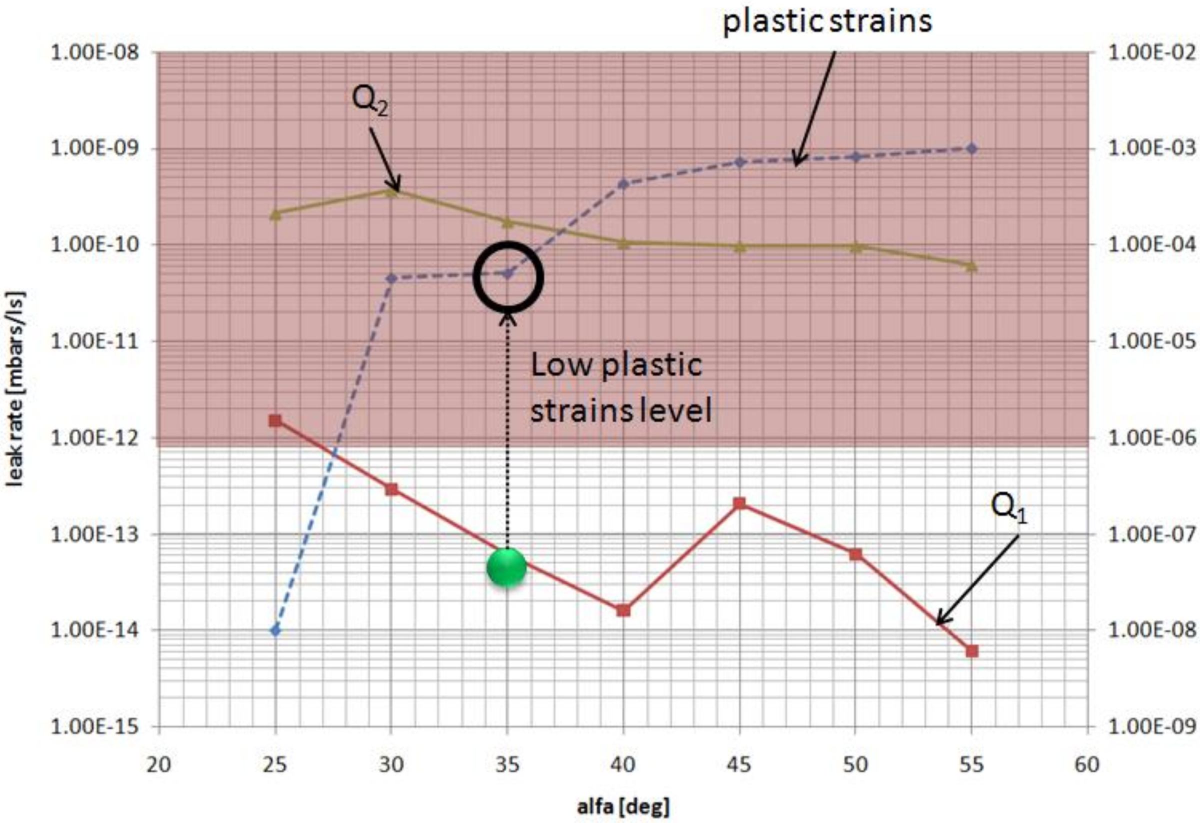

Figure 76 : Calculated leak rate vs. α angle

The last step is to define the optimal β angle value (see Figure 77). The optimum value is when the knife and the gasket are in contact up to the inner gasket diameter (no gap in the flange-gasket-flange transitions). A flat surface could have been used but a slope ensures no trapped volume is created during the clamping process. It also locally increases the contact pressure near the knife tip which gives better sealing properties. According to the FE calculation there is no gap between gasket and flanges when the β value is lower than 7.5º. Taking these factors into account, the β angle is set to 5º.

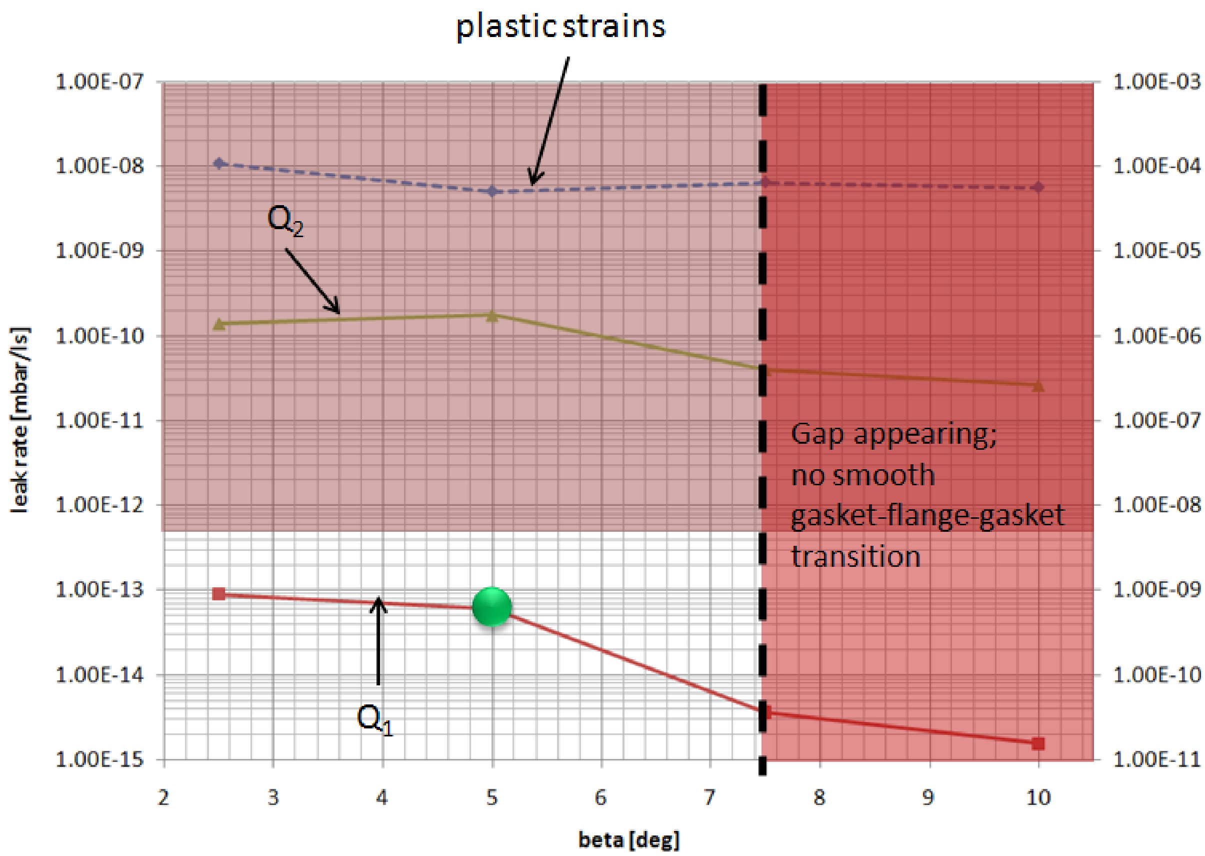

Figure 77 : Calculated leak rate vs. β angle

5.6 Experimental cross-check

Two types of tests have been performed. The first consists of measuring gasket protrusion into the aperture and the second is a standard leak-tightness test. These tests have been performed for two geometries: the initial geometrical parameters with knife contact between the gasket and flange collar, and optimized parameters combined with no collar to gasket interaction.

Both assemblies were leak-tight, with background on the detectors of $4.8\text{x}10^{-11}$ mbar l/s. A leak rate of $1.4\text{x}10^{-10}$ mbar l/s leak rate was achieved with about 60% of nominal clamping displacement after 3 minutes pumping. For a 0.35 mm imprint depth (116% of nominal clamping) plastic deformation of the knife was observed and knifes went about 0.08 mm into the beam aperture (plastic deformations). That value compares well with the FE results (0.12mm). Finally the $1.4\text{x}10^{-10}$ mbar l/s leak rate was achieved (see section 7.3.2).

For the second geometry, a leak rate of 10^{-10} mbar l/s was obtained for about 57% of nominal clamping displacement and kept at the same level for 98% and 117% of nominal clamping displacement. After pumping the background leak rate level was obtained. No plastic deformation of knifes has been observed. The gasket protrudes 0.13 mm from the initial position (0.1mm offset) into the aperture for a 0.334 mm imprint depth. It corresponds well with the displacement value taken from FE calculations, which was 0.154 mm for 0.35 mm nominal imprint depth.

Additionally, leak-tightness tests were performed for 2 and 3 mm gasket thickness and the results confirm FE predictions of better tightness for higher gasket thicknesses.

Chapter VI:

Analysis based on CDM principles

6 ANALYSIS BASED ON CDM PRINCIPLES

The present chapter is driven by an attempt to explain a frequent and difficult problem of loss of tightness in ultra-high vacuum systems, equipped with metallic seals, by means of continuum damage mechanics (CDM) and FE formulation. This problem has broader meaning and the results of the present study can be extrapolated to pressurized systems and pressure vessels. The present description of loss of tightness in vacuum systems, operating at room and at low temperatures, is based on the evolution of micro-damage fields reflecting the texture induced anisotropy observed as a function of manufacturing technology. It is postulated that the mechanism of loss of tightness is related to evolution of plastic strain induced fields of micro-voids and micro-cracks, generated in the transition components (metal gaskets or seals) subjected to combined loads. Such fields result from a contact between two metallic objects, one of them playing role of stiff edge (rigid punch) and the second one being rather a soft elastic-plastic foundation (seal). The sealing mechanism consists in pushing the rigid edge (knife) against soft foundation, thus causing development of local plastic strain fields and related micro-damage. It is strongly believed that the micro damage fields may contribute to the mechanism of loss of tightness, especially in the case when on one side of the seal ultrahigh vacuum exists. A deep insight into the mechanism of loss of tightness is fundamental for such scientific instruments like modern accelerators of particles for high energy physics that require the UHV of the order of 10^{-10} mbar. Similar problems occur in the joints used in vacuum technology for spacecraft and orbital stations. When analyzing the evolution of plastic strain fields in the seals of vacuum systems a contact problem has to be solved. The difficulty consists in the fact that the contact zone evolves as a function of depth of indentation which results in significant evolution of width of plastic strain fields. Here, shape and intensity of plastic strain fields depends on the geometry of rigid edge (punch, knife). Such problem is well known already in the theory of elastic solids as the rigid punch indentation into elastic half-space and has been solved by many authors. The problem of rigid punch indentation into elastic-plastic half-space is more complex and not many solutions can be found in the literature. Here, certainly the paper by Ivlev [55] is worth mentioning. Another paper on the the stress fields around elastic-plastic indentation has been published by Feng et al. [38]. A finite element solution of the Prandtl flat punch problem has been presented by Tan et al. [118].

The present chapter has been separated into two parts related to mechanically induced and irradiation induced micro-damage, respectively. The most innovative feature of the Thesis is certainly related to the irradiation aspect. The irradiation is treated as the damage source and the reason of evolution of material properties. An extended CDM theory formulation has been proposed and is now used in the FE calculations. A new finite element was defined by using the formulation presented in section 3.

The FEM analysis was performed by using FE code CASTEM. It is more research oriented tool and based on the open source idea. It was developed in France in the Laboratoire de Mécanique Systèmes et Simulation within the Commissariat Français à l'Energie Atomique (CEA). It also consists of pre-processing, solver and post-processing modules. All constitutive models were developed by using a high level macro-language GIBIANE. Working with CASTEM consists in much more mathematical thinking in the model composition than it is usually done in ANSYS. The basic structure in GIBIANE is that of an operator acting on complex objects (data structures) to produce other objects. The advantage od such application is a free access to all procedures and possibility of changing them or implementing new ones by using ESOPE (similar to FORTRAN) language. It is really important in the case of implementation of new constitutive equations. This FE code was used to perform the CDM analysis and to extend the classical CDM beyond the current limits in order to accommodate the irradiation and post irradiation damage features by means of new finite elements.

In the present chapter the fully coupled analysis has been carried out using self implemented element. This approach is well adapted to structures that develop rather high and not highly localized plastic strains as well as micro-damage. On the other hand, in some specific cases more simple "uncoupled" approach might be applied. The uncoupled analysis neglects the influence of damage on stresses. Usually, it consists of two steps: elastic – plastic analysis combined with post-processing in order to evaluate damage evolution along the critical path. For strain controlled conditions, the method is conservative and offers lower bound on the critical time to rapture. Sometimes, locally coupled analysis, suitable for highly localized damage in a volume small with respect to the RVE scale, is applied. In such a case a post-processor that links the microscopic scale variables (stress, strain, damage) to the mesoscopic ones has to be developed. In any case, the fully coupled analysis offers complete constitutive formulation with the effect of damage on the state variables taken into account. The model has been implemented in the finite element code CASTEM. The method of type ''radial return,'' originally proposed by Wilkins [127], is used to integrate the constitutive equations for an active plastic process. The radial return algorithm is based on the elastic-plastic split, by first integrating the elastic equations to obtain an elastic predictor, which is used as initial condition for the plastic return (Ortiz and Simo [90]). A plastic corrector is calculated, whereby the elastically predicted stresses are relaxed onto a suitable updated yield surface. The numerical algorithm can be illustrated in the following way:

- Current state variables:

$$\underline{\underline{\sigma}}_n,\ \underline{\underline{\varepsilon}}^p_n,\ \underline{\underline{X}}_n,\ R_n,\ \underline{\underline{D}}_n,\ p_n$$

- Elastic predictor defined from a total strain increment:

$$\underline{\underline{\sigma}}^0_{n+1},\ \underline{\underline{\varepsilon}}^{p^0}_{n+1}=\underline{\underline{\varepsilon}}^p_n,\ \underline{\underline{X}}^0_{n+1}=\underline{\underline{X}}_n,\ R^0_{n+1}=R_n,\ \underline{\underline{D}}^0_{n+1}=\underline{\underline{D}}_n,\ p^0_{n+1}=p_n$$

- Test if the new state is elastic or not,

- If not ($f^0_{c\,n+1}>0$), the plastic corrector increment $\Delta\lambda$ is computed from the consistency equation (*$df_y=0$*). Then, the increments Δp and $\Delta\underline{\underline{\varepsilon}}^p$ are deduced,

- The increment $\Delta\underline{\underline{D}}$ is calculated as a function of Δp

- The state variable (q) is updated from the evolution law,

$$q^{i+1}_{n+1}=q^i_{n+1}+\Delta q$$

- The condition $D_{n+1}^{i+1} \le D_L$ is checked. If $D_{n+1}^{i+1} > D_L$, no further accumulation of damage takes place. Damage parameter has just reached the limit value D_L,
- The iterative process stops for $f_{c\,n+1}^{\;i+1} \le 0$,

6.1 The mechanically induced micro-damage

It is worth pointing out, that the analysis based exclusively on the evolution of plastic strain fields indicates localizations characterized by the highest plastic strain intensity. On the other hand, such analysis does not answer two fundamental questions: when does the plastic strain intensity reaches a critical level corresponding to enhanced probability of macro-crack propagation and what direction will the macro-crack follow. A much better tool in this respect offers Continuum Damage Mechanics (CDM) where the intensity of micro-damage is strictly related to the probability of macro-crack formation and the distribution of micro-damage fields indicates probable path the macro-crack will follow. Anisotropic description of damage fields turns out to be particularly useful in tracing trajectories of macro-cracks. As the seal is usually made of a ductile material (typically copper) the nature of micro-damage evolution is also ductile and implies application of ductile damage mechanics. Within the CDM, two original formulations are well known: by Kachanov [56-57] and by Chaboche [24] and Lemaitre [70-71]. The latter is certainly well adapted to ductile damage evolution driven by plastic strain fields. Here, the conjugate force coupled to damage is the strain energy density release rate and the driving force of damage is the accumulated plastic strain. Another well known approach to micro-damage analysis is based on Gurson model [49], developed further by Tvergaard [119] and later on by Needleman and Tvergaard [86]. The model has been successfully implemented and is certainly more accurate in the case of porous materials. It incorporates well the nucleation and growth of voids under the hydrostatic stress. However, it still suffers from a limitation related to prediction of damage evolution under shear strains (cf. Hambli [50]). In the indentation problem both the evolution of micro-damage due to hydrostatic pressure and shearing mechanism are important. For this reason the CDM based models prove more efficient in the cases where the shear component plays a crucial role.

Evolution of micro-damage may result in formation of larger entity like a small crack. Such effect is certainly detrimental to the tightness conditions required for the UHV systems. In the present section the conditions of ductile damage evolution in the seals operating at cryogenic temperatures as well as their consequences for the tightness of UHV systems are studied in the framework of CDM. Moreover, certain aspects of application of UHV seals at cryogenic temperatures will be explained.

In the beginning a general elastic-plastic half space subjected to loading by means of a rigid punch is analysed. This is an introduction to the problem related to operating mode of all metal joints. Afterwards, the results of computation for a specific example of CF joint are presented. Finally, a comparison between the classical CDM formulation and the irradiation induced damage model is presented.

6.2 Locally loaded elastic-plastic half space

The problem of locally loaded elastic-plastic half space refers either to the half-space subjected to load distributed over a restricted area (type Hertz problem) or to the half-space subjected to a rigid punch (type Sadowsky problem). In both cases the closed form solutions based on suitable Green functions exist in the elastic domain and can serve as a benchmark for the numerical solutions.

Solution of the problem of elastic half-space subjected to distributed load (see Figure 78) is based on the Boussinesq solution for half-space subjected to concentrated force.

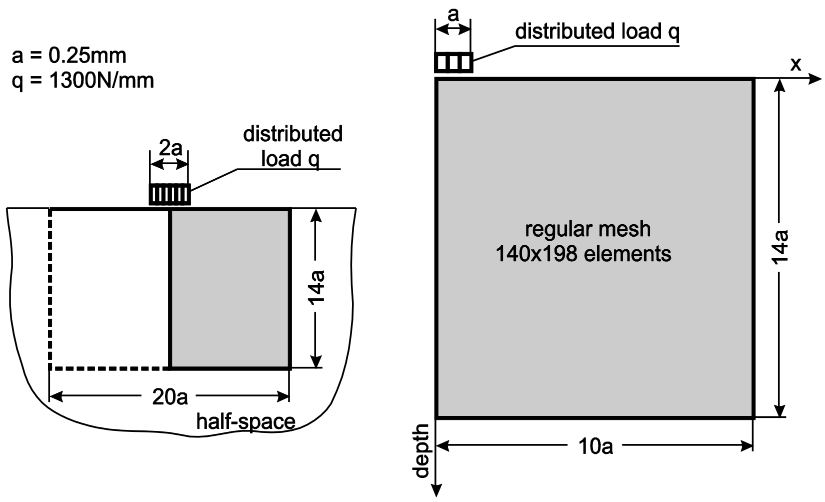

Figure 78 : Half-space subjected to distributed load – scheme

Closed form solution of this problem in terms of displacements has been derived by Hertz. FEM code CASTEM was used to model this problem. The values of stresses were extracted as average values for elements in the 1st column next to the symmetry line. The analytical solution for surface load uniformly distributed over a finite strip is compared with the numerical solution. Both solutions practically coincide, which confirms validity of the FE model. The same problem has been solved for elastic-plastic half-space. The material has been defined as elastic-plastic with linear kinematic hardening. Here, small hardening modulus has been chosen in order to obtain a solution close to perfect plasticity. In addition the model was equipped with the micro-damage feature (both isotropic and anisotropic), which enables a direct comparison between the elastic, elastic-plastic and elastic-plastic-damage solutions.

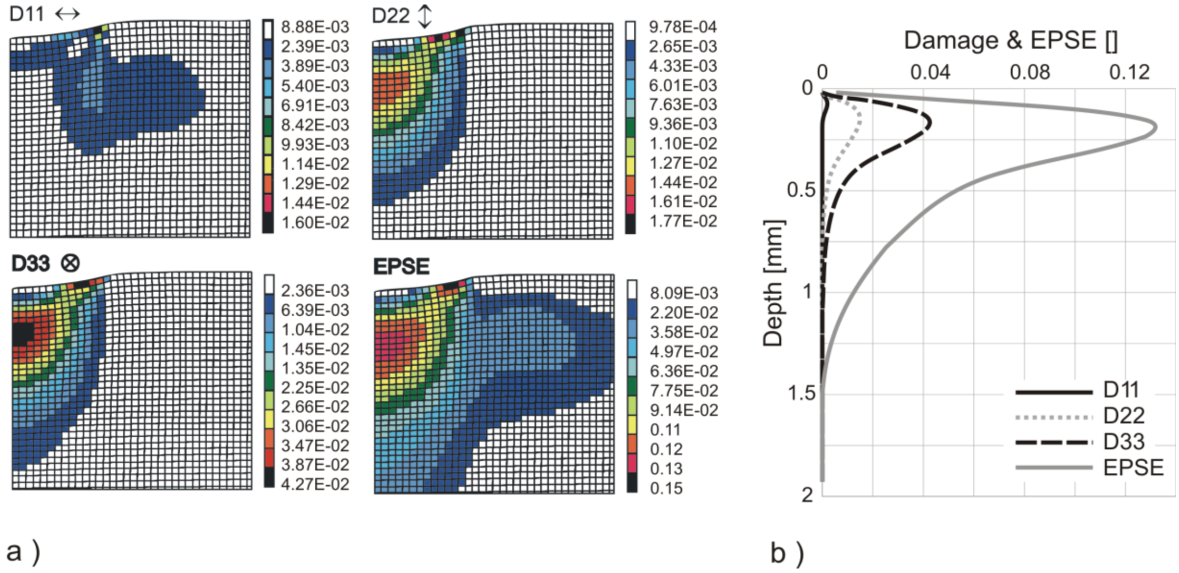

Figure 79 : a; Distribution of micro-damage (D11, D22, and D33) compared to the evolution of plastic strain intensity (EPSE) b; Evolution of micro-damage components as a function of depth

Evolution of micro-damage components as a function of depth for a half-space subjected to distributed load is plotted in Figure 79. The values correspond to the elements located in the 3rd column from the symmetry line in order to minimize the influence of boundary conditions (de Saint-Venant principle). It is worth pointing out that the maximum plastic strain intensity occurs underneath the free surface, at a depth corresponding to the Hertz solution. Similarly, a concentration of micro-damage has been found in the region of maximum plastic strain intensity, as illustrated in Figure 79. Also the driving force of micro-damage has been attributed to the accumulated plastic strain, which is a scalar parameter. On the other hand, the principal components of damage tensor may considerably differ from each other. This feature may be attributed to anisotropic character of ductile damage evolution. Also, the probable macro-crack propagation path is determined by distribution of damage tensor components: D11 (Drr), D22 (Dθθ) and D33 (Dξξ).

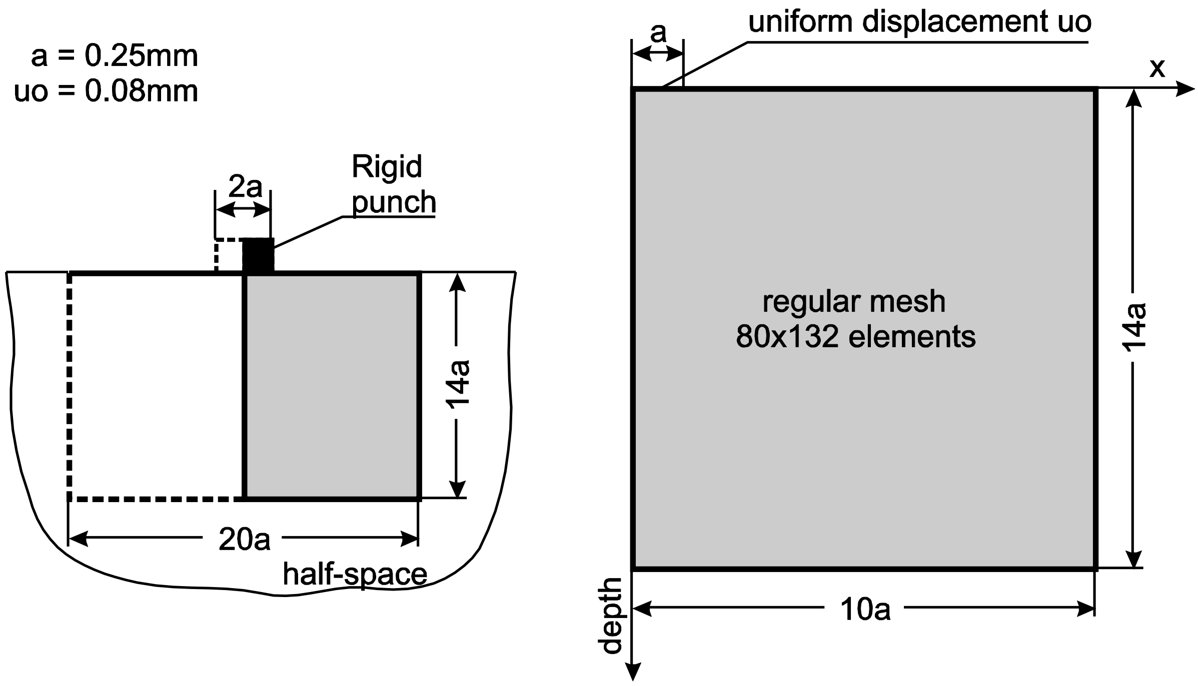

Figure 80 : Half-space subjected to rigid punch load – scheme

Rigid punch indentation into elastic half-space (see Figure 80) implies different formulation when compared to the problem discussed in previously. Now, distribution of contact pressure between the punch and free surface of the half-space is searched as a solution of the contact problem. Here again the Boussinesq solution for elastic half-space subjected to concentrated force can be used as a Green function. Solution of the problem of flat rectangular punch acting on free surface of elastic half-space has been derived by Sadovsky, 1928. The problem becomes more complicated when the response of the half-space is extrapolated to the plastic domain. This problem has been investigated first by Prandtl, 1920 and then by Hill, 1949. Prandtl introduced a rigid-perfectly plastic semi-infinite continuum subjected to flat punch without friction in the contact zone. Uniform distribution of contact pressure has been assumed. The solution was presented in terms of the slip lines and five distinct areas: "rigid" triangular region moving downwards with the punch velocity, two symmetric zones of circular flow around the punch corners and two symmetric zones of flow in the direction opposite with respect to punch. The solution by Hill was slightly different and did not require a "rigid" triangular region beneath the punch. Also, in the Hill solution the flow velocity was higher than in the Prandtl solution. It is worth pointing out that the validity of both solutions depends on the amount of friction between the punch and the half-space. Some further development in this domain has been carried out by Ivlev [55], who investigated indentation of wedge-like and rectangular punches into the plastic half space. Closed form solutions for velocity fields were obtained.

In order to solve a complete elastic-plastic problem including strain hardening a finite element method has been applied based on the same bilinear kinematic hardening model as in the previous section. Stress concentration close to the extremities of the punch leads to creation of local zones of plastic strains, and corresponding evolution of micro-damage fields. The zone of intensive yielding generates fields of ductile micro-damage, as illustrated in Figure 81.

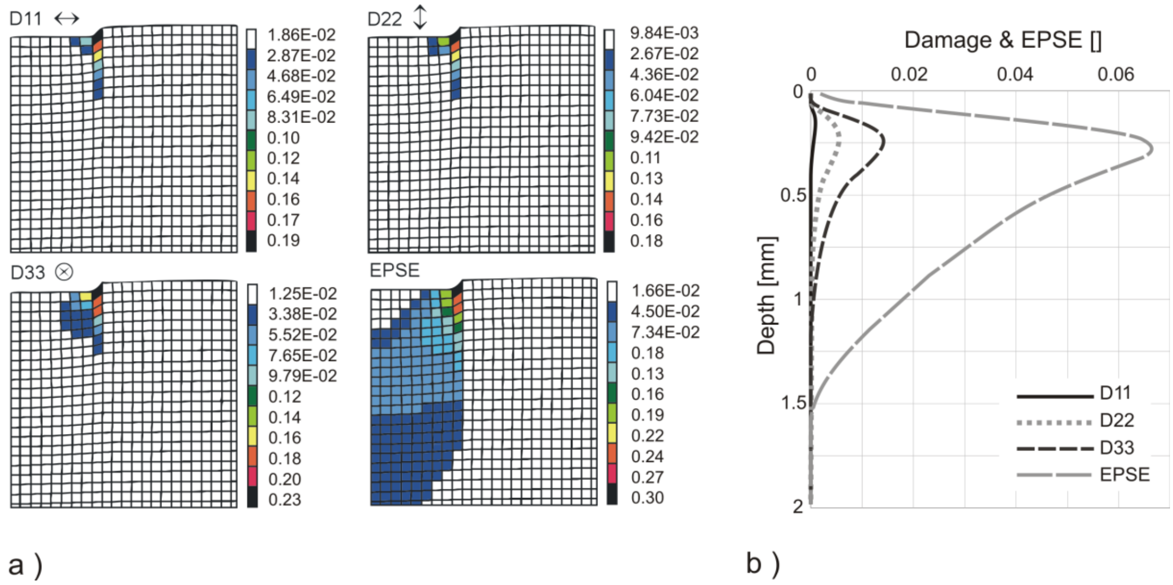

Figure 81 : a; Distribution of micro-damage (D11, D22, and D33) compared to the evolution of plastic strain intensity (EPSE), b; Evolution of micro-damage components as a function of depth

Evolution of micro-damage (D11, D22, D33 in the 2nd column of elements from the symmetry line) compared to the evolution of plastic strain intensity is presented as a function of depth in Figure 81. It is worth stressing, that there exists a local micro-damage concentration close to the extremities of the punch. This effect is related to all three principal components of damage tensor. Here, also the stress and the local maxima of micro-damage are located underneath the free surface near the symmetry axis, at a depth roughly corresponding to the Hertz solution. However, the intensity of micro-damage is 3 directions and the depths corresponding to local maxima of damage considerably differ from each other.

6.3 ConFlat joint analysis

Tightness of ultra-high vacuum systems is usually assured by a configuration of edge (knife) and gasket (seal), where the edge is regarded as infinitely rigid and the gasket as elastic-plastic continuum. As the shape of the edge is rounded a strong concentration of stress is avoided and the plastic strain fields correspond to the whole width of the edge. Typical distribution of the plastic strain intensity (EPSE) and damage parameters (D11, D22, D33) in the gasket are illustrated in Figure 82.

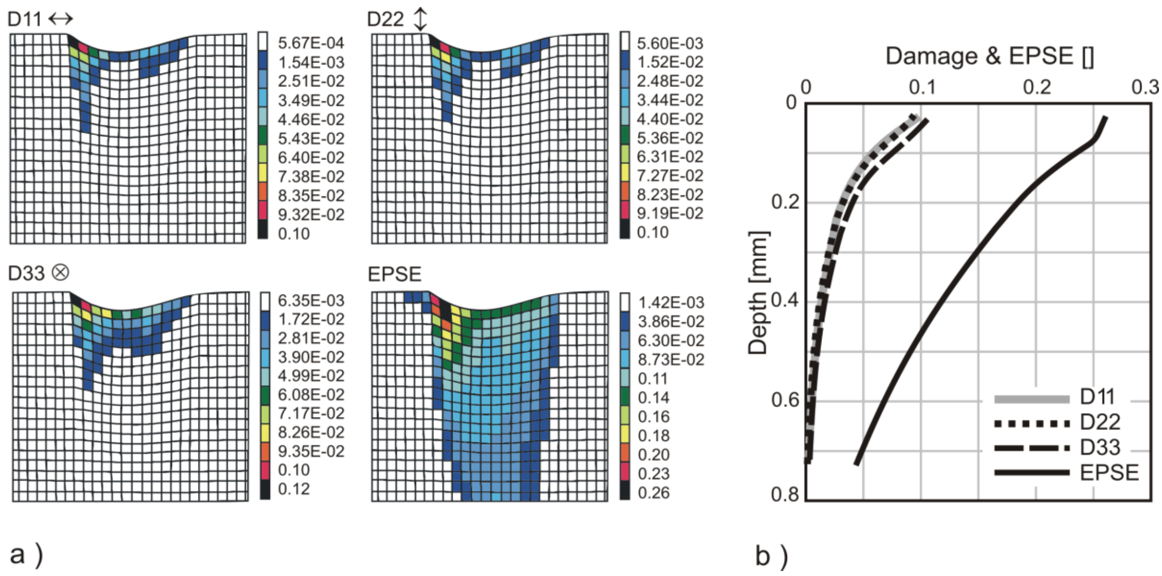

Figure 82 : Isotropic results: a; Distribution of micro-damage (D11, D22, and D33) compared to evolution of plastic strain intensity (EPSE), b; Evolution of micro-damage components as a function of depth

In principle, D11 indicates a possibility of in-plane damage in the direction tangent to the edge/gasket surface, D22 in the direction through thickness and D33 in the direction perpendicular to the cross-section plane. It is worth pointing out, that the solution obtained carries similar features like the solutions discussed in the previous section. On the other hand, the micro damage fields are localized close to the steep extremity of the knife. This is also the place where the tightness of the UHV system may be compromised. In this region the micro-damage is created rather by the mechanism of shear stress than by hydrostatic stress. Here, the tri-axiality factor is equal to 0.092. In Figure 82 several details of micro-damage evolution in the critical zone of the gasket are presented. In particular, maximum damage occurs on the free surface. This is also the place where macro-crack will be initiated. Also, it is worth pointing out that the active sealing surface, characterized by much smaller micro-damage intensity, becomes the surface of smaller slope. Here, the risk of macro-crack propagation is rather limited. Damage values are around one order of magnitude smaller than for the opposite slope of the knife. Also, the damage origin looks different. Because of high tri-axiality ratio (equal to 1.36) the damage evolution is rather due to hydrostatic than shear stress. For comparison the same problem has been solved by using anisotropic damage material properties. The results are presented in Figure 83.

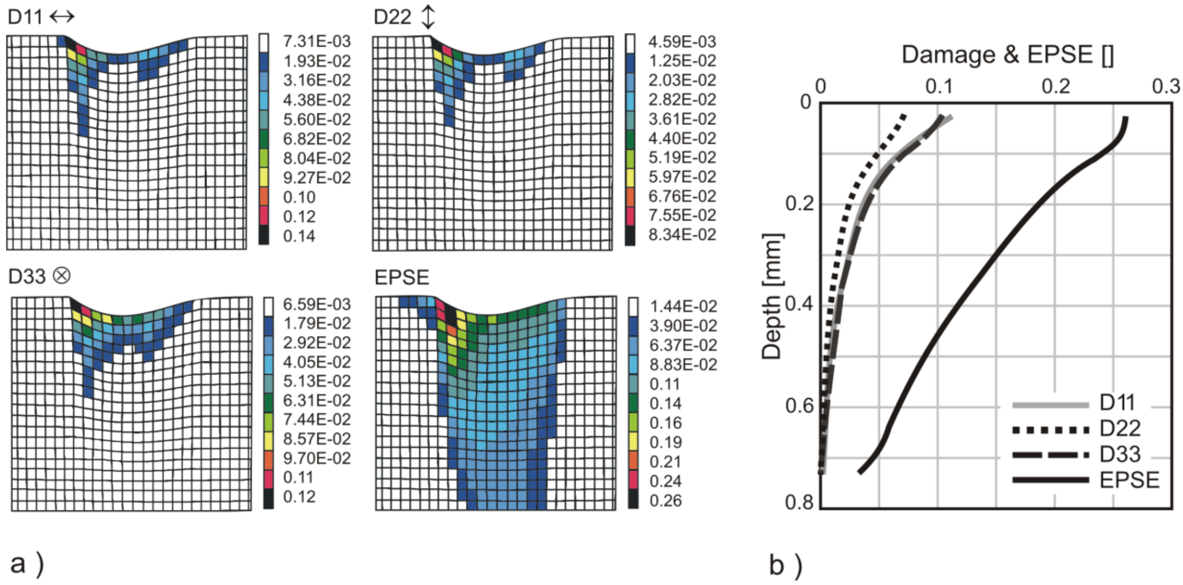

Figure 83: Anisotropic results: a; Distribution of micro-damage (D11, D22, and D33) compared to evolution of plastic strain intensity (EPSE), b; Evolution of micro-damage components as a function of depth

Micro-damage evolution as a function of the compression force in the UHV joint under consideration is presented in Figure 84. During the monotonic loading the micro-damage evolves in three stages. At first, two local damage maxima located on both sides of the knife appear (see Figure 82 and Figure 83). When the sealing slope gets into the contact with the gasket surface, both local damage maxima evolve simultaneously and the damage intensity increases. This process starts when the load reaches some 80kN. Both local maxima reach the same level in terms of damage intensity for the load equal to 117 kN. Above this value one damage maximum starts dominating and the damage intensity grows much faster. In Figure 84 this stage corresponds to the load ranging roughly from 117 to 140 kN. Further rapid damage growth is related to the plastic zone spreading over the entire thickness of the gasket and to the mechanism of coalescence of micro-cracks and micro-voids.

Damage evolution as a function of the compression force in the joint is presented in Figure 84. During the monotonic loading the micro-damage evolves in three stages. At first there are two local damage maxima located on both sides of the knife edge. They have the same damage intensities and are accompanied by nearly symmetrical damage fields. This stage can be observed in Figure 84 for the force smaller than 117 kN. When the sealing slope comes into the contact with the gasket surface, one local damage maximum is starts dominating. This stage corresponds to the force value ranging from 117 to 140 kN. Then the third stage appears and the damage intensity grows rapidly. This is certainly related to the plastic zone spread over the entire thickness of the gasket. The probability of macro-crack initiation and propagation becomes very high.

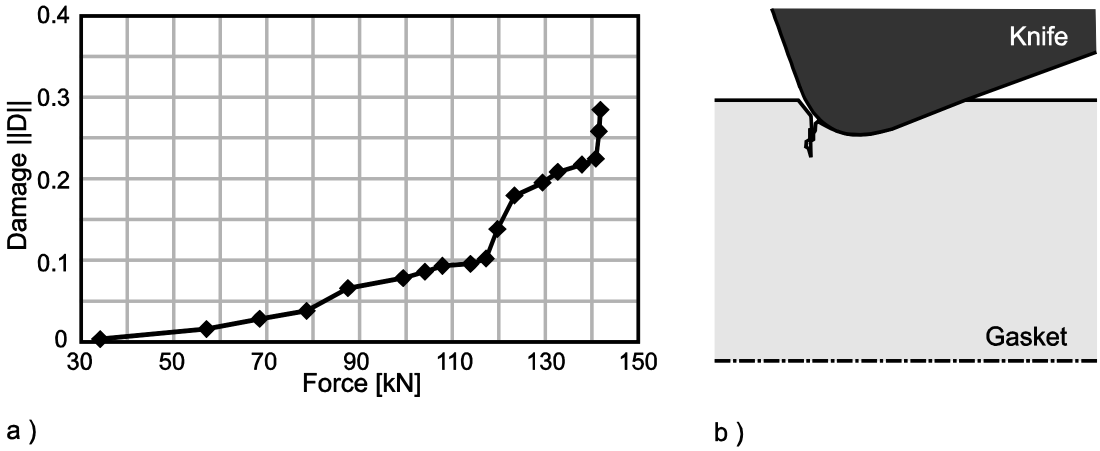

Figure 84 : a; Damage evolution as a function of the joint compression force, b; prediction of macro-crack propagation

Although localization of the crack onset has ben experimentally validated the critical load equal to 91 kN seams to be too conservatively predicted (see section 3.1.5). In the so-called CF joints (CERN, 120 mm seal diameter) small cracks have been recorded in the knife region for fully loaded joints (140-180 kN). In the light of this fact, an additional criterion based on the damage/force diagram (Figure 84) and related to fast increase of damage parameter as a function of force might be used. Indeed, for the load exceeding 140 kN the value of dD/dF substantially increases, which can be interpreted as an acceleration of micro-damage evolution at a nearly constant load. Such effect corresponds to the process of energy release without significant increase of load and – from the point of view of micro-mechanics – to the phenomenon of coalescence of micro-cracks and micro voids accompanied by formation of a macro-crack. Using such criterion brings the prediction of the macro-crack onset much closer to the experimentally confirmed critical load values. A similar criterion was used also by other authors (cf. Nahshorn and Xue [87]).

In the light of the above presented analysis the following algorithm leading to a better prediction of macro-crack onset is proposed (cf. Lutkiewicz et al. [78]):

- Experimental identification of the critical damage value in one-dimensional case (see section 3.1.5) for a given material and for a given temperature,

- Estimation of the critical value of damage parameter in 3-D case (see section 3.1.5) including the triaxiality function,

- Verification of the criterion $\left\| \underline{\underline{D}} \right\| = D_{cr}$ (see section 3.1.5) and estimation of the lower bound for critical load (in the present case 91 kN),

- Cross-check of the computed critical load with the damage/force diagram obtained by means of FE analysis,

- Identification of the load for which dD/dF tends to infinity (upper bound for the critical load; in the present case some 141 kN),

- Cross-check of the lower and the upper bounds for critical load with the experimentally confirmed values (complementary metallurgical analysis),
- Final identification of the critical load for a given type of UHV seal (geometry, configuration), material and temperature (in the present case - 140 kN).

It is worth pointing out that the critical load identified on the basis of the above presented algorithm represents high probability of macro-crack onset and does not lead to instantaneous failure (decohesion) of the material. In the context of ultra-high vacuum systems it should be rather regarded as an imminent step to loss of tightness in the system. Finally, a good correlation of numerically computed and experimentally identified critical load values constitutes a solid basis for further design and optimization of the configuration of UHV joints.

The results clearly indicate high probability of formation of micro-damage fields close to the steep extremity of the edge, regarded as rigid punch interacting with elastic-plastic foundation. The opposite extremity with smaller slope does not induce high intensity damage fields and plays a role of the so called "sealing surface". However, in view of distribution of all three principal components of damage tensor a macro-crack propagation spoiling integrity of UHV system is highly probable. This conclusion has been confirmed by suitable experimental evidence. In order to obtain a reasonably good estimation of the critical load (contact pressure) representing the onset of macro-crack an algorithm based on the numerical analysis and the experimentally collected data has been developed. The model is capable of predicting the lower and the upper bound for the critical load, which in the context of UHV systems should be understood as the load range creating favourable conditions for the loss of tightness of the seal. The algorithm is currently applied in the design of UHV systems for superconducting particle accelerators.

6.4 The irradiation induced micro-damage

The irradiation induced micro-damage is caused by the particles with the energy high enough to eject the original atoms from their lattice positions. The irradiation level can be measured than by means of the dpa unit which indicates how many times each atom in the lattice was displaced from its initial position (the average value per unit volume, see section 3.2). The irradiation level in the LHC accelerator can be predicted only approximately. Precise measurements have to be carried out during the operation of the collider (Figure. 85).

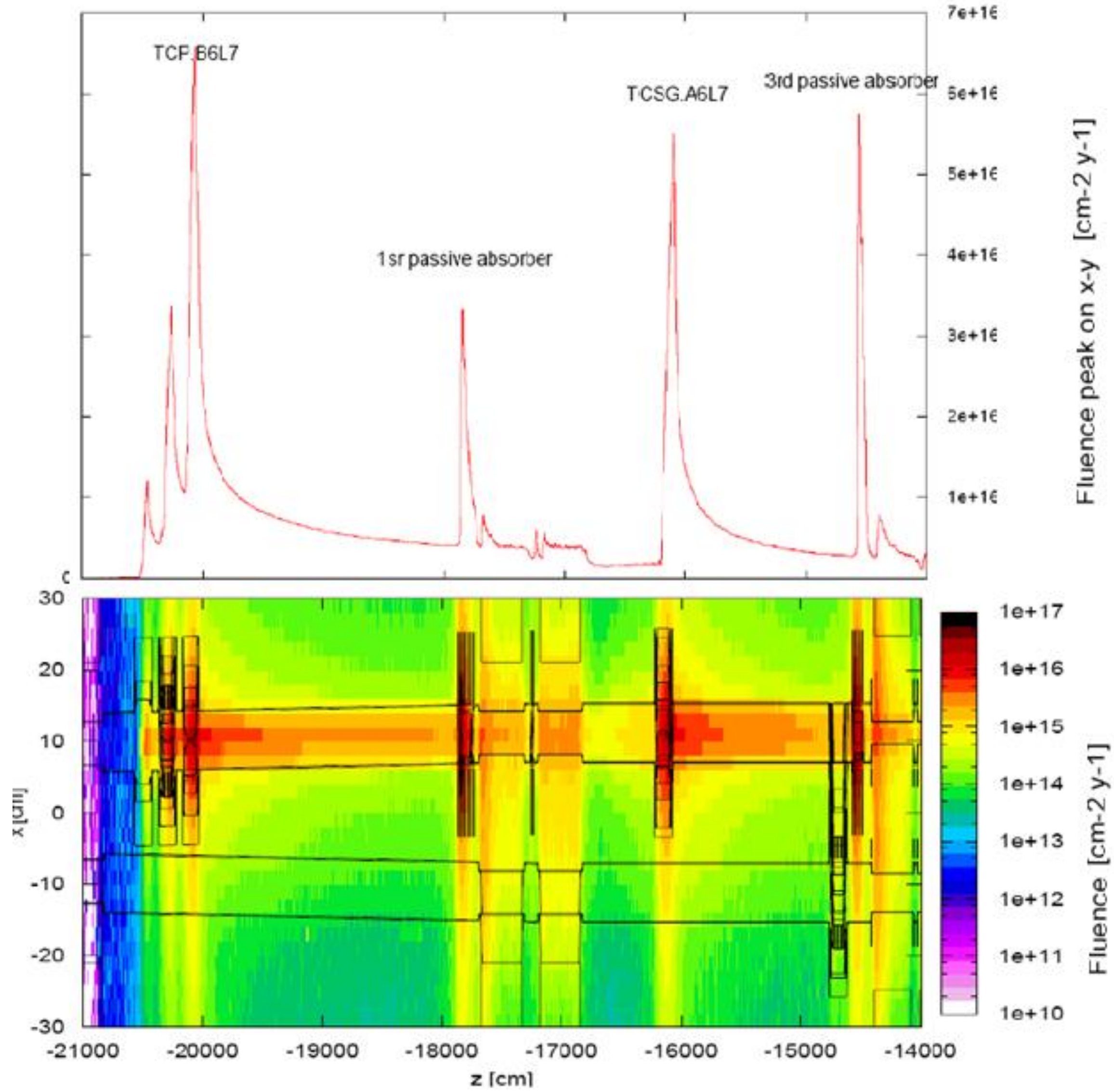

Figure 85 : Radiation dose for most critical section of LHC accelerator

Maximum value of radiation dose expected in the LHC is equal to about $6.5x10^{16}$ and corresponds to the TCP.B6L7 collimator flange. The experiment is planned to be 10 to 20 years in operation. It leads to the total flux of 10^{17} to $1.3x10^{18}$ neutrons cm^{-2}. This corresponds roughly to about $6x10^{-5}$ to $8x10^{-4}$ dpa value. This value can be much higher because of the extremely strong synchrotron light creation. In such a case, the photons carry so high energies that they can act as an additional source of atoms displacement in the material lattice. The irradiation can be much higher for other nuclear plants (like ITER). It can easily reach even several dpa units. Because of these facts, all results are presented for several dpa doses to cover wide spectrum of possibilities in the Thesis. Copper (gasket material) has lower resistance against irradiation and shows rather high plastic deformation when compared to the knife, which acts more like a rigid body. Based on the dpa value it is possible to predict the number of interstitial atoms and vacancies produced in the material. Moreover, it is possible to predict how many of them will be integrated to form the clusters. The clusters themselves can be treated as micro-voids (see section 3.3).

6.5 FE calculations and results

Finite element (FE) analysis involves a 2D model loaded in-plane and keeping the axial symmetry conditions. For the sake of simplicity, the model consists of the seal and rigid knife only. The knife penetrates the soft seal and the tightness conditions are obtained by means of plastic flow under contact pressure acting between both components. However, large plastic deformations can spoil integrity of the seal and create favourable conditions for gas molecules flow through the gasket material. In addition to mechanically induced creation of micro-cracks, in the accelerator environment the irradiation and postirradiation micro-damage appears. The FE model is capable of taking into account both damage evolution mechanisms presented in the previous sections.

Different irradiation levels (0.001, 0.01, 0.1, and 1.0 dpa) were studied at room temperature and in the cryogenic conditions. The results for 0.01 dpa will be presented mostly, which corresponds roughly to the accelerator conditions.

In the FE model the entire joint is exposed to the same dose, therefore the irradiation damage is uniformly distributed. The irradiation damage parameter corresponding to different irradiation levels is presented in Figure 86. The irradiation damage exhibits saturation for the doses higher than 0.1 dpa. This effect corresponds well to the D_S threshold, indicated in eq.141. Moreover, similar saturation threshold can be found in the yield point diagram (Figure 86).

It is worth pointing out, that doses close to or above D_s creates similar contribution to total damage production. Also, the radiation induced yield point increment ($\Delta\sigma_y$) for copper is significant, even for low dose values (14 MPa for 10^{-5} *dpa*).

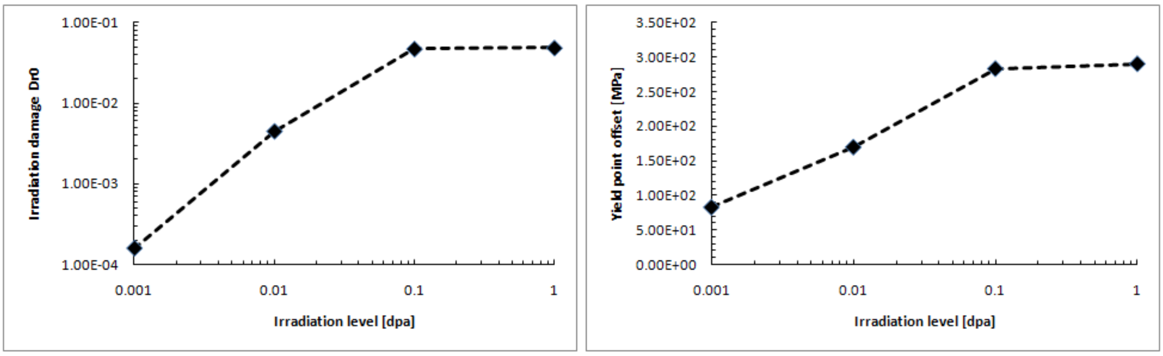

Figure 86 : Irradiation damage Dr_0 and yield point increment $\Delta\sigma_y$ as a function of irradiation level

The mechanical load is applied to the irradiated material of the seal. The knife penetrates the seal to the depth of 0.15 mm. Both damage parameters (post-irradiation and mechanical) increase in the proximity of the contact area (Figure 87), driven by the accumulated plastic strain.

It is worth pointing out, that deeper penetration of the knife (up to 0.15 mm) causes strong localization of micro-damage, especially of the postirradiation component. Moreover, both the maximum of mechanical damage and the maximum of postirradiation damage are shifted with respect to the seal surface by some 0.1 mm. This corresponds well to the Hertz solution of a contact problem.

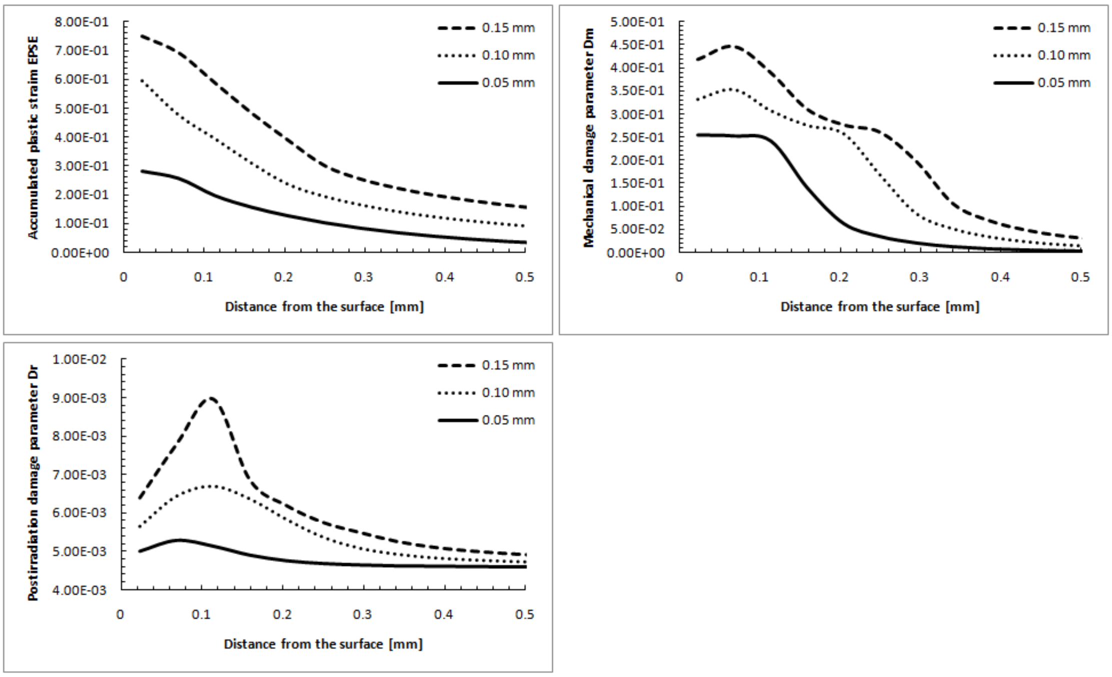

Figure 87 : Accumulated plastic strain, post-irradiation damage *Dr* and mechanical damage *Dm* as a function of distance from the surface (the "through the thickness" direction). Irradiation level is equal to *0.01 dpa*; temperature *T=4.2K*

Distribution of the accumulated plastic strain, the mechanical damage and the post-irradiation damage along the contact zone is illustrated in Figure 88. Both damage parameters are strongly correlated to the accumulated plastic strain and reach their maximum in the region where the plastic strains are the highest. Double peak observed in the plots of accumulated plastic strain and micro-damage is due to double slope in the configuration of the knife. In the zone of higher slope (left hand side) strong tensile stresses appear. Just under the knife tip tri-axial compression exists. On the right hand side of the knife tip (smaller slope), uniform compression assures correct mechanism of keeping the tightness in the joint. It is worth pointing out, that the post-irradiation damage is located mainly in the narrow region of higher slope (Figure 88).

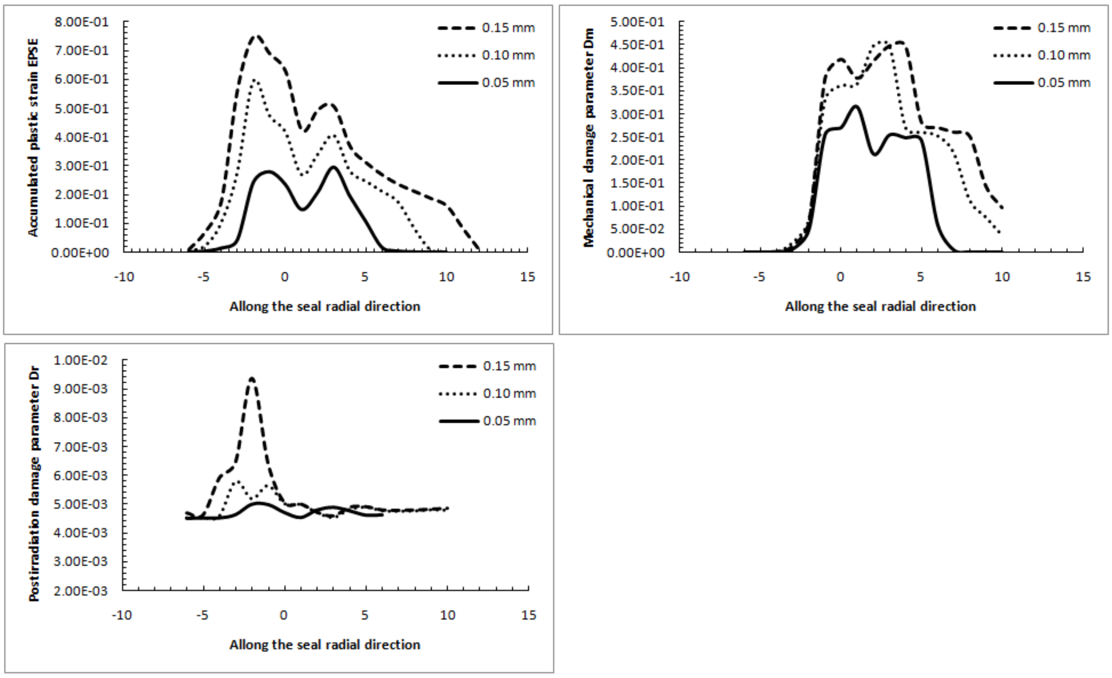

Figure 88 : Accumulated plastic strain, post-irradiation damage *Dr* and mechanical damage *Dm* along the knife/seal contact interface. Irradiation level is equal to *0.01 dpa*; temperature *T=4.2K*

On the other hand, in the case of mechanically induced damage (driven by the accumulated plastic strain) much wider region under the knife is critical (Figure 88). The profiles of postirradiation and mechanical damage parameters corresponding to different depths under the contact surface are shown in Figure 89.

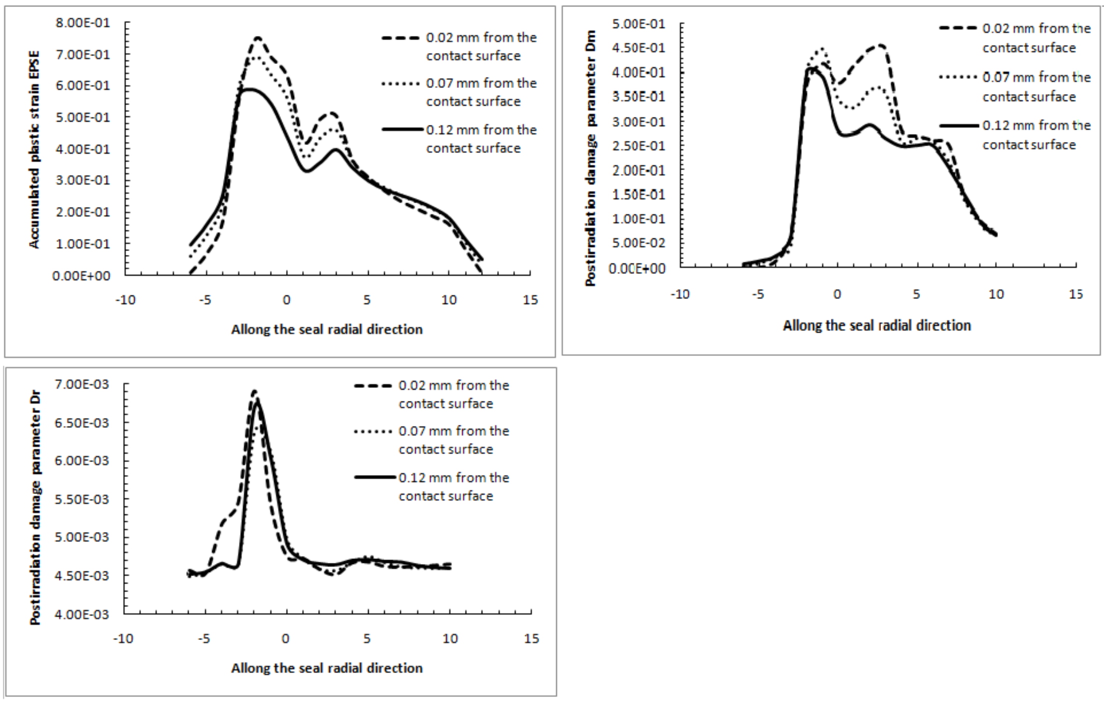

Figure 89 Accumulated plastic strain, post-irradiation damage *Dr* and mechanical damage *Dm* at different depths under the contact interface between the knife and the

seal. The knife imprint depth equal to *0.15 mm*. Irradiation level is equal to *0.01 dpa*; temperature *T=4.2K*

Individual damage components and their sum for moderate irradiation level of 1 dpa are shown in Figure 90. The maximum post-irradiation damage corresponding to 1 dpa is equal to 0.077 whereas the mechanical component is equal to 0.524. Thus, the contribution of post-irradiation damage amounts to some 15% of the plastic strain induced damage component. Consequently, the radiation induced damage can not be neglected and brings a significant contribution to dissipation of energy in the material subjected to loads beyond the yield point.

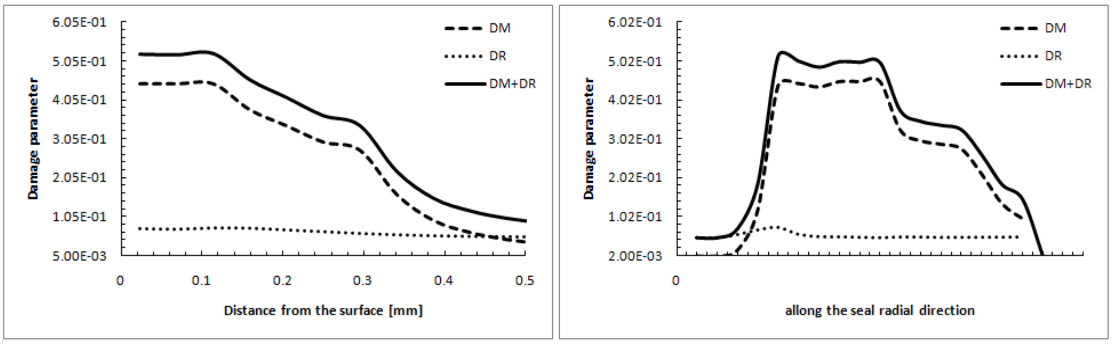

Figure 90 : Mechanical damage *Dm*, postirradiation damage *Dr* and their sum (*Dm+Dr*): (a) along the most critical path through thickness; (b) along the knife/seal contact interface. Imprint depth is equal to *0.15 mm*; irradiation level is equal to *1 dpa*; temperature *T=4.2K*

Another important issue is related to the influence of temperature. It turns out that the material behaviour is strongly temperature dependent. The yield point increases by some 75% at 4.2K, when compared to room temperature. Also, the hardening modulus becomes function of temperature. Generally, the accumulated plastic strains as well as both damage components are much higher at room temperature. A comparison of damage components D_m *and* D_r along the most critical path through thickness, for two temperature levels: 293 K and 4.2 K, is shown in Figure 91. Similar plot corresponding to the knife/seal contact interface is presented in Figure 92.

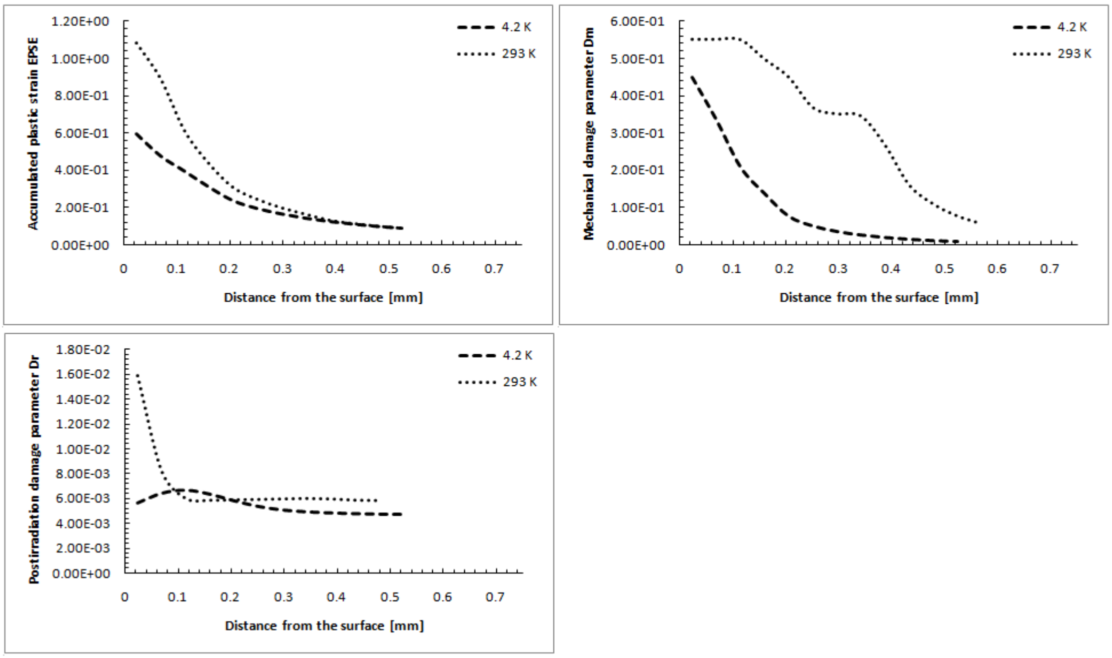

Figure 91 : Accumulated plastic strain, post-irradiation damage *Dr* and mechanical damage *Dm* along the most critical path through thickness, for two temperature levels: *293 K* and *4.2 K*. Knife imprint depth is equal to *0.1 mm*; irradiation level is equal to *0.01 dpa*

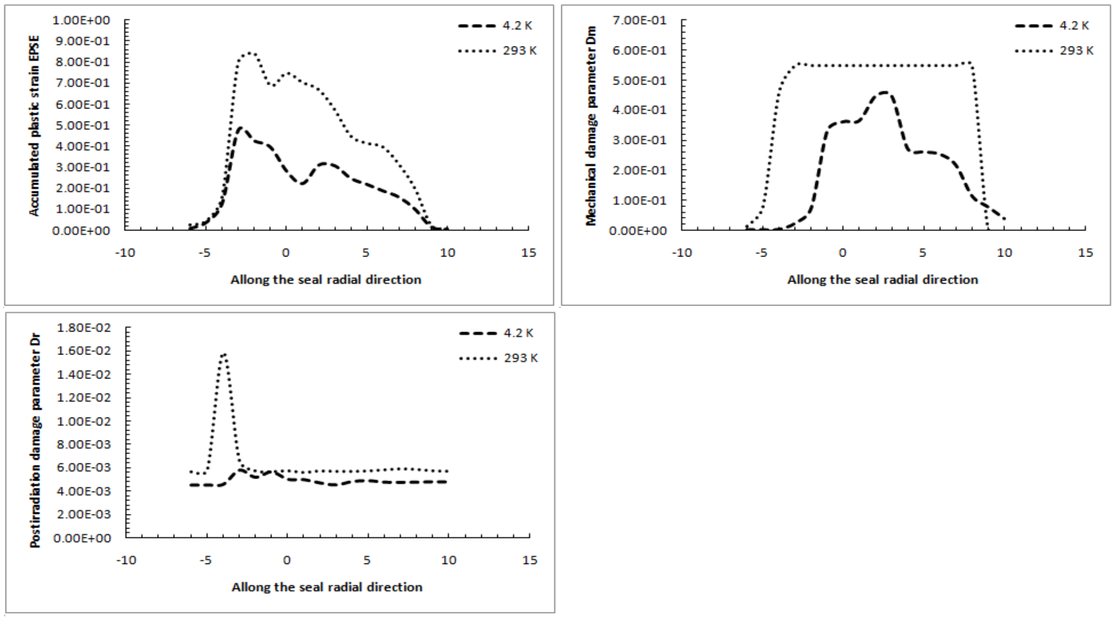

Figure 92 : Accumulated plastic strain, post-irradiation damage *Dr* and mechanical damage *Dm* along the knife/seal contact interface for two temperature levels: *293 K* and *4.2 K*. Knife imprint depth is equal to *0.1 mm*; irradiation level is equal to *0.01 dpa*

However, it should certainly be underlined that in case of irradiation damage the same particle flux can create higher dpa level at cryogenic temperatures when compared to ambient conditions. This is because of the defects recombination effect, which increases at higher temperatures (Figure 45). The ratio of clusters of defects left after recombination at the temperatures close to absolute zero is equal to some 30%, whereas at ambient temperature the ratio of surviving defects reaches 10% only.

A ductile material subjected to flux of particles of sufficiently high energy suffers from formation of local defects in the form of clusters of Frenkel pairs. The volume fraction of clusters of defects decreases after the so-called recombination effect (Figure 45) and the remaining fraction is highly temperature dependent. The remaining defects can be described as some sort of porosity coexisting with the classical defects like micro-cracks and micro-voids of mechanical origin (Figure 41). The evolution of classical defects is described by the Continuum Damage Mechanics (CDM), whereas the evolution of radiation induced defects has to be described rather in the framework of theories related to porosity of materials. In the case of micro-cracks and micro-voids induced by inelastic strain fields the so-called ductile damage mechanics offers suitable kinetic laws of damage evolution. On the other hand, in the case of radiation induced damage fields evolving under the mechanical loads the Gurson type description appears more relevant. Assuming the coexistence of mechanically induced micro-damage fields and the fields of defects induced by radiation, both the kinetic law of evolution of Lemaitre-Chaboche type and the kinetic law of voids growth of Gurson type are applied. It is worth pointing out, that in the present chapter interaction between the mechanically and radiation induced damage fields is not taken into account (mainly because of lack of experimental evidence). On the other hand, the evolution of both fields coexisting in the same RVE is induced by plastic strains related to the mechanical loads applied to the material. Moreover, both damage fields are regarded as isotropic and total damage parameter is constructed in an additive way as a sum of damage parameters individually related to different fields. Such approach allows detecting localisations where the total damage intensity reaches critical level and the conditions of macro-crack propagation are satisfied.

Chapter VII:

Experiments

7 EXPERIMENTS

Experiments were performed for two main reasons. First reason was related to identification data used in the FE calculation. The second reason was related to cross-check of the results of FE calculations and to verification of response of components in real environment. Experiments and measurements were also performed to understand the influence of imperfections on the components behaviour. It can help to clarify the difference between the FE calculated perfect behaviour and the actual response.

7.1 Specification of material properties

At first the material properties were defined. The experiments were focused on the gasket material. The tensile tests were performed in order to identify the elastic-plastic and damage parameters. The experiments were carried out both at room and at cryogenic temperatures. Additionally, the tests were performed on the samples subjected to thermal treatment (24hours at 300°C) which simulates the bake-out process.

7.1.1 Cryogenic temperature

For all calculations the material properties were set for OFE copper at cryogenic temperatures (4.2 K). The tests were performed on the standard bar tensile specimens with 3mm wide quadratic cross-section. The specimen length was equal to 14.2 mm (see Figure 93). Tensile testing machine UTS 200 (1995) was used (see Figure 94).

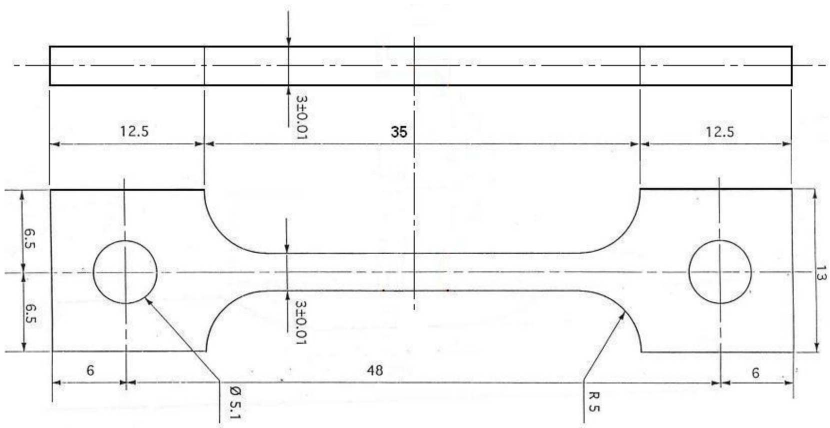

Figure 93 : The specimen dimensions for tensile tests

The instrumented specimens (temperature sensors, internal load cell, LVDT transducers (see Figure 94) were installed in the cryostat located in the tensile machine. The stroke speed was set to 0.025 mm/s and the sampling frequency was equal to 20 Hz. The temperature was stabilized at 4.2 K by a suitable connection with the liquid helium source.

Figure 94 : The tensile/compression machine, cryostat and liquid helium

The tensile tests were performed with 12 unloading steps. For strains equal to 0.175 and 0.320 the unloading was complete, down to zero stress, and recalibration process took place (displacement range of the extensometer is smaller than the total elongation). The damage evolution was identified by measuring the evolution of elastic modulus for each unloading step. The elastic moduli were defined by taking the linear part of the unloading curve and trimming it about 10% at the top and at the bottom points. Based on these experimental data, the evolution of elastic modulus (Figure 95) was approximated by the 3rd order function (for smoothing reasons). Finally, the damage parameter was calculated and its evolution as a function of plastic strain is presented in Figure 95.

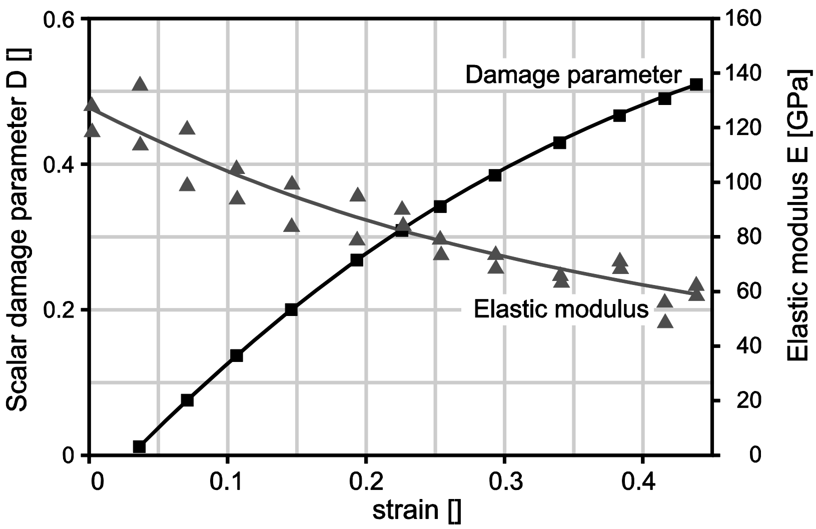

Figure 95 : Damage parameter *D* and elastic unloading modulus *E* as a function of strain at 4.2 K

It is worth pointing out, that the threshold strain has been measured and is close to 0.03. For what concerns the plastic part of the model, the linear hardening was identified by means of the stress-strain curve. The basic material parameters are presented in Table 13.

Table 13 Parameters of the material model (isotropic/anisotropic* damage)

E [GPa]	σ_0 [MPa]	*H* [MPa]	p_D	*S* [MPa]	C_{11}	C_{22}	C_{33}
127.3	370	975	0.03	11.1	0.3 0.33*	0.3 0.27*	0.3 0.3*

Because of lack of suitable experimental data, the damage parameters for anisotropic model were estimated by taking into account the gaskets production process (rolling). The gaskets are produced from copper plates. The rolling process induces different material properties in each principal direction. The length of grains is expanded in the rolling direction and is significantly reduced through thickness. This phenomenon is enhanced close to the gasket surfaces in the so-called surface layers. Based on this observation the principal components of tensor of material properties ($\underline{\underline{C}}$) were estimated (Tab. 1). Generally, the micro-damage is expected to propagate faster in the direction of grains expansion and slower in the direction through thickness.

7.1.2 Room temperature – first setting

Tensile tests were performed on specimens made from OFC copper. Two specimens (bar shaped) were cut from the gasket using electro-erosion. Gasket was manufactured by stumping and after machining from the rolled plate (standard producing process). The average dimensions were as follows: length of 26.5 mm, height of 2.0 mm and width of 2.18 mm. Those bars were composed into standard tensile test specimen shape by welding the heads on both sides (Figure 96).

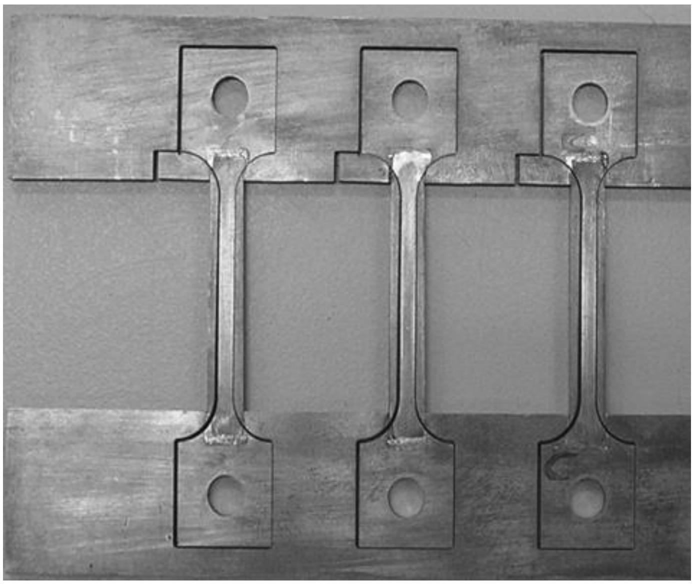

Figure 96 : Specimens for tensile tests

For the measurements a tensile testing machine UTS 200 (1995) was used. The maximum force capacity was equal to 200 kN and the displacement precision was of 1 µm. The machine was controlled by a processor and force and displacements were registered. The elastic modulus E, yield point σ_{02} and tangent hardening modulus H were determined. The hardening modulus H was specified as secant value between two points with 0.03 and 0.045 strain values. The results are presented in Figure 97.

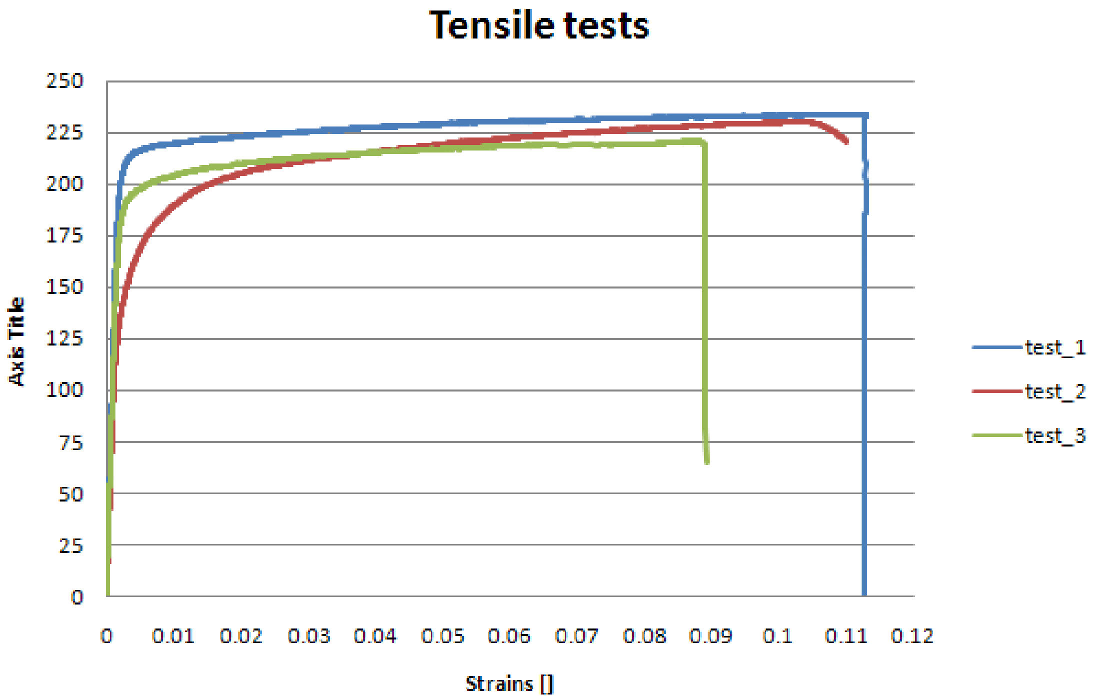

Figure 97 : The tensile test results – stress - strain curves

During the test the differences related mainly to the yield point value were observed. The maximum yield point value was equal to 214.2 MPa whereas the minimum value was about 156.5 MPa. Also, the maximum elongation was different for each sample. It varied from 8.64% for 3rd specimen up to 11.13% for 1st one. All material data are collected in Table 14.

Table 14 Elastic and plastic parameters of tested material

Sample no.:	**1**	**2**	**3**
$R_{p0.2}$ [MPa]	214.2	194.4	156,5
R_m [MPa]	234.0	230.0	220.0
H [MPa]	203.0	209.0	321.0
E [GPa]	133.0	116.3	100.8
A [%]	11.13	8.64	10.30

The samples were cut from the same seal but they were oriented differently w.r.t. rolling direction. The anisotropic properties were expected to be the main reason of difference in the material parameters.

7.1.3 Room temperature – second set

To check the anisotropic properties the additional tests were run. The row material was extracted from the samples provided by the CERN ConFlat supplier. From each square plate (200x200 mm) two standard tensile specimens were cut to represent the rolling (RD) and the transversal (TD) directions. Also the ConFlat standard seal was cut from each plate (see Figure 98).

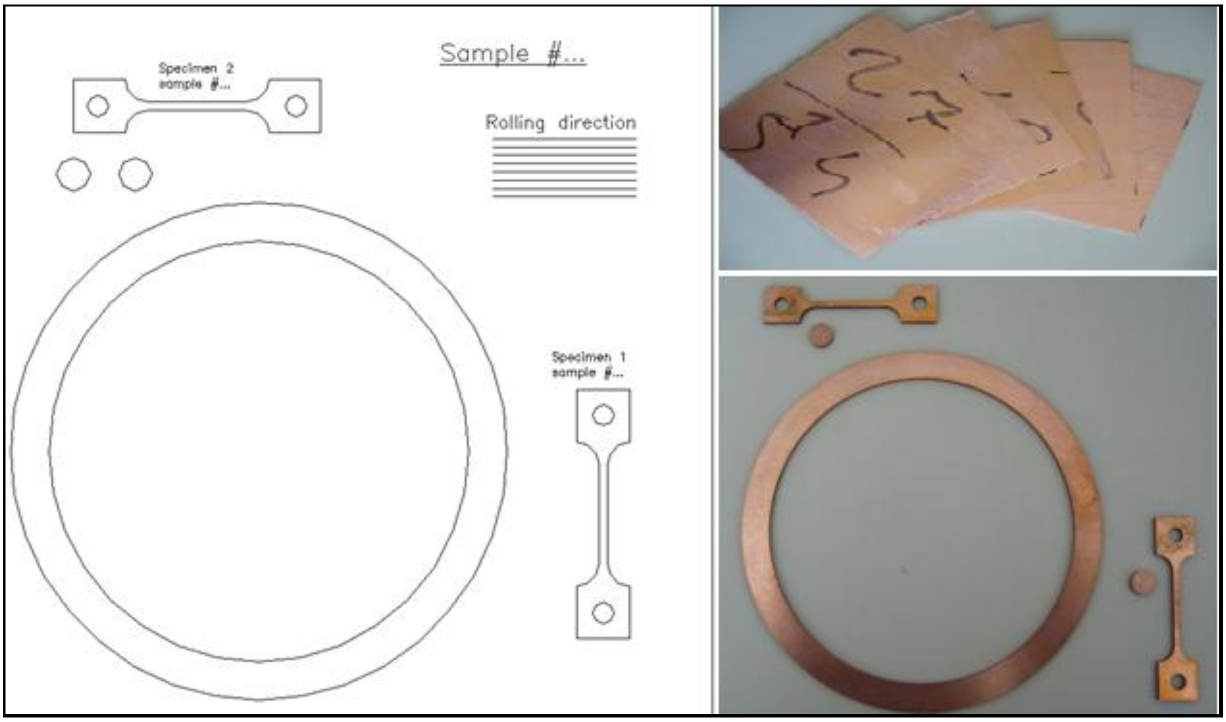

Figure 98 : Preparation of the specimens

The tests were performed by using the specimens representing two different directions. The specimens with RD labels represent the material properties in the rolling direction (they were cut out in this direction from the copper plates). In the same way the specimens with TD labels represent the material properties in the direction perpendicular to the rolling direction (they were cut out in the transversal direction from the copper plates). The tensile test results are plotted in Figure 99 for RD direction and in Figure 100 for TD direction.

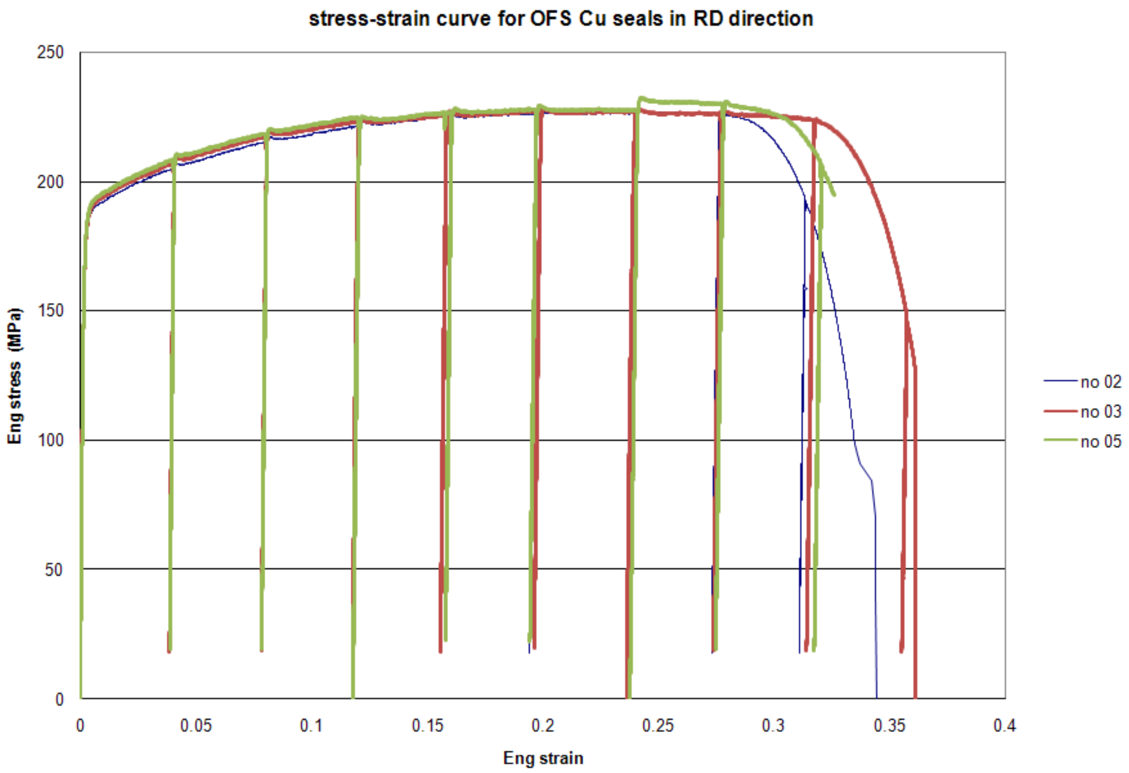

Figure 99 : The tensile tests for the specimens in the rolling direction

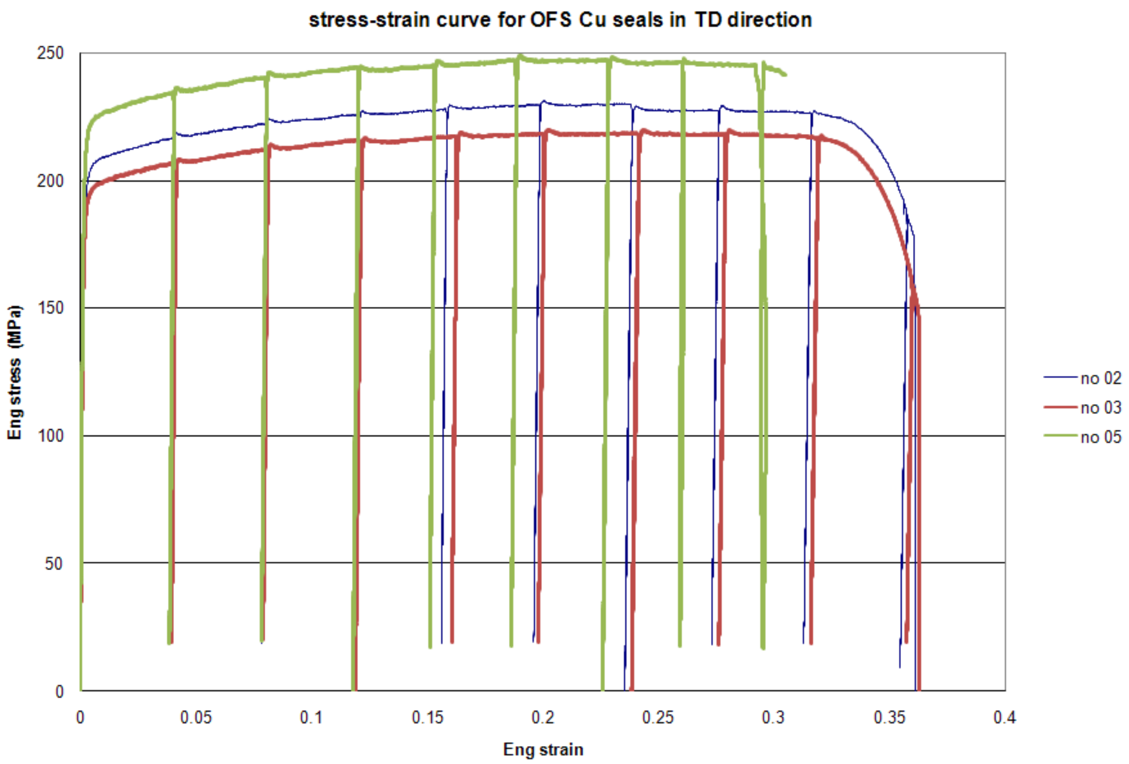

Figure 100 : The tensile test for the specimens in the direction perpendicular to the rolling direction

The material properties for both direction (RD and TD) are collected in Table 15. The collected data constitute the elastic and the plastic material parameters. The hardening modulus H was specified as the secant value between two points with 0.05 and 0.25 strain values, respectively.

Table 15 Elastic and plastic material properties

Sample no.:	Direction RD			Direction TD		
	01	02	03	01	02	03
$R_{p0.02}$ [MPa]	197	200	200	212	202	229
R_m [MPa]	292	294	295	298	285	317
H [MPa]	343	344	344	362	335	369
E [GPa]	128	124	122	154	142	158
A [%]	0.29	0.32	0.30	0.32	0.32	0.30

In order to identify the evolution of damage parameter all tests were accompanied by several unloading cycles for different strain values. The purpose of this operation was to identify evolution of the elastic modulus during the unloading. The elastic modulus is lower for higher strains which is a direct result of micro-damage evolution. The drop of the modulus of elasticity depends linearly on the strain value. This evolution is shown in Figure 101.

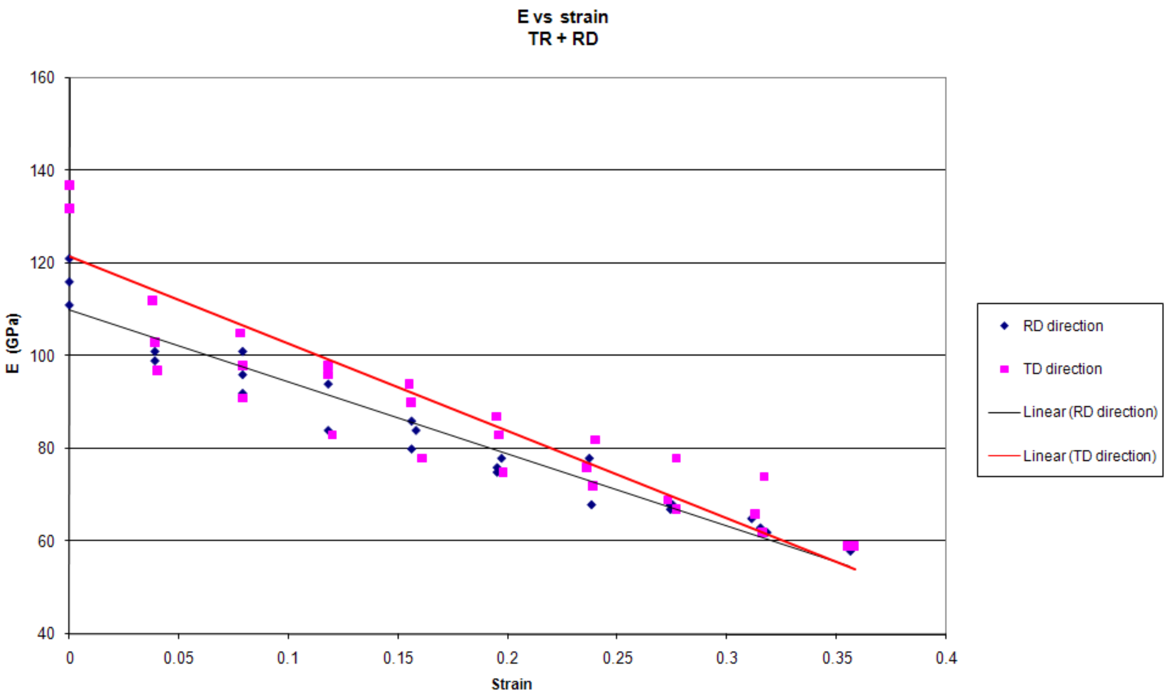

Figure 101 : Evolution of the elastic modulus

Evolution of the elastic modulus in both directions is similar. For the strain value close to the maximum elongation there is about 40% drop. It corresponds to the damage parameter D equal to 0.5. The material properties related to damage were calculated from the evolution of elastic modulus and are presented in Table 16.

Table 16: The damage material properties

Sample no.:	Direction RD			Direction TD		
	01	02	03	01	02	03
S [MPa]	0.238	0.237	0.246	0.239	0.220	0.279
s []	1.0	1.0	1.0	1.0	1.0	1.0
C []	2.051	2.054	2.017	2.045	2.132	1.892

7.2 ConFlat joint

ConFlat joint is a well known type of UHV connection. It is recognized as a cheap and reliable solution. However there is no information in the literature about its behaviour during the tightening process. In the previous chapters this problem was studied by using the FE analysis and the CDM theory. In the present chapter the experimental study is presented. The experiments are divided in two main sections. In the first section the geometrical measurements of the joint parts (gaskets and flanges) are described. Also, the influence of the manufacturing process (rolling, stumping and machining) on the gasket was investigated. In the second section the joint behaviour during the tightening process was studied. Also, the tightening influence on the gasket material was experimentally measured.

7.2.1 Alignment issues

The alignment between joint parts was studied. For that the gasket flatness the measurements were done before test and the knife shape was measured (before and after tests). Additionally, the manufacturing process induced anisotropy of gasket material was investigated. During this study the grain size/shape observation and micro-hardeners measurements were done.

7.2.1.1 Metallurgical analysis of gasket anisotropy

CF gasket is made from copper plate obtained by the rolling process. The gasket is punched from plate and afterwards it is machined to improve the inside and the outside surfaces. The anisotropic properties can influence strongly the gasket behaviour under the high load made by the flange knife. Because of these facts (production process and anisotropy influencing the joint behaviour) the check of CF Gasket against anisotropy was made. The check was carried out as a two-step process. At first the grain size and shape was measured. The measurements were performed for two gasket cross-sections and, additionally, on the top gasket surface. The examined cross-sections were chosen as perpendicular and parallel to the rolling direction. The grain structure pretends to be the same for all surfaces (see Figure 102).

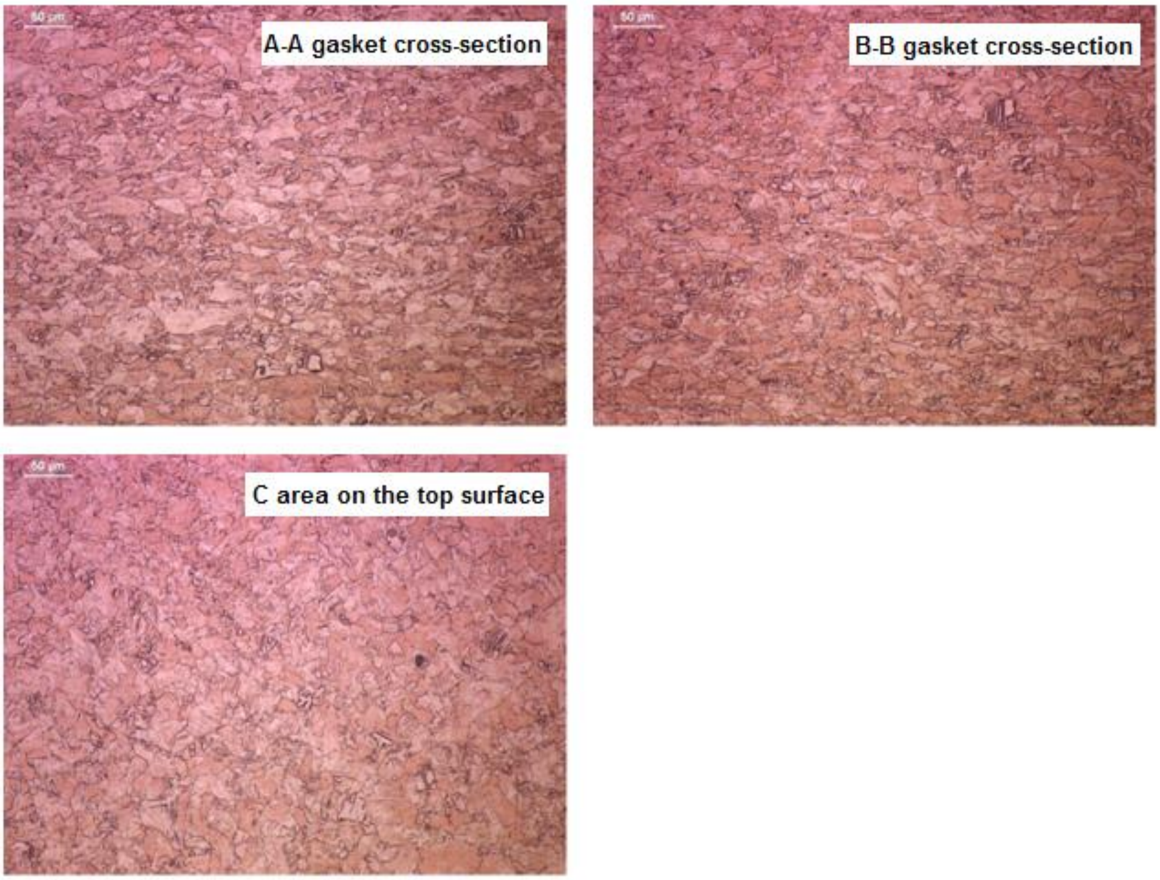

Figure 102 : Grain structure of CF standard gasket

The second step of investigation consisted in the hardness measurements. First the hardness measurements were performed for the top surface of the gasket in the circumferential direction. The measurements were carried out for a quarter of the seal circumference (Figure 103). It corresponds to 90 deg section (from the cross-section parallel w.r.t. the rolling direction to the cross-section perpendicular w.r.t. the rolling direction).

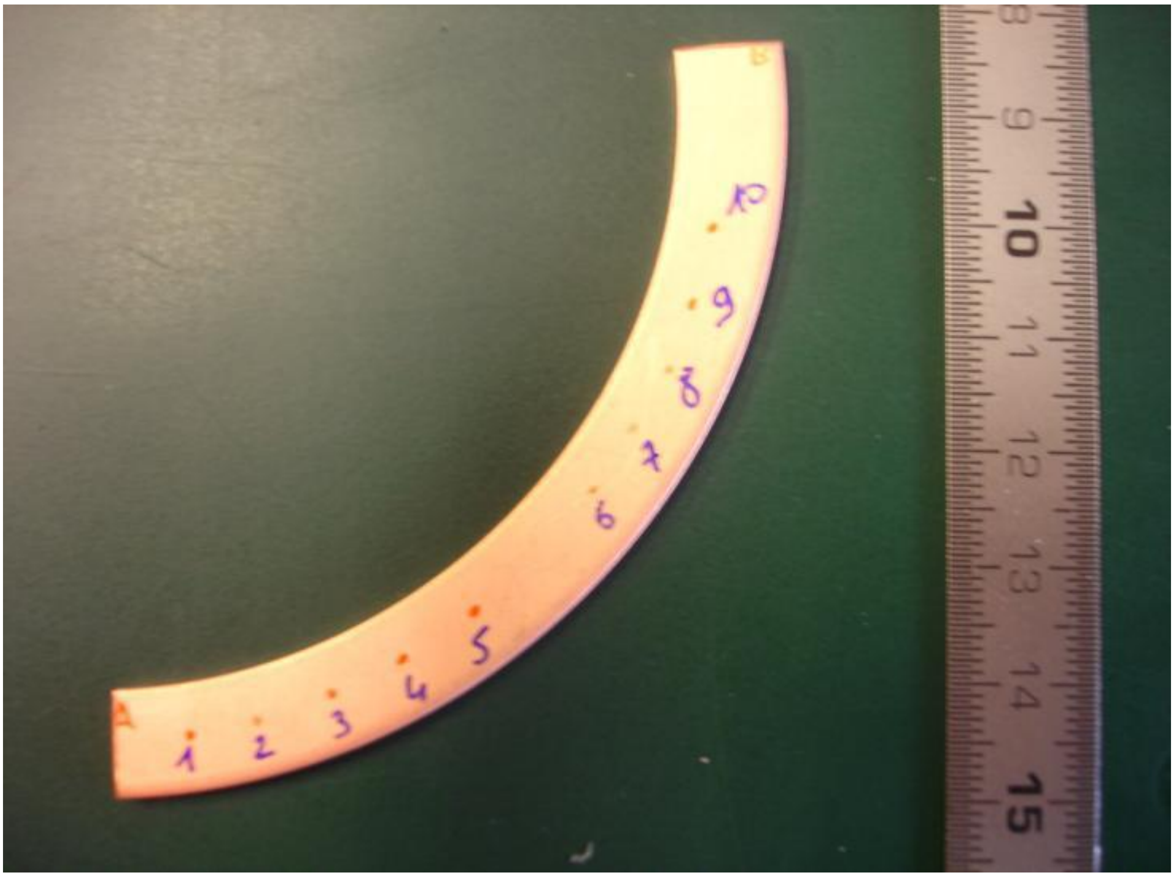

Figure 103 : Setting the points for micro-hardness measurements through the gasket circumference

The results are presented in the Table 17. The maximum value was equal to 126 and the minimum to 95, which makes the difference of 31. No trends or smooth distribution pattern was noticed.

Table 17: Results of micro-hardness measurements along the gasket circumference

Measurements	1	2	3	4	5	6	7	8	9	10
HV0.1	95	112	109	102	126	96	100	98	97	111

The measurements were carried out for A-A gasket cross-section (perpendicular to the rolling direction) following four paths (see Figure 104):

- Across all width in the middle of the gasket thickness
- Through the thickness near the inside gasket surface
- Through the thickness in the middle of the gasket
- Through the thickness near the outside gasket surface

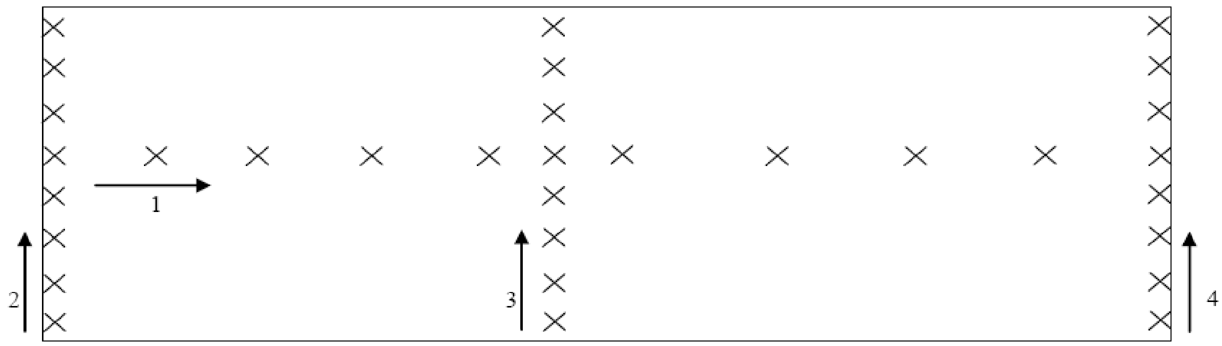

•

Figure 104: Setting the points for micro-hardness measurements through the gasket cross-section

The aim of the measurements was to check if there is any regular, smooth distribution of micro-hardness, which can prove the isotropic properties of the gasket material. The results are collected in Table 17.

Table 18: Results of micro-hardness measurements through the gasket cross-section

Path	Micro-hardness in the measurement points									
	1	2	3	4	5	6	7	8	9	10
1	114	115	107	112	114	106	118	100	109	103
2	110	117	120	123	128	133	143	120		
3	103	121	106	108	114	101	110	114		
4	117	129	119	121	131	132	122	116		

The maximum value was equal to 143 and the minimum to 100, which makes the difference of 43. Also, like before neither visible trends nor smooth distribution were noticed. These tests results lead to the conclusion that the material response is rather isotropic and no direction is preferred.

7.2.1.2 Knife shape measurements

Before and after the compression tests the profile of the flange knife was measured using Mahr Perthen MFU7 contour measuring machine. The measurements were made at the same location of the knife edge (four radial scans on the circumference). No significant changes in profile were observed (see Figure 105).

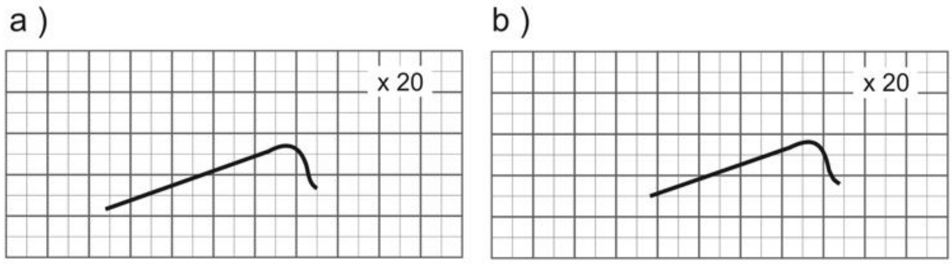

Figure 105 : Contour measurements for flange knife: a) before and b) after joint compression tests

7.2.1.3 Gasket flatness measurements

The flatness of the gaskets was measured before compression tests. Each gasket was supported on three points. The difference between the lowest and the highest profile value was measured and defined as flatness deviation. The measurements were done using a mechanical Mahr Perthen MFU7 form measuring machine (2D profile scanner) with the possibility of 5x, 10x, 20x, 50x, 100x and 200x magnification. The maximum flatness deviation (peak to peak) value measured for ten samples is presented in Table 19.

Table 19: Flatness deviation - peak to peak measurements

Sample no.:	1	2	3	4	5	6	7	8	9	10
Peak to peak deviation [mm]	0.30	0.10	0.04	0.10	0.08	0.04	0.23	0.06	0.10	0.04

7.2.2 Joint behaviour under the load and after tightening

ConFlat joint is known as reliable UHV connection. However compression process has never been studied. How does the joint work? What is the mechanism of leak tightness? What is important and what is not essential for tightness issue? These questions will be answered in the course of experiments presented below.

7.2.2.1 Fitting process verification

To verify the theory which says that at the beginning all joint parts are in contact only locally the experiment was made. Copper gasket was installed between flanges and thereafter compressed with the force of about 1000N and later on, the joint was opened. Gasket surfaces were carefully examined. Small marks made by the knife were found and can be observed in Figure 106. These marks were seen only locally and not in the same places for both gasket sides. This is the influence of the thickness variation and imperfect gasket surface flatness. It confirms that the gasket and the flanges are not in touch at the beginning. The contact is achieved at first only locally and afterwards it expands e all around the joint.

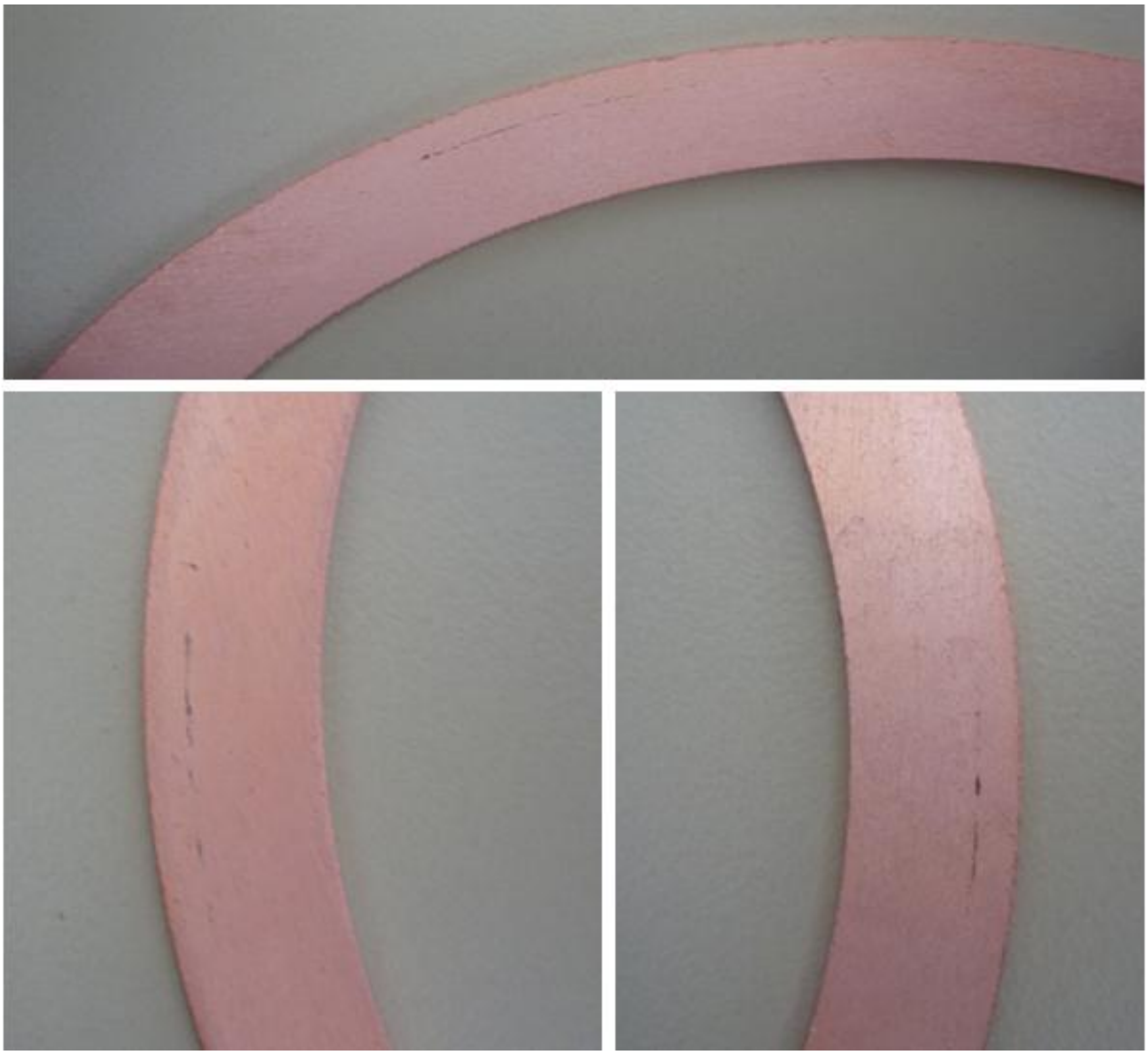

Figure 106 : Knife marks on the gasket surface under 1000N load

7.2.2.2 Joint compression test

Compression tests were performed on CF joints, by using OFS and OFS Ag-coated copper gaskets. The silver layer was maximum 5 µm thick for the coated gaskets. The gaskets were characterized by 101.7 mm inside and 120.4 mm outside diameters and the thickness of 2.0 mm. Two blank stainless steel 316LN flanges were used with the gasket in between them (as shown in Figure 107).

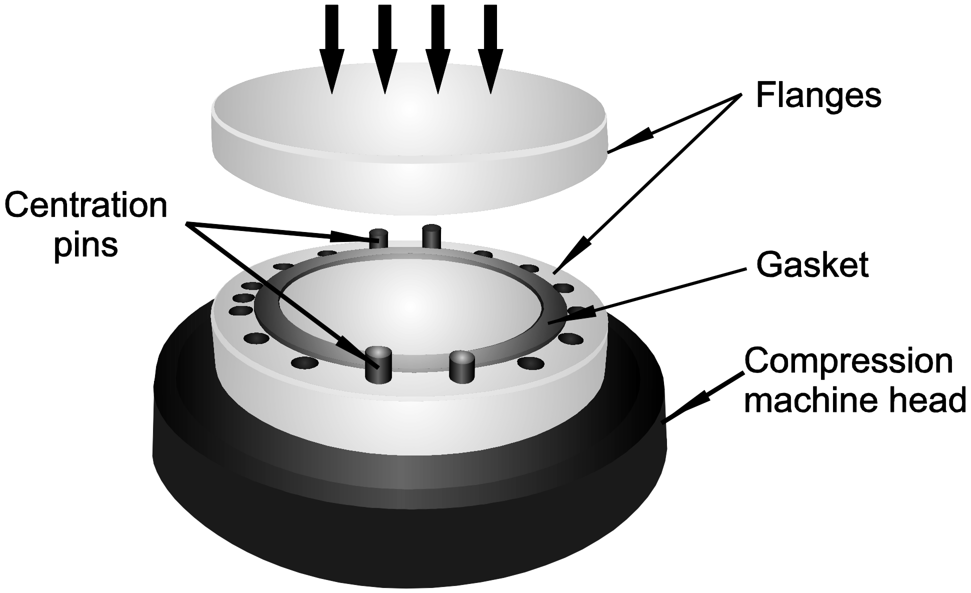

Figure 107 : The compression test setup

Centring was done using four pins. The flanges were machined following CERN standards. The same tensile-compression machine as for the tensile test was used. The results of compression tests are shown in Figure 108.

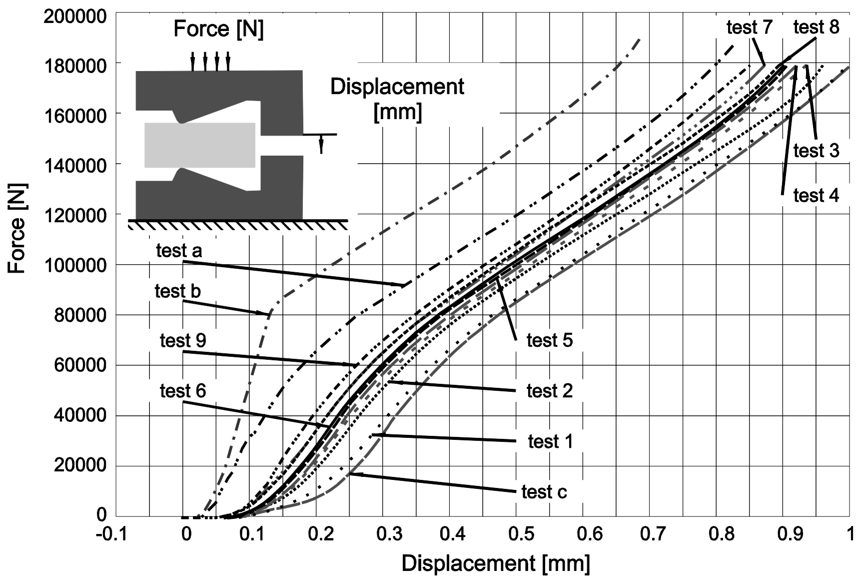

Figure 108 : The results of joint compression test

Compared with the FEM results the evolution of compression force shows an additional flat part at the beginning (usually up to about 0.1 mm in terms of displacement value). Only for test a & b this flat part was shorter (about 0.025 mm). Such behaviour is believed to come from the alignment process between the knife edge and the gasket surfaces. It will be called alignment pre-stage. It is worth pointing out, that in all experimental results the bi-linear behaviour is visible in the curves. There are differences in the slope for the first sealing stage. For these cases with short alignment pre-stage the line describing the first stage has bigger slope than in the other cases. For the tests 1 to 10 a correlation with the results of flatness measurements has been done.

The knife edge imperfections and the assembling precision are supposed to influence the compression force evolution. There is no strict relation between the flatness imperfections and the alignment pre-stage. Flange to gasket alignment has big influence on the first stage, and induced lateral offset for the second stage line, if compared to FE results. The lateral offset between the line which describes the second stage of FE results and experiments remains in the range of 0.15 mm to about 0.35 mm. The slope of the second stage is the same for all samples and for the FE model. The "plastic" stage lines are offset laterally. That comparison is clearly illustrated in Figure 109.

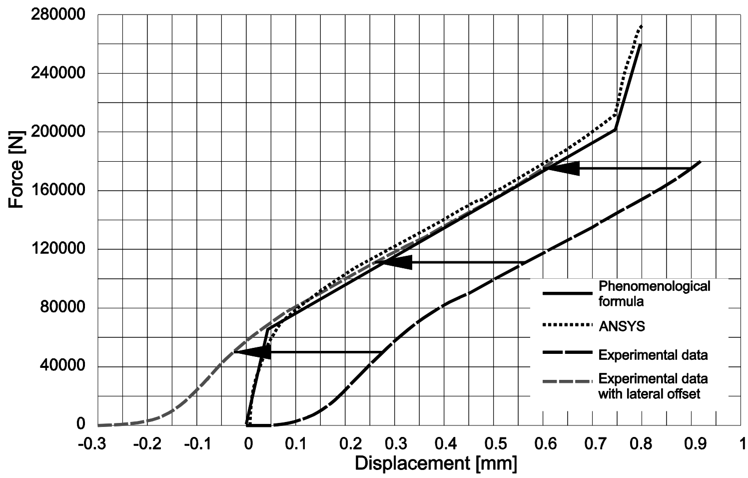

Figure 109: Comparison between the experiments and the FE analysis

7.2.2.3 Leak tightness test

The compression tests were performed four times for the complex joint. The difference w.r.t. the standard compression test setup consisted in the fact that the vacuum between blanked flanges was produced (see schema in Figure 110).

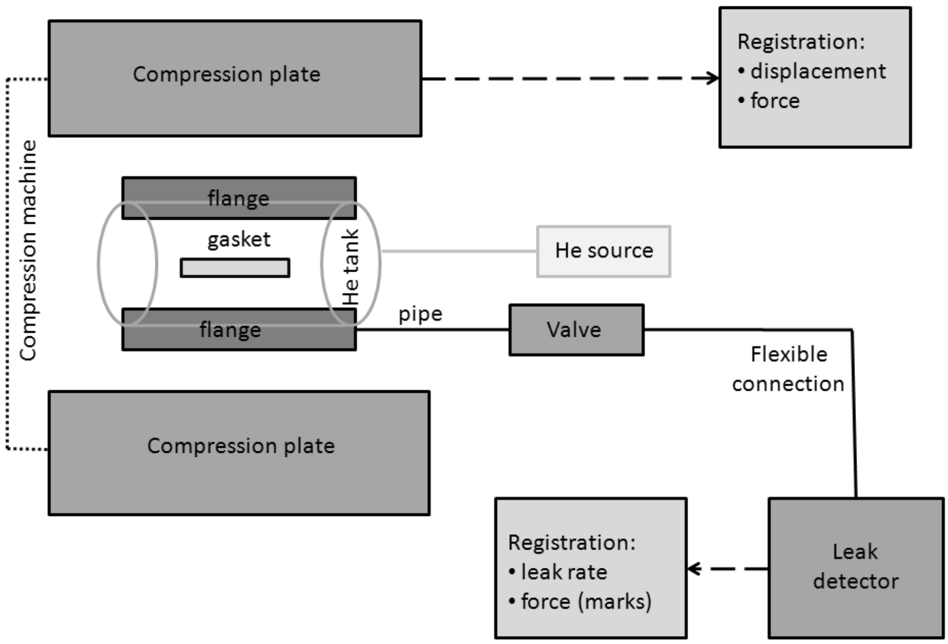

Figure 110 : Test setup schema

Also, the leak detector was connected to the joint for leak rate measurements. The experiment was carried out in steps. Each step consists of the following sub-steps:

- Increment of the force,
- Reading the displacement value,
- Delay for the leak rate stabilization,
- Reading the leak rate for air,
- He implementation into "helium reservoir",
- Delay for the leak rate stabilization,
- Reading the leak rate for helium test,

The force increment was set to 5 or 10 kN. The joint reached stable vacuum for the force value in the range from 10 to 20 kN. The leak rate was decreasing continuously up to certain force value. Afterwards the leak rate drastically fell down to zero (10^{-10}) and the joint got leak tight (Figure 111).

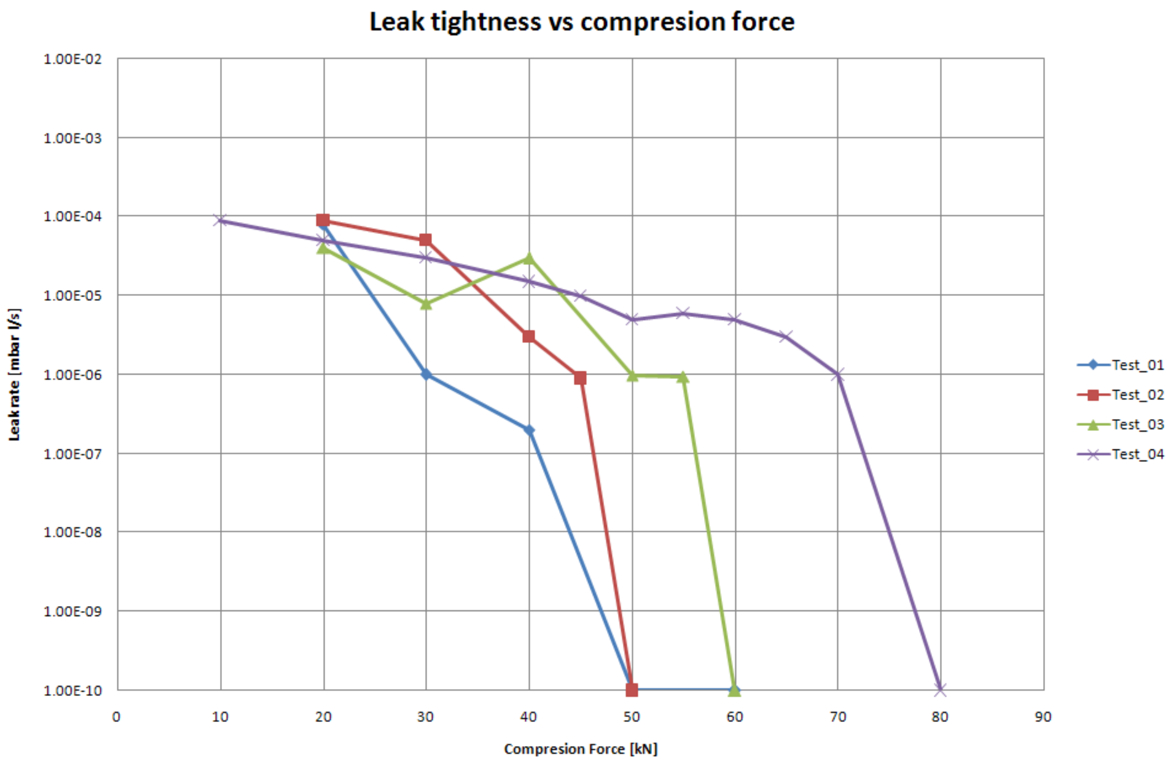

Figure 111 : Leak rate evolution

Compression test was carried out up to the 160kN force value. When comparing the evolution of the compression force (Figure 112) with two-phase sealing process (described in section 4), one finds that the leak tightness is obtained just at the end of the first elastic-plastic phase or at the beginning of the second phase.

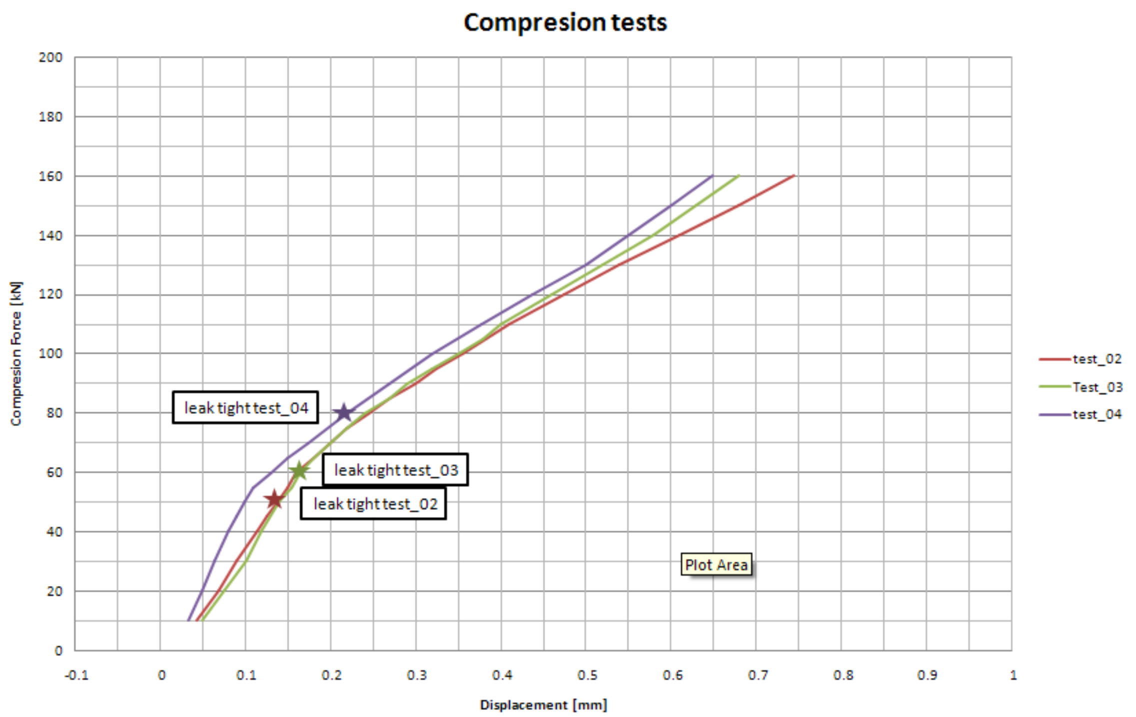

Figure 112 : Compression force evolution

7.2.2.4 Imprint depth measurements

The imprint depth measurements were carried out for two specimens (no. 4 and 5) after the compression test. Specimens 4 and 5 represent the main pattern observed in compression tests (see Figure 108). A Veeco NT3300 contactless, optical 3D surface topography machine was used. Each measurement profile (A, B, C, D) is separated in 90 deg angular steps. The measurements are compared in Table 20.

Table 20: Imprint depth measurements

Samples	Imprint depth [mm]	Profile A	Profile B	Profile C	Profile D
4	Side Up	0.324	0.249	0.274	0.356
	Side Down	0.216	0.285	0.407	0.310
	Total	0.540	0.534	0.681	0.666
5	Side Up	0.403	0.298	0.270	0.385
	Side Down	0.291	0.346	0.347	0.270
	Total	0.694	0.644	0.617	0.655

Big differences of the imprint value were noticed around the circumference. In addition, differences between the total imprint and maximum displacement applied during the compression test were observed (from 0.219 mm to 0.366 mm). This fact reflects an imperfect contact between the knife and the gasket at the beginning of compression test. It corresponds well with the lateral offset value explained before.

7.2.2.5 Micro-hardness measurements

The specimens were prepared by sectioning the gasket in the angular direction. The cross-sections were carefully grounded and polished (manually and using a Phoenix 4000 machine). The measurements were made using a Wild Leitz Durimet micro-hardness test machine with a Vickers diamond indenter. The measurement points were laid on four lines equidistant the knife imprint, with a distance of 35, 70, 210, and 350 μm from the gasket surface. In addition, micro-hardness measurements on the planar symmetry lines of the gasket cross-section were done.

A comparison between micro-hardness measurements and the plastic strain values extracted from FE calculations is shown in Figure 113. The variations of the field distributions were compared only.

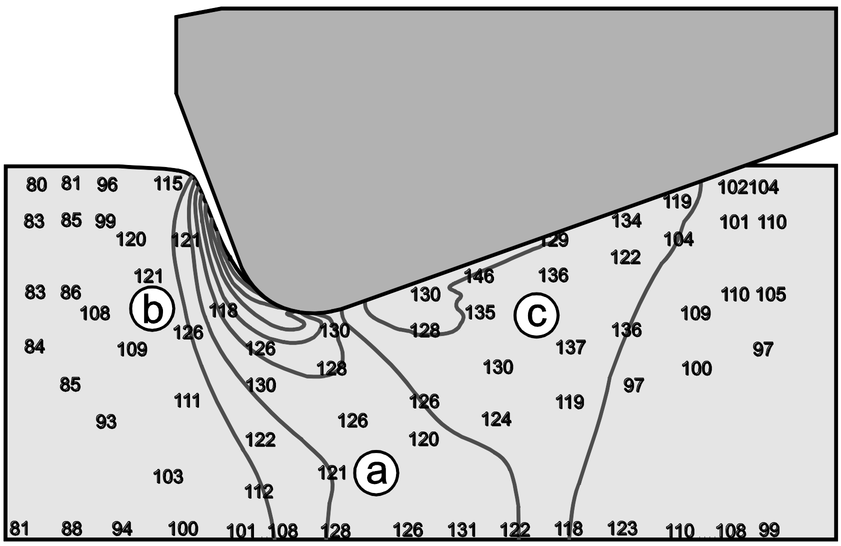

Figure 113 : A comparison between micro-hardness measurements and the plastic strain values from FE calculations

The micro-hardness distribution fits quite well at the taper knife side to the plastic strain distribution (b). There is a high value of micro-hardness under the flat knife side, which is not in good correlation with the plastic strain distribution (c). For what concerns the measurements made on the planar symmetry line for gasket cross-section a peak occurs under the flat knife side next to the knife tip (a). The highest plastic strain values (FE calculation) are observed it the same place.

7.2.2.6 Micro damage examination

Micro-damage examination was performed in four positions of the knife imprint. A Veeco NT3300 contactless, optical 3D surface topography machine was used. Microscopic investigations for cracks near the knife tip were made, using an optical microscope Leica

MZ16 and an electron microscope Leica Cambrige S360. The sample formed a slice from the gasket in the radial direction. The magnification of 2500x and 5000x for the electron microscope was applied. During the surface damage examination with the Veeco NT3300 no crack was found. Using the electronic microscope, cracks were found just under the knife tip (Figure 114).

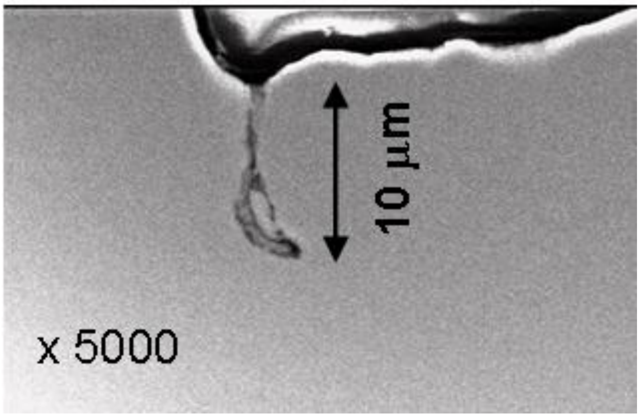

Figure 114 : Micro-crack under the knife tip

Also, the gasket compressed by using sharp flanges (knife tip radius equal to 0.01 mm) was examined. For CF joint with sharp knife edge, cracks were found in the gasket cross-section under the knife tip. A bifurcation crack was observed. The crack length was of around 10-15 µm. Cracks were noticed on both sides of the gasket. Because of the strong plastic flow in this region, it was impossible to visualize the grain boundaries after pickling (see Figure 115).

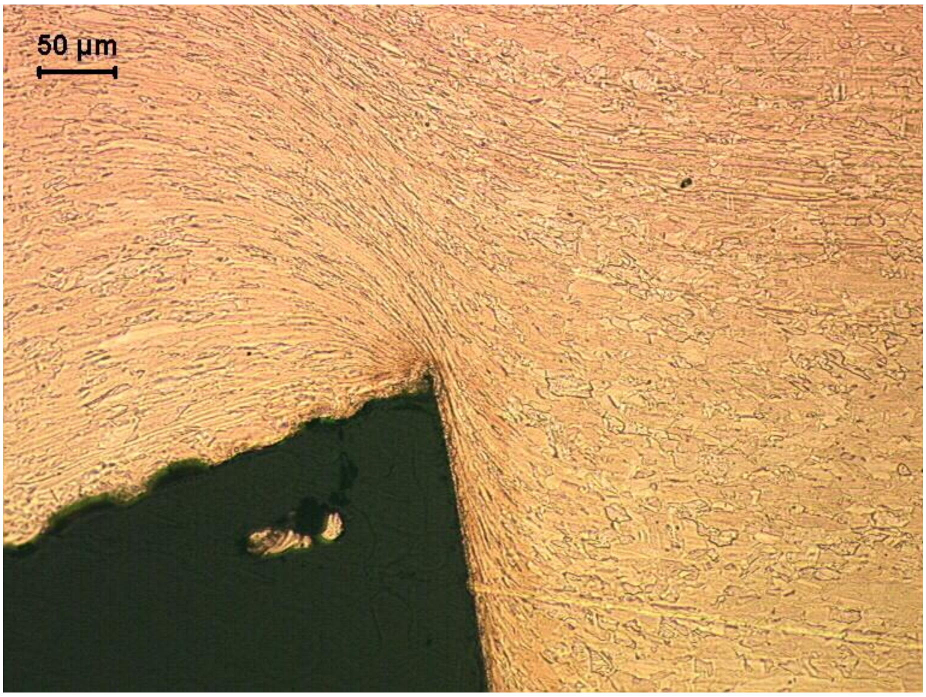

Figure 115 : The plastic flow near the knife tip

7.3 The CLIC joint

Lots of components were adopted from other existing accelerators (for example SLAC), but even these component need revision, changes or replacements. The UHV joint for beam line of CLIC was at first adopted from SLAC design, but after careful studies new design variants were proposed. As the next point, the experimental studies carried out on the new UHV joint are presented.

7.3.1 The maximum displacement checking

The joint should fulfil the minimum displacement requirements and provide the smooth transition from flange through the gasket to the second flange. There should be no gap between the parts. To check this experimentally, the profile measurements were performed for all new joint variants. The profile was measured by means of the couture graph machine (see Figure 116) by measuring the shape changes on flange-gasket-flange surface in the aperture.

Figure 116 : The couture graph machine

The measurements were done for 4 faces (A, B, C and D) of the aperture shape on each specimen. A typical shape profile (specimen 1, face B) is presented in Figure 117.

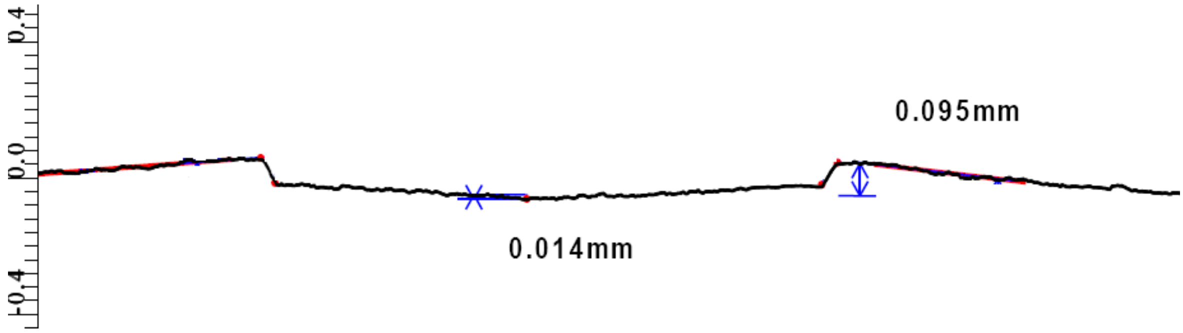

Figure 117 : Shape profile for proposed joint, specimen no. 1, face B

The measurements were done for new CLIC design (specimens 1, 2) and for improved new design (specimen 3). All data collected from measurements are presented in Table 21.

Table 21: Displacement into the aperture

	Specimen no.:	Maximum imprint	Position	Profile A	Profile B	Profile C	Profile D
New design	1	0.22	Knife	0.068	0.095	0.063	0.100
	1	0.22	Gasket	-0.118	-0.014	-0.081	-0.038
	2	0.21	Knife	0.063	0.109	0.076	0.098
	2	0.21	Gasket	-0.129	-0.012	-0.087	-0.032
Improved new design	3	0.35	Knife	0.403	0.298	0.270	0.385
	3	0.35	Gasket	0.291	0.346	0.347	0.270

Also, the shape was controlled after unbolting to check if the “knife” deformations were elastic or plastic. The “knife” displacements for specimens 1, 2, 3 were of permanent (plastic) type.

7.3.2 Leak tightness tests

All joints used in the UHV systems should be leak tight. To check this, the leak detector is used. The leak detector consists of the primary pump, the ion pump, the leak rate and the pressure measurement devices. The setup for measurements was filled by using helium bottle and connected to leak detector by means of the bolted joint (see Figure 118).

Figure 118 : Leak tightness testing setup

To carry out the test, the joint was assembled together with two flanges with blanked aperture. The aperture volume was closed by welding the blanking plates on either flange. Also, one flange was drilled and a small pipe was welded to connect the leak detector with the volume clamped inside the joint. The joint was fixed by eight bolts M8. The air was evacuated from the system and the helium sensitivity was checked by spraying the helium close to the joint and constructing a helium reservoir (plastic bag) all around the joint. At first the joint failed the test. The reason was bad machining quality of the knife surfaces. Scratches and irregular and bumpy surface of flange knife were detected (see Figure 119).

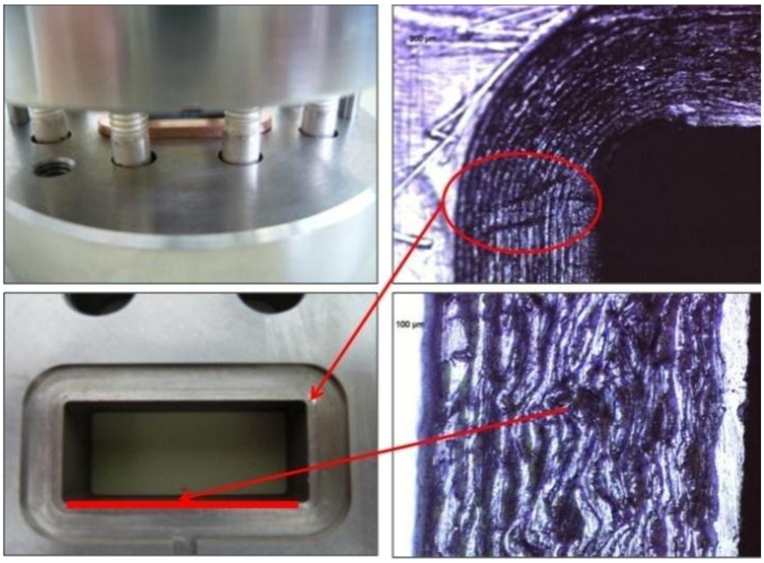

Figure 119 : Scratches and bad machining knife surface

For this reason the second prototype was manufacture. The test setup and the procedure was exactly the same. The leak tightness test was passed and was confirmed four times. The 1.4E-10 mbar/ls leak rate level was achieved with about 60% of clamping load (lack of flange to flange contact). The measurement and comparison between the test imprint and the maximum possible imprint is shown in Figure 120.

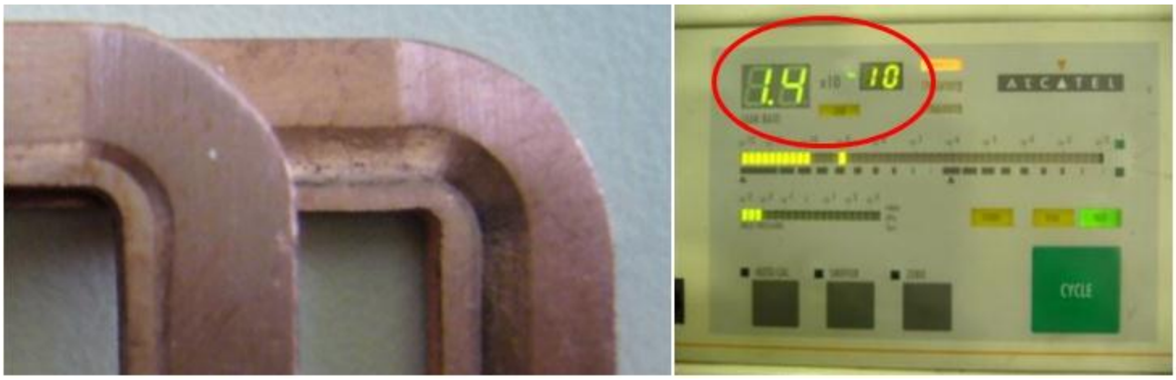

Figure 120 : Comparison between test and maximum imprints , and leak rate measurement

Chapter VIII:

Conclusions And Perspectives

8 CONCLUSIONS AND PERESPECTIVES

The present Thesis covers a large spectrum of problems: from the practical engineering problems to the complex academic aspects. Knowledge and experience gained during the research created strong basis for future design methods related to all-metal joints. The following points covered by the Thesis deserve special attention and should be highlighted:

- Analysis and description of the phenomena induced by irradiation process in the lattice and their influence on material properties.
- New kinetic law of evolution of irradiation induced damage embedded in the CDM.
- Implementation of new finite element in CASTEM (open architecture FE program) suitable to perform analysis of evolution of irradiation induced damage fields under mechanical loads. Proposal of a method of ultimate load estimation in the contact problem involving edge (knife) – gasket (seal) configuration.
- FE analysis of standard ConFlat joints widely used in the Large Hadron Collider at CERN.
- Optimum parametric design of UHV joint for CERN future facility - CLIC linear collider.

The present Thesis constitutes an attempt at understanding the phenomena related to loss of tightness in the ultra-high vacuum systems for accelerators and other high energy physics related constructions. In particular, a classical edge (knife) – gasket (seal) configuration of the joint has been analyzed in the framework of rate independent plasticity and continuum damage mechanics (CDM).

The CDM calculations clearly indicate high probability of formation of micro-damage fields close to the steep extremity of the edge, regarded as rigid punch interacting with elastic-plastic foundation. The opposite extremity with smaller slope does not induce high intensity damage fields and plays the role of the so called “sealing surface”. In view of distribution of all three principal components of damage tensor a macro-crack propagation spoiling integrity of UHV system is highly probable. This conclusion has been confirmed by suitable experimental evidence. In order to obtain a reasonably good estimation of the critical load (contact pressure) representing the onset of macro-crack an algorithm based on the numerical analysis and the experimentally collected data has been developed. The model is capable of predicting the lower and the upper bounds for the critical load, which in the context of UHV systems should be understood as the load range creating favourable conditions for the loss of tightness of the seal. The algorithm is currently applied in the design of UHV systems for superconducting particle accelerators.

The extended CDM constitutive model developed in the Thesis includes motion of the yield surface defined in the space of effective parameters. The back-stress evolution law, expressed in terms of increment of plastic strains, is based on the hardening modulus being a function of the volume fraction of clusters of defects. This is due to the Orowan mechanism of interaction of dislocations with the lattice defects, including enhanced shear stress necessary for a dislocation to overcome obstacles. Also, the yield point becomes a function of the accumulated dose, expressed in terms of dpa, which corresponds to the experimentally confirmed effect where the measured hardening curve (for a given dose) can be shifted along the strains axis to meet some sort of unified hardening curve for a given material. Finally, a finite element model has been built in order to compute evolution of both types of damage fields (mechanically and radiation induced) as a function of plastic strains in an UHV seal subjected to radiation.

It is believed that the above presented constitutive model will help to understand the mechanism of evolution of mechanically and radiation induced ductile damage as well as the related hardening effects. The model can be used to describe many structures subjected to radiation, including ductile targets.

Using a phenomenological formula of the compression force evolution based on FE results, it is possible to estimate the sealing loss for ConFlat joint in the case of the material property changes for example, during annealing at elevated temperatures or irradiation process without employing time consuming calculations. It should be mentioned that there exist different copper grades which have drastically different properties. For example, fully annealed copper has the yield point equal to about 50 MPa whereas for the OFHC grade it is equal to about 210 MPa at room temperature. It corresponds with different joint behavior even for the same joint geometry. It is worth pointing out, that joints can change their behavior globally and locally during the operation time. For this reason, the temperature influence during bake-out process, cryogenic background and irradiation background should definitely be taken into account. For example, OFE copper at cryogenic temperatures has yield point equal to about 370 MPa instead of 210 MPa at room temperature. Also, after the irradiation process, the changes in yield point value are strongly notable for copper irradiated to 0.1 dpa. The yield point value has increased to about 200 MPa. With the simple analytical formula presented in the Thesis it is possible to estimate the spring rate or the force evolution for ConFlat gasket by using the results of simple tensile test: the elastic modulus E, the yield point σ_0, and the hardening modulus H. This is very helpful in the design process of ultra-high vacuum installations.

Based on this knowledge a new concept and design of UHV joint for the CLIC accelerator was created and tested. The requirements were the leak tightness, good electro wave transmission, optimum cost in production and easy assembly process. The new design has been proposed after detailed studies based on the concept adopted from the SLAC accelerator. The leak tightness capacity estimation combined with the FE calculations were used during the design process of the new connection type called CLIC RF waveguides joint. The advantages of new joint are the symmetry and small displacements inside the aperture. This makes the joint easy in use, rather cheap and keeping good electro wave transmission properties. The tightness has also been experimentally confirmed.

For what concerns the perspectives of future research, the following problems have to be solved:

- Given the localization of strains in the seal a constitutive model based on large strains has to be developed,

- Coupling between the mechanically and radiation induced damage fields has to be taken into account,
- Experimental analysis of possible anisotropy in the evolution of radiation induced damage fields subjected to mechanical loads has to be carried out,
- Interaction between the inclusions and both types of damage in the heterogeneous continua needs further insight,
- Asymmetric behaviour of micro-cracks and micro-voids under tension and compression should be accounted for in the constitutive model,
- Evolution of damage fields under cyclic loads is certainly worth investigating,
- Optimum design of ultra-high vacuum joints subjected to radiation and mechanical loads against reliability needs certainly further studies in view of future applications in modern instruments of high energy physics and nuclear power plants,

REFERENCES

1 R.K. Abu Al.-Rub and G.Z. Voyiadjis, "On the coupling of anisotropic damage and plasticity models for ductile materials", International Journal of Solids and Structures 40, pp. 2611-2643, 2003

2 A. Akkerman, J. Barak, M.B. Chadwick, J. Levinson, M. Murat, Y. Lifshitz, "Updated NIEL calculation for estimating the damage induced by particles and γ-rays in Si and GaAs", Radiation Physics and Chemistry 62, pp. 301-310, 2001

3 A. Akkerman, J. Barak, J. Levinson, Y. Lifshitz, "Modeling of proton induced SEUs", Radiation Physics Chemistry 48(1), pp. 11-22, 1996

4 D.E. Alexander, L.E. Rehn, K. Farrel, R.E. Stoller, "Gamma-ray (electron) irradiation effects on tensile properties of ferritic alloys", Journal of Nuclear Materials 228(1), pp. 68-76, 1996

5 D.J. Bacon, F. Gao, Yu.N. Osetsky, "The primary damage state in fcc, bcc and hcp metals as seen in molecular dynamics simulations", Journal of Nuclear Materials 276 (1-3), pp. 1-12, January 2000

6 D.J. Bacon, Yu.N. Osetsky, "Modelling dislocation-obstacle interactions in metals exposed to an irradiation environment", Materials Science and Engineering A 400-401, pp. 353-361, July 2005

7 Bacon D.J., Osetsky Yu.N, "Multiscale modeling of radiation damage in metals: from defect generation to material properties", Materials Science and Engineering A365 (1-2), pp. 46-55, January 2004

8 Bacon D.J., Osetsky Yu.N., Stoller R., Voskoboinikov R.E., "MD description of damage production in displacement cascades in copper and α-iron", Journal of Nuclear Materials 323, pp. 152-162, 2003

9 M. Basista, W.K. Nowacki, "Modeling of Damage and Fracture Processes in Engineering Materials", IPPT PAN, Warsaw 1999

10 B. Battacharya and B. A. Ellingwood, "CDM analysis of stochastic ductile damage growth and reliability", Problematic Engineering Mechanics 14, pp. 45-54, 1999

11 M. Battaglia, A. de Roeck, E. Richard and D.J. Schulte, "Physics at the CLIC Multi-TeV Linear Collider", report of the CLIC Physics Working Group, CERN, Geneva 2004

12 M.B. Bernard, M.R. Bernard, M. Monne, "Caracteristiques du joint metallique a elasticite induite", Colloque International sur L'utra-Vide, Paris Faculte des Sciences, Juin 1967

13 J. Boehmert, H.W. Viehrig, A. Ulbritcht, “Correlation between irradiation-induced Changes of Microstructural Parameters and Mechanical Properties”, Journal of Nuclear Materials 334(1), pp. 71-78, August 2004

14 N. Bonora and P.P. Milella, “Constitutive modelling for ductile metals behaviour incorporating strain rate, temperature and damage mechanics”, International Journal of Impact Engineering 26(1-10), pp. 53-64, December 2001

15 Brunig M., “An anisotropic ductile damage model based on irreversible thermodynamics”, International Journal of Plasticity 19, pp.1679-1713, 2003

16 M. Brunig, “Eshelby stress tensor in large strain anisotropic damage mechanics”, International Journal of Mechanical Science 46, pp.1763-1782, 2004

17 M. Brunig and S. Ric, “Nonlocal continuum Theory of anisotropically damaged metals”, International Journal of Plasticity 21, pp.1346-1382, 2005

18 R. Brymer, W. Steckelmacher, “Demountable vacuum seal for operation at temperatures from -188°C to 800°C”, Journal of Scientific Instruments .36, pp. 278-281, June 1959

19 T.S. Byun, K. Farrell, “Irradiation hardening behavior of polycrystalline metals after low temperature irradiation”, Journal of Nuclear Materials 326, pp. 86-96, 2004

20 T.S. Byun, K. Farrell, “Plastic instability in polycrystalline metals after low temperature irradiation”, Acta Materialia 52 (6), pp. 1597-1608, 2004

21 T.S. Byun, K. Farrell, N. Hashimoto, “Plastic instability behavior of bcc and hcp metals after low temperature neutron irradiation”, Journal of Nuclear Materials 329-333(2), pp. 998-1002, August 2004

22 T.S. Byun, N. Hashimoto, K. Farrell, “Deformation mode map of irradiated 316 stainless steel in true stress-dose space”, Journal of Nuclear Materials 351(1-3), pp. 303-315, June 2006

23 M.J. Caturla, N. Soneda, E. Alonso, B.D. Wirth, T. Diaz de la Rubia, J.M. Perlado, ”Comparative study of radiation damage accumulation in Cu and Fe”, Journal of Nuclear Materials 276, pp. 13-21, 2000

24 J.L. Chaboche, “Anisotropic Creep Damage in the Framework of Continuum Damage Mechanics”, Nuclear Engineering and Design 79, pp.309-319, 1983

25 X.F. Chen and C.L. Chow, “On damage strain energy release rate Y”, International Journal of Damage Mechanics 4, pp. 251-263, 1995

26 J.P. Cordebois and F. Sidoroff, “Endommagement anisotrope en elasticite et plasticite”, J. Mec. Theor. Appl., Numero Special., pp.45-60, 1982

27 J.P. Corcebois and F. Sidoroff, “Damage induced elastic anisotropy” in : “Mechanical Behavior of Anisotropic Solids”, J. P. Boehler, ed., Martinus Nijhoff, pp.761-774, Boston 1983

28 C.L. Chow and T.J. Lu, “An analytical and experimental study of mixed-mode ductile fracture under nonproportional loading”, International Journal of Damage Mechanics 1, pp. 192-236, 1992

29 C.L. Chow and X. J. Yang, “A Generalized Mixed Isothropic-kinematic hardening Plastic Model Coupled with Anisotropic Damage for Sheet Metal Forming”, International Journal of Damage Mechanics 13, pp. 81-101, 2004

30 P.M. Danielson, “Investigation of gasket coating materials for Ultrahigh-Vacuum seals”, Journal of Vacuum Science and Technology 7(3), pp. 449-452, May 1970

31 L. Davison and A.L. Stevens, “Thermodynamical constitution of spalling elastic bodies”, Journal of Applied Physics 44, pp. 668-674, 1773

32 T. Diaz de la Rubia, W.J. Phythian, ”Molecular dynamics studies of defect production and clustering in energeting displacement cascades in copper”, Journal of Nuclear Materials 191-194, pp. 103-115, 1992

33 P. Diepens, “Ultra-high vacuum demountable all-metal joints”, CERN internal report 1987

34 D. Edwards, D. McCafferty, L. Rios, “Sealing of knife-edge flanges after a high temperature vacuum firing”, Journal of Vacuum Science and Technology A16(6), p. 2114, November-December 1979

35 T.J. Edwards, J.R. Budge, W. Hauptli, “Thin-film polyimide gasket seals for ultrahigh vacuum”, Journal of Vacuum Science and Technology 14(2), p. 740, March-April 1977

36 L. Elsworth, L. Holland, L. Laurenson, “Bakeable vacuum seals using aluminium wire gaskets”, 3rd International Conference do Fluid Sealing Cambridge, England April 1967

37 H. Frend, “Progress in metal sealing techniques”, Vacuum 47(6-8), pp. 527-529, June-August 1996

38 G. Feng, S. Qu, Y. Huang, W.D. Nix, “An analytical expression for the stress field around an elastoplastic indentation/contact”, Acta Materialia 55 (9), pp. 2929-2938, 2007

39 R.B. Fleming, R.W. Brocker, D.H. Mullaney, “Development of bakeable seals for large noncircular ports on the Tokamak Fusion Test Reactor”, Journal of Vacuum Science and Technology A 17(1), p. 337, January-February 1980

40 W.R. Fowkes, R.S. Callin, A.E. Vlieks, “ High power RF window and waveguide component development and testing above 100 MW at X-band”, Linac’92 Conference, Ottawa, August 24-28, 1992

41 A.O. Fuente, "Thermal cycling and torque analysis of an ultrahigh vacuum flange", Journal of Vacuum Science and Technology A1(2), pp. 220-223, April-Jun 1983

42 A. Frohn, J.H. Schafer, J. Seidensticer, "Reusable metal sealing gasket", Review of Scientific Instruments 42, pp. 727, 1971

43 C. Garion, B. Skoczen, "Modeling of plastic strain induced martensitic transformation for cryogenic applications", Journal of Applied Mechanics 69 (6), pp.755–762, November 2002

44 C. Garion, B. Skoczeń, "Combined model of strain-induced phase transformation and orthotropic damage in ductile materials at cryogenic temperatures", International Journal of Damage Mechanics, 12(4), pp.331-356, 2003

45 W.B. Gauster, "Study of radiation damage in metals by positron annihilation", Journal of Vacuum Science and Technology 15 (2), pp. 688-696, March-April 1978

46 N.M. Ghoniem, S.H. Tong, J. Huang, B.N. Singh, M. Wen, "Mechanisms of dislocation-defect interaction in irradiated metals investigated by computer simulations", Journal of Nuclear Materials 307-311, pp. 843-851, December 2002

47 H. Gillette, "Choix et controle des O-ring", Revue Technique Suisse 62 (33), 1965

48 J.D. Gonczy, R.J. Ferry, R.C. Niemann, B. Roop, "UHV seal studies for the advanced photon source storage ring vacuum system", Proceeding of the 1991 IEEE Particle Accelerator Conference (APS Beam Physics), pp. 2304, San Francisco CA, May1991

49 A.L. Gurson, "Continuum theory of ductile rupture by void nucleation and growth", Journal of Engineering Materials and Technology-Transactions of the ASME 99 (1), pp. 2-15, 1977

50 R. Hambli, "Finite element simulation on fine blanking processes using pressure-dependent damage model", Journal of Material Processing Technology 116 (2-3), pp. 252-264, October 2001

51 K.E. Holbert, "Radiation Effects Damage", course on School of Electrical, Computer and Energy Engineering, Arizona State University, 2009

52 J. Holden, L. Holland, L. Laurenson, "Bakeable vacuum seals using aluminium-wire gaskets", Journal of Scientific Instruments 36(6), pp. 281-283, Jun 1959

53 M. Huhtinen, "Simulation of non-ionizing energy loss and defects formation in silicon", Nuclear Instruments and Methods in Physics Research A 491 (1-2), pp. 194-215, September 2002.

54 L.I. Ivanov, Yu.M. Platov, "Radiation Physics of Metals and its Applications", Cambridge International Science Publishing, Cambridge UK, 2004

55 D.D. Ivlew, “Rigid punch indentation into a plastic half-space”, PMM 23(2), pp. 274-284, 1959

56 L.M. Kachanov, “Time of the rupture process under creep conditions”, Izv. AN SSR, Otd. Tehk. Nauk 8, pp. 26-31, 1958

57 L.M. Kachanov, “Foundations of Fracture Mechanics” , Nauka, Moscow 1974

58 W.G. Kim, W.S. Ryu, K.N. Chaoo, S.B. Ahn, “Material Properties of Irradiated Type 304 and 316 Stainless Steels”, Proceeding of the International Symposium on Research Reactor and Neutron Science, Daejeon, Korea, April 2005

59 K. Kitamura, K. Itoh, T. Uchida, M. Kondoh, “Experimental and analytical studies on mechanical behaviour of knife-edge-type metal-seal flange for fusion vacuum sealing”, Journal of Vacuum Science and Technology A12(6), pp. 3217-3223, November-December 1994

60 J.R. Knaster, “The vacuum chamber in the interaction region of particle colliders: a historical study and developments implemented in the LHCb experiment at CERN”, CERN-ETSII, May 2004.

61 S. Kurokouchi, “Influence of lubricating conditions of fixing bolts on penetration of ConFlat® flange knife edge into gasket”, Journal of Vacuum Science and Technology A18(1), pp. 288-289, January-February 2000

62 S. Kurokouchi, S. Morita, “Reconsideration of the seal mechanism in the ConFlat® system”, Journal of Vacuum Science and Technology A19(2), pp. 693-696, March-April 2001

63 S. Kurokouchi, S. Morita, M. Okabe, “Characteristic of a taper-seal type gasket for Conflat® sealing system”, Journal of Vacuum Science and Technology A19(6), pp.2963-2967, November-December. 2001

64 S. Kurokouchi, S. Shinoda, Sh. Morita, ”Dependence of the seal property of ConFlat-type flanges on the final dimensions of the knife edge”, Journal of Vacuum Science and Technology A 21(2), pp. 438-448, May-April 2003

65 D. Krajcinovic, “Damage Mechanics”, Elsevier, Amsterdam 1996

66 D. Krajcinovic, “Damage mechanics: accomplishment, trends and needs”, International Journal of Solids and Structures 37(1-2), pp. 267-277, January 2000

67 R.A. Langley, “Simple aluminium gasket for use with both stainless steel and aluminium flange”, Journal of Vacuum Science and Technology A10(4), pp. 1185-1187, July-August 1992

68 H. Lamer and Ch. Tsakmakis, “Discusion of coupled elastoplasticity and damage constitutive equations for small and finite deformation”, International Journal of Plasticity 16(5), pp. 495-523, April 2000

69 E.H. Lee, M.H. Yoo, T.S. Byun, J.D. Hunn, K. Farrell, L.K. Mansur, “On the origin of deformation microstructures in austenitic stainless steel: part II – mechanisms”, Acta Materiallia 49 (16), pp. 3277-3287, 2001

70 J. Lemaitre, “A course on Damage Mechanics”, Springer-Verlag, Berlin, Germany 1999

71 J. Lemaitre, “Evaluation of dissipation and damage in metals submitted to dynamic loading” in: Proc. I.C.M. Kyoto, Japan 1971

72 J. Lemaitre, J.L. Chaboche, “Mechanics of solid materials”, Cambridge University Press, Cambridge UK 1994

73 J. Lemaitre, J.L. Chaboche, “Aspect phenomenologique de la rupture par endommagement”, Journal de Mecanique Appliquee 3 , pp.317-365, 1978

74 A. Litewka, “Effective material constants for orthotropically damaged elastic solid”, Archives of Mechanics 37, pp. 631-642, 1985

75 L. Luneville, S. Simeone, C. Jouanne, “Calculation of radiation damage induced by neutron in compound materials”, Journal of Nuclear Materials 353 (1-2), pp.89-100, July 2006

76 P. Lutkiewicz, Ch. Rathjen, “Finite element modelling and experimental validation of the sealing mechanism of the ConFlat joint”, Journal of Vacuum Science and Technology A 26 (3), pp. 537-544, May-Jun 2008

77 P. Lutkiewicz, C. Garion, Ch. Rathjen, “Design of a new UHV all-metal joint for CLIC”, Vacuum 84(1), Aug 2009, 289-292

78 P. Lutkiewicz, B. Skoczeń, C. Garion, ”Micro-damage propagation in ultra-high vacuum seals”, International Journal of Pressure and Piping, in print, doi:10.1016/j.ijpvp.2009.10.002.

79 P. Lutkiewicz, B. Skoczeń, ”Evolution of irradiation induced micro-damage fields in ductile materials subjected to plastic deformation”, submitted to the Journal of Nuclear Materials, under review, 2009

80 F.J. Magee, “The use of Teflon rope as a vacuum sealing material”, Journal of Vacuum Science and Technology 17(4), pp. 850, July-August 1980

81 M. Mapes, “Summary of quick disconnect vacuum flanges”, Journal of Vacuum Science and Technology A 19(4), pp. 1693-1698, July-August 2001

82 J. Marian, D. Wirth Brian, R. Schaublin, G.R. Odette, J. Manuel Perlado, “MD modeling of defects in Fe and their interactions”, Journal of Nuclear Materials 323 (2-3), pp. 181-191, December 2003

83 J. Matthews, “New perspectives on the theory of radiation damage in metals”, International Journal of Pressure Vessels and Piping 81(8), pp. 667-671, August 2004

84 B.C. Moore, "Vacuum sealing rough surfaces", Journal of Vacuum Science and Technology 2(3), pp. 160-161, May 1965

85 S. Murakami and N. Ohno, "A continnum theory of creep and creep damage," in: "Creep in Structures", A. R. S. Ponter and D. R. Hayhust, eds., Springer-Verlag, pp. 422-444, 1981

86 A. Needleman, V. Tvergaard, "An analysis of ductile rupture in notched bars", J. Mech. Phys. Sol. 32 (6), pp. 461-490, 1984

87 K. Nahshorn, Zhenyu Xue, "A modified Gurson model and its application to punch-out experiments", Engineering Fracture Mechanics 76 (8), pp. 997-1009, May 2009

88 N. Nita, R. Schaeublin, M. Victoria, "Impact of irradiation on the microstructure of nanocrystalline materials", Journal of Nuclear Materials 329-333(1), pp. 953-957, August 2004

89 M.J. Norgett, M.T. Robinson, I.M. Torrens, "A proposed Method of Calculating displacement dose rates", Nuclear Engineering and Design 33, pp. 50-54, 1975

90 M. Ortiz, J.C. Simo "An Analysis of a New Class of Integration Algorithms for Elastoplastic Constitutive Relations", International Journal for Numerical Methods in Engineerinag 23(3), pp. 353–366, May 1985

91 Yu.N. Osetsky, A. Serra, V. Priego, "Interaction between mobile dislocation loop in Cu and α-Fe", Journal of Nuclear Materials 276(1-3), pp. 202-212, January 2000

92 Yu.N. Osetsky, D.J. Bacon, A. Serra, B.N. Singh, S.I. Gulobov, "Stability and mobility of defect clusters and dislocation loops in metals", Journal of Nuclear Materials 276 (1-3), pp. 65-77, January 2000

93 Yu.N. Osetsky, D.J. Bacon, "Atomic-scale modelling of primary damage and properties of radiation defects in metals", Nuclear Instrumentations and Methods in Physics Research B 202, pp. 31-43, April 2003

94 J. Pamin, "Gradient plasticity and damage models: a short comparison", Computational Materials Science 32(3-4), pp. 472-479, March 2005

95 T. Pardoen, I. Doghri, F. Delannay, "Experimental and numerical comparison of void growth models and void coalescence criteria for the prediction of ductile fracture in copper bars", Acta mater 46(2), pp. 541-552, January 1998

96 A. Parraras, S.T. Ceyer, J.T. Yates, "An O-ring sealed rotary feedthrough for UHV applications", Journal of Vacuum Science and Technology 21(4), November-December 1982

97 H.H. Patte, "A demountable ultra-high vacuum joint", Review of Scientific Instruments 25, pp. 1132-1133, July 1954

98 R.N. Peacock, “Practical selection of elastomer material for vacuum seal”, Journal of Vacuum Science and Technology A17(1), January-February 1980

99 R.H.J. Peerling, M.D.G. Geers, R. de Borst and W.A.M. Brekelmans, “A critical comparison of nonlocal and gradient-enhanced softening continua”, International Journal of Solids and Structures 38, pp. 7723-7746, 2001

100 W.G. Perkins, “Permeation and outgassing of vacuum materials”, Journal of Vacuum Science and Technology 10(4), July-August 1973

101 M.A. Puigvi, Yu.N. Osetsky, A. Serra, “Interaction between vacancy and glissile interstitial cluster in iron and copper”, Material Science and Engineering A365(1-2), pp. 101-106, January 2004

102 Yu.N. Rabotnov, “Damage from creep” Zhurn. Prikl. Mekh. Tekhn. Phys. 2, pp. 113-123, 1963

103 Yu.N. Rabotnov, “Creep rupture” in: Proceeding 12 International Congress of Applied Mechanics, pp. 342-349, Standford 1968

104 Yu.N. Rabotnov, “Creep Problems in Structural Members”, North-Holland, Amsterdam 1969

105 K.C. Russell, B.K. Kim, “Void nucleation with embryo injection”, Journal of Nuclear Materials 251(1-3) , pp. 100-108, March 2006

106 I.M. Robertson, J. Robach, B. Wirth, “Mechanical Properties of Irradiated Materials”, Internationl Conference : Nuclear Energy in Central Europe, Portoroz, Slovenia 2001

107 A. Roth, “The interface-contact vacuum sealing processes”, Journal of Vacuum Science and Technology 9(1), pp.14-23, January 1972

108 A. Roth, “Vacuum sealing techniques”, Springer-Verlag, New York 1994

109 G. Rousselier, “Ductile Fracture models and their potential in local approach of fracture”, Nuclear Engineering and Design 105(1), pp. 97-111, December 1987

110 J.C. Schuchman, “Metal vacuum seals for the AGS”, Brookhaven National Laboratory internal report, 1965

111 W. Schulz, “Vacuum tight gold seals of any size made of wire and sheet”, CERN internal report, 1965

112 F. Sidoroff, “Description of anisotropic damage application to elasticity” in: “Physical Non-Linearities in Structural Analysis”, J. Hult and J. Lemaitre, eds., Springer, pp. 237-244, Berlin 1981

113 B.N. Singh, A.J.E. Foreman, H. Trinkaus, “Radiation hardening revisited: role of intracascade clustering”, Journal of Nuclear Materials 249 (1997), pp. 103-115, October 1997

114 J.C. Simo and J.W. Ju, "Strain- and stress-based continuum damage models: I-Formulation, II-Computational aspects" International Journal of Solid Structures 23, pp. 821-869, 1987

115 B. Skoczeń, "Functionally graded structural members obtained via the low temperatures strain induced phase transformation", International Journal of Solid Structures 44(16), pp. 5182-5207, August 2007

116 A. Souidi, C.S. Becquart, D. Domain, D. Terentyev, L. Malerba, A.F. Calder, D.J. Bacon, R.E. Stoller, Yu.N. Osetsky, M. Hou, "Dependence of radiation damage accumulation in iron on underlying models of displacement cascades and subsequent defect migration", Journal of Nuclear Materials 355 (1-3), pp. 89-103, 2006

117 Y. Suetsugu, M. Shirai, "Application of a Matsumoto-Ohtsuka-type vacuum flange to beam ducts for future accelerators", Journal of Vacuum Science and Technology A23 (6), pp. 1721-1727, November-December 2005

118 T.-M. Tan, S. Li, P.C. Chou, "Finite element solution of Prandtl's flat punch problem", Expert Systems with Applications: An International Journal 1 (1), pp.173-186, 1990

119 V. Tvergaard, "Influence of voids on shear band instabilities under plane strain conditions", International Journal of Fracture 17 (4), pp. 389-407, August 1981

120 W. Unterlerchner, "The influence of the mechanical properties of gasket materials on the reliability of bakeable ultrahigh vacuum flanges", Proc. 7th Intern. Vac. Congr. & 3rd International Conference of Solid Surfaces, Vienna 1977

121 W. Unterlerchner, "Some improvement work on ConFlat joints and their limit of reliability in large-size ultrahigh vacuum systems", Journal of Vacuum Science and Technology A 5(4), July-August 1987

122 K.M. Welch, G.T. McIntyre, J.E. Tuozzolo, D.J. Pate, "Brief comments on test results of both metal and elastomer vacuum seals", International symposium on electron beam ion sources and their applications, AIP Conference Proceeding 188, pp. 303-313, 1989

123 W.R. Wheeler, "The design of large vacuum seals for nuclear fusion machines", Proc. 7th Intern. Vac. Congr. & 3rd International Conference of Solid Surfaces, Vienna 1977

124 W.R. Wheeler, "Theory and application of metal gasket seals", The 10th National Vacuum Symposium (American Vacuum Society), pp.159, New York 1963

125 T. Wikberg, "Investigations of faulty ConFlat flanges on the ISR beam transfer prototype kicker magnet tanks" ISR-VA/TW/ck engineering note CERN, 1968

126 T. Wikberg, "Improvements of UHV copper gaskets", Journal of Vacuum Science and Technology 5(6), 1968

127 M. L. Wilkins, "Calculation of Elastic-Plastic Flow", Methods Comput. Phys. 3, pp. 211-263, 1964

128 B.D. Wirth, M.J. Caturla, T. Diaz de la Rubia, T. Khraishi, H. Zbib, "Mechanical property degradation in irradiated materials: A multiscale modelling approach", Nuclear Instrumentations and Methods in Physic Research B 180 (1-4), pp. 23-31, June 2001

129 C.H. Woo, A.A. Semenov, B.N. Singh, "Analysis of microstructural evolution driven by production bias", Journal of Nuclear Materials 206(2-3), pp. 170-199, November 1993

130 A.A. Vaculenco and M. Kachanov, "Continuum theory of medium with cracks" Izv. A. N. SSSR, M. T. T. 4, pp. 159-166, 1971

131 L. Verheyden, K. Klein, "New metallic seals for high and ultra-high vacuum – description and performances", Vacuum 21(9), pp. 401-411, September 1971

132 L. Verheyden, K. Klein, "The metallic four-lip seal description and analysis of the performances at different working conditions of this new static seal", 5th International Conference do Fluid Sealing Warwick, England, March-April 1971

133 G.Z. Voyiadis and T. Park, "Anisotropic damage for the characterization of the onset of macro-crack initiation in metals", International Journal of Damage Mechanics 5, pp. 68-92, 1996

134 G.Z. Voyiadis and T. Park, "The kinematics of damage for finite-strain elasto-plastic solids", International Journal of Engineering Science 37(7), pp.803-830, May 1999

135 G.Z. Voyiadjis and B. Deliktas, "A coupled anisotropic damage model for the inelastic response of composite materials", Computational Methods in Applied Engineering 183(3-4), pp. 159-199, March 2000

136 G.Z. Voyiadjis and B. Deliktas, "Multi-scale analysis of multiple damage mechanisms coupled with inelastic behaviour of composite materials", Mechanical Research Communications 27(3),pp.295-300, May-June 2000

137 M. Zanolli, "A new UHV flange connection using approved techniques", PS/ML/Note Tech. 82-12, 1982

138 J.F. Ziegler, "SRIM-2003", Nuclear Instrumentations and Methods in Physic Research B 219-220, pp. 1027-1036, 2004

139 S.J. Zinkle, Y. Matsukawa, "Observation and analysis of defect cluster production and interactions with dislocations", Journal of Nuclear Materials 329-333, pp. 88-96, 2004

140 S.J. Zinkle, B.N. Singh, “Analysis of displacement damage and defect production under cascade damage conditions”, Journal of Nuclear Materials 199, pp. 173-191, 1993

141 N. Yoshimura, “Water vapour permeation through Viton O-ring seals”, Journal of Vacuum Science and Technology A7(1), Jan/Feb, 1989

142 ”Joint metallique etuvable”, SEVA company prospect

143 “Varian vacuum views”, the Varian company prospect, Jan, 1967

144 www.cern.ch - official CERN website

145 “Advanced Analysis Techniques Guide”, ANSYS 11

FIGURE CAPTIONS